A Stromal CCL2/CCR2 Signaling Axis Regulates Chemotherapeutic Response in a Mouse Model of Breast Cancer

Elizabeth S. Nakasone
Watson School of Biological Sciences
31 March 2012

Māhalo Nui Loa

I would like to extend a deep and heartfelt thank you to all of those people who have provided me with endless aloha and kōkua throughout this incredible adventure.

Marilynn and Nelson Nakasone
Thomas Nakasone
Henry and Carmen Fukuda
Elsie Nakasone

Kara Dixon • Kimberly Ishimoto • Vickey Lee and Joseph Rogers
Katie Liberatore • Carrie Clendaniel • Mélanie Eckersley-Maslin

St. Andrew's Priory School
Joseph Pacific

University of Hawai'i at Mānoa
Maqsudul Alam, Ph.D.
Shaobin Hou, Ph.D.
Stuart P. Donachie, Ph.D.

Alla Pikina, Ph.D.
Charles W. Riley, Ph.D.

Tracey A. K. Freitas, Ph.D.
Jennifer A. Saito, Ph.D.
Jimmy H. Saw
Kit Shan Lee, M.D.
Xuehua Wan
Mandelle Ruiz

University of Hawai'i
John A. Burns School of Medicine
George Hui, Ph.D.

University of Southern California
Steven E. Finkel, Ph.D.
Alison Kraigsley, Ph.D.
Vyacheslav Palchevskiy, Ph.D.
Evan Pepper, Ph.D.

Michael S. Waterman, Ph.D.

WSBS Entering Classes of 2008 and 2007

Marja Timmermans and her laboratory

Watson School of Biological Sciences
Leemor Joshua-Tor, Ph.D.
Dawn Meehan Pologruto
Alyson Kass-Eisler, Ph.D.
Kimberley Geer
Keisha John, Ph.D

Cold Spring Harbor Laboratory
Mikala Egeblad, Ph.D.
Hanne A. Askautrud
Jing Qiu
Tim Kees, Ph.D.
Juwon Park, Ph.D.
Jae-Hyun Park, Ph.D.
Pranay Sinha
Miriam Fein

Alea A. Mills, Ph.D.
Linda Van Aelst, Ph.D.
David L. Spector, Ph.D.

Lisa Bianco
Eileen Earl
Pamela Moody
Aigoul Nourjanova
Raisa Puzis

Memorial Sloan-Kettering Cancer Center
Scott W. Lowe, Ph.D.

University of California, San Francisco
Zena Werb, Ph.D.
Valerie M. Weaver, Ph.D.

Leslie C. Quick Foundation Fellowship
William Randolph Hearst Foundation Fellowship
U.S. Department of Defense Breast Cancer Research Program Pre-Doctoral Traineeship Award

Contents

Project Summary 1

Author Contributions 2

List of Abbreviations 3

List of Tables and Figures 7

Rationale 10

Introduction 11

Breast cancer: a primer 11

Therapeutic resistance and cancer 13

Solid tumors are complex systems comprised of cancer cells and stromal components that promote progression 17

Tumor-associated inflammation in breast cancer 20

Therapeutic targeting of the tumor microenvironment 21

Mouse models of breast cancer 24

Intravital imaging as a tool for studying the tumor microenvironment *in vivo* 26

Results 29

MMTV-PyMT mammary tumors respond to doxorubicin 29

MMTV-PyMT tumors relapse despite initial response 29

Doxorubicin response is tumor stage-dependent 32

In situ differences in cancer cell proliferation do not account for differences in doxorubicin sensitivity 40

Tumor stage-associated doxorubicin sensitivity is microenvironment-dependent 42

Doxorubicin treatment alters the tumor-associated inflammatory microenvironment 44

Doxorubicin induces necrosis *in vivo* 49

The presence of necrotic debris is sufficient to recruit myeloid cells 51

Recruitment of myeloid cells to areas containing necrotic debris is dependent on chemokine receptor signaling …… 53

Intratumoral expression of the chemokines CCL2 and CCL12 is upregulated following doxorubicin treatment ……... 53

CCL2 is stromally-derived …… 56

CCL2 recruits CCR2-positive monocytes …… 58

Small molecule antagonism of CCR2 *in vivo* ……... 64

Loss of CCR2 expression in the stromal compartment delays host relapse following cessation of doxorubicin treatment …… 69

The tumors of *Ccr2*$^{-/-}$ mice show differences in histopathology following doxorubicin treatment …… 72

Phenotypic changes in tumor vasculature are apparent when CCR2 expression is lost in the stromal compartment ……... 72

Transgenic MMTV-PyMT;*Ccr2*$^{-/-}$ mice respond better to doxorubicin than their heterozygous littermates …… 76

The enhanced response to doxorubicin following loss of CCR2 expression is a general phenomenon applicable to other classes of cytotoxic chemotherapeutics …… 81

Discussion ……..... 84

Tumor stage-dependent sensitivity to doxorubicin …… 84

Stromal CCL2/CCR2 signaling as a modulator of myeloid cell recruitment to tumors …… 85

Inhibiting myeloid cell recruitment to enhance chemotherapeutic response …….. 88

Altering tumor grade after chemotherapy treatment …… 89

Normalization of tumor vasculature …….. 90

Perspectives …… 92

Innate immunity as a modulator of therapeutic response …….. 92

Questions that remain 93

A toolkit for the future 97

Is antagonism of CCL2/CCR2 signaling clinically relevant? 100

Concluding Remarks 102

Experimental Methods 103

Animals 103

Tumor transplantation experiments 103

Tumor response to doxorubicin, cisplatin, and cyclophosphamide 103

Tumor response to combination therapy with doxorubicin and RS 504393 104

Detection of necrosis and intratumoral cysts by ultrasound 104

Spinning disk confocal imaging of live mice 104

Analysis of *in vivo* imaging experiments 106

Histology and immunostaining 107

Analysis of myeloid cell infiltration by flow cytometry 109

Cytokine/chemokine array and ELISA 109

In vitro drug sensitivity 110

Vascular permeability 111

Statistical methods 112

References 113

Appendices 127

I. Isolation of primary cancer cells 128

II. Transplantation of primary cancer cells 130

III. Treatment of animals with chemotherapy 133

IV. Treatment of animals with RS 504393 and doxorubicin 135

V. Isolation of primary tumor cells for flow cytometric analyses 136

VI. Immunohistochemical staining of phospho-histone H3 (DAB staining) …… 139

VII. Immunofluorescence staining of α-SMA (Mouse on Mouse staining) …… 142

VIII. Immunofluorescence staining of CD206 (staining of frozen tissue) …… 145

IX. Immunofluorescence staining of CCR2 and 7/4 (double label staining) ……..... 147

X. Detection of vascular permeability by lectin staining ……... 150

XI. Operating the Egeblad laboratory spinning disk confocal microscope ……... 152

XII. Preparation of animals for intravital imaging …… 154

XIII. Using Imaris …… 158

XIV. Immunostaining antibody information …… 181

XV. Flow cytometry antibody information ……... 184

Project Summary

The complex array of extracellular matrix molecules, immune cells, blood and lymph systems, and fibroblasts that comprises the tumor's stromal compartment influences tumor initiation, progression, metastasis, and therapeutic response. In breast cancer, myeloid cells make up a prominent proportion of the tumor stroma, and enhanced infiltration of these immune cells into tumors is associated with advanced disease and decreased relapse-free survival. Furthermore, high-level infiltration of myeloid cells into tumors following radiation therapy and chemotherapy is frequently observed in pre-clinical models. We therefore sought to determine the significance of myeloid cell recruitment following chemotherapy treatment and their role in therapeutic resistance.

Using intravital imaging of tumors in live mice, we observed that the tumors of the polyoma middle T antigen (PyMT) mouse model of luminal breast cancer show a stage-dependent sensitivity to treatment with doxorubicin. Doxorubicin treatment induces necrosis in drug-sensitive lesions, which consequently results in the recruitment of $CCR2^{+}Gr1^{+}7/4^{+}CD11b^{+}$ immature myeloid cells with monocytic morphology. Inhibiting recruitment of these cells via orthotopic transplantation of $Ccr2^{+/+}$ cancer cells from PyMT mice into $Ccr2^{-/-}$ mice delays tumor relapse indicating a role for these monocytic cells in chemoresistance. Changes in tumor vasculature and tumor grade accompany the delay in host relapse, indicating that CCR2 signaling may also have important effects on tumor angiogenesis and cancer cell differentiation and proliferation. This is further confirmed by the fact that transgenic PyMT;$Ccr2^{-/-}$ mice respond better to doxorubicin from the outset. The data herein presented show that antagonism of CCR2 signaling in combination with cytotoxic chemotherapy treatment may be a potentially powerful therapeutic strategy for the treatment of breast cancer.

Author Contributions

I would like to acknowledge the following people who contributed to the manuscript Nakasone *et al*, 2012. Hanne A. Askautrud performed some of the experiments treating cohorts of mice with doxorubicin and some of the imaging experiments, and assisted with the analyses of all imaging experiments and most of the immunostains. Jing Qiu performed some of the experiments treating cohorts of mice with doxorubicin or cisplatin. Tim Kees performed flow cytometric analyses for transplant mice and the *in vitro* doxorubicin sensitivity assays. Miriam Fein performed the *in vitro* lapatinib analyses. Jae-Hyun Park performed and quantified vasculature-associated immunostains. Juwon Park assisted in quantifying some of the immune cell stains. Pranay Sinha performed the BrdU incorporation experiments. Mikala Egeblad performed the necrotic debris-dependent myeloid cell recruitment imaging experiments.

List of Abbreviations

αSMA	α-Smooth muscle actin
ABCB2	ATP-binding cassette, sub-family B (MDR/TAP), member 2 (also known as BCRP)
ACTB	Chicken β-actin promoter
ACTB-ECFP	Reporter mouse line in which cells express enhanced cyan fluorescent protein (ECFP) under the control of the chicken β-actin promoter
ANOVA	Analysis of variance
Arg-1	Type 1 arginase
BCL-2	B-cell CLL/lymphoma 2
BCRP	Breast cancer resistance protein (also known as ABCB2)
bFGF	Basic fibroblast growth factor
BrdU	5-bromo-2′-deoxyuridine
C3(1)-Tag	Rat C3(1) promoter-driven simian virus 40 large T antigen mouse model
c-fms	Colony-stimulating factor receptor 1
c-fms-EGFP	Reporter mouse line in which cells express the enhanced green fluorescent protein under the control of the colony-stimulating factor receptor 1 promoter
CAF	Carcinoma-associated fibroblast
CCD	Charge-coupled device
CCL2	Chemokine C-C motif ligand 2
CCL12	Chemokine C-C motif ligand 12
CCR2	Chemokine C-C motif receptor 2 (receptor for CCL2 and CCL12)
CSF-1	Colony-stimulating factor-1 (see also, M-CSF)
CTLA-4	Cytotoxic T lymphocyte antigen-4

CXCL12	Chemokine C-X-C motif ligand 12 (also known at stromal cell-derived factor 1)
CXCR4	Chemokine C-X-C motif receptor 4 (receptor for CXCL12)
DC	Dendritic cell
ECFP	Enhanced cyan fluorescent protein
ECM	Extracellular matrix
ECFP	Enhanced cyan fluorescent protein
EGFP	Enhanced green fluorescent protein
EGFR	Epidermal growth factor receptor (also known as ErbB1, HER1)
ELISA	Enzyme-linked immunosorbent assay
ER	Estrogen receptor
FAP	Fibroblast activating protein
FOV	Field of view
GFP	Green fluorescent protein
G_iPCR	G_i-protein-coupled receptor
H2B-EGFP	Reporter mouse line in which the chicken β-actin promoter drives expression of a histone H2B-EGFP fusion protein
HE	Hematoxylin and eosin
HER2	Human epidermal growth factor receptor 2 (also known as ErbB2, neu)
HIF-1	Hypoxia inducible factor-1
IFN-γ	Interferon-γ
ICCD	Intensified charge-coupled device
IL-6	Interleukin-6
IL-10	Interleukin-10
IL-12	Interleukin-12
iNOS	Inducible nitric oxide synthase

i.p.	Intraperitoneal
i.v.	Intravenous
LPS	Lipopolysaccharide
MCP-1	Monocyte chemoattractant protein-1, also known as CCL2
MCP-5	Monocyte chemoattractant proteint-5, also known as CCL12
M-CSF	Macrophage colony-stimulating factor (see also, CSF-1)
MDSC	Monocyte-derived suppressor cell
MMP	Matrix metalloproteinase
MMTV-PyMT	Murine mammary tumor virus promoter-driven polyoma middle T antigen mouse model
MSC	Mesenchymal stem cell
NCI	National Cancer Institute
PBS	Phosphate-buffered saline
PDGFR	Platelet-derived growth factor receptor
P-GP	P-glycoprotein
PFA	Paraformaldehyde
PI	Propidium iodide
PI3K	Phosphoinositide-3-kinase
PR	Progesterone receptor
PyMT	Polyoma middle T antigen
RFP	Red fluorescent protein
ROI	Region of interest
STAT3	Signal transducer and activator of transcription 3
Tag	Large T antigen
TGF-β	Tumor growth factor-β
TIMP-1	Tissue inhibitor of metalloproteinase-1

TNF-α	Tumor necrosis factor-α
VEGF	Vascular endothelial growth factor

List of Tables and Figures

Table 1. Stromal components of solid tumors and their effects on tumor progression.

Figure 1. Type 1 and type 2 inflammatory responses in tumor progression.

Table 2. Fluorescent labels used to visualize components of the tumor microenvironment.

Figure 2. Histopathologic progression in two mouse models of breast cancer.

Figure 3. Tumor response to doxorubicin.

Figure 4. MMTV-PyMT tumors show therapeutic resistance to doxorubicin.

Figure 5. Tumor response to doxorubicin can be detected by caliper measurement as early as 24 hours following treatment.

Figure 6. Representative still image from a time-lapse movie of a multi-color spinning disk confocal intravital imaging experiment.

Figure 7. Progressive MMTV-PyMT mouse model allows for imaging different tumor stages in the same mouse.

Figure 8. Intravital imaging shows lesions resembling early carcinomas are the most sensitive to doxorubicin.

Figure 9. γ-H2AX staining for DNA damage confirms stage-specific doxorubicin sensitivity observed in intravital imaging experiments.

Figure 10. Differences in proliferation between tumor stages do not account for differential sensitivity to doxorubicin.

Figure 11. MMTV-PyMT cancer cells show tumor stage-dependent sensitivity to the ErbB1/2 inhibitor lapatinib *ex vivo*.

Figure 12. MMTV-PyMT cancer cells do not show tumor stage-dependent sensitivity to doxorubicin *ex vivo*.

Figure 13. Doxorubicin treatment alters the innate inflammatory microenvironment.

Figure 14. Intravital imaging shows that the highest degree of myeloid cell infiltration occurs in areas exhibiting the highest degree of cell death.

Figure 15. Myeloid cell recruitment occurs after induction of cell death.

Figure 16. *In vivo* dynamics of cell death show doxorubicin primarily induces necrosis in cancer cells.

Figure 17. Tumor-derived necrotic debris recruits myeloid cells.

Figure 18. Inhibition of G_i-protein-coupled receptor signaling abrogates recruitment of myeloid cells.

Figure 19. The chemokines CCL2 and CCL12 are upregulated in tumors of doxorubicin-treated mice.

Figure 20. CCL2 is stromally derived.

Figure 21. Double label immunostains show that CCL2 is expressed by some CD206-positive macrophages, but not expressed by fibroblasts, pericytes, endothelial cells, or neutrophils.

Figure 22. Flow cytometric analyses show increased numbers of $Gr1^+7/4^+CD11b^+$ immature myeloid cells in the tumors of doxorubicin-treated mice.

Figure 23. Double label immunostains for 7/4 and CCR2 show increased numbers of double-positive immune cells exhibiting a monocytic phenotype in the tumors of doxorubicin-treated mice.

Figure 24. Treatment of MMTV-PyMT tumor-bearing mice with the CCR2 inhibitor (CCR2i) RS 504393 has no effect on the tumor response to doxorubicin.

Figure 25. Flow cytometric analyses of vehicle-treated control mice show trends opposite to those observed in mice treated with PBS or doxorubicin alone.

Figure 26. Intravital imaging experiments of mice treated with RS 504393 shows cancer cell death in PBS-treated mice and stromal cell death in doxorubicin-treated mice.

Figure 27. Loss of CCR2 expression in the stromal compartment does not affect tumor take or tumor growth.

Figure 28. Flow cytometric analyses show no change in the numbers of $Gr1^{+}7/4^{+}CD11b^{+}$ immature myeloid cells in the tumors of *Ccr2*$^{-/-}$ hosts treated with doxorubicin.

Figure 29. Tumor relapse is delayed in *Ccr2*$^{-/-}$ hosts treated with doxorubicin.

Figure 30. The tumors of *Ccr2*$^{-/-}$ hosts are more cystic with fewer cells than those of wildtype hosts, 48 hours after doxorubicin treatment.

Figure 31. The tumors of *Ccr2*$^{-/-}$ hosts are of a lower grade and more differentiated than those of wildtype hosts, 6 weeks after the first doxorubicin treatment.

Figure 32. The tumors of *Ccr2*$^{-/-}$ mice show increased blood vessel density per tumor area with decreased leaky vasculature per tumor area, 48 hours after doxorubicin treatment.

Figure 33. The tumors of *Ccr2*$^{-/-}$ mice show an increase in pericyte coverage of blood vessels, as compared to the tumors of wildtype hosts, 48 hours after doxorubicin treatment.

Figure 34. The tumors of *Ccr2*$^{-/-}$ mice show a slight decrease in phosphorylation of VE-cadherin, as compared to the tumors of wildtype hosts, 48 hours after doxorubicin treatment.

Figure 35. Transgenic MMTV-PyMT;*Ccr2*$^{-/-}$ mice respond better to doxorubicin than their heterozygous littermates.

Figure 36. The tumors of MMTV-PyMT mice respond to both cisplatin and cyclophosphamide.

Figure 37. The tumors of *Ccr2*$^{-/-}$ mice respond better to cisplatin than those of wildtype hosts.

Figure 38. Hypothesis describing how stromal CCL2/CCR2 signaling might influence chemotherapeutic response.

Rationale

Despite major scientific advancements that have resulted in improvements in early detection and therapeutics, stabilization of incidence rates, and a decline in death rates, breast cancer remains the second leading cause of cancer-related mortality in women in the United States. Furthermore, approximately 30% of women who are diagnosed with early breast cancer and successfully enter remission will present with recurrent local or metastatic breast cancer that, if not intrinsically refractory, acquires resistance to standard systemic chemotherapies, which are the only options available for the treatment of disseminated disease (Siegel et al., 2011, Brewster et al., 2008).

We have an excellent understanding of how cytotoxic therapies induce cell death and how cancer cells acquire resistance to these drugs *in vitro* (Gonzalez-Angulo et al., 2007). Such knowledge has resulted in the development of strategies to overcome resistance to cytotoxic therapies (Fojo and Bates, 2003). But the biggest challenge at present is the fact that tumors are continually evolving tissues, adept at finding ways of circumventing strategies aimed at eliminating malignancies and therapeutic resistance.

What has become evident over the past few decades is that the microenvironment in which cancer cells reside is crucial to the development of disease, its progression, and chemotherapy resistance, and that targeting different components of the tumor microenvironment may be an important and viable strategy in the treatment of both locally advanced and recurrent, chemotherapy refractory breast cancer (Hiscox et al., 2011). Thus, we have focused our efforts on determining how one component of the breast tumor microenvironment – the myeloid cell – interacts *in vivo* with cancer cells, how these interactions influence therapeutic response, and identifying ways of altering these interactions to improve this response.

Introduction

Breast cancer: a primer

Breast cancer is currently the most common malignancy and the leading cause of cancer-related mortality in women world-wide (Jemal et al., 2011). Despite these global trends, we have achieved major advancements in our understanding of the basic biology underlying tumor initiation, progression, and metastasis, as well as in our standards of care in the clinic, especially with respect to prevention, diagnosis, and treatment (AACR Cancer Progress Report 2011). These advancements have resulted in improved early detection of breast cancers, stabilizing incidence rates, and decreasing mortality rates (DeSantis et al., 2011).

One of the most important recent advancements in our understanding of breast cancer has been the classification of tumors based on molecular subtype. Traditionally, breast cancers were diagnosed based on histopathologic analyses that were broadly classified as *in situ* (tumors that have not yet breached the basement membrane surrounding the mammary epithelium in which the lesion has arisen) or invasive (tumors that have breached the basement membrane and invaded the surrounding tissues). The type of tumor the patient presented with was then identified based on specific morphological features (reviewed in Malhotra et al., 2010). At the turn of the twenty-first century, three pivotal studies that analyzed expression data derived from the tumors of human patients showed that breast tumors, regardless of whether they are *in situ* or invasive, could be classified based on specific molecular characteristics (Perou et al., 2000; Sorlie et al., 2001; Sorlie et al., 2003). This classification system identifies four major molecular subtypes of breast cancer – luminal A, luminal B, $HER2^{+}$, and the triple negative/basal-like – as well as two less common subtypes (normal breast-like and $Claudin^{low}$), that can be identified based on the presence (or absence) of a short list of immunohistochemical markers.

Luminal A tumors account for approximately 40% of the breast cancer cases diagnosed, and are characterized by low proliferation (by Ki67 staining), expression of the estrogen receptor (ER) and/or the progesterone receptor (PR), with low expression of HER2 (human epidermal growth factor

receptor 2, also known as ErbB2, neu). These tumors frequently display low to moderate histopathologic tumor grade, and have the best prognosis of the six molecular subtypes. Luminal B tumors are the second most commonly diagnosed breast cancer subtype, accounting for approximately 20% of breast cancers. These tumors are characterized by high proliferation, low expression of ER and/or PR, and variable expression of HER2. They often exhibit poorer histopathologic grade as compared to luminal A tumors, as well as frequent mutations in the *p53* tumor suppressor gene. The $HER2^+$ subtype accounts for approximately 10-15% of all breast cancers, and is characterized by expression of HER2 without expression of ER and PR. Like luminal B tumors, tumors of the $HER2^+$ subtype frequently display poorer histopathologic grade than those of the luminal A subtype and often harbor *p53* mutations. The fourth major subtype, the triple negative/ basal-like tumors, also account for approximately 10-15% of all breast cancer cases and are the most aggressive of the four major molecular subtypes. Triple negative breast cancers, as their name implies, lack expression of ER, PR, and HER2, and frequently exhibit mutations in *p53*. Importantly, not all triple negative breast cancers are basal-like, and not all basal-like breast cancers are triple negative. Basal-like tumors are derived from the myoepthelial layer of cells that lines the epithelial cells of mammary ducts, and frequently express epidermal growth factor receptor (EGFR, also known as ErbB1 or HER1). In contrast, triple negative breast cancers can arise from either this myoepithelial cell population or the epithelial cells that form the mammary ductal structures, and frequently result from mutations in *p53*. *BRCA1/2*-mutant breast cancers frequently fall into the triple negative/basal like subtype (reviewed in Malhotra et al., 2010).

Standard of care for breast cancer continues to consist of breast-conserving surgery to remove the primary tumor followed by radiation therapy (this is a preventative measure used to ensure the cancer has been completely eradicated, and is preferred over chemotherapy as it is a localized therapy). However, in patients where the primary tumors are large, neoadjuvant chemotherapy is used to shrink tumors prior to surgery, while in patients with disseminated disease, adjuvant chemotherapy is used as the preventative measure instead of radiation therapy. Most chemotherapeutic regimens

used to treat breast cancers are anthracycline-based (usually doxorubicin in combination with cyclophosphamide), and are often followed by treatment with a taxane (usually paclitaxel). Furthermore, patients with tumors positive for hormone receptors receive some form of hormone therapy, such as the small molecule antagonist of ER, tamoxifen. With the identification of molecular subtypes, novel targeted therapies have also been added to these drug combinations to improve tumor shrinkage. For example, patients that are HER2 positive will receive either herceptin, a monoclonal antibody that antagonizes HER2, or lapatinib, a small molecule antagonist of EGFR/HER2 (recommendations for standard of care by the NCI breast cancer work group as described in Carlson et al., 2009). Stratification of patients in this manner and the use of these molecular targeted therapies have dramatically improved our ability to treat breast cancers.

Therapeutic resistance and cancer

Despite the major advancements that have been made in breast cancer therapy, resistance to systemic therapy is a major obstacle in the treatment of these tumors. It is estimated that approximately 30% of patients with breast cancer will present with local and distant recurrences (Gonzalez-Angulo et al., 2007). Resistance to systemic therapies (these include cytotoxic chemotherapies and hormone therapies) may be intrinsic, that is, due to certain pre-existing qualities of the cell, or it may be acquired following prolonged exposure to therapeutic agents. Resistant cells that remain undetected after treatment and elimination of the bulk tumor mass (termed minimal residual disease) contribute to tumor relapse, both locally and systemically. Furthermore, cancer cells that acquire resistance to the chemotherapies used during treatment of the primary tumor are frequently resistant to other classes of chemotherapeutics used to treat recurrent (usually metastatic) breast cancer, a phenomenon termed cross-resistance. Frequently cross resistance is due to the increased expression of drug efflux transporters like the ATP-binding cassette transporter MDR1 or anti-apoptotic proteins like BCL-2 (Gonzalez-Angulo et al., 2007).

Intrinsic resistance, that is, resistance already inherent to cancer cells before any type of therapy is administered, is a relatively infrequent phenomenon when compared with acquired resistance. The two most frequently observed examples of intrinsic resistance are pre-existing genetic mutations and the exhibition of stem-like properties. Identification of mutations that exist in cancer cell populations prior to any form of therapy is becoming an important area of study, especially with respect to molecular targeted therapies in leukemias. For example, new studies are focused on developing methods for identifying clones of cells containing resistance-conferring mutations in the tyrosine kinase domains of the *Bcr-Abl* fusion oncogene prior to therapeutic treatment to tailor molecular targeted therapies (Leder et al., 2011; Pfeifer et al., 2012).

The second form of intrinsic resistance frequently cited is resistance arising from the properties attributed to having a stem-like phenotype. Cancer cells exhibiting stem-like properties (whether they are bona fide [Li et al., 2008] or merely exhibit a mesenchymal phenotype with the functional characteristics of stem cells [Mani et al., 2008; Blick et al., 2010]) are characterized by decreased proliferation, self-renewal, and pluripotency (Visvader and Lindeman, 2008). The slow proliferation rate of these stem-like cells is one mechanism that can drive therapeutic resistance in this population (Dembinsk and Krauss, 2009). More recently, it has been shown that normal tissue stem cells frequently express high levels of ATP-binding cassette transporters that allow for drug efflux (expression is turned off following differentiation) to protect this population from drug-induced cytotoxicity, and that this is also true of cancer cells exhibiting a stem-like phenotype (reviewed in Dean et al., 2009).

In contrast to intrinsic mechanisms of resistance, acquired resistances are more common, and generally come in two flavors: intrinsic and environment-mediated. Intrinsic acquired resistance results from adaptations inherent to cancer cells that protect them from drug-induced cytotoxicity. Many of the mechanisms by which cancer cells acquire this type of resistance have been elucidated *in vitro* in cancer cell lines. Some of the most common of these mechanisms include altered repair mechanisms (e.g. activation of DNA damage repair pathways following cisplatin therapy; reviewed in

Martin et al., 2008), mutation of molecular targets (e.g. mutations of *Her2* conferring resistance to lapatinib; Tortora et al., 2011), and enhanced drug efflux (e.g. through upregulation of drug transporters like the breast cancer resistance protein, BCRP; reviewed in Leonessa and Clarke, 2003). Although many of these acquired intrinsic resistances have been mechanistically described *in vitro*, few of these mechanisms – with the exception of mutation-driven resistances – have been confirmed *in vivo*, as animal models of minimal residual disease do not currently exist, and the cohorts of patients and patient tissues required to do the types of analyses required to confirm these processes are widely unavailable (Gilbert and Hemann, 2011).

The second type of acquired resistance is environment-mediated drug resistance, and it is a unique form resistance, in that it is entirely dependent on interactions between cancer cells and their surrounding environment, disappearing when cancer cells are removed from this environment. One important example that illustrates this type of resistance was published in 1990 by Teicher et al. In this study, the group generated mammary carcinoma cell lines (derived from the EMT-6 cell line) that were highly resistant to various alkylating agents *in vivo* by serial passage in chemotherapy-treated mice. However, *ex vivo* testing for therapeutic sensitivity showed that in early passage cultures, these same cell lines that showed a high degree of therapeutic resistance *in vivo* were as sensitive to drug treatment as the parental cell line *in vitro*. Moreover, treatment and further passaging *ex vivo* did not alter *in vivo* resistance to therapeutic treatment when cell lines were re-implanted into mice.

As the importance of the microenvironment in therapeutic response has only recently become a major area of research, few mechanisms of environment-mediated resistance have been identified. The majority of the earlier studies on this type of resistance have focused on the biochemical and biophysical properties of tumors that regulate drug distribution and drug activity. These mechanisms include abnormal interstitial pressure (usually due to abnormalities in blood and lymphatic circulation) that impedes diffusion of drugs from capillaries into tumor tissues (reviewed in Heldin et al., 2004), and unusually acidic or anoxic environments in tumor tissues removed from blood vessels that can prevent drug activity both by limiting cancer cell proliferation – which is necessary for many

cytotoxic chemotherapies to function – or by directly modifying chemotherapies (Mahoney et al., 2003; Rohwer and Cramer, 2011 [review]; Teicher et al., 1981 [*in vitro* study]).

Mechanisms of environment-mediated resistance that involve biological mechanisms, such as cell adhesion and soluble factors (e.g. cytokines), have also been identified. Like cancer cell intrinsic-mechanisms of therapeutic resistance, a majority of the studies that demonstrate these two types of resistance have been performed using *in vitro* co-culture systems. The most common adhesion-mediated resistance mechanism arises from integrin-mediated (mostly β1 integrins) interactions between cancer cells and extracellular matrix components that either activate signaling pathways (e.g. the interleukin-6 [IL-6]/signal transducer and activator of transcription 3 [STAT3] pathway) to promote cancer cell survival or enhance degradation of pro-apototic proteins (Shain et al., 2009; Shain et al., 2001; Hazlehurst et al., 2007). Resistance mediated by soluble factors frequently involves paracrine signaling between cancer cells and stromal cells, in which a factor produced by cancer cells induces expression of a pro-survival signal in a stromal cell that then acts on the cancer cells. For example, in a primary multiple myeloma / bone marrow stromal cell co-culture system, cancer cell-derived basic fibroblast growth factor (bFGF) induces expression of IL-6 in bone marrow stromal cells, which then promotes cancer cell survival (Bisping et al., 2003).

More recently, tumor microenvironment groups have begun to combine *ex vivo* organotypic co-culture systems involving primary cancer and stromal cell types with *in vivo* manipulations of mouse models of cancer to study environment mediated-resistance; however, only a handful of these studies have been performed. One of the earliest of these studies is one that shows that in a mouse model of Burkitt's lymphoma, doxorubicin-induced genotoxic stress induces the production of IL-6 in thymic endothelial cells, which then goes on to promote the survival of minimal residual disease (Gilbert and Hemann, 2010). More recently, blockade of macrophage recruitment into tumors in a mouse model of breast cancer via neutralizing antibodies against colony stimulating factor-1 (CSF-1), has been shown to improve therapeutic response to paclitaxel and cisplatin (DeNardo et al., 2011). These studies have been important in underscoring the necessity of utilizing *in vivo* systems to

identify mechanisms of environment-mediated drug resistance, given the fact that *in vivo* targeting many of the resistance pathways identified using *in vitro* systems is often unsuccessful. Frequently, because of the complexity of the tumor microenvironment, mechanisms of environment-mediated resistance identified *in vitro* either contribute very little to chemoresistance or only account for a part of the resistance phenotype.

Solid tumors are complex systems comprised of cancer cells and stromal components that promote progression

Normal organs consist of two major compartments: the cellular compartment responsible for organ function, and the stromal compartment responsible for supporting and maintaining the environment in an appropriate homeostatic state for proper function. In much the same way, solid tumors can be thought of as being similarly organized, although they are structurally and functionally abnormal. Taking carcinomas as an example, the epithelial cell population that comprises the structures involved in primary organ function, are replaced by cancer cells that hijack and alter normal stromal processes to support proliferation and invasiveness (Egeblad et al., 2010). The tumor stroma is comprised of two major classes of constituents – a diverse cellular component and extracellular matrix (ECM) molecules – which have important functions in cancer cell survival and tumor progression (Table 1).

The primary cellular components of solid tumors include those derived from mesenchymal stem cells and cells of the vascular and immune systems. Mesenchyme-derived cells are those that differentiate from a tissue-resident mesenchymal stem cell (MSC) niche that exists to replenish the cells of the normal tissue stroma required for maintaining proper function. These MSCs can differentiate into a wide variety of cell types, including (but not limited to) chondrocytes, osteoblasts, adipocytes, and fibroblasts (Kolf et al., 2007). In most tissues, fibroblasts represent one of the major MSC-derived cell types in the stroma. Solid tumors will produce factors to activate these fibroblasts, generating carcinoma-associated fibroblasts (CAFs), which play active roles in tumor initiation and

Cell type	Effect on tumors	References
Normal epithelial cells	Inhibit	(Dong-Le Bourhis et al., 1997)
Myoepithelial cells	Inhibit (invasion, growth)	(Gudjonsson et al., 2002; Hu et al., 2008)
Fibroblasts	Promote (proliferation, angiogenesis, invasion)	(Bhowmick et al., 2004; Olumi et al., 1999; Orimo et al., 2005)
Mesenchymal stem cells	Promote (metastasis)	(Karnoub et al., 2007)
Adipocytes	Promote (tumor growth, survival, angiogenesis)	(Iyengar et al., 2005; Landskroner-Eiger et al., 2009)
Endothelial cells	Promote (angiogenesis, niche?)	(Ausprunk and Folkman, 1977; Calabrese et al., 2007)
Perivascular cells	Promote (vascularization) Inhibit (metastasis)	(Song et al., 2005) (Xian et al., 2006)
Bone marrow-derived cells	Promote (proliferation, invasion angiogenesis)	(Coussens et al., 2000; Du et al., 2008; Lyden et al., 2001)
Dendritic cells	Inhibit (stimulate antitumor immunity)	(Knight et al., 1985; Mayordomo et al., 1995)
Myeloid derived suppressor cells; Immature myeloid cells	Promote (angiogenesis, metastasis, reduce antitumor immunity)	(De Palma et al., 2005; Sinha et al., 2007; Yang et al., 2004; Yang et al., 2008b)
Macrophages, M1-like	Inhibit	(Sinha et al., 2005)
Macrophages, M2-like	Promote (invasion, angiogenesis)	(DeNardo et al., 2009; Lin et al., 2006; Lin et al., 2001)
Mast cells	Promote (angiogenesis)	(Coussens et al., 1999; Soucek et al., 2007; Yang et al., 2008a)
Neutrophils, N1	Inhibit (stimulate antitumor immunity)	(Fridlender et al., 2009)
Neutrophils, N2	Promote (angiogenesis, reduce antitumor immunity)	(Nozawa et a., 2006; Schmielau and Finn 2001; Shojaei et al., 2008)
T cells, $CD4^+$, T helper 2	Promote (metastasis)	(DeNardo et al., 2009)
T cells, $CD8^+$, cytotoxic	Inhibit (tumoricidal)	(Romero et al., 1998)
T cells, $CD4^+CD25^+$ regulatory	Promote (reduce antitumor immunity)	(Casares et al., 2003; Curiel et al., 2004)
T cells, gamma/delta	Inhibit (stimulate antitumor immunity)	(Girardi et al., 2001)
T cells, Th17	Promote (proliferation, angiogenesis) Inhibit (stimulate T cell antitumor immunity)	(Numasaki et al., 2005) (Hirahara et al., 2001)
B cells	Promote (reduce antitumor immunity)	(Inoue et al., 2006)
B cells, Immunoglobulins	Promote (stimulate inflammation-associated progression)	(Andreu et al., 2010)
Platelets	Promote (metastasis)	(Camerer et al., 2004; Nieswandt et al., 1999)

Table 1: Stromal components of solid tumors and their effects on tumor progression. From Egeblad et al., 2010.

progression. CAFs are the primary source of ECM molecules in solid tumors, and have been shown to stimulate cancer cell growth via the production of growth factors like transforming growth factor-β (TGF-β, Bhowmick et al., 2004), and promote angiogenesis, invasion, and metastasis through the production of chemokines like CXCL12 (also known as stromal cell-derived factor 1, Orimo et al., 2005).

Cells of the vascular system – the endothelial cells that form blood and lymphatic vessels and the pericytes that wrap and support these vessels – comprise another important component of the tumor microenvironment. As is true of normal tissues, tumors require blood vessels to deliver nutrients and oxygen, and lymphatic vessels to return excess fluid and molecules to the blood circulation. In order to generate blood vessels, tumors may co-opt existing vessels for their use (Holash et al., 1999), recruit endothelial cells and pericytes (angiogenesis, Carmeliet, 2000), or they may recruit bone marrow-derived cells that will differentiate into endothelial cells or pericytes in the tumor (vasculogenesis, Song et al., 2005). Unlike the vasculature of normal tissues, however, tumor blood vessels are highly abnormal, exhibiting disorganized architecture often with non-functional branches that do not reconnect to systemic circulation, irregular capillary beds, altered basement membrane structure, disrupted associations between endothelial cells and pericytes, and increased permeability. These changes disrupt normal blood flow and interstitial pressure gradients, which can impede nutrient, oxygen, and drug delivery and lead to compensatory shifts in expression, including upregulation of factors that can further promote angiogenesis, such as hypoxia inducible factor-1 (HIF-1, Bergers and Benjamin, 2003). In addition, lymphatic vessels that can assist in relieving interstitial pressure and returning excess fluids and proteins to blood circulation, also provide a means by which cancer cells can metastasize (Skobe et al., 2001).

The final group of cellular components of the tumor stroma consists of inflammatory cells of both the innate and adaptive immune systems. While inflammatory cells can have both pro- and anti-tumor effects, tumor-associated leukocytes generally show phenotypic and functional traits that allow them to provide signals that promote angiogenesis, proliferation, invasion, and subversion of anti-

tumor immune responses (Coussens and Werb, 2002). Some of the best characterized tumor-associated leukocytes are myeloid-derived suppressor and regulatory T cells that inhibit anti-tumor T cell responses (Sinha et al., 2007; Casares et al., 2003), macrophages that promote angiogenesis and invasion (Lin et al., 2001; Wyckoff et a., 2007), and $CD4^+$ T cells that promote metastasis (DeNardo et al., 2009). These interactions will be expanded on and discussed with respect to their effects on breast tumors in the following section.

The ECM of solid tumors includes proteoglycans, hyaluronic acid, collagen, fibronectin, and laminin. ECM molecules comprise a structural platform that provides physical support for tissues; however, changes in the organization of these fibers can promote tumor invasion and progression (Provenzano et al., 2006; Levental et al., 2009), and are equally important for tumor angiogenesis (Heissig et al., 2003). Interactions between the ECM and cell adhesion molecules (β1 integrin, for example) on cancer cells have also been shown to mediate both tumor progression and chemotherapeutic resistance (Park et al., 2006; Weaver et al., 1997; Hazlehurst et al., 2007). In addition to exerting effects dependent on direct interaction with cancer cells or other stromal cells, the ECM can also alter the bioavailability of various growth factors and chemokines (Hawinkels et al., 2008).

Tumor-associated inflammation in breast cancer

Interactions between tumor cells and the immune system play a critical role in the progression and metastasis of many types of cancers. Leukocytes of both the myeloid (innate) and lymphoid (adaptive) lineages exert tumor-promoting and tumor-inhibiting effects, depending on context, cell type, and mode of activation (Coussens and Werb, 2002). The two major tumor-associated inflammatory cell types – T cells and macrophages – exhibit dichotomous functional properties that can have dramatic effects on tumor progression and metastasis (Sato et al., 1998). These functional states have been extrapolated from the T_H1 and T_H2 helper T cell polarization states exhibited in response to pathogenic infections, are defined by distinct cytokine and chemokine

expression profiles (Mosmann and Coffman, 1989), and exhibit opposing functions (Kidd, 2003) (Figure 1). Furthermore, this same classification system for helper T cell effector functions has been applied to macrophages (Mantovani et al., 2002). In tumors, this polarization of T cells and macrophages in one direction heavily influences progression and development. In the simplified generalization of these polarization schemes, type 1 responses represent the acute inflammatory response and are generally associated with anti-tumor immunity, while type 2 responses represent the chronic inflammatory response and tend to promote progression and metastasis (DeNardo and Coussens, 2007).

In breast tumors, the primary leukocyte population is the tumor-associated macrophage, which can account for up to 80% of the entire tumor-associated leukocyte population (O'Sullivan and Lewis, 1994; this number is about 70% in the MMTV-PyMT mouse model [Egeblad et al., 2008]). These macrophages exhibit a type 2 (M2-like or alternatively activated) phenotype, and have been shown to promote tumor angiogenesis (Lin et al., 2006), interact with cancer cells to promote intravasation (Wyckoff et al., 2007), and contribute to chemotherapeutic response (Ahn et al., 2010; DeNardo et al., 2011; Shree et al., 2011). Moreover, immunohistochemical analyses of human breast tumors show that high numbers of macrophages in tumors is associated with both tumor progression and decreased relapse-free survival (Leek et al., 1996). These tumor-associated macrophages are predicted to be derived from tumor-infiltrating monocytes (Sica et al., 2000), which, if prevented from maturing into tumor-associated macrophages, can also promote progression by inhibiting anti-tumor T cell responses (Gabrilovich and Nagaraj, 2009). Thus, therapeutic targeting of these tumor-associated macrophages – perhaps by depletion, inhibition of recruitment, re-polarization, or antagonism of M2 effector functions – may prove to be a potentially powerful means of treating breast cancer (Bingle et al., 2002; Luo et al., 2006).

Therapeutic targeting of the tumor microenvironment

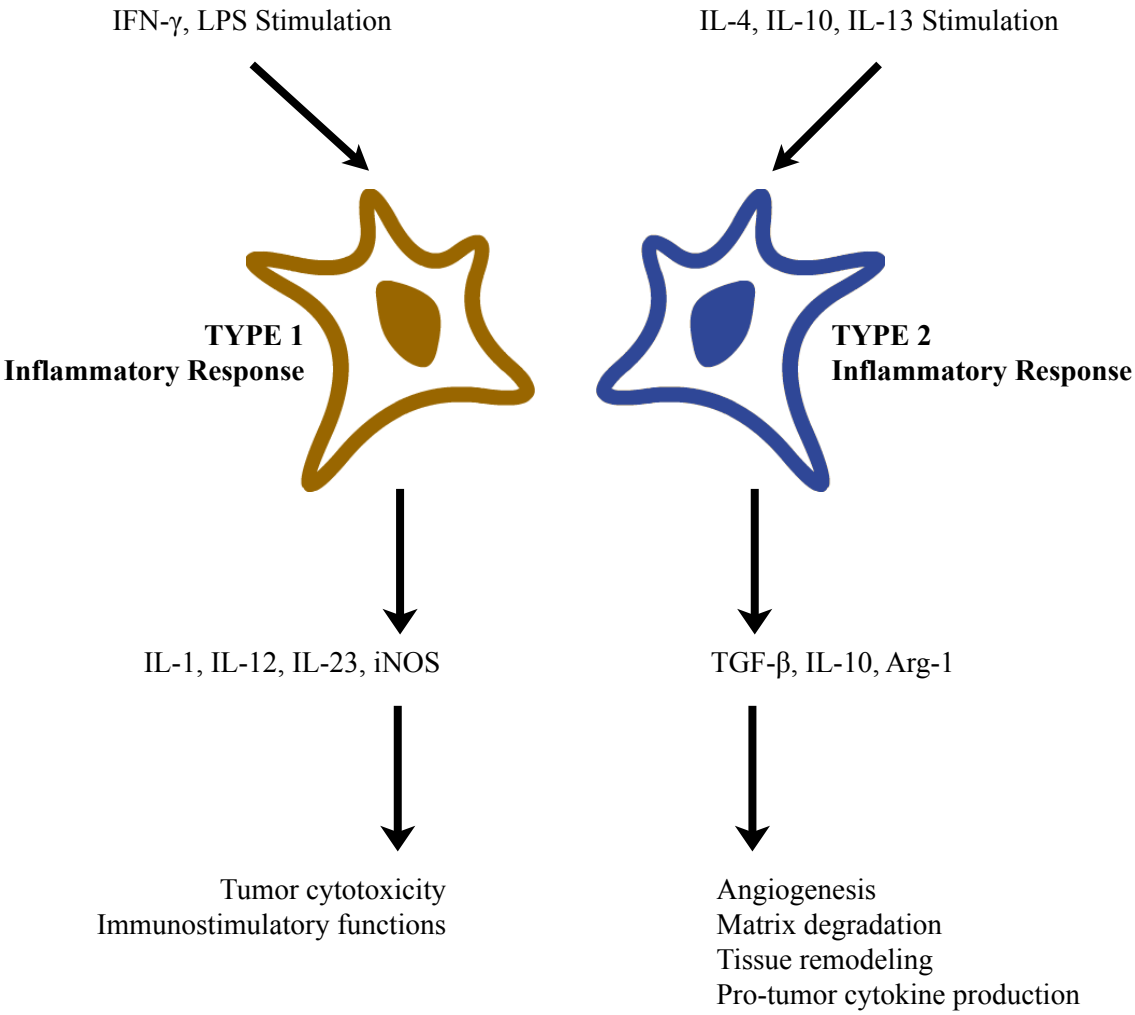

Figure 1. Type 1 and type 2 inflammatory responses in tumor progression. Polarized immune cell responses can influence tumor initiation and progression. In its simplest representation, type 1 responses occur following stimulation with interferon-γ (IFN-γ) or bacterial lipopolysaccharide (LPS), inducing expression of various cytokines and pro-inflammatory markers and promotoing anti-tumor effects. Conversely, type 2 responses occur following stimulation with interleukins -4, -10, and -13, and produce cytokines and anti-inflammatory markers that promote various pro-tumorigenic effects.

Over the past few decades, there has been a vast increase in our understanding of the complexities of solid tumor organization, the cues present in the microenvironment, and the physical and biochemical interactions that occur between cancer cells, stromal cells, and the ECM (Tlsty and Coussens, 2006). What has become apparent from this research field is that the microenvironment in which cancer cells reside plays as important a role in tumor initiation, progression, metastasis, and therapeutic response, as do the genetic alterations driving carcinogenesis (Liotta and Kohn, 2001). Thus, therapeutic targeting of the interactions between cancer cells and stromal components as prophylactic and therapeutic strategies has become an increasingly important area of research (Albini and Sporn, 2007; Joyce, 2005). Some of the stromal targets that are currently being studied include ECM-remodeling enzymes, fibroblasts, cells of the vasculature, and the signals regulating angiogenesis, tumor-associated immune cells, and chemokine-receptor pairs involved in drug resistance and metastatic spread.

Interactions between cancer cells and the ECM, as well as remodeling of the ECM, have been shown to be important for tumor progression and invasion. Disruption of ECM-cancer cell interactions – for example, by blocking β1 integrin signaling (White et al., 2004; Park et al., 2006; Bhaskar et al., 2007) – or inhibiting tissue proteases such as matrix metalloproteinases involved in cleavage of ECM proteins (Goss et al., 1998; Maquoi et al., 2004) have been shown to impede tumor progression and angiogenesis. Fibroblasts provide a variety of ECM proteins, growth factors, and chemokines that promote tumor progression. Targeting of factors such as fibroblast activation protein (FAP, Lee et al., 2005) or CXCL12 (Orimo et al., 2005) have also shown promise as therapeutics. In addition to these targets, fibroblasts express many of the same cell-surface markers and tyrosine kinase receptors that the cells of the vascular system express, and so targeting of some of these proteins (e.g., the platelet-derived growth factor receptor [PDGFR]) has been shown to impede angiogenic processes (Bergers et al., 2003; Sumida et al., 2011). Other anti-angiogenic therapies include inhibition of bone-marrow derived progenitor cell homing to tumors (DePalma et al., 2003), disruption of VEGF signaling (Yu et al., 2012), or induction of vascular normalization (Jain et al.,

2001). Modulation of tumor-associated inflammation has been one of the largest areas of stroma-targeted cancer therapeutics research. These strategies include depletion of specific immune cell populations, inhibition of downstream products of immune cell activation (e.g. cathepsins), blocking immune cell recruitment, and re-polarization of tumor-resident immune cells (reviewed in Demaria et al., 2010). In addition, some of the chemokine-receptor signaling pathways that are important in immune cell recruitment also play roles in chemotherapeutic resistance and cancer cell metastasis, and inhibition of some of these pathways, including the CXCL12/CXCR4 (Kim et al., 2010) has shown therapeutic promise.

While pre-clinical models have shown that components of the tumor microenvironment are important therapeutic targets, few of these strategies have entered the clinic, indicating that more research is needed. Two therapeutics targeting the microenvironment currently approved for clinical use include: the anti-angiogenic therapy bevacizumab (trade name Avastin), a monoclonal antibody that targets vascular endothelial growth factor-A (VEGF-A, Giantonio et al., 2007), and the immunomodulatory therapy ipilimumab (trade name Yervoy), a monoclonal antibody that depletes T cells expressing the inhibitory co-stimulatory signal cytotoxic T lymphocyte antigen-4 (CTLA-4) to potentiate anti-tumor immune responses (Hodi et al., 2010). Another drug currently on the market but not yet approved as a stroma-targeting agent, is the Bcr-Abl tyrosine kinase inhibitor imatinib (trade name Gleevec), which targets fibroblasts, endothelial cells, and pericytes, by inhibiting PDGFR (Bergers et al., 2003; Sumida et al., 2011).

Mouse models of breast cancer

Mouse models of cancer have proven to be an important tool in cancer biology both in basic and translational research. The most widely used models of breast cancer are transgenic models that employ the use of viral oncogenes (e.g., simian virus 40 [SV40] large T antigen [Tag], polyoma middle T antigen [PyMT]), growth factors (e.g. transforming growth factor-β [*Tgf-β*]) or their receptors (e.g. *ErbB2*/*neu*), cell cycle regulators (e.g. *Myc*), regulators of differentiation (e.g. *Wnt1*),

and knockouts models of tumor suppressor genes (e.g. *trp53*, *pRb*). The majority of the transgenic models that have been developed use the mouse mammary tumor virus long terminal repeat (MMTV) or whey acidic protein (WAP) promoter/enhancer regions to drive gene expression in mammary epithelial cells (Hennighausen, 2000).

The two mouse models we employ are the polyoma middle T antigen (PyMT) model in which MMTV drives expression of the PyMT tyrosine kinase oncoprotein (Guy et al., 1992), and the large T antigen model in which the rat C3(1) prostatic steroid binding protein promoter drives expression of the Tag oncogene (Maroulakou et al., 1994). Tumor formation in the MMTV-PyMT model usually occurs through the formation of a PyMT-p60$^{c\text{-}src}$ complex, which results in autophosophorylation of p60$^{c\text{-}src}$ tyrosine kinase, resulting in enhanced activity and transformation (Courtneidge and Smith, 1983; Courtneidge et al., 1986). In contrast, tumor formation in the C3(1)-Tag model results from binding and inactivation of the p53 and pRB tumor suppressor genes (reviewed in Ali and DeCaprio, 2001).

These two mouse models have been useful in the study of breast cancer, because they histopathologically and molecularly recapitulate human breast cancers. MMTV-PyMT tumors represent the luminal B molecular subtype, exhibiting low expression of the estrogen receptor with variable expression of ErbB2 in lesions at the carcinoma stage. C3(1)-Tag tumors represent basal-like breast cancers, showing a distinct lack of expression of both the estrogen and progesterone receptors, as well as ErbB2, and aberrant expression of cell cycle proteins. Furthermore, both models show progressive histopathologic tumor progression that are similar in organization to human breast tumors (Lin et al., 2003; Green et al., 2000k). In addition to being relevant models of human breast cancer, these transgenic models are useful in that they provide intact microenvironments and immune systems that are necessary for studying the contributions of tumor stroma to disease progression and therapeutic response.

While these transgenic models have proven to be very useful, there are a few shortcomings of these systems that include non-specific expression of viral oncogenes and large tumor burden. The

promoters used to drive expression of PyMT or Tag are active in other tissues in addition to the mammary glands; in both the MMTV-PyMT and C3(1)-Tag models, the primary tissue outside of the mammary glands in which tumors arise are the salivary glands. It is interesting to note that the C3(1)-Tag model was originally developed as a prostate cancer model, and that C3(1) is a "prostate specific" promoter. Indeed, while male mice develop prostate intraepithelial neoplasias that progress to invasive carcinomas similar to those observed in humans, female mice develop mammary tumors with 100% penetrance, although the reasons for mammary-specific expression of C3(1) are still unknown. Another shortcoming of both these models is that multiple tumors form in multiple mammary glands, resulting in high overall tumor burden that is often not physiologically relevant to human cancers.

Intravital imaging as a tool for studying the tumor microenvironment *in vivo*

The primary means of studying cancer processes *in vivo* have been measurements of tumor size and the immunohistochemical (or immunofluorescent) staining of tissues derived from animal models. However, advancements in microscopy and fluorescent reporters over the past two decades have enabled the visualization of various inter- and intracellular processes at high resolution in live, anesthetized animals (Pittet and Weissleder, 2011). These intravital microscopy technologies have proven to be especially invaluable for spatially and temporally dissecting the *in vivo* dynamics of tumor-stroma interactions (Lohela and Werb, 2010). Processes that have been unraveled by intravital imaging include anti-tumor T cell cytotoxicity (Boissonnas et al., 2007; Breart et al., 2008), the dynamics of changes in collagen composition and organization following therapeutic treatment (Brown et al., 2003), macrophage-dependent cancer cell intravasation and metastasis (Wyckoff et al., 2007), and vascular permeability (Yuan et al., 1994).

There are three major requirements for intravital imaging. These include appropriate preparation and exposure of tissues for imaging, fluorescent labeling of the tissue components of interest, and a paired microscopy-camera system capable of acquiring images (Jain et al., 2002). The

most common strategies used to address the these requirements include: heterotopic preparations (e.g. inoculation of the ear or eye orbital), permanent imaging windows, or exteriorized preparations (e.g. dorsal skin flap); transgenic fluorescent reporters and fluorescent injectables to label tissues; and multiphoton or confocal microscopy systems paired with charge-coupled device (CCD) cameras (Lohela and Werb, 2010). In our laboratory, using the polyoma middle T antigen mouse model of luminal breast cancer as our primary experimental system, we combine transgenic reporters with fluorescent injectables (Table 2) to visualize different components of the tumor microenvironment. Animals are anesthetized and a skin flap is surgically prepared to expose the inguinal mammary gland for imaging. Images are obtained over a period of 12 to 40 hours using an intensified CCD (ICCD) camera paired with a four-laser spinning disk confocal microscope system (Egeblad et al, 2008). Imaging in this manner has allowed us to study such processes as *in vivo* drug distribution, stage-dependent chemotherapeutic responses, *in vivo* mechanisms of chemotherapy-induced cell death, and myeloid cell behavior (Nakasone et al., 2012).

Label	Type	Localization
ACTB-ECFP	Transgenic	All cells; used to identify cancer cells
ACTB-H2B-EGFP	Transgenic	Nuclei; most visible in nuclei in which the chromatin is decondensed
c-fms-EGFP	Transgenic	All myeloid cells
Lycopersicon esculentum lectin	Injectable	Blood vessels
Propidium Iodide	Injectable	Dead/dying cells
Ricinus communis agglutinin I	Injectable	Blood vessels; basement membrane exposed to the vascular lumen

Table 2. Fluorescent labels used to visualize components of the tumor microenvironment.

Results

MMTV-PyMT mammary tumors respond to doxorubicin

In order to understand how various components of intact tumor tissues respond to cytotoxic chemotherapeutics, we needed a system in which tumors respond reasonably well to treatment. We examined two different mouse models representing two major molecular subtypes of breast cancer, whose tumors undergo stage-specific progression and show distinct, but relatively homogeneous molecular and histological pathologies (Herschkowitz et al., 2007, Figure 2A-B). These two models are the luminal-like MMTV-PyMT model where the murine mammary tumor virus promoter drives expression of the polyoma middle T antigen (Guy et al., 1992), and the basal-like C3(1)-Tag model where the rat C3(1) promoter drives expression of the simian virus 40 large T antigen (Maroulakou et al., 1994).

MMTV-PyMT and C3(1)-Tag tumor-bearing mice were administered doxorubicin or phosphate-buffered saline (PBS) on days 0, 7, and 14, and tumors were measured 2-3 times a week by caliper. Doxorubicin treatment significantly reduced tumor volume in MMTV-PyMT mice, as compared to PBS-treated control mice (Figure 3A, error depicted as mean ± SEM, where n = 11 doxorubicin-treated mice with 73 tumors, n = 12 PBS-treated mice with 56 tumors, $p < 0.0001$ at all time points, two-tailed Student's t-test). In contrast, treatment with doxorubicin did not reduce tumor volume in C3(1)-Tag mice as compared to PBS-treated controls (Figure 3B, error depicted as mean ± SEM, n = 7 PBS-treated mice with 23 tumors, n = 9 doxorubicin-treated mice with 23 tumors, p = NS at all time points, Student's t-test). Thus, we focused the remainder of our studies on the MMTV-PyMT mouse model.

MMTV-PyMT tumors relapse despite initial response

Although MMTV-PyMT mice treated with doxorubicin respond well to treatment, showing a decrease in total tumor burden (defined as the sum of the volumes of each tumor present/measured in the animal), virtually all tumors relapse following cessation of chemotherapy. Throughout the course

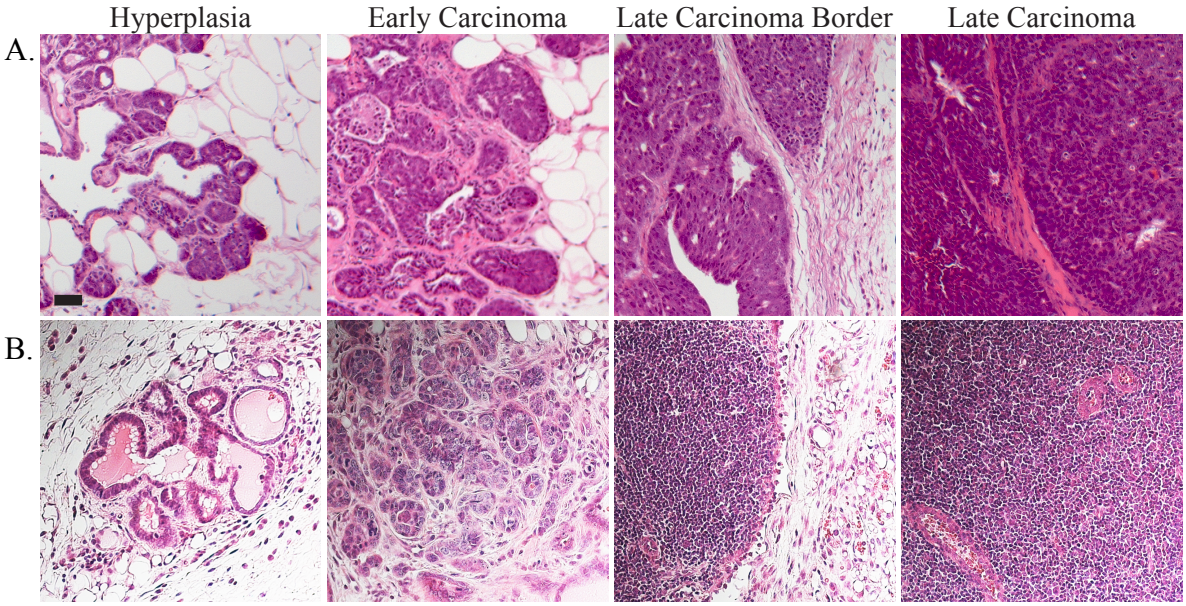

Figure 2. Histopathologic progression in two mouse models of breast cancer. (A) MMTV-PyMT model of luminal breast cancer. (B) C3(1)-Tag model of basal breast cancer. Scale = 50 μm.

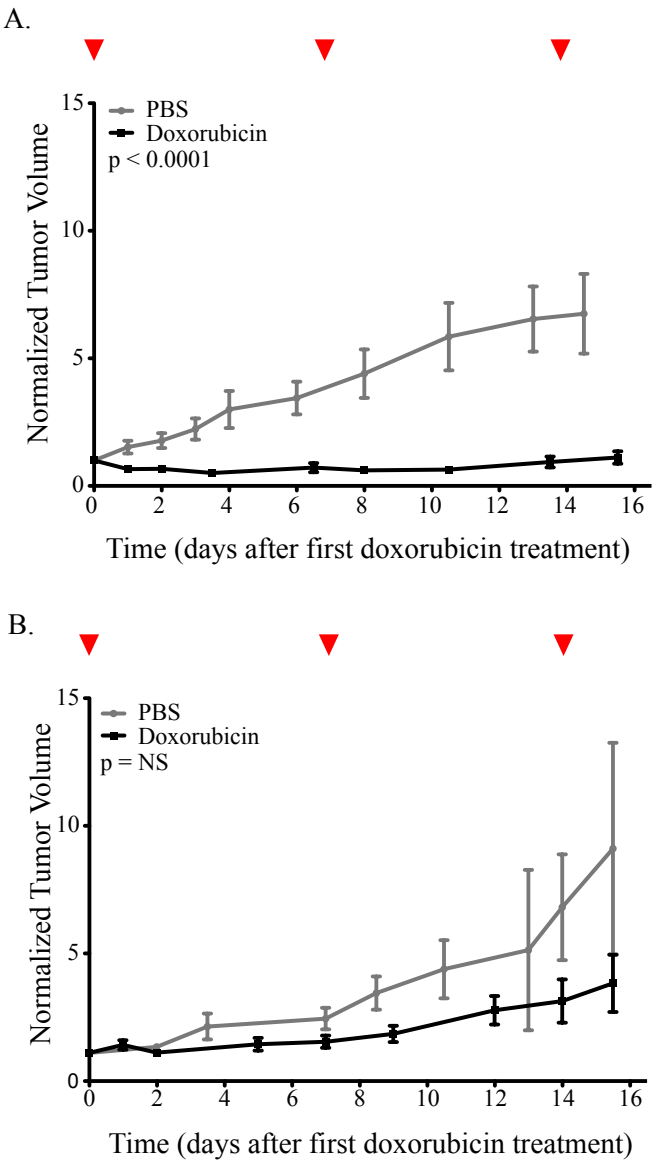

Figure 3. Tumor response to doxorubicin. (A) Tumors of MMTV-PyMT mice are sensitive to doxorubicin, while tumors of C3(1)-Tag mice are not (B). Doxorubicin was administered on the days desginated with red arrowheads. Error given as mean ± SEM, p-value based on two-tailed Student's t-test at each time point.

of chemotherapy treatment, the smallest and largest tumors showed a trend toward being refractory to treatment (Figure 4A, n = 10 mice, tumors sorted based on size at the start of treatment, % change in volume shown for each tumor 18 days after the first doxorubicin treatment, each color represents a different mouse), and new tumor lesions continued to form, albeit at a slower rate, throughout the treatment period (Figure 4B, error depicted as mean ± SEM, n = 12 PBS-treated mice with 20 new tumors appearing during treatment, n = 11 doxorubicin-treated mice with 18 new tumors appearing).

MMTV-PyMT tumors that did respond to doxorubicin treatment (usually those measuring approximately 8 to 12 mm in the longest diameter) showed signs of becoming refractory to treatment (Figure 4C, n = 73 tumors from 11 doxorubicin-treated mice, error depicted as mean ± SEM). On average, tumors that responded to the first dose of doxorubicin were less responsive and quicker to re-grow after each subsequent dose was administered. In addition, by three weeks after the first dose, nearly every one of these tumors had reached or surpassed its volumetric size at the start of treatment.

Doxorubicin response is tumor stage-dependent

That the smallest and largest tumors were mostly insensitive to doxorubicin, and that lesions sensitive to doxorubicin at the start of treatment became increasingly resistant to therapy with each subsequent dose, led us to hypothesize that doxorubicin response might be tumor stage-dependent. To determine the effect of doxorubicin treatment on different tumor stages, we used a combination of spinning disk confocal microscopy of live, tumor-bearing mice (Egeblad et al., 2008) and immunohistological analyses. While volumetric measurements based on caliper readings are difficult to translate into histopathologic staging of tumors, we used the generalization that small tumors tend to consist primarily of hyperplastic lesions, while large tumors tend to contain primarily late carcinoma lesions. Furthermore, for the pathologic staging of tumors in intravital imaging experiments and tissue stains, we classified lesions based on our own modification of a system previously described for MMTV-PyMT tumors, that takes into account cell morphology, organization of the ECM, and immune cell infiltration (Lin et al., 2003). We staged tumors for intravital imaging

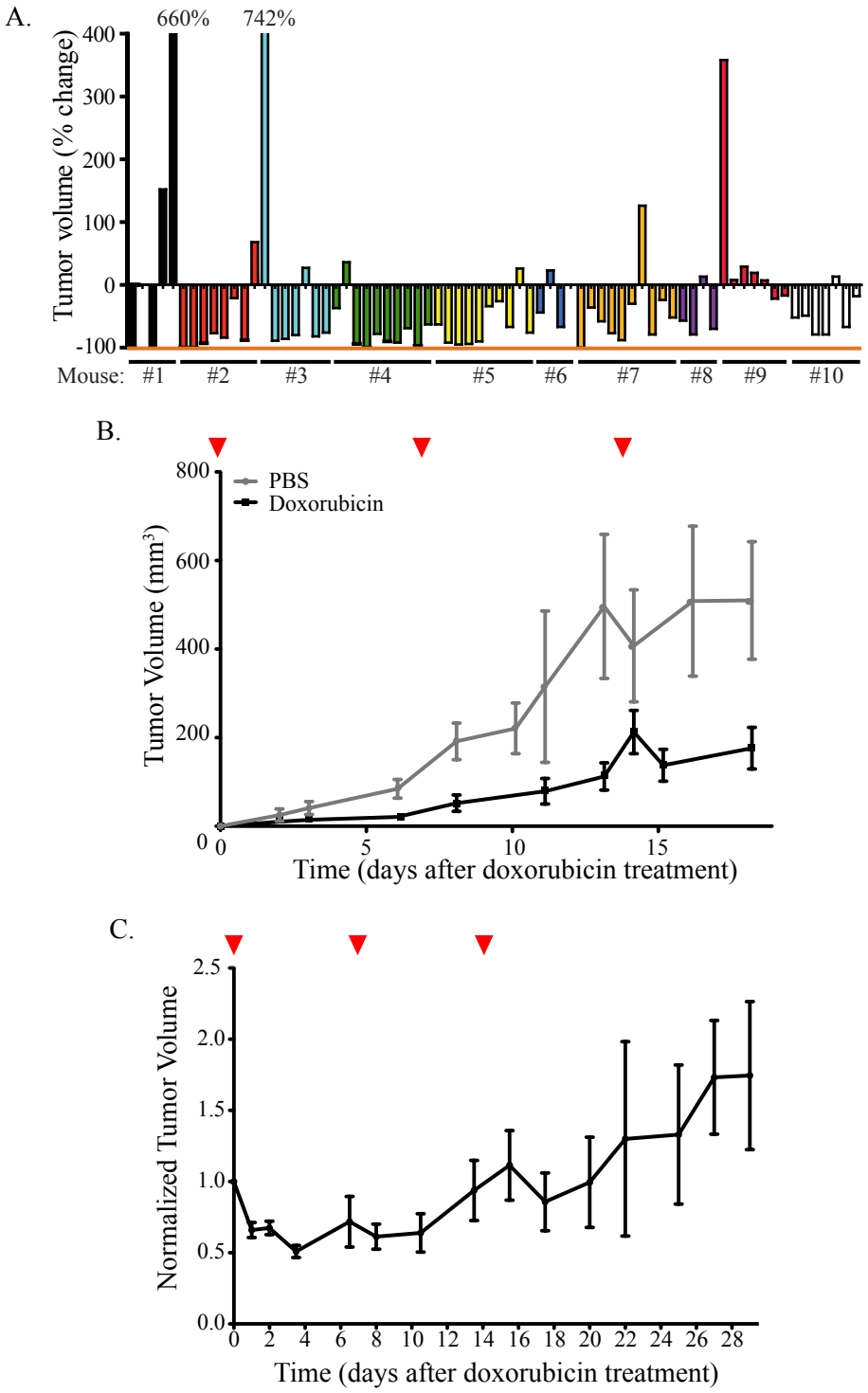

Figure 4. MMTV-PyMT tumors show therapeutic resistance to doxorubicin. (A) Waterfall plot of the percent change in tumor volume 18 days after the first doxorubicin treatment shows that the smallest and largest tumors tend to be refractory to treatment. Each color represents a different mouse, and tumors are arranged from smallest to largest as measured at the start of treatment. (B) New tumors form, albeit at a slower rate, after doxorubicin treatment. (C) Tumors of doxorubicin-treated mice relapse and become increasingly refractory to treatment despite initial response. Error depicted as mean ± SEM. Doxorubicin was administered on the days desginated with red arrowheads.

experiments as follows: hyperplastic lesions were small lesions with very few infiltrating myeloid cells; early carcinoma stages were larger, and showed myeloid cell infiltration and a few blood vessels; late carcinomas were large, very densely packed lesions containing many highly abnormal blood vessels (see Figure 7 for example, see Egeblad et al., 2008 for further details). We staged tumors for histopathologic and immunohistochemical analyses as follows: hyperplastic lesions were those exhibiting cancer cell hyperproliferation, with intact basement membrane and remnants of ductal structures; early carcinomas were those that exhibited cancer cell invasiveness without any recognizable ductal structures, immune cell infiltration, and maintained some degree of "normal" stromal tissue (e.g. adipocytes); late carcinomas were very densely packed tissues with highly invasive and often undifferentiated cancer cells, exhibiting high degrees of immune cell infiltration and areas of high ECM deposition (see Figure 2 for example).

We found that tumors responded to doxorubicin with significant decreases in tumor volume that are measurable by caliper as early as 24 hours after treatment (Figure 5, error depicted as mean ± SEM, n = 89 tumors from 9 mice for PBS-treated controls, and n = 96 tumors from 10 mice for doxorubicin-treated mice; change in tumor volume as compared to 0 h for PBS-treated animals, p = NS at both time points, change in tumor volume as compared to 0 h for doxorubicin-treated animals, $p = 4.5 \times 10^{-6}$ at 24h, $p = 3.0 \times 10^{-10}$ at 48h using a paired two-tailed Student's t-test; difference in tumor volume between PBS- and doxorubicin-treated mice, p = 0.88 at start of treatment, p = 0.02 at 24h, $p = 4.2 \times 10^{-10}$ at 48h using a two-tailed Student's t-test). In order to analyze the effects of doxorubicin on different tumor stages, we therefore chose to study the acute response to doxorubicin treatment, up to 48 hours after treatment.

For *in vivo* imaging experiments, MMTV-PyMT mice were first crossbred with ACTB-ECFP and c-fms-EGFP reporter mice, so that cancer cells were labeled with enhanced cyan fluorescent protein (ECFP) and all myeloid cells were labeled with enhanced green fluorescent protein (EGFP), (Figure 6). Expression of these reporters enabled visualization of tumor lesions at different stages and tracking of myeloid cells, which represent one of the most abundant stromal components of murine

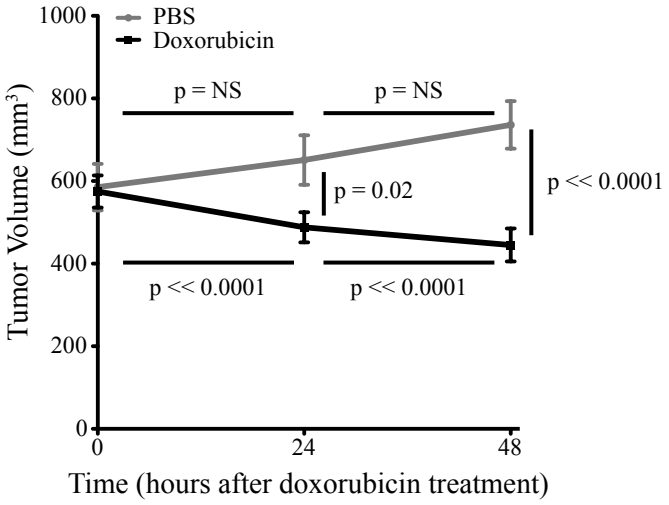

Figure 5. Tumor response to doxorubicin can be detected by caliper measurement as early as 24 hours after treatment. Error depicted as mean ± SEM. p-value based on two-tailed Student's t-test.

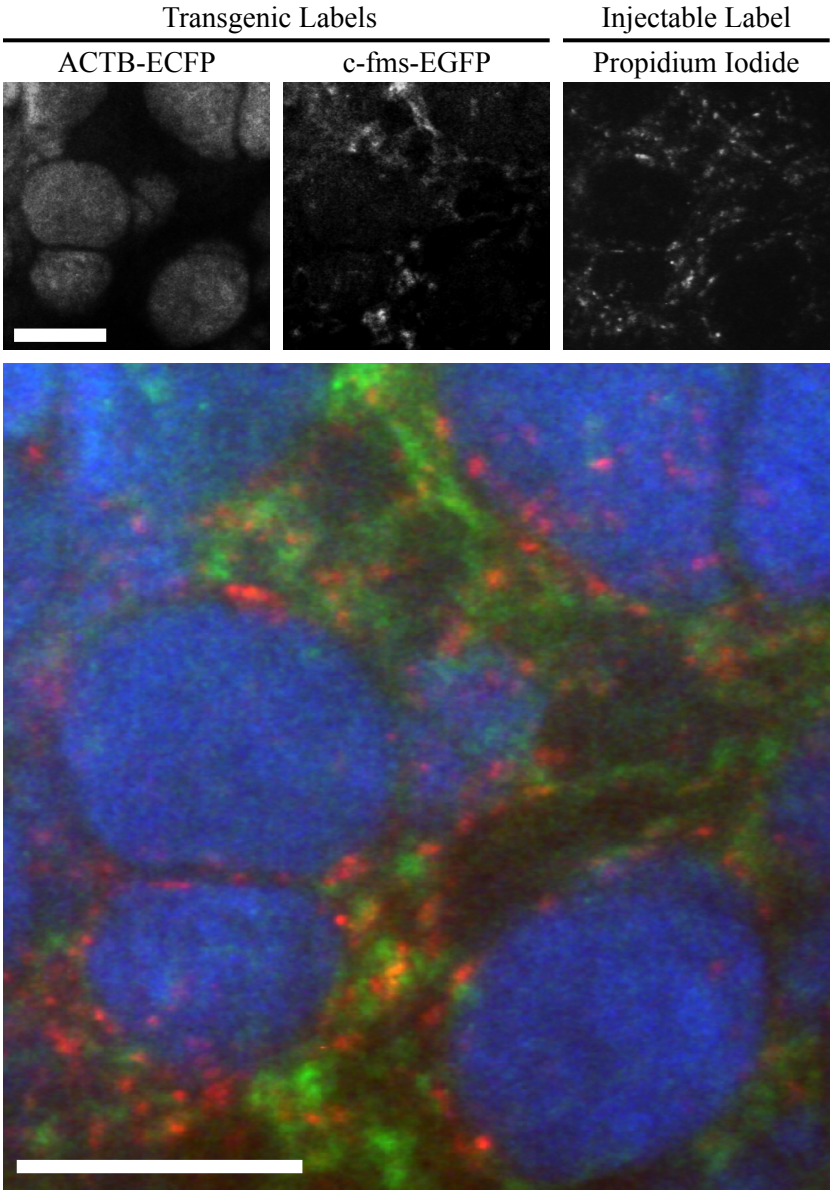

Figure 6. Representative still image from a time-lapse movie of a multicolor spinning disk confocal intravital imaging experiment. ACTB-ECFP labels cancer cells. c-fms-EGFP labels myeloid cells. Propidium iodide labels dying cells. Scale = 100 μm.

breast tumors (Egeblad et al., 2010). Dead cells were labeled during the imaging session by *i.p.* administration of propidium iodide (PI). Because the mammary glands of MMTV-PyMT mice frequently harbor multiple lesions often at different stages of progression, we were able to image doxorubicin responses at different tumor stages within the same mouse (Figure 7), controlling for mouse-to-mouse variation.

Mice with inguinal mammary tumors measuring approximately 8 to 10 mm in size were administered a single dose of doxorubicin 14 to 30 hours prior to imaging, and imaged for 8 to 40 hours. Untreated control mice were imaged for similar lengths of time to control for photo-damage and any other artifacts that may arise due to the imaging procedure. We imaged approximately five fields per tumor, with three optical slices per field in the z-plane.

Visual inspection of these movies revealed that cell death preferentially occurs in early carcinoma lesions. On average, 86% of the Fields Of View (FOV) at the early carcinoma stage were positive for PI 31 hours after doxorubicin-treatment, as compared to 12.5% of the FOV of the controls (Figure 8A, for = 4 of 23 total FOV from 4 control mice and n = 16 of 25 total FOV from 4 doxorubicin-treated mice where p = 0.001; for hyperplastic FOV, n = 1 of 8 control versus 1 of 4 doxorubicin-treated, where p = NS; for early carcinoma FOV, n = 1 of 8 control versus 12 of 14 doxorubicin-treated, where p = 0.002; for late carcinoma FOV, n = 2 of 7 control versus 3 of 7 doxorubicin-treated, where p = NS; statistics based on Fisher's exact test). In contrast, cell death did not increase in hyperplastic or late carcinoma lesions after doxorubicin treatment as compared to control lesions. Furthermore, quantification of the percentage of tumor area in each field that is positive for PI shows a significantly higher average amount of PI in early carcinomas treated with doxorubicin as compared to control tumor fields at both 26 hours (Figure 8B, error depicted as mean ± SEM, n = 8 control and 4 doxorubicin-treated hyperplastic FOV where p = NS, n = 8 control and 14 doxorubicin-treated early carcinoma lesions where p = 0.04, n = 7 control and 7 doxorubicin-treated late carcinoma lesions where p = NS, two-tailed Student's t-test) and 31 hours (Figure 8C, error depicted as mean ± SEM, n = 8 control and 4 doxorubicin-treated hyperplastic FOV where p = NS, n

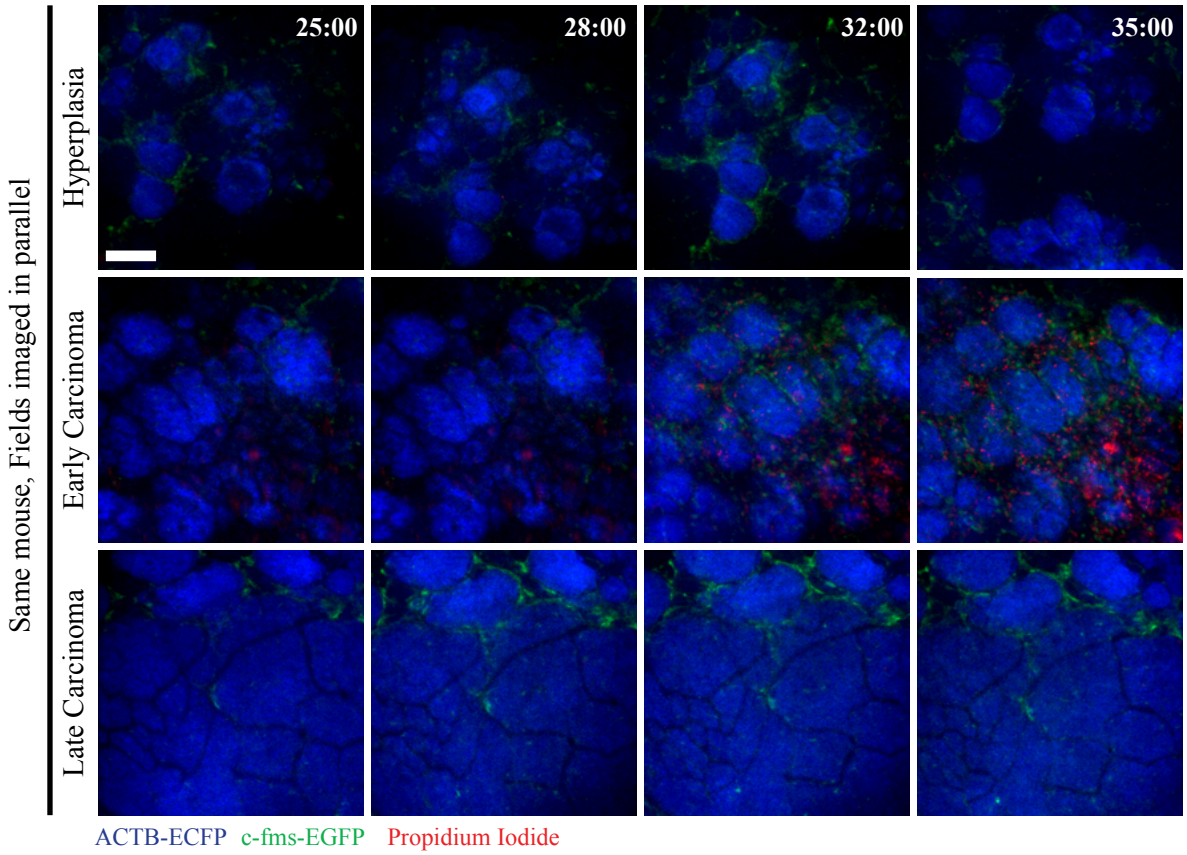

Figure 7. Progressive MMTV-PyMT mouse model allows for imaging different tumor stages in the same mouse. Time indicates hh:mm elapsed since doxorubicin treatment. Scale = 100 μm. Note: shifts in field position (observe the hyperplasia panels) occur due to breathing and other small movements of the animal.

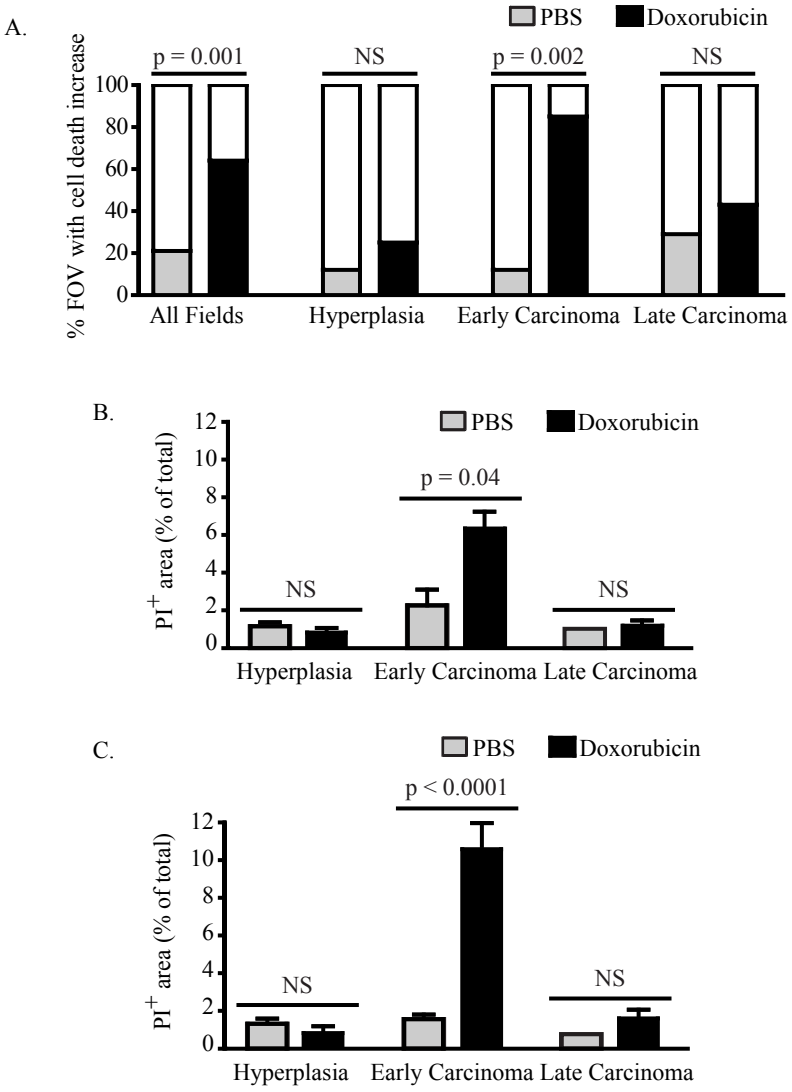

Figure 8. Intravital imaging shows lesions resembling early carcinomas are the most sensitive to doxorubicin. (A) Cell death increases primarily in early carcinoma lesions during the time period between 26 and 31 hours following doxorubicin treatment. p-values are based on Fisher's exact test. (B) Quantification of cell death (as the average of the percent area of the field positive for propidium iodide) in hyperplastic, early, and late carcinoma lesions of doxorubicin-treated mice as compared to those of PBS-treated mice 26 hours after injection. (C) Quantification of cell death 31 hours after treatment. p-values for (B) and (C) are based on two-tailed Student's t-tests.

= 8 control and 14 doxorubicin-treated early carcinoma lesions where $p < 0.0001$, n = 7 control and 7 doxorubicin-treated late carcinoma lesions where p = NS, two-tailed Student's t-test). Again, there is no difference in the average percentage of PI-positive tumor areas between control fields and doxorubicin-treated tumor fields at both the hyperplastic and late carcinoma stages at either time point. These data suggest marked differences in drug sensitivity between tumor stages.

To corroborate these finding, we performed immunohistochemical staining for phosphorylation of histone H2A variant H2AX at serine 139 (also known as γ-H2AX), a marker of DNA double-stranded breaks (Redon et al., 2002). We used γ-H2AX as a surrogate marker for doxorubicin activity, as doxorubicin is a DNA-intercalating agent that inhibits type II topoisomerases, and leads to double-stranded breaks (Pommier et al., 2010). Furthermore, this method of tissue staining afforded us a more reliable means of staging tumors, as hematoxylin counterstaining provides details about tissue structure that are not clear by intravital imaging. By this analysis, cancer cells in the early carcinoma stage also accumulate more DNA damage 48 hours after doxorubicin treatment, as compared to those at the hyperplastic or late carcinoma stages (Figure 9, error depicted as mean ± SEM, p-value by one-way ANOVA < 0.0001, n = 5 mice, 1 tumor per mouse with 21 hyperplastic FOV, 25 early carcinoma FOV, and 24 late carcinoma FOV; for hyperplasia versus early carcinoma, $p < 0.01$ with Bonferroni post-test; for early carcinoma versus late carcinoma, $p < 0.0001$ with Bonferroni post-test). Thus, doxorubicin sensitivity is tumor stage-dependent.

In situ differences in cancer cell proliferation do not account for differences in doxorubicin sensitivity

As previously mentioned, doxorubicin is a DNA-intercalating agent and a type II topoisomerase inhibitor (Pommier et al., 2010). As topoisomerases are active during cell proliferation, acting to relieve DNA supercoils introduced during replication, actively cycling cells are expected to be most sensitive to doxorubicin (Campiglio et al., 2003). We therefore tested whether the differences in doxorubicin response between tumor stages are due to differences in

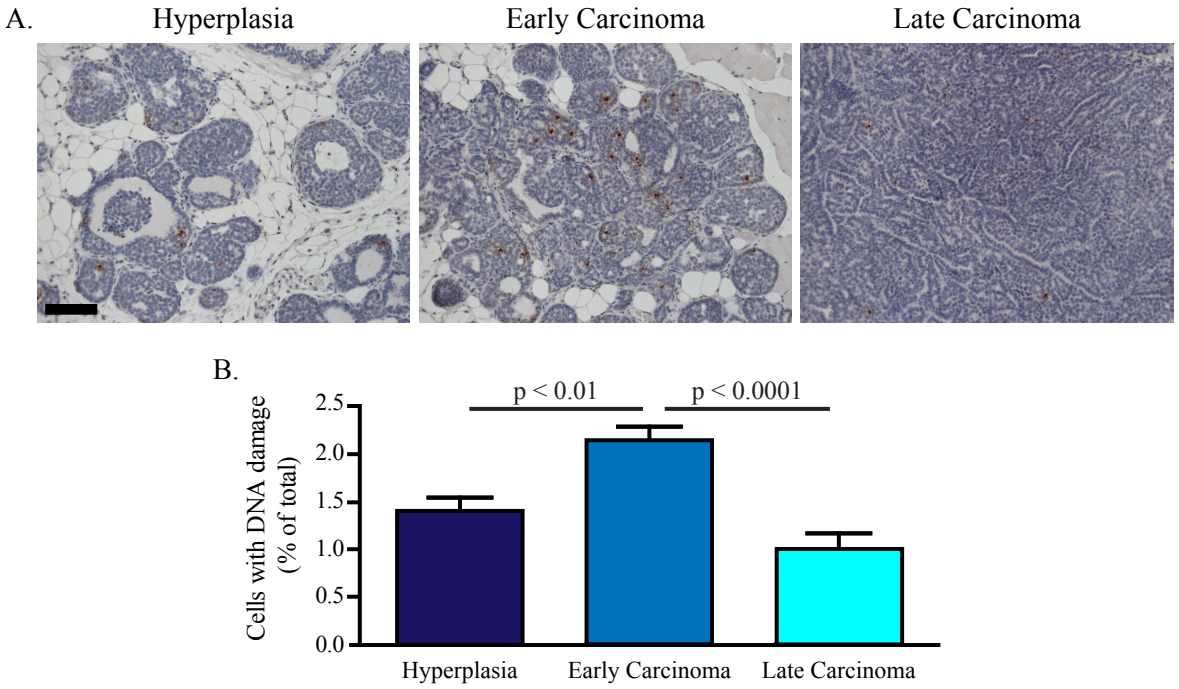

Figure 9. γ-H2AX staining for DNA damage confirms stage-specific doxorubicin sensitivity observed in intravital imaging experiments. (A) Representative images of anti-γ-H2AX immunohistochemical staining. Scale = 50 μm. (B) Quantification of γ-H2AX staining. p-values based on two-tailed Student's t-test.

proliferation. MMTV-PyMT tumor-bearing mice were administered 5-bromo-2′-deoxyuridine (BrdU) prior to doxorubicin treatment, and tumors were harvested 24 or 48 hours after doxorubicin treatment. Immunohistochemical staining for BrdU (Figure 10A) showed non-significant differences in proliferation between hyperplastic, early, and late carcinoma stages. (Figure 10B, error depicted as mean ± SEM, p = NS by one-way ANOVA, n = 6 tumors from 3 mice, with 13 hyperplastic FOV, 19 early carcinoma FOV, and 28 late carcinoma FOV). This suggests that differences in cellular proliferation between tumor stages are not sufficient to explain differences in doxorubicin sensitivity *in vivo*.

Tumor stage-associated doxorubicin sensitivity is microenvironment-dependent

Breast cancer cells can acquire various molecular changes as they progress from hyperplastic lesions to invasive tumors (Bombonati and Sgroi, 2011), and frequently, these changes can give rise to changes in sensitivity to chemotherapeutic treatment (Gonzalez-Angulo et al., 2007). Thus, we tested whether differences in doxorubicin sensitivity could be attributed to molecular differences specific to different tumor stages. To focus exclusively on cancer cell-dependent resistance, cancer cells isolated from different tumor stages were tested in the same microenvironment by culturing *in vitro*, either in standard two-dimensional cultures or embedded as carcinoma organoids in Matrigel™ in three-dimensional cultures. To determine whether intrinsic differences contributed to stage-specific differences in doxorubicin sensitivity, we needed a molecular target that could act as a positive control. MMTV-PyMT is a useful model system, because in addition to showing stage-specific histopathology, tumors also undergo characteristic molecular changes through progression, including down-regulation of the estrogen (ER) and progesterone (PR) receptors and upregulation of the ErbB2/Neu receptor tyrosine kinase (Lin et al., 2003).

We used sensitivity to lapatinib ditosylate (trade name Tykerb, hereafter referred to as lapatinib), an ErbB1/2 inhibitor used in the clinic to treat $HER2^+$ breast cancers (Bilancia et al., 2007) as our positive control. Tumors at the hyperplastic, early, and late carcinoma stages in

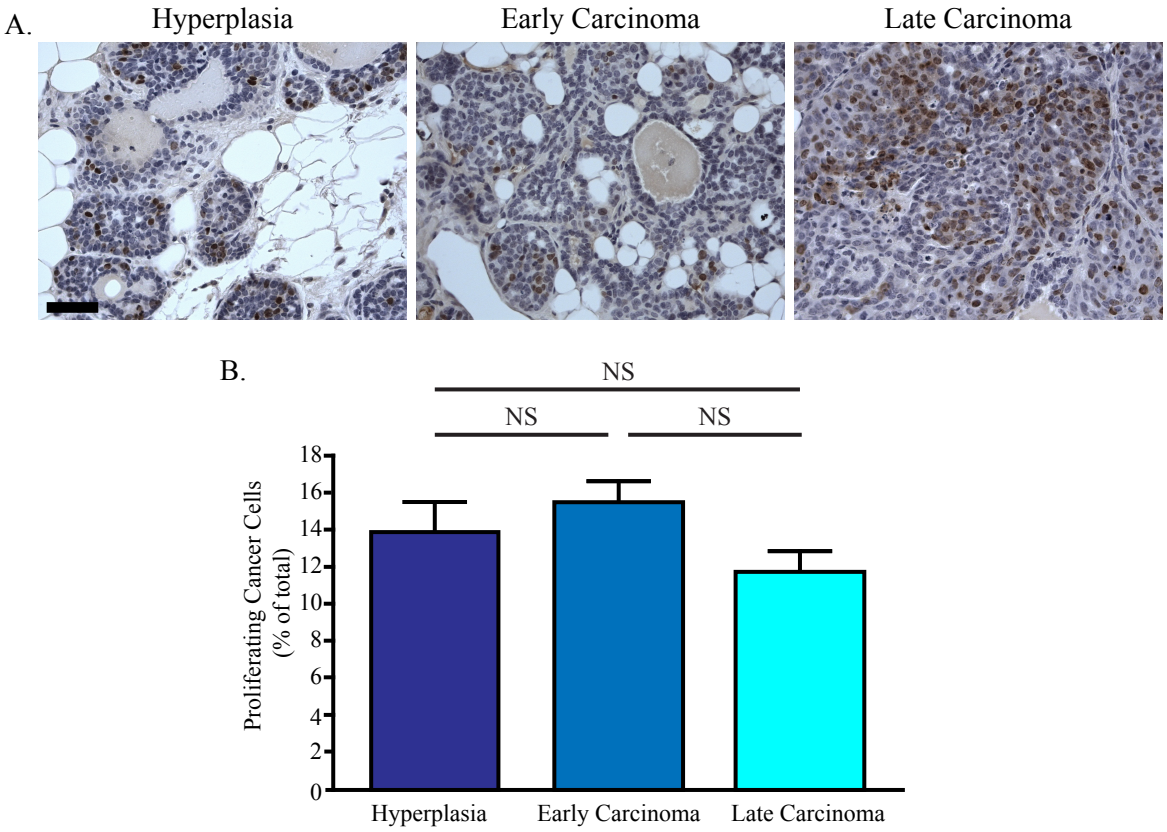

Figure 10. Differences in proliferation between tumor stages do not account for differential sensitivity to doxorubicin. (A) Representative images of anti-BrdU immunohistochemical staining. Scale = 25 μm. (B) Quantification of BrdU staining. p-values based on one-way ANOVA.

untreated MMTV-PyMT;ACTB-ECFP mice were microdissected using a fluorescence dissecting microscope (Figure 11A). Cancer cells from different tumor stages were separated from stromal components, grown in two-dimensional culture, and treated with increasing doses of lapatinib. As expected, tumors at the late carcinoma stage were highly sensitive to lapatinib treatment, even at low doses, while hyperplastic and early carcinoma lesions were insensitive to lapatinib unless high doses were used (Figure 11B, error depicted as mean ± SEM, values represent 4 experiments, each done in triplicate, $p = 0.04$ for cancer cells from hyperplastic lesions as compared to cancer cells from early carcinomas at 1 μM [lapatinib], $p = 0.02$ for cancer cells from early carcinomas as compared to cancer cells from late carcinomas at 1 μM [lapatinib], using a two-tailed Student's t-test).

We then tested the sensitivity of cancer cells isolated from different tumor stages to doxorubicin in three-dimensional organoid culture. Unlike the results obtained for the lapatinib experiments, cancer cells showed no difference in tumor stage-dependent doxorubicin sensitivity *ex vivo* (Figure 12A-B, error depicted as mean ± SEM, values are representative of 4 experiments, each done in triplicate, p = NS for all stages at all doxorubicin concentrations, using two-tailed Student's t-tests). These results indicate that the stage-dependent doxorubicin sensitivity we observe *in vivo* is most likely due to differences in the tumor microenvironment.

Doxorubicin treatment alters the tumor-associated inflammatory microenvironment

In addition to cancer cell-intrinsic changes, the microenvironment undergoes changes in both composition and organization during progression and chemotherapy response (Polyak and Kalluri, 2010). Intravital imaging experiments of MMTV-PyMT;ACTB-ECFP;c-fms-EGFP mice showed that myeloid cells were recruited into tumors after doxorubicin treatment (Figure 13, n = 12 of 16 fields for doxorubicin-treated tumors, n = 3 of 16 movies for control tumors, $p = 0.004$ using Fisher's exact test). Furthermore, the highest degree of myeloid cell infiltration occurred in areas exhibiting a high degree of cell death (Figure 14). The structures formed by these infiltrating myeloid cells appeared to be similar to granulomas, which are frequently formed in response to chronic infection.

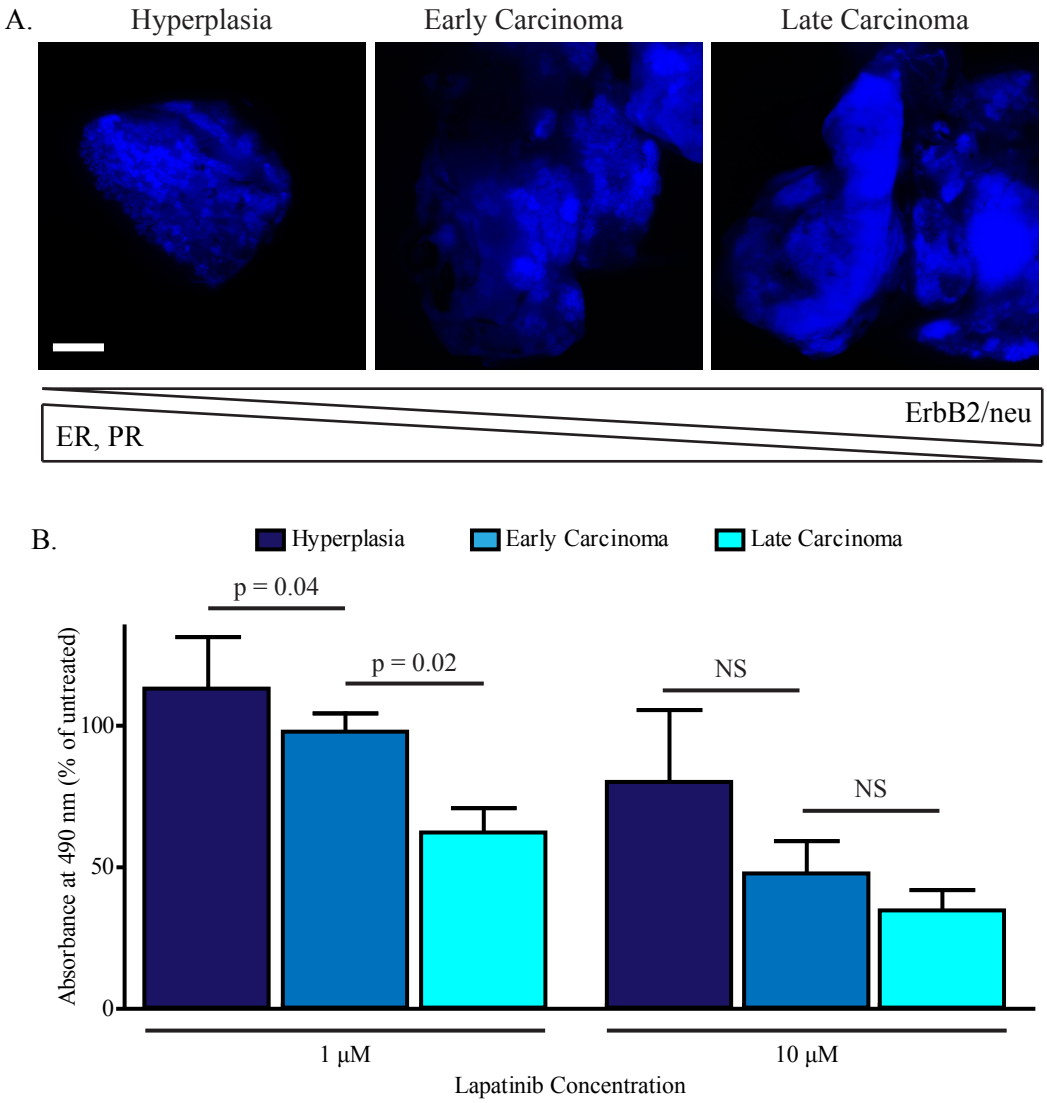

Figure 11. MMTV-PyMT cancer cells show tumor stage-dependent sensitivity to the ErbB1/2 inhibitor lapatinib *ex vivo*. (A) Microdissected lesions from MMTV-PyMT; ACTB-ECFP mice at the indicated stages of tumor progression. Below are the associated changes in expression of hormone receptors and the ErbB2 receptor. Scale = 1 mm. (B) Tumors show increasing sensitivity to lapatinib with progression. Error depicted as mean ± SEM. p-value based on two-tailed Student's t-test.

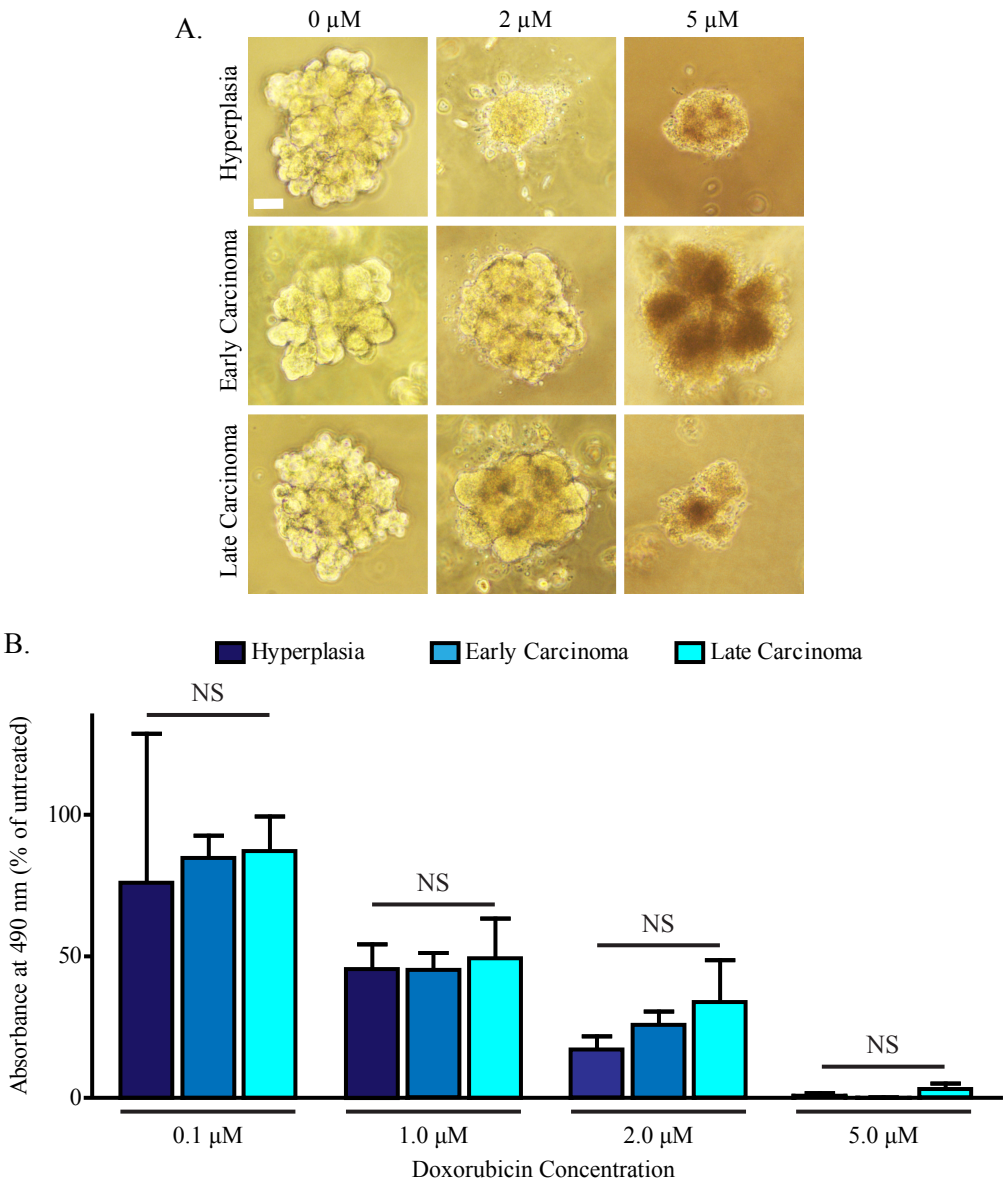

Figure 12. MMTV-PyMT cancer cells do not show tumor stage-dependent sensitivity to doxorubicin ***ex vivo*****.** (A) Representative images of *ex vivo* doxorubicin response. Scale = 50 µm. (B) Quantification of doxorubicin response in 3D culture shows no difference in tumor stage-dependent drug sensitivity. Error depicted as mean ± SEM. p-value based on two-tailed Student's t-test.

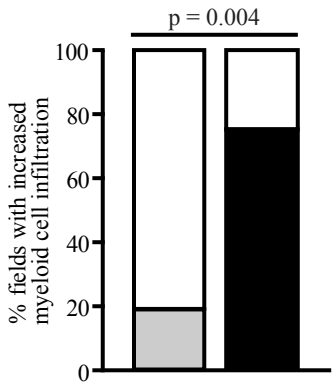

Figure 13. Doxorubicin treatment alters the innate inflammatory microenivronment. Quantification of myeloid infiltration during intravital imaging. p-value based on Fisher's exact test.

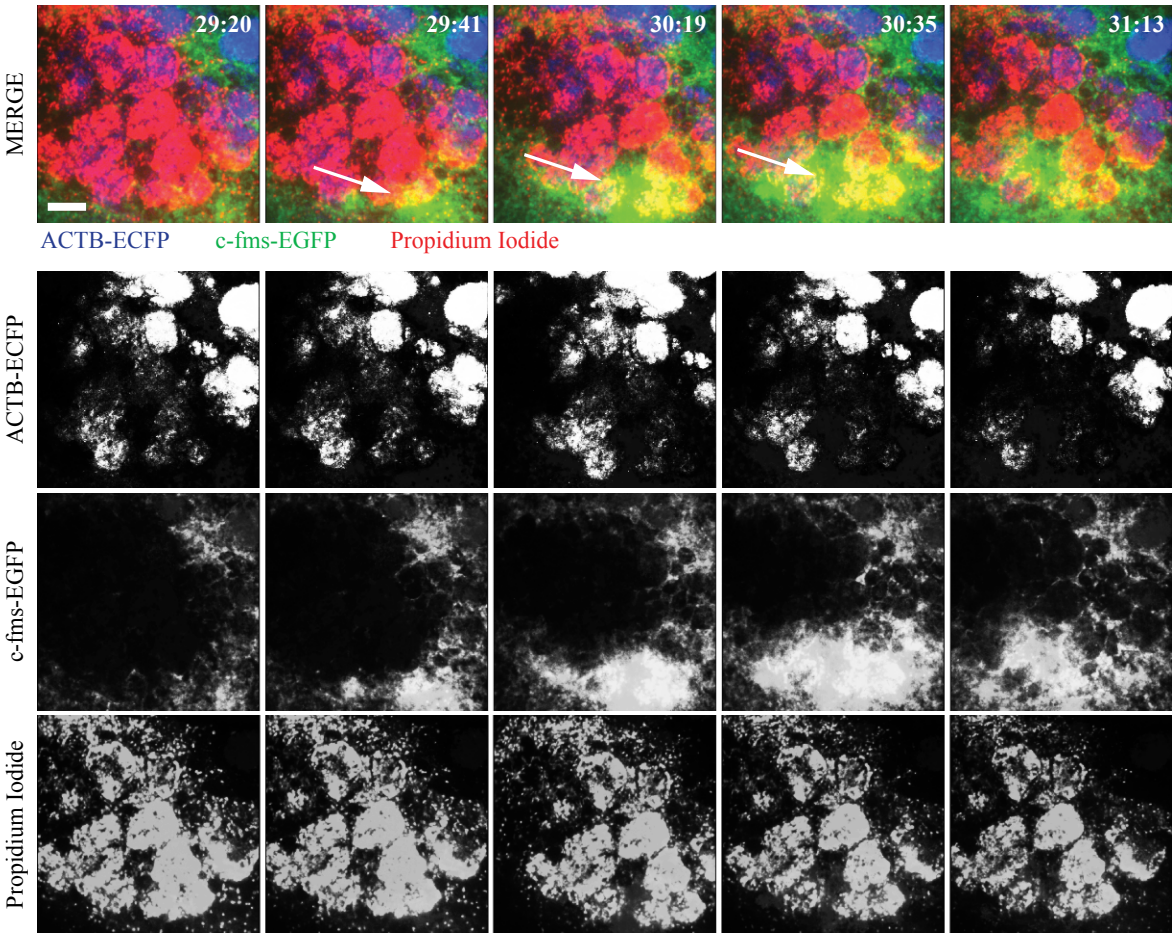

Figure 14. Intravital imaging shows that the highest degree of myeloid infiltration occurs in areas exhibiting the highest degrees of cell death. Representative time series. Time represents hh:mm elapsed since doxorubicin treatment. Scale = 100 μm.

We could further confirm this by imaging the tumors of MMTV-PyMT;ACTB-ECFP;c-fms-EGFP mice treated with doxorubicin at high-resolution (40×) magnification, which allowed us to observe chemotherapy-induced death in individual cancer cells. These experiments confirmed that cancer cell death, as evidenced by the accumulation of PI staining in single cells, was followed by infiltration of immune cells into the area surrounding these dying cells (Figure 15).

Doxorubicin induces necrosis *in vivo*

Anthracyclines have been reported to induce two forms of cell death capable of activating an immune response, necrosis and apoptosis (Demoy et al., 2000). To better understand the mechanism by which myeloid cells are being recruited into dying tumors and the impact of this recruitment in tumor response, we first needed to determine how doxorubicin was inducing cell death.

We therefore performed intravital imaging at high magnification (40×) of tumors from MMTV-PyMT mice cross-bred with ACTB-ECFP and ACTB-H2B-EGFP (Hadjantonakis and Papaioannaou, 2004, hereafter referred to as H2B-EGFP) reporter mice. Expression of these reporters allowed us to visualize all cancer cells (ECFP) and their nuclei (EGFP). MMTV-PyMT;ACTB-ECFP;H2B-EGFP mice were administered doxorubicin approximately 30 hours before the start of imaging (this time point was chosen because our previous imaging experiments showed that cell death started becoming apparent between 24 and 30 hours after doxorubicin treatment, see Figure 7). Dead cells were labeled during the imaging session with PI.

Visual inspection of these movies indicated that there were at least two observable mechanisms by which doxorubicin induces cell death *in vivo*. By far the most common mechanism was one in which nuclei maintained their morphology, but gradually acquired PI staining, indicating late breakdown of plasma membrane integrity and necrosis. Much less common was a mechanism in which major nuclear changes were followed by the formation of chromatin foci that eventually became PI positive, a sign typical of apoptosis (Dive et al., 1992). We quantified these two mechanisms using the following criteria: a necrotic phenotype was defined as one in which PI-

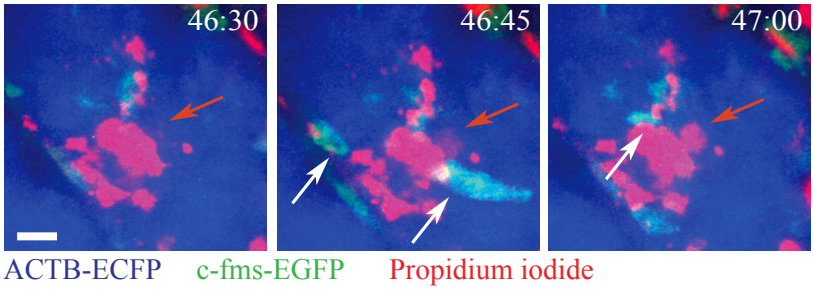

Figure 15. Myeloid cell recruitment occurs after induction of cell death. Red arrows indicate dying cancer cells, as determined by the appearance of propidium iodide staining. White arrows indicate myeloid cells recruited to dying tissue. Time represents hh:mm elapsed since doxorubicin treatment. Scale = 10 μm.

positive cells showed maintenance of normal nuclear morphology over time, while an apoptotic phenotype was one in which PI-positive cells showed abnormal nuclear morphology resembling apoptotic bodies (Figure 16A). These two mechanisms were quantified manually in maximum intensity projections (3 z-planes) acquired for each field at the 32- and 42-hour time points after doxorubicin administration. This analysis showed us that at both time points, the predominant form of doxorubicin-induced cell death was necrosis (Figure 16B, error depicted as mean ± SEM n = 18 fields from 3 mice, $p = 0.009$ at 32 h, $p < 0.001$ at 42 h, two-tailed Student's t-test).

The presence of necrotic debris is sufficient to recruit myeloid cells

Necrosis is known to be a highly immunogenic form of cell death, capable of recruiting cells of both the innate and adaptive arms of the immune systems (Kepp et al., 2009; Vakkila and Lotze, 2004). In order to confirm that debris generated from cancer cells that had undergone necrosis was stimulating the recruitment of myeloid cells into tumors following doxorubicin treatment, we wanted to use a system that was independent of any tumor-derived factors that may influence recruitment, as well as any effects beyond induction of cancer cell death that doxorubicin might have, such as killing of myeloid cells. Thus, we first harvested tumors from MMTV-PyMT mice, labeled them *ex vivo* with CellTracker^{TM} Red, and generated necrotic debris. These cells were then combined with a fluorescently conjugated dextran (to label host tissue) and injected directly into mammary glands of non-tumor bearing c-fms-EGFP reporter mice. Control areas in the same mammary gland were injected with dextran alone.

We observed that in areas injected with the dextran alone, there was very little recruitment of myeloid cells. However, in areas in which we had injected necrotic debris, there was massive infiltration of the tissue with myeloid cells and the formation of granuloma-like structures, similar to what we previously observed in tumor areas with large regions of dead or dying cancer cells. Because the presence of necrotic debris is sufficient to trigger myeloid cell recruitment, we concluded that doxorubicin-induced necrosis probably plays a major role in the recruitment of myeloid cells into

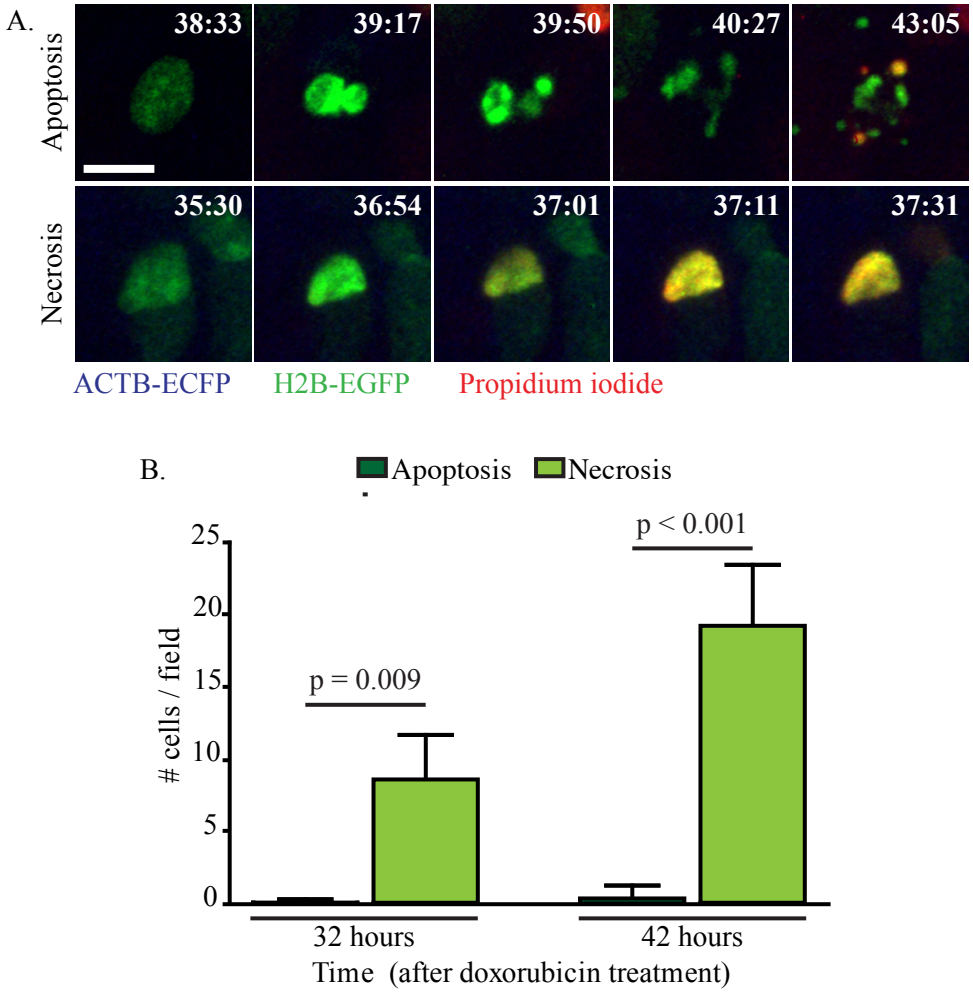

Figure 16. *In vivo* dynamics of cell death show doxorubicin primarily induces necrosis in cancer cells. (A) Representative images of apoptotic and necrotic cell death *in vivo*. Scale = 10 μm. (B) Quantification of cell death based on morphology at 32 and 42 hours after doxorubicin treatment. p-values based on two-tailed Student's t-test.

tumors (Figure 17).

Recruitment of myeloid cells to areas containing necrotic debris is dependent on chemokine receptor signaling

Further analysis of the movies generated from imaging necrotic debris injected into normal mammary glands showed that directional migration toward areas containing debris occurred only after tissue-resident myeloid cells had interacted with and recognized the debris. This implied that resident myeloid cells that detected the debris were releasing some sort of chemoattractant signal. The signaling molecules usually responsible for directional migration of myeloid cell are chemokines, and the receptor systems that respond to these signals belong to the G_i-protein-coupled receptor family (G_iPCR, Balkwill, 2004). To confirm that signaling through a chemokine/chemokine receptor pathway was regulating myeloid cell infiltration into areas containing necrotic debris, we pre-treated non-tumor bearing c-fms-EGFP reporter mice with pertussis toxin, a pan-GPCR inhibitor (Cubillos et al., 2010), 12 hours before injection of necrotic debris into the mammary gland, and once again just prior to injection of debris and imaging. Inhibition of G_iPCR signaling dramatically inhibited the recruitment of myeloid cells into areas containing necrotic debris (Figure 18, error depicted as mean ± SD, n = 6 fields per condition from two mice; * $p = 0.003$, ** $p < 0.0001$, two-tailed Student's t-test at each time point), confirming that this process is dependent on chemokine receptor signaling.

Intratumoral expression of the chemokines CCL2 and CCL12 is upregulated following doxorubicin treatment

Because inhibition of G_iPCR signaling prevented the recruitment of myeloid cells into tissues containing necrotic debris, we predicted that this same type of signaling pathway was at play when myeloid cells were recruited to MMTV-PyMT tumors undergoing doxorubicin-induced necrosis. To determine the chemokine/chemokine receptor pair(s) responsible for myeloid cell infiltration, we assayed for both cytokines and chemokines that were differentially expressed in the tumors of PBS-

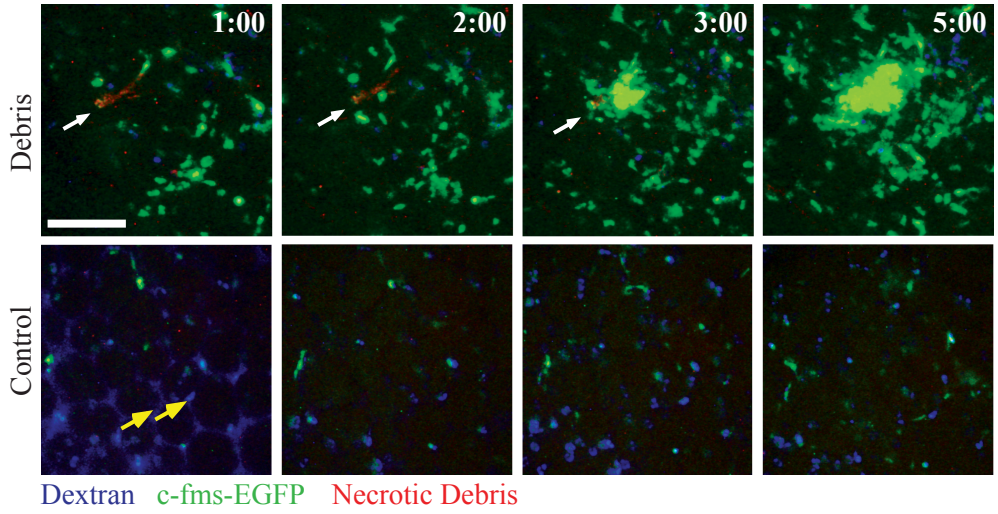

Figure 17. Tumor-derived necrotic debris recruits myeloid cells. Injection of necrotic debris (with dextran to label the surrounding tissue) into the normal mammary glands of c-fms-EGFP reporter mice results in the recruitment of myeloid cells (top). Injection with dextran alone is not sufficient to recruit myeloid cells (bottom). White arrow indicates necrotic debris. Yellow arrows indicate myeloid cells that have ingested dextran. Time represents h:mm elapsed since injection. Scale = 100 μm.

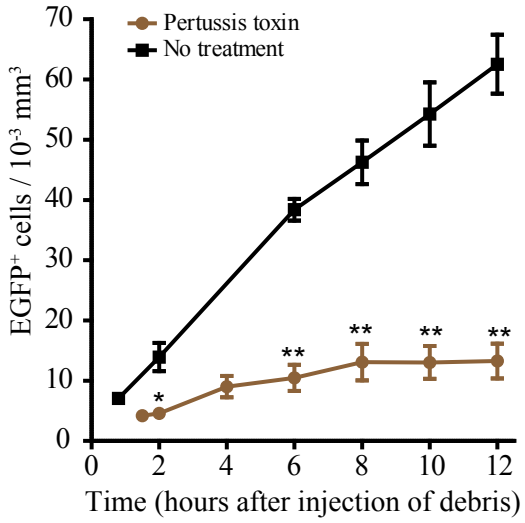

Figure 18. Inhibition of G_i-protein-coupled receptor signaling abrogates recruitment of myeloid cells. c-fms-EGFP reporter mice were pre-treated with pertussis toxin 12 hours before and again immediately prior to injection with necrotic debris and imaging. p-values based on two-tailed Student's t-test at each time point. * $p = 0.003$, ** $p < 0.0001$.

and doxorubicin-treated mice. Whole tumor lysates of tissues harvested from mice 48 hours after treatment were applied to a spotted antibody array that detects ~40 cytokines and chemokines (R&D Systems). Two chemokines, CCL2 and CCL12, showed increased expression in the tumors of doxorubicin-treated mice, as compared to those of PBS-treated controls. Expression of two other molecules, macrophage colony stimulating factor (M-CSF/CSF1) and tissue inhibitor of metalloproteinase 1 (TIMP-1) were also slightly upregulated in the tumors of doxorubicin-treated mice (Figure 19A, n = 6 mice per treatment, 1 tumor per mouse).

To confirm the upregulation of CCL2 and CCL12, we performed enzyme-linked immunosorbent assays (ELISA). There was a strong trend for increased expression of these two chemokines in the tumors of doxorubicin-treated mice as compared to those of PBS-treated control mice (Figure 19B-C, n = 12 mice per treatment, 1 tumor per mouse, p = NS for both CCL2 and CCL12, two-tailed Student's t-test). The results did not reach significance, most likely a reflecting the heterogeneity of MMTV-PyMT tumor responses to doxorubicin, and the difficulties of detecting chemokines in whole tumor lysate.

CCL2 is stromally-derived

Mouse CCL2 (also known as monocyte chemoattractant protein-1, MCP-1) and CCL12 (also known as MCP-5) are both orthologues of the human CCL2 gene (Yoshimura et al., 1989; Sarafi et al., 1997) and potent chemoattractants for monocytes (Tsui et al., 2007). We focused our efforts on understanding the consequences of CCL2 upregulation, as it is one of the best-studied (and first-identified) chemokines whose functions overlap with those of CCL12. CCL2 is known to be involved in the recruitment of myeloid cells into sites of inflammation, as well as into tumor tissues, and has been highly implicated in autoimmune and chronic disease (Deshmane et al., 2009).

We first sought to identify the cell population that expresses CCL2. We used immunofluorescence staining for CCL2, as this would provide us with the ability to both quantify the number of cells that express CCL2 and determine their localization. CCL2 immunostaining was

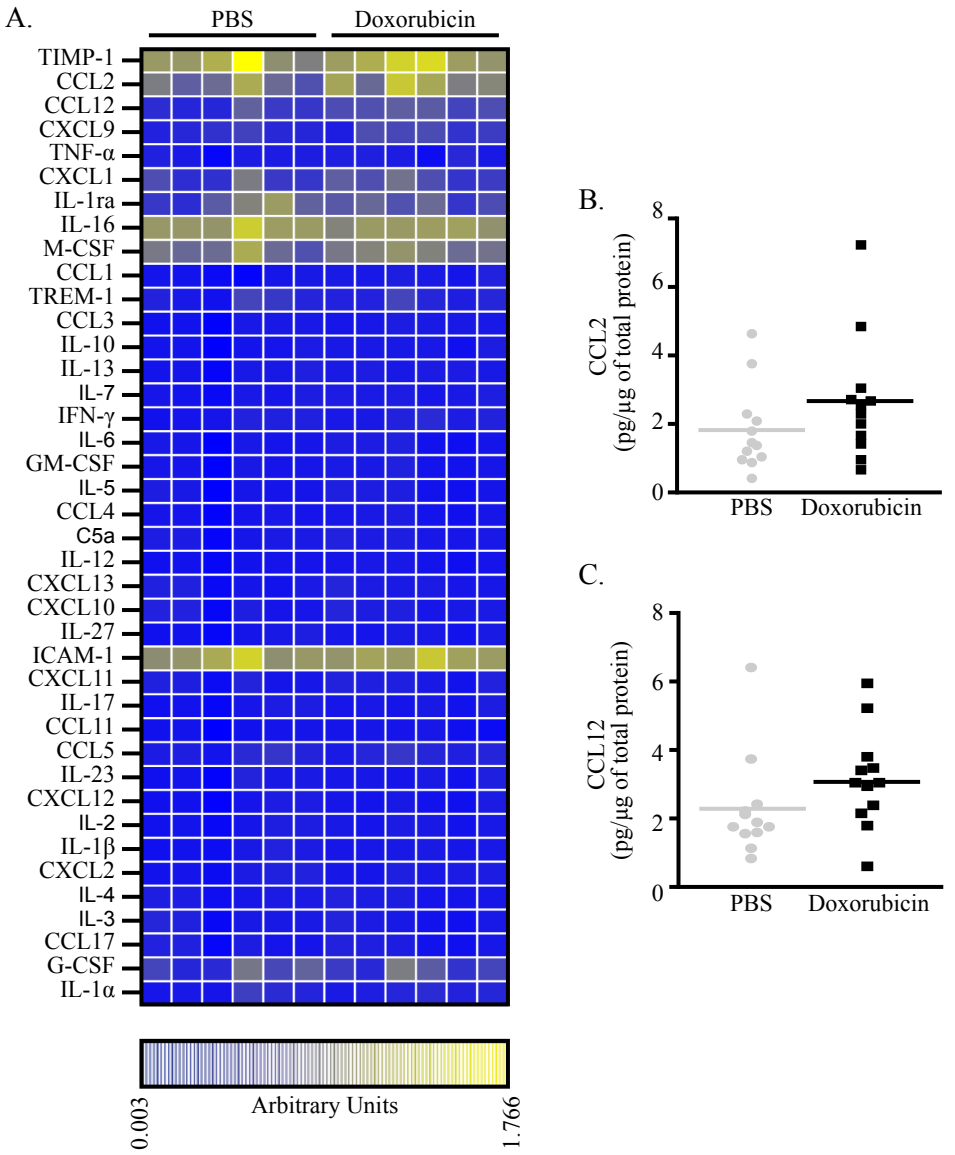

Figure 19. The chemokines CCL2 and CCL12 are upregulated in tumors of doxorubicin-treated mice. (A) Cytokine array on whole-tumor lysate shows upregulation of CCL2 and CCL12. CCL2 (B) and CCL12 (C) ELISA confirm upregulation.

performed on tumor tissues harvested 48 hours after treatment. These stains showed a significantly higher number of CCL2-postive cells in tumors derived from doxorubicin-treated mice as compared to those from PBS-treated controls (Figure 20B, n = 6 mice per treatment, 1-2 tumors per mouse, 80 fields from PBS-treated mice, 66 fields from doxorubicin-treated mice, error depicted as mean ± SEM). Furthermore, cells that stained positively for CCL2 were confined to the stromal compartment (Figure 20A)

We performed double label immunofluorescence stains to identify the stromal cell population that expresses CCL2. We combined staining of CCL2 with staining for the 7/4 (neutrophils and monocytes), CD206 (tumor-associated macrophages), α-smooth muscle actin (αSMA, fibroblasts and pericytes), and MECA-32 (endothelial cells) markers. We did not detect any CCL2 expression among neutrophils, fibroblasts, pericytes, and endothelial cells. Some monocytes and macrophages do express CCL2, but they did not account for the majority of the CCL2-positive cells (Figure 21). We speculate that CCL2 is expressed by dendritic cells (DC) based on the localization and morphology of these cells, but we were unable to confirm this prediction, as markers for DCs did not stain our tissues.

CCL2 recruits CCR2-positive monocytes

We next determined the cell population(s) that were responding to stromal CCL2. CCL2, as well as CCL12, are unique chemokines in that they bind exclusively to one receptor, the G_iPCR CCR2 (Deshmane et al., 2009). Thus, we used a combination of flow cytometry and double label immunofluorescence staining to determine the population of cells expressing CCR2.

We performed flow cytometric analyses on tumors isolated from transplantation models in which MMTV-PyMT cancer cells were orthotopically transplanted into syngeneic wildtype hosts. Mice were administered PBS or doxorubicin 48 hours prior to euthanization and harvesting of tumors. Staining for the CD11b (myeloid cell) and F4/80 (macrophage) markers, we observed no difference in the total number of $CD11b^+$ nor the $F4/80^+CD11b^+$ double-positive immune cell populations by flow

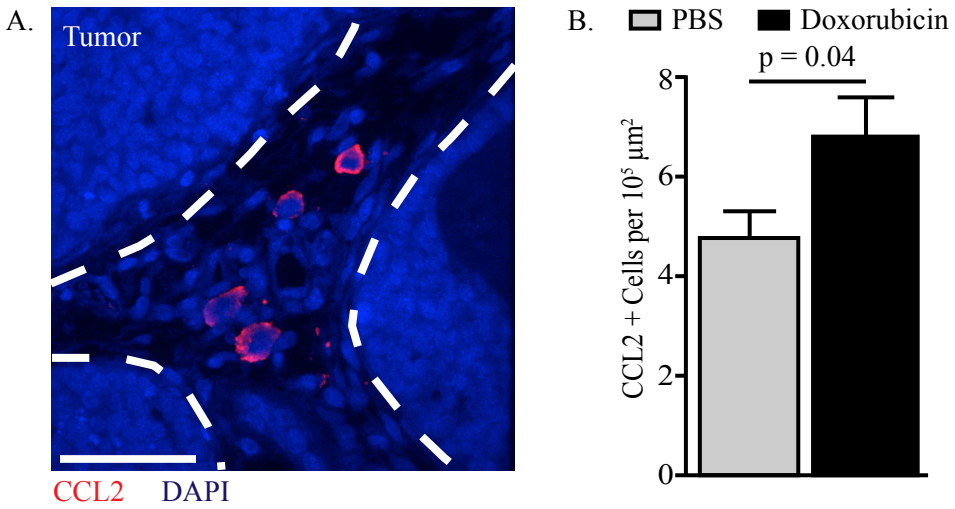

Figure 20. CCL2 is stromally derived. (A) Representative image of an immunofluorescence stain for CCL2. Scale = 50 µm. Dashed lines indicate the boundary between tumor and stromal compartments. (B) Quantification of CCL2 stains performed on tissue from tumors harvested 48 hours after treatment. p-value based on two-tailed Student's t-test.

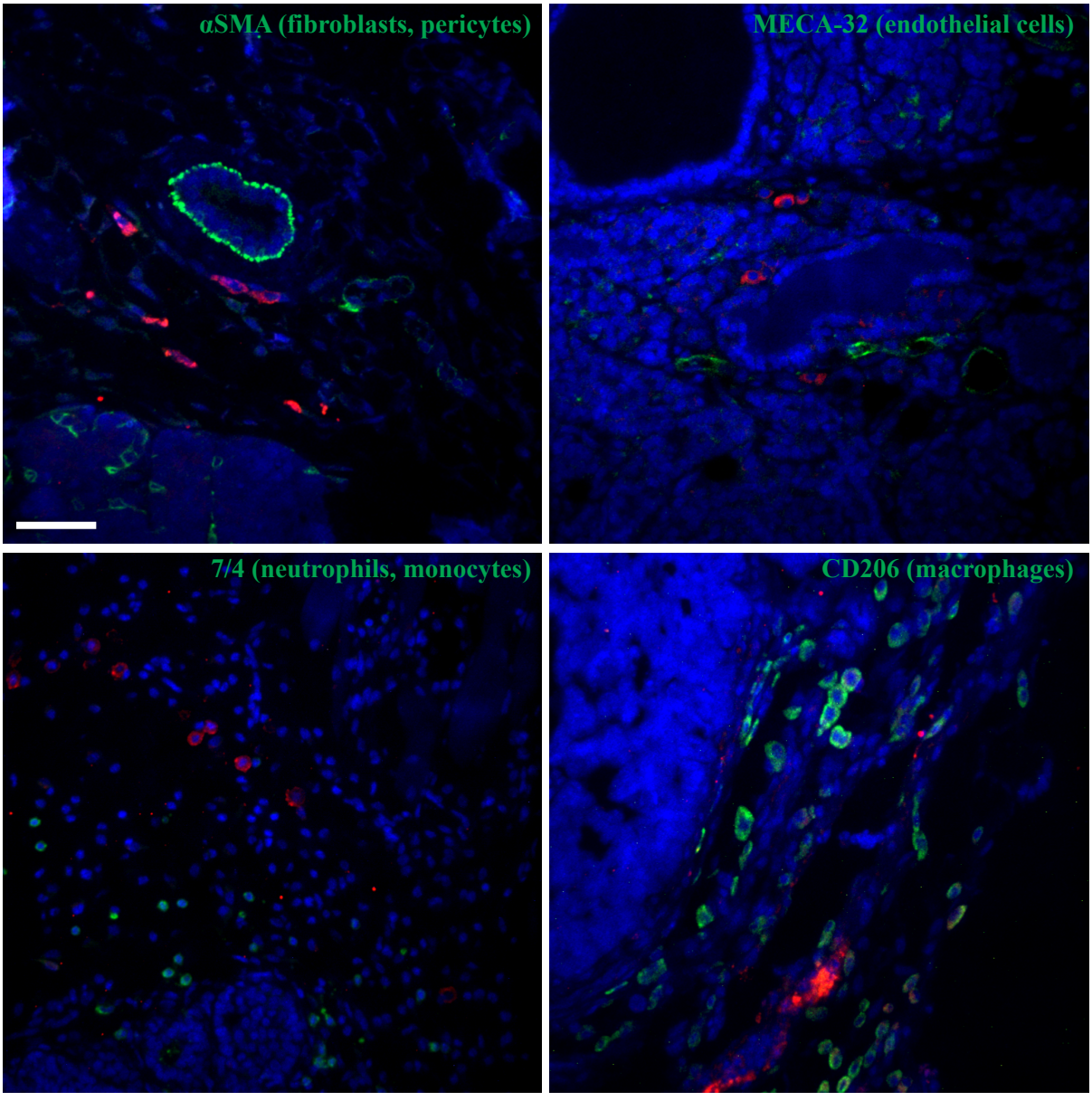

Figure 21. Double label immunostains show that CCL2 is expressed by some CD206-positive macrophages, but is not expressed by fibroblasts, pericytes, endothelial cells, or neutrophils. Representative images of indicated stains. Scale = 50 μm.

cytometry (Figure 22C-D, error depicted as mean ± SEM, n = 11 PBS-treated mice with 1 tumor per mouse, n = 10 doxorubicin-treated mice with 1 tumor per mouse, two-tailed Student's t-test), in the tumors of doxorubicin-treated mice, as compared to those of PBS-treated controls. We did, however, observe an increase in cells triple-positive for Gr1 (immature myeloid cells), 7/4, and CD11b (Figures 22A-B, error depicted as mean ± SEM, n = 11 PBS-treated mice with 1 tumor per mouse, n = 10 doxorubicin-treated mice with 1 tumor per mouse, two-tailed Student's t-test).

We could not confirm that the $Gr1^{+}7/4^{+}CD11b^{+}$ population was also CCR2 positive by flow cytometry, as the antibodies targeting CCR2 that we tested detected a population of cells in *Ccr2*$^{-/-}$ mice (data not shown). Instead, we performed double-label immunostains for 7/4 and CCR2 in tumor tissue sections (the Gr1, 7/4, and CCR2 triple label stain could not be performed due to species limitations of the primary antibodies). Double label immunostains were quantified based on positivity for one or both of the markers used, as well as nuclear morphology. Differentiation based on nuclear morphology was important because the 7/4 marker detects both neutrophils and monocytes, which exert different effects on tumors (see Table 1), and monocytes have the propensity to differentiate into the tumor-associated macrophages that promote progression (Mantovani et al., 2002). Characterization of neutrophils and monocytes is simple, as they exhibit distinct nuclear morphologies: neutrophils, referred to as polymorphonuclear leukocytes, have multi-lobed nuclei; monocytes, referred to as mononuclear leukocytes, have single-lobed nuclei (Figure 23A).

Quantification of these immunostains confirmed the increase in $7/4^{+}$ cells, and showed that this increase was almost exclusively confined to cells that expressed CCR2 and exhibited monocytic nuclear morphology (Figure 23B, error depicted as mean ± SEM, n = 4 mice with 1 tumor per mouse and a total of 104 FOV for the PBS group, n = 5 mice with 1 tumor per mouse and a total of 113 FOV for the doxorubicin group, p-values indicated are based on two-tailed Student's t-tests). Although a small number of $7/4^{+}$ cells exhibiting neutrophilic morphology and positive for CCR2 were detected, there was no difference in the numbers of this cell population between tumors from doxorubicin- as compared to PBS-treated mice. This trend was also true of cells that expressed CCR2 but were

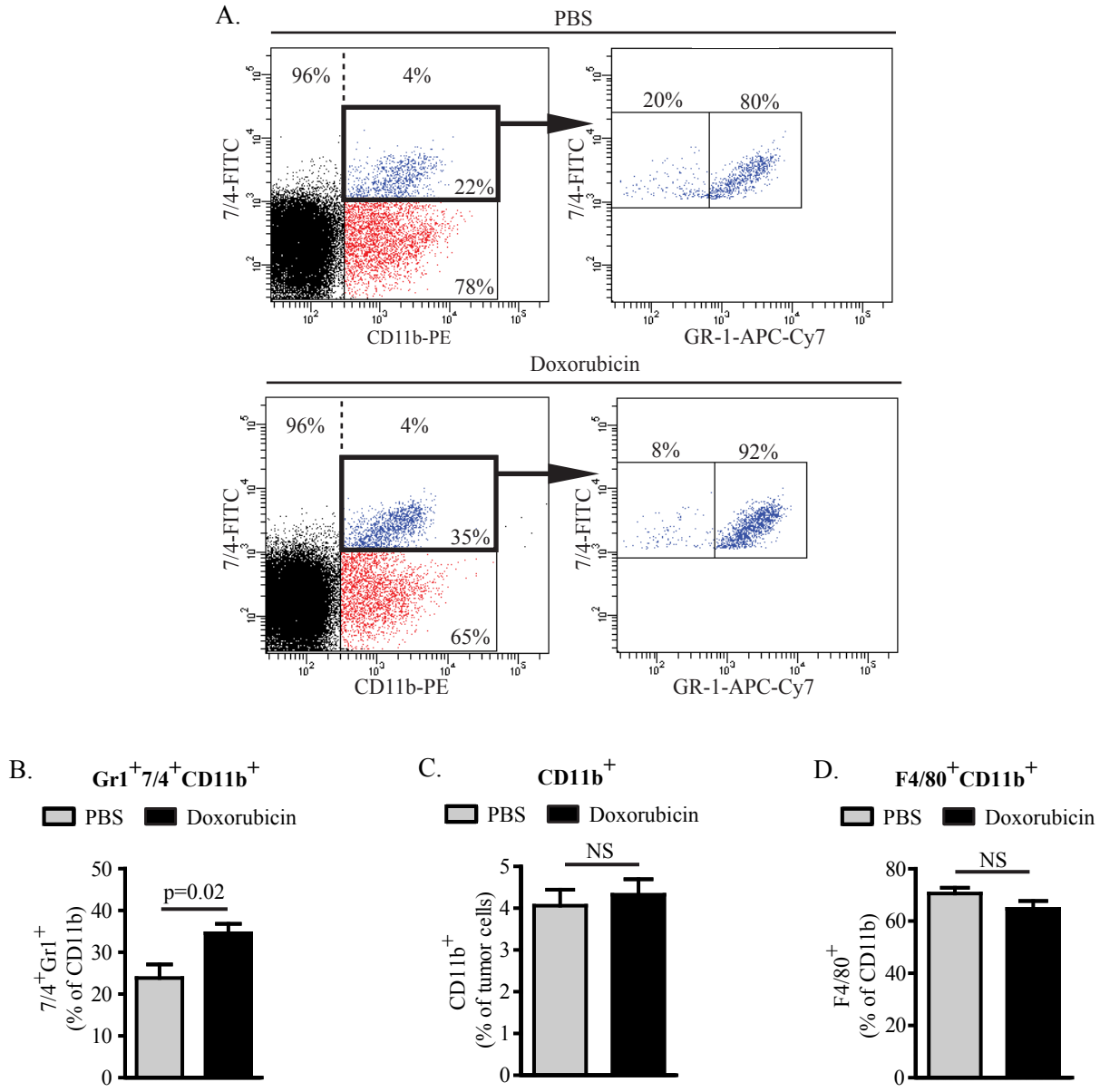

Figure 22. Flow cytometric analyses show increased numbers of Gr1$^+$7/4$^+$CD11b$^+$ immature myeloid cells in the tumors of doxorubicin-treated mice. (A) Representative FACS plots for Gr1$^+$7/4$^+$CD11b$^+$ triple stains of cells harvested from tumors 48 hours after the indicated treatment. (B) Quantification of Gr1$^+$7/4$^+$CD11b$^+$ myeloid cells. (C) Quantificationof total CD11b$^+$ myeloid cells. (D) Quantification of F4/80$^+$CD11b$^+$ macrophages. p-values based on two-tailed Student's t-test. Error depicted as mean ± SEM.

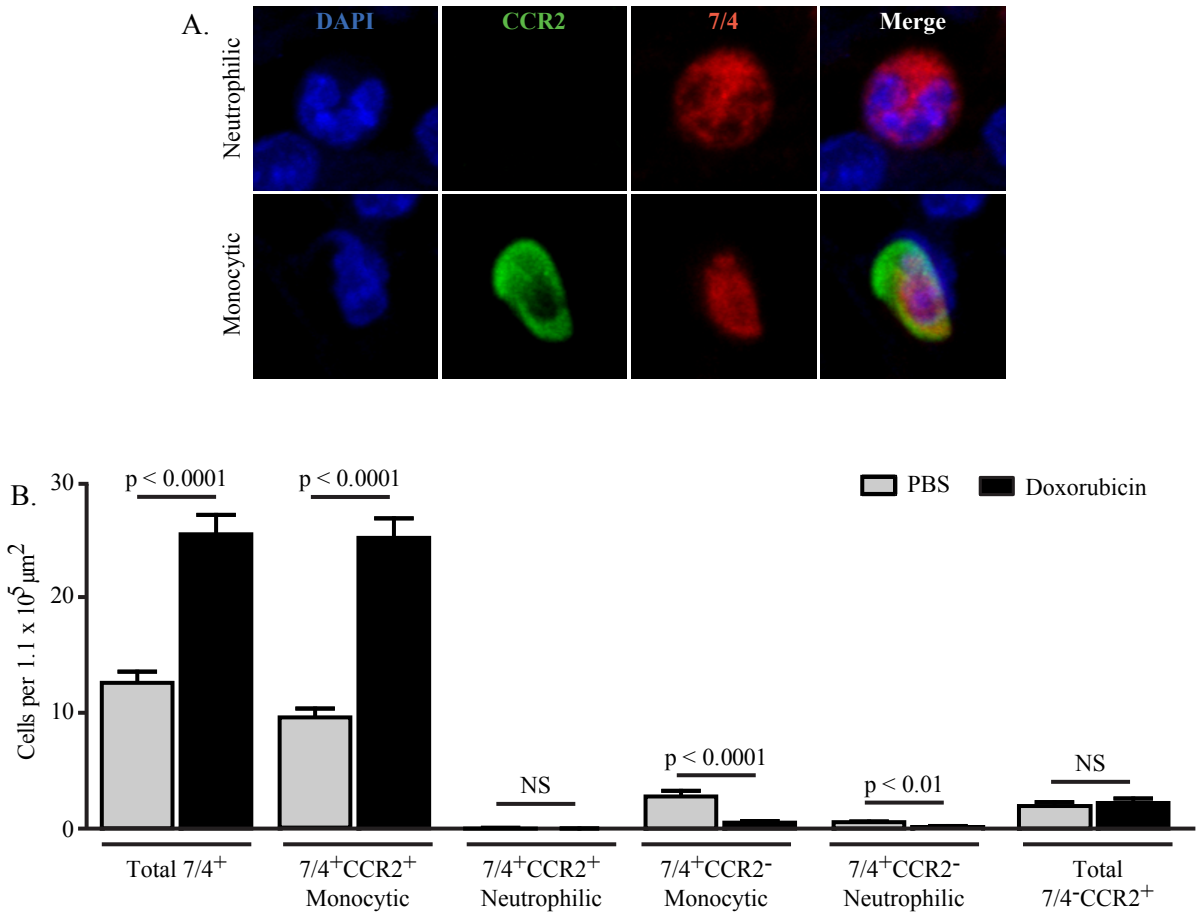

Figure 23. Double label immunostains for 7/4 and CCR2 show increased numbers of double-positive immune cells exhibiting a monocytic phenotype in the tumors of doxorubicin treated mice. (A) Representative images of neutrophils and monocytes and their staining patterns with 7/4 and CCR2. Images taken at 63× magnification. (B) Quantification of double label immunofluroescence stains. p-values based on two-tailed Student's t-test.

negative for the 7/4 antigen. Additionally, the tumors of doxorubicin-treated mice showed a significant decrease in the number of cells that expressed the 7/4 antigen but were negative for CCR2, regardless of whether they exhibited a monocytic or neutrophilic morphology (Figure 23B).

Small molecule antagonism of CCR2 *in vivo*

The monocytic cells that are recruited to tumors can either be myeloid-derived suppressor cells (MDSCs) that inhibit anti-tumor immune responses (Lesokhin et al., 2011), or true monocytes that will differentiate into tumor-associated macrophages based on microenvironmental cues and promote tumor progression (Pollard, 2004). Distinguishing these two populations is, at present, difficult as they express the same cell-surface markers (CD11b and Gr1) and exhibit similar morphological properties. We hypothesized that the myeloid cells recruited after doxorubicin treatment are monocytes, as it has recently been shown that CCL2 recruits monocytes to primary murine breast tumors as well as metastatic sites (Qian et al., 2011). Furthermore, stromal expression of CCL2 in human breast cancers is associated with both macrophage infiltration and decreased relapse-free survival (Fujimoto et al., 2009). For these reasons we predicted that inhibition of CCL2/CCR2 signaling would enhance the response to doxorubicin treatment.

Inhibiting CCL2/CCR2 signaling is challenging because CCL12 – which is also upregulated in the tumors of doxorubicin-treated mice – also activates CCR2 and may compensate for loss of CCL2 activity. We therefore decided to focus on antagonizing CCR2, testing the small molecule inhibitor RS 504393 (CCR2i, Roche/Iconix, Higgins et al., 2007), which has been previously used successfully to inhibit monocyte recruitment in infection and autoimmune models (Yang et al., 2009; Yang et al., 2010).

MMTV-PyMT tumor-bearing mice were pre-treated with either vehicle or RS 504393 every 12 hours beginning three days before doxorubicin (or PBS) treatment and continuing until just before euthanization. Tumor measurements were taken at the start of treatment with vehicle or the inhibitor, and on days 0, 1, and 2 of doxorubicin or PBS treatment. Ultrasound was performed on 2-3 tumors

per mouse on days -3, 0, and 2 following doxorubicin treatment to determine whether inhibitor treatments influenced the degree of tumor necrosis or the occurrence of cystic areas. Flow cytometric analyses for the myeloid markers 7/4, F4/80, and Gr1 were performed on cells isolated from one tumor from each mouse to determine the effects of the CCR2i on myeloid cell recruitment. In addition, we imaged two mice treated with the inhibitor plus doxorubicin and two mice treated with the inhibitor plus PBS.

The inhibitor treatment did not influence the tumor size in either doxorubicin- or PBS-treated mice (Figure 24, error depicted as mean ± SEM, n = 9 mice for vehicle with PBS, n = 10 mice for all other groups, p = NS for vehicle with PBS as compared to CCR2i with PBS at all time points, p = NS for vehicle with doxorubicin as compared to CCR2i with doxorubicin at all time points, two-tailed Student's t-test). Furthermore, ultrasound also revealed no effects of CCR2i treatment on the response to doxorubicin (data not shown). Surprisingly, flow cytometric analyses showed a non-significant trend toward an increase in the $F4/80^{+}CD11b^{+}$ population, as well as a decrease in the $7/4^{+}CD11b^{+}$ and $Gr1^{+}CD11b^{+}$ populations in tumors after doxorubicin plus CCR2i vehicle (DMSO) treatment as compared to the tumors of mice that received PBS plus the vehicle (Figure 25, error depicted as mean ± SEM, n = 3 mice per group with 1 tumor per mouse). These results are opposite to those obtained in the comparison of the tumors from mice treated with doxorubicin to PBS without the CCR2i vehicle (see Figure 22).

Imaging of inhibitor-treated mice also displayed results that are different from those observed in animals treated with PBS or doxorubicin alone (Figure 26). In the tumors of inhibitor-treated mice that received PBS, high degrees of cancer cell death and myeloid cell infiltration were observed. These results were surprising, as PBS treatment by itself does not result in the recruitment of myeloid cells, but might be caused by cancer cell death induced by CCR2i (although it is generally not the case, some cancer cells do stain positively for CCR2 by immunofluorescence, data not shown). In contrast, the tumors of inhibitor-treated mice that received doxorubicin, showed virtually no cancer cell death, but a high degree of myeloid cell death. The inhibitor is expected to affect myeloid cells,

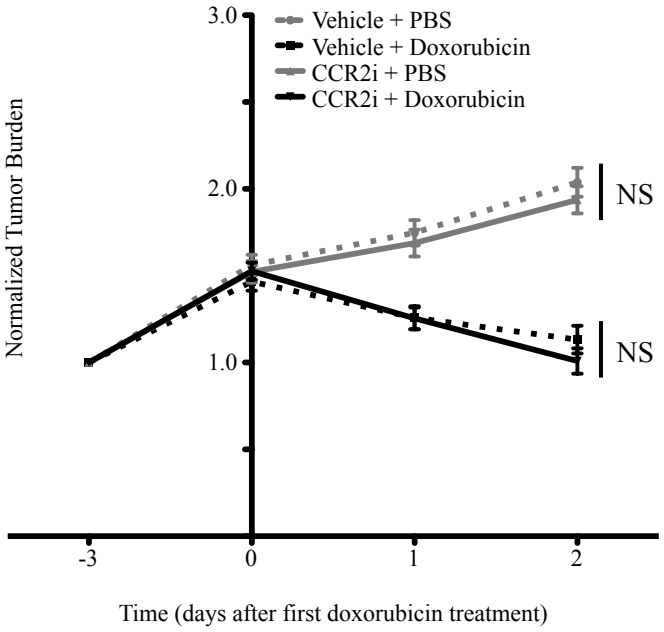

Figure 24. Treatment of MMTV-PyMT tumor-bearing mice with the CCR2 inhibitor (CCR2i) RS 504393 has no effect on tumor response to doxorubicin. p-values based on two-tailed Student's t-test at each time point.

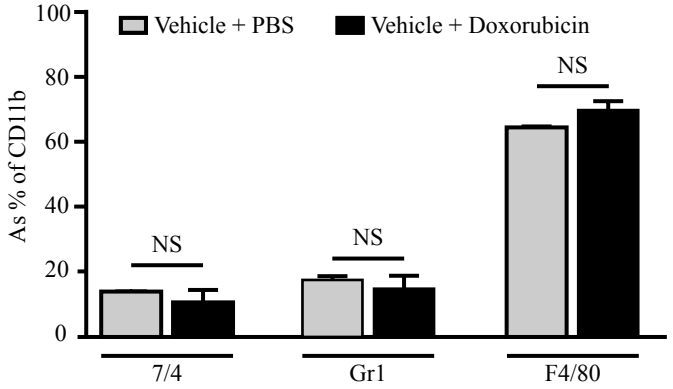

Figure 25. Flow cytometric analyses of vehicle-treated mice shows trends opposite to those observed in mice treated with PBS or doxorubicin alone. The comparison between mice treated with PBS or doxorubicin alone shows increases in the $7/4^{+}CD11b^{+}$ and $Gr1^{+}CD11b^{+}$ populations after doxorubicin treatment, with a slight (but non-significant) decrease in the numbers of $F4/80^{+}CD11b^{+}$ population. Adding vehicle (DMSO) to these treatments shows trends towarad the opposite. p-values based on two-tailed Student's t-test.

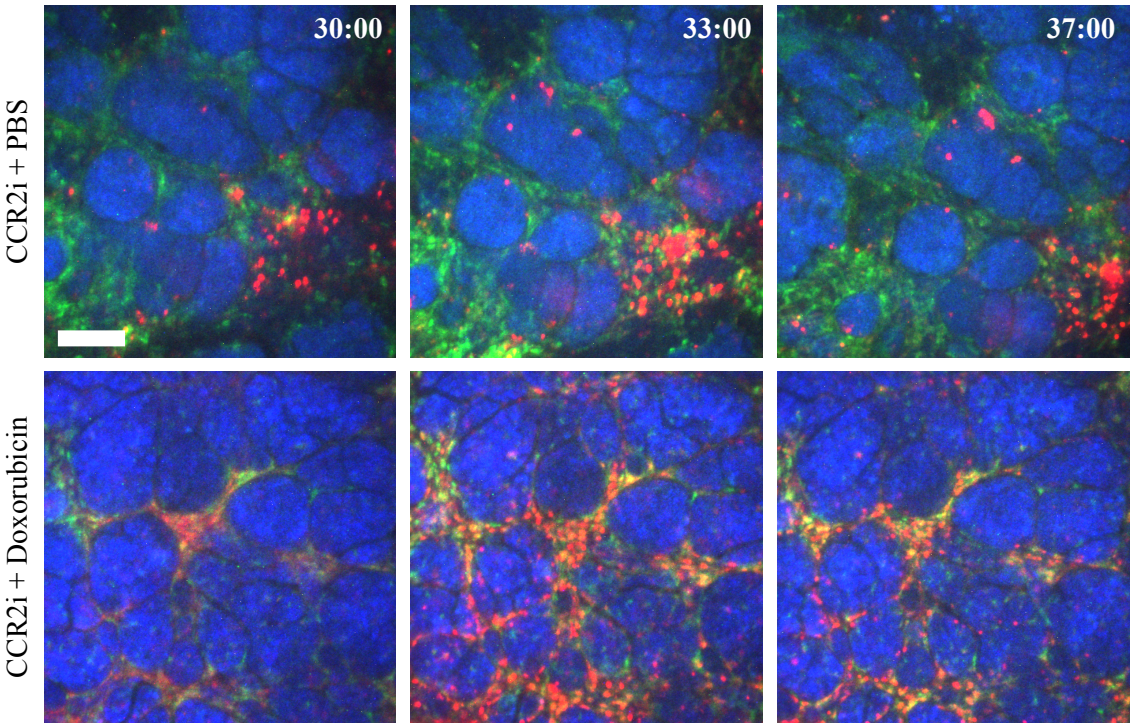

Figure 26. Intravital imaging experiments of mice treated with RS 504393 shows cancer cell death in PBS-treated mice and stromal cell death in doxorubicin-treated mice. Animals treated with the inhibitor and PBS show high degrees of cancer cell death, while animals treated with the inhibitor and doxorubicin show high degrees of stromal cell death but virtually no cancer cell death. Both treatments result in the recruitment of myeloid cells. Time represents hh:mm elapsed since doxorubicin treatment. Scale = 100 μm.

and it is possible that this could induce myeloid cell death. However, the absence of cancer cell death was highly unexpected. We speculate that the vehicle (DMSO) had a direct effect on the mice, as mice receiving vehicle alone showed signs of irritation, including sensitivity to touch. In conclusion, we have no data supporting that RS 504393 inhibited CCR2 at the dose and schedule used.

Loss of CCR2 in the stromal compartment delays host relapse following cessation of doxorubicin treatment

Because we were unable to use RS 504393, we decided to use a transplantation approach that would allow us to remove CCR2 expression from the stromal compartment. We harvested *Ccr2*$^{+/+}$ cancer cells from the tumors of MMTV-PyMT (C57BL/6) donors and orthotopically injected them into *Ccr2*$^{+/+}$ and *Ccr2*$^{-/-}$ (C57BL/6) hosts.

We observed no differences in tumor take or tumor growth rate between wildtype and *Ccr2*$^{-/-}$ hosts following cancer cell transplantation (Figure 27, n = 17 mice per treatment, log-rank score for survival curve, two-tailed Student's t-test for growth curve). To confirm that loss of stromal CCR2 prevented myeloid cell recruitment, we performed flow cytometric analyses on tumors harvested from mice euthanized 48 hours after doxorubicin treatment. Similar to the results we observed in wildtype hosts (Figure 22C-D), we saw no differences in the total CD11b^{+} and F4/80^{+}CD11b^{+} populations between the tumors of doxorubicin- and PBS-treated mice (Figure 28C-D, error depicted as mean ± SEM, n = 11 PBS-treated mice with 1 tumor per mouse, n = 11 doxorubicin-treated mice with 1 tumor per mouse, two-tailed Student's t-test). However, unlike wildtype hosts (Figure 22B), *Ccr2*$^{-/-}$ hosts showed a slight but non-significant increase in the number of Gr1^{+}7/4^{+}CD11b^{+} myeloid cells recruited into the tumors of doxorubicin- as compared to those of PBS-treated mice (Figure 28B, error depicted as mean ± SEM, n = 11 PBS-treated mice with 1 tumor per mouse, n = 11 doxorubicin-treated mice with 1 tumor per mouse, two-tailed Student's t-test), indicating that CCR2-dependent recruitment of myeloid cells into tumors after doxorubicin treatment was abrogated in our transplantation system.

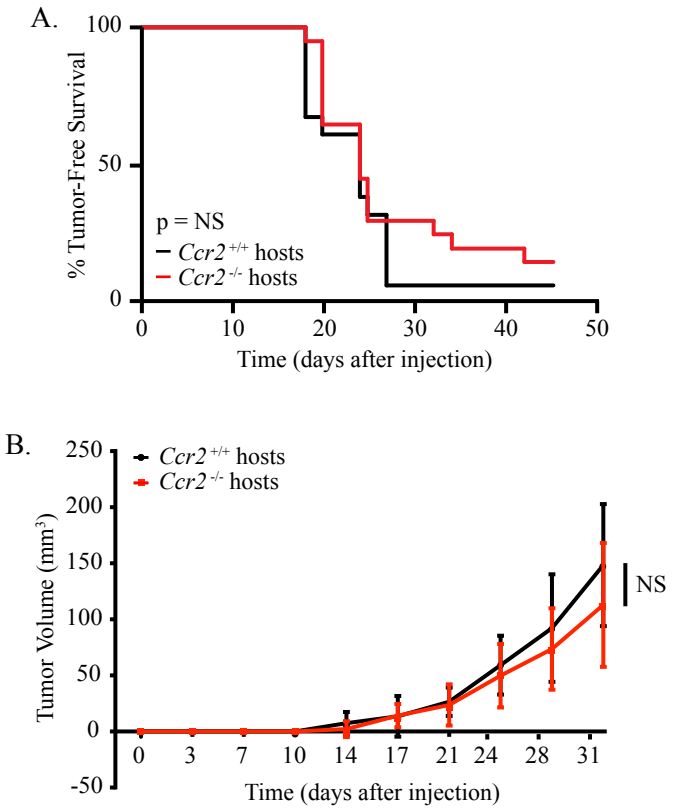

Figure 27. Loss of CCR2 expression in the stromal compartment does not affect tumor take or tumor growth. (A) Tumor-free survival of *Ccr2*$^{+/+}$ and *Ccr2*$^{-/-}$ hosts orthotopically transplanted with *Ccr2*$^{+/+}$ MMTV-PyMT cancer cells. p-value based on log-rank test. (B) Growth curves of tumors of *Ccr2*$^{+/+}$ and *Ccr2*$^{-/-}$ hosts orthotopically transplanted with *Ccr2*$^{+/+}$ MMTV-PyMT cancer cells. p-value based two-tailed Student's t-test at each time point. Error depicted as mean ± SEM.

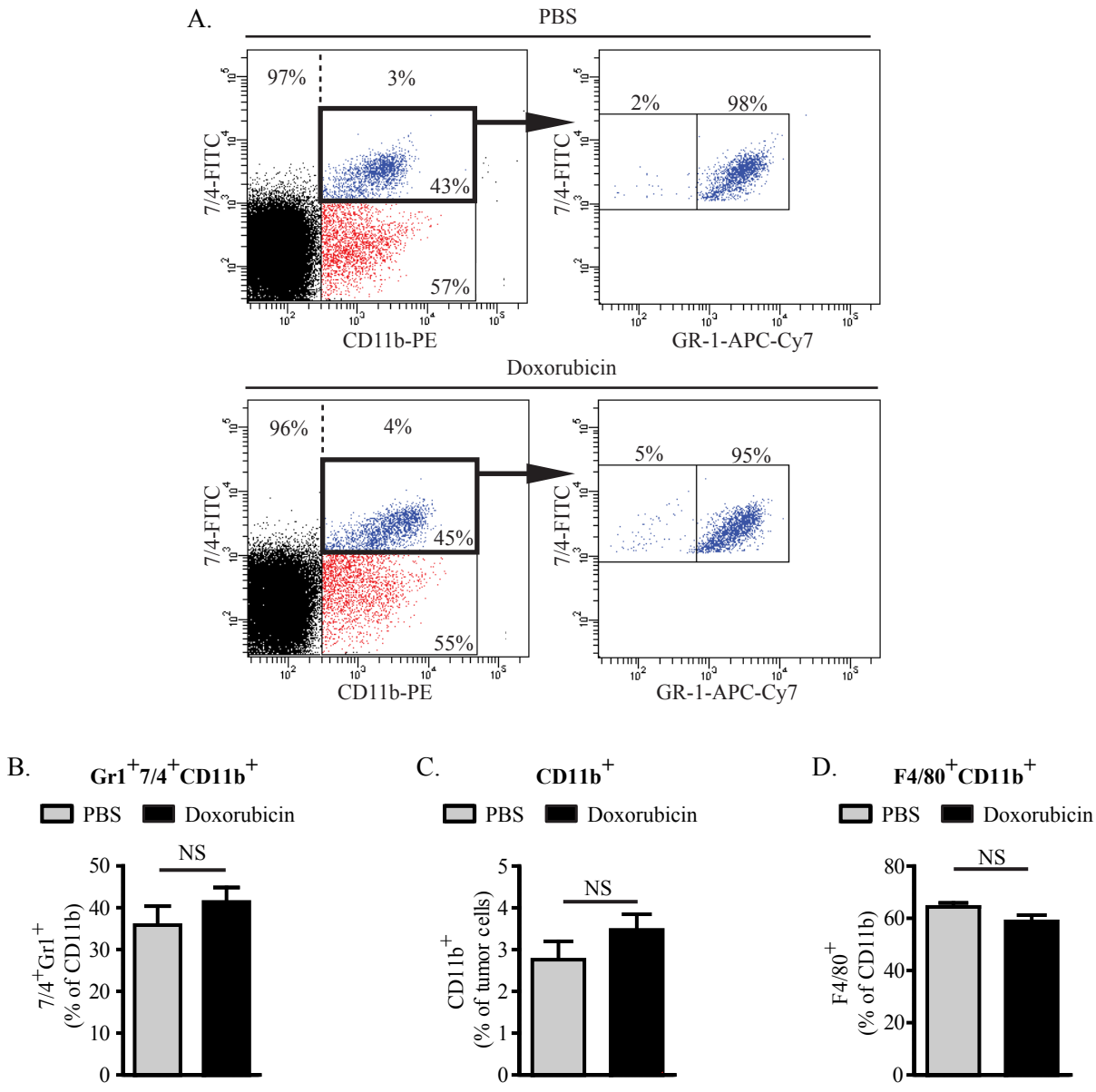

Figure 28. Flow cytometric analyses shows no change in the numbers of Gr1$^+$7/4$^+$CD11b$^+$ immature myeloid cells in the tumors of *Ccr2*$^{-/-}$ hosts treated with doxorubicin. (A) Representative FACS plots for Gr1$^+$7/4$^+$CD11b$^+$ triple stains of cells harvested from tumors 48 hours after the indicated treatment. (B) Quantification of Gr1$^+$7/4$^+$CD11b$^+$ myeloid cells. (C) Quantification of total CD11b$^+$ myeloid cells. (D) Quantification of F4/80$^+$CD11b$^+$ macrophages. p-values based on two-tailed Student's t-test. Error depicted as mean ± SEM.

When tumor-bearing wildtype and *Ccr2*$^{-/-}$ hosts were treated with doxorubicin for 3 weeks, we found that the initial response to doxorubicin was the same regardless of host genotype. However, mice lacking CCR2 expression in the stroma showed a delay in relapse following cessation of therapy (Figure 29, n = 8 tumors per genotype, mean ± SEM, * indicates $p < 0.05$, two-tailed Student's t-test; two mice from each genotype were unhealthy and so they were euthanized on days 13-16).

The tumors of *Ccr2*$^{-/-}$ mice show differences in histopathology following doxorubicin treatment

To characterize the effects of losing CCR2 expression on histopathology of doxorubicin-treated tumors, we performed hematoxylin and eosin (HE) staining on tumors harvested 48 hours after doxorubicin treatment. Tumors from *Ccr2*$^{-/-}$ hosts were far more cystic with decreased cellularity as compared to tumors removed from wildtype hosts (Figure 30). Furthermore, tumors removed from *Ccr2*$^{-/-}$ mice 6 weeks after treatment (4 weeks after the last dose) showed a dramatic reduction in tumor grade as compared to those harvested from the tumors of wildtype mice at the same time point (Figure 31, n = 1 low-grade and 11 high-grade tumors from *Ccr2*$^{+/+}$ hosts, n = 10 low-grade and 5 high-grade tumors in *Ccr2*$^{-/-}$ hosts, $p = 0.005$, Fisher's exact test).

Phenotypic changes in tumor vasculature are apparent when CCR2 expression is lost in the stromal compartment

One of the best-characterized effects of monocyte and macrophage infiltration into tumors is their ability to promote angiogenesis by producing factors such as VEGF (Dirkx et al., 2006). Thus, we wanted to determine whether there was an effect on the architecture of the tumor vasculature. We assessed vascular permeability using lectin staining for *Lycopersicon esculentum* (tomato) lectin, which labels all functional vasculature and *Ricinus communis* agglutinin I, which labels areas of increased vascular leakiness (Thurston et al., 1996). Analyses of these stains showed that the density of functional vasculature (as determined by tomato lectin staining) was higher in the tumors of *Ccr2*$^{-/-}$ hosts, while there was no change in the density of leaky vasculature, as determined by

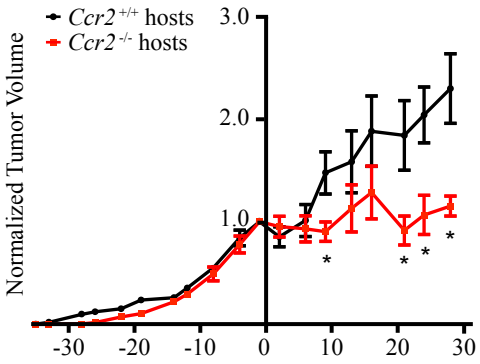

Figure 29. Tumor relapse is delayed in *Ccr2*$^{-/-}$ hosts treated with doxorubicin. * $p < 0.05$. p-values based on two-tailed Student's t-test at each time point. Error depicted as mean ± SEM.

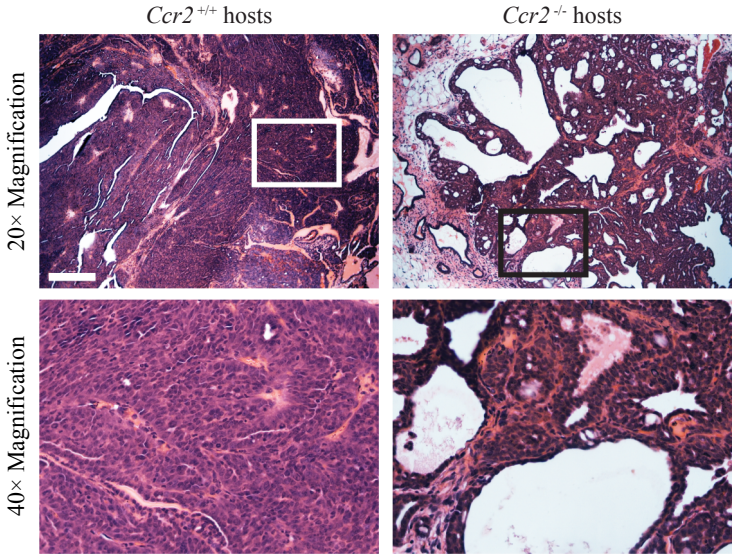

Figure 30. The tumors of *Ccr2*$^{-/-}$ hosts are more cystic with fewer cells than those of wildtype hosts, 48 hours after doxorubicin treatment. Hematoxylin and eosin stain. Scale = 100 μm.

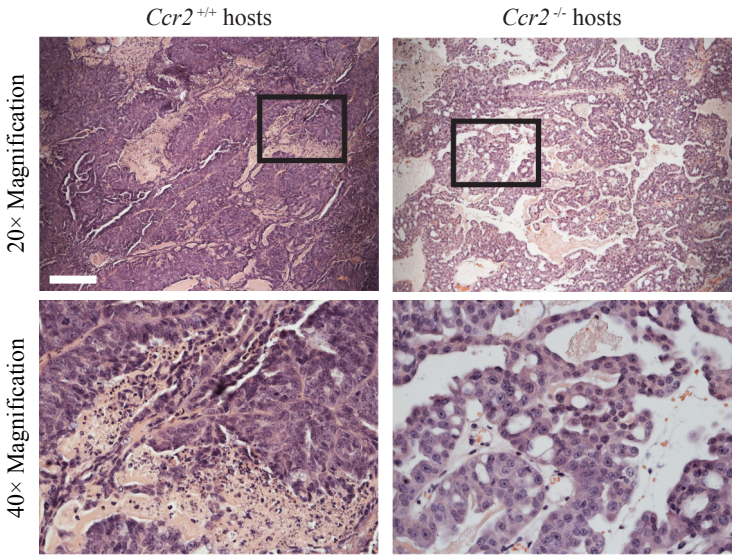

Figure 31. The tumors of *Ccr2*$^{-/-}$ hosts are of a lower grade and more differentiated than those of wildtype hosts, 6 weeks after the first doxorubicin treatment. Hematoxylin and eosin stain. Scale = 100 μm.

Ricinus communis agglutinin I staining (Figure 32A-C, n = 6 mice per genotype with 2 tumors per mouse, 48 total fields for *Ccr2*$^{+/+}$ hosts and 46 total fields for *Ccr2*$^{-/-}$ hosts, mean ± SEM, p = 0.005 for total vasculature, p = NS for leaky vasculature, two-tailed Student's t-test). The net result of this change is a significant reduction in leaky tumor vasculature (Figure 32D).

To further analyze the vascular structure, we performed immunofluorescence analyses of tumor tissues harvested from *Ccr2*$^{+/+}$ and *Ccr2*$^{-/-}$ hosts harvested 48 hours after doxorubicin treatment to look at pericyte coverage and phosphorylation of vascular endothelial cadherin (VE-cadherin). Double label immunofluorescence staining for CD31 (a marker of endothelial cells) and αSMA (a marker of pericytes) showed increased pericyte coverage of blood vessels (Figure 33, n = 3 mice with 1 tumor per mouse and 19 total fields for *Ccr2*$^{+/+}$ hosts, n = 4 mice with 1 tumor per mouse and a total of 27 fields for *Ccr2*$^{-/-}$ hosts, mean ± SEM, p = 0.0268, two-tailed Student's t-test). Staining for phospho-VE-cadherin (a marker of disrupted endothelial-endothelial adherens junctions, (Dejana et al., 2008) showed a slight, but non-significant decrease in this parameter (Figure 34, n = 3 mice with 1 tumor per mouse and 25 total fields for *Ccr2*$^{+/+}$ mice, and n = 4 mice with 1 tumor per mouse and 30 total fields from *Ccr2*$^{-/-}$ mice, mean ± SEM, p = 0.1890, two-tailed Student's t-test).

Transgenic MMTV-PyMT;*Ccr2*$^{-/-}$ mice respond better to doxorubicin than their heterozygous littermates

To further confirm that loss of CCR2 expression improved the response to chemotherapy, we crossbred MMTV-PyMT (C57BL/6) mice with *Ccr2*$^{-/-}$ (C57BL/6) mice to generate MMTV-PyMT;*Ccr2*$^{+/-}$ and MMTV-PyMT;*Ccr2*$^{-/-}$ transgenic mice. Unlike our transplantation model, the loss of CCR2 expression in our transgenic model resulted in a better response to doxorubicin from the outset, compared to heterozygous controls. Despite this, tumors from MMTV-PyMT;*Ccr2*$^{-/-}$ mice appear to relapse at approximately the same rate as their heterozygous counterparts (Figure 35, n = 15 tumors for 8 heterozygous mice, n = 26 tumors from 10 knockout mice, mean ± SEM, p < 0.05 for all

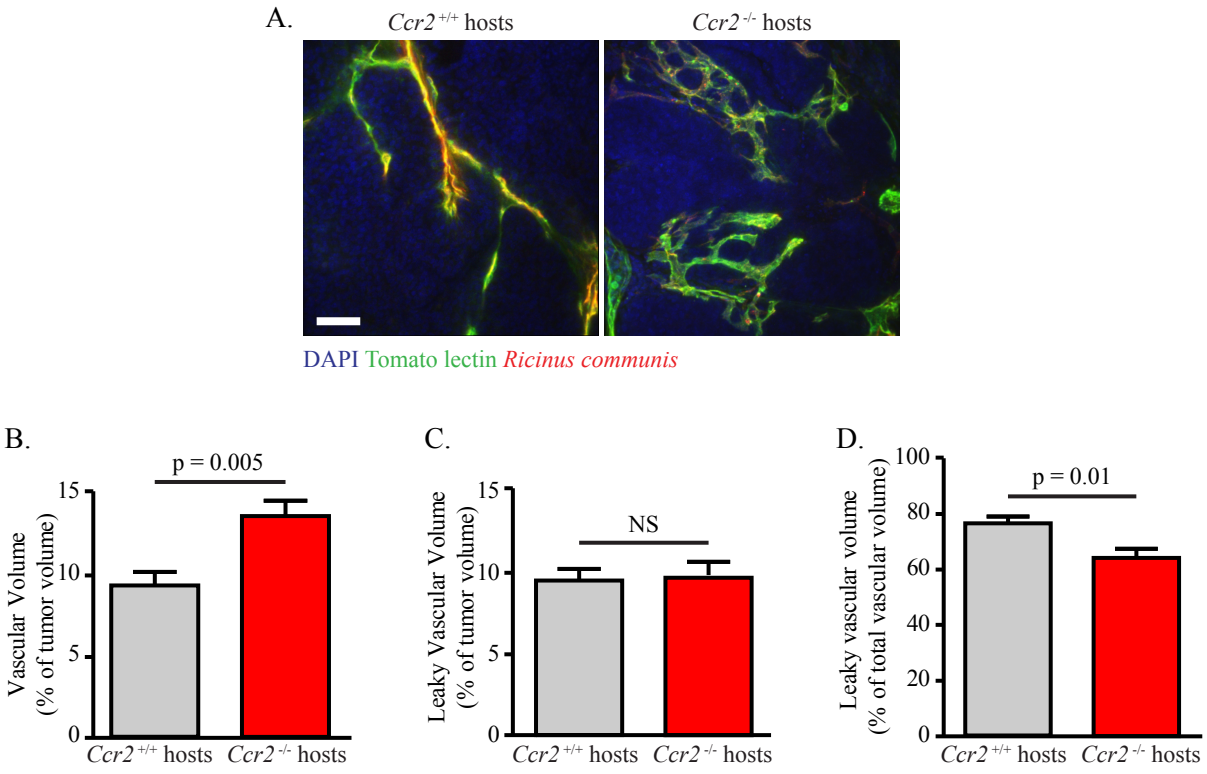

Figure 32. The tumors of *Ccr2*$^{-/-}$ mice show increased blood vessel density per tumor area with decreased leaky vasculature per tumor area, 48 hours after doxorubicin treatment. (A) Represetative fluorescence staining for tumor vasculature. Scale = 100 μm. (B) Quantification of total blood vessel volume (tomato lectin signal). (C) Quantification of leaky vascular volume (*Ricinus communis* agglutinin I signal). (D) Degree of vascular leakiness (as the precentage of total vascular volume that also stains positively for *Ricinus communis* agglutinin I). Error depicted as mean ± SEM. p-value based on two-tailed Student's t-test.

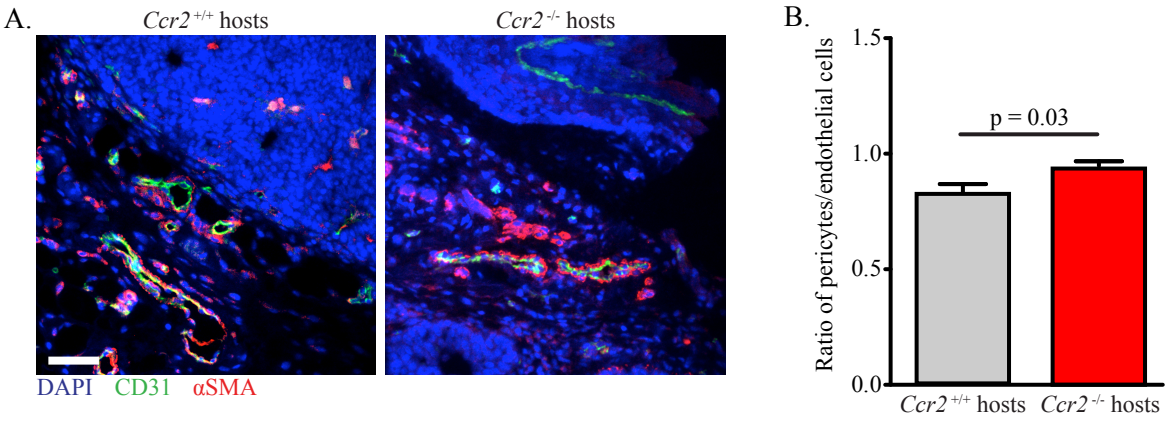

Figure 33. The tumors of *Ccr2*$^{-/-}$ mice show an increase in pericyte coverage of blood vessels, as compared to the tumors of wildtype hosts, 48 hours after doxorubicin treatment. (A) Representative images of double label immunofluorescence stains for blood vessels (CD31) and pericytes (αSMA). Scale = 50 μm. (B) Quantification of perciyte coverage. Error depicted as mean ± SEM. p-value based on two-tailed Student's t-test.

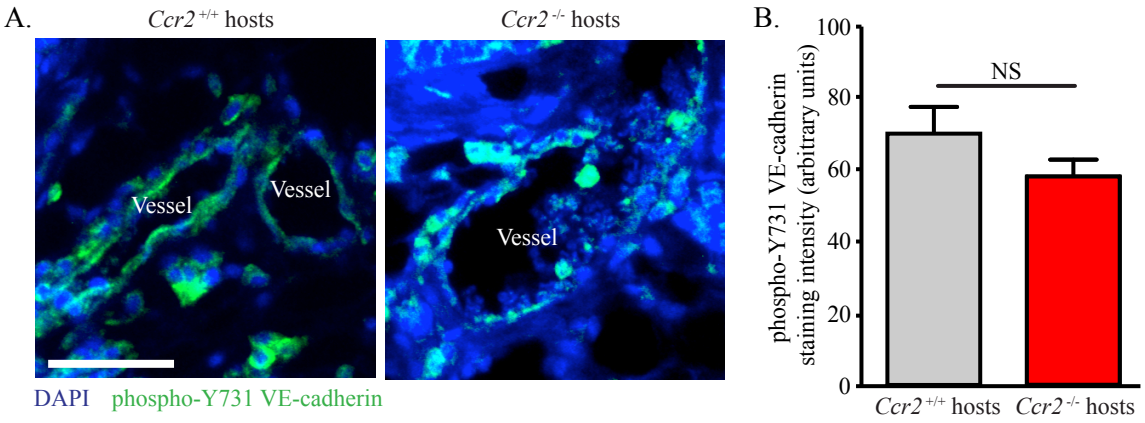

Figure 34. The tumors of *Ccr2*$^{-/-}$ mice show a slight decrease in phosphorylation of VE-cadherin, as compared to the tumors of wildtype hosts, 48 hours after doxorubicin treatment. (A) Representative image of immunofluorescence stains for blood vessels VE-cadherin phosphorylation. Scale = 50 μm. (B) Quantification of VE-cadherin phsophorylation. Error depicted as mean ± SEM. p-value based on two-tailed Student's t-test.

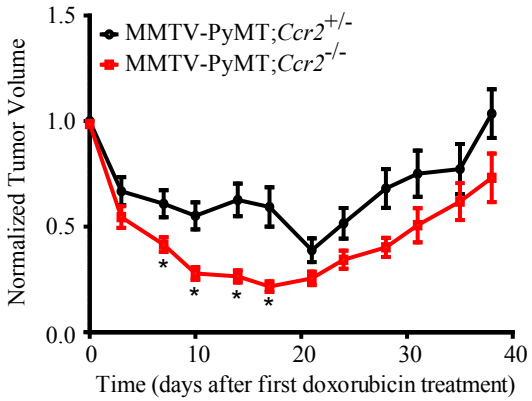

Figure 35. Transgenic MMTV-PyMT;*Ccr2*$^{-/-}$ mice respond better to doxorubicin than their heterozygous littermates. Mice were treated with doxorubicin on days 0, 14, and 21, and tumors were measured by caliper twice a week. Error depicted as mean ± SEM. p-values based on two-tailed Student's t-test.

*, two-tailed Student's t-test).

The enhanced response to doxorubicin following loss of CCR2 expression is a general phenomenon applicable to other classes of cytotoxic chemotherapeutics

We wanted to determine whether the loss of CCR2 expression in the stromal compartment would delay relapse or enhance the response to another class of chemotherapeutic drugs. To do so, we first tested two drugs representing two major classes of clinically relevant chemotherapeutics – the alkylating agent cyclophosphamide (trade name Cytoxan) and the platinum-based drug cisplatin – to confirm that the tumors of MMTV-PyMT mice respond to these therapies. MMTV-PyMT tumor-bearing mice were treated on days 0, 7, and 14 and followed for 2 to 3 weeks. Mice responded well to both treatments, showing a significant reduction in overall tumor burden as compared to PBS-treated control mice (Figure 36, error depicted as mean ± SEM, n = 6 mice per treatment group, ** indicates $p < 0.004$, *** indicates $p < 0.001$, two-tailed Student's t-test at the last time point).

Because cisplatin was significantly more effective in our system than cyclophosphamide, we enrolled wildtype and *Ccr2*$^{-/-}$ hosts transplanted with cancer cells in a cisplatin regimen, treating them on days 0, 7, and 14 and then following the mice for up to two weeks. *Ccr2*$^{-/-}$ hosts displayed a better tumor response to cisplatin from the outset, but relapsed at approximately the same rate as wildtype hosts (Figure 37, error depicted as mean ± SEM, n = 11 *Ccr2*$^{+/+}$ hosts with 22 tumors, n = 12 *Ccr2*$^{-/-}$ hosts with 24 tumors, * $p < 0.05$, ** $p < 0.01$, two-tailed Student's t-test at each time point), indicating that the CCR2-dependent recruitment influences the therapeutic response to a range of different chemotherapeutic drugs.

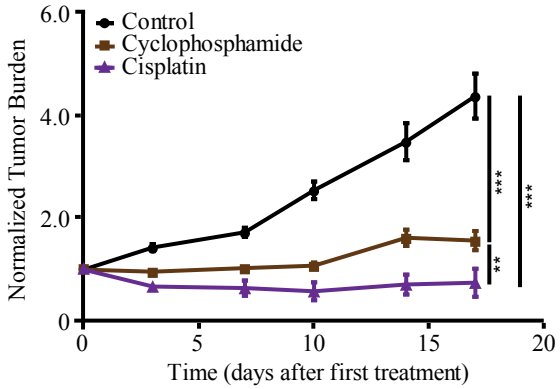

Figure 36. The tumors of MMTV-PyMT mice respond to both cisplatin and cyclophosphamide. Mice were treated on days 0 and 14. Error depicted as mean ± SEM. ** $p < 0.004$, *** $p < 0.0001$. p-value based on two-tailed Student's t-test at each time point.

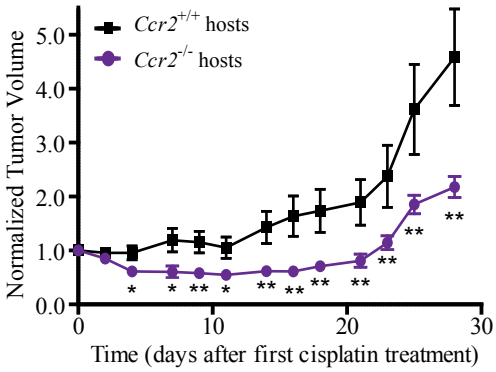

Figure 37. The tumors of *Ccr2*$^{-/-}$ mice respond better to cisplatin than those of wildtype hosts. Mice were treated with cisplatin on days 0, 14, and 21, and tumors were measured by caliper twice a week. Error depicted as mean ± SEM. * $p < 0.05$, ** $p < 0.01$. p-values based on two-tailed Student's t-test.

Discussion

Using the MMTV-PyMT mouse model of luminal breast cancer, we show that sensitivity to doxorubicin *in vivo* is influenced by the evolving tumor microenvironment. Tumors at the early carcinoma stage (as defined by *in vivo* imaging or histopathology) are highly sensitive to doxorubicin treatment, which induces necrosis, a highly immunogenic form of cell death that triggers the recruitment of $CCR2^{+}$ monocytic cells. Loss of CCR2 expression in the stromal compartment results in a delay in tumor relapse and a lower histological grade six weeks after doxorubicin treatment. Global loss of CCR2 expression enhances the overall response to doxorubicin from the outset. These results provide strong evidence that manipulating components of the tumor microenvironment – in this case, the tumor-associated myeloid population – in the adjuvant setting can improve chemotherapeutic response.

Tumor stage-dependent sensitivity to doxorubicin

In our mouse model, tumors exhibit stage-dependent sensitivity to doxorubicin that can be primarily contributed to the microenvironment. Furthermore, doxorubicin sensitivity itself results in necrotic cell death that initiates a reactive change in the tumor-associated inflammatory environment with major implications for tumor relapse. While the data herein presented focus on the latter process, there are many factors that can contribute to drug sensitivity *in vivo*. Some of these include increased interstitial pressure resulting from abnormal leakage from blood vessels and drainage into lymphatics, physical barriers presented by changes in the composition of the extracellular matrix, altered tissue oxygenation and pH, limited diffusibility of the drug, and drug uptake by stromal cells (Egeblad et al., 2010).

Other lines of work in our laboratory have shown that the differences in doxorubicin sensitivity among tumor stages are due in part to differences in vascular permeability, and by extension, drug distribution. While the exact mechanism by which this difference in vascular permeability is unclear, it appears as though myeloid cells may have an important role in this process,

as intravital imaging experiments show that when animals are intravenously injected with a fluorescently conjugated dextran, areas exhibiting the highest degree of dextran leakage into tissues are those in which there are high numbers of myeloid cells associated with the tumor vasculature (Nakasone et al., 2012). Furthermore, preliminary immunohistological analyses performed in our laboratory, as well as work from others, show that the degree to which tumors are infiltrated with immune cells is highly correlated with tumor stage and angiogenesis in both the MMTV-PyMT mouse model and human breast cancers (Egeblad et al., 2008; Leek et al., 1996, Lin et al., 2003).

In addition to the role of myeloid cells in regulating tumor stage-dependent doxorubicin sensitivity, other factors in the stromal compartment are capable of regulating drug distribution and chemotherapy resistance (Trédan et al., 2007, Meads et al., 2009). The effects of these cancer cell-stromal component interactions may be additive, synergistic, and perhaps even compensatory (in the case of depletion), to those exerted by tumor-associated myeloid cells. At present few tractable models are available for studying effects attributable to a single component of the tumor stroma *in vivo* due to the complex nature of tumor tissues, and so teasing apart the cells and molecules involved in the processes that drive environment-mediated drug resistance will necessitate a combination of intravital imaging, immunohistochemistry, and careful manipulation of tumor tissue components in both a spatial and temporal manner.

Stromal CCL2/CCR2 signaling as a modulator of myeloid cell recruitment to tumors

Here we show that expression of CCL2 is upregulated in the stromal compartment following doxorubicin treatment, and that the increased presence of this signal mediates the recruitment of monocytic cells expressing the Gr1 and 7/4 markers. The functional ramifications of recruiting immature myeloid cells ultimately depend on the phenotype they acquire when they reach the tumor. Double positivity for the pan-myeloid marker CD11b and Gr1 is used as the primary phenotypic identifier of both myeloid-derived suppressor cells (MDSC) and monocytes. MDSCs are a myeloid subpopulation that remains undifferentiated even after infiltration into the tumor and functions

primarily in the suppression of anti-tumoricidal T-cell activity thereby allowing for tumor progression (Gabrilovich and Nagaraj, 2009). While it is tempting to assume that MDSCs are the population that is being recruited to MMTV-PyMT tumors after doxorubicin treatment, there is little evidence in either the pre-clinical or clinical setting to suggest that MDSC recruitment occurs post-chemotherapy. We believe that these tumor-infiltrating myeloid cells are instead monocytes with the propensity to mature into M2-like, tumor-associated macrophages. As previously mentioned, monocytes also express high levels of both CD11b and Gr1, but in addition to these two antigens, they express high levels of CCR2 (Strauss-Ayali et al., 2007).

Thus, we propose the following model for CCL2/CCR2-dependent recruitment of immature myeloid cells to tumors after doxorubicin treatment. A stromal cell population (potentially dendritic cells) recognizes necrotic debris generated by doxorubicin-induced cell death, and subsequently upregulates expression of CCL2. This CCL2 signal recruits $CCR2^{+}Gr1^{+}7/4^{+}CD11b^{+}$ monocytes that mature into macrophages once they infiltrate the tumor tissue. Tumor-derived signals then push the polarization of these macrophages towards that of pro-tumorigenic macrophages that go on to produce cytokines and growth factors important for tumor proliferation and progression, ultimately resulting in host relapse (Figure 38).

Derivation of tumor-associated macrophages (TAMs) from tumor-infiltrating monocytes is the predicated mechanism for generating TAMs (Mantovani et al., 2002). While there is at present little scientific evidence for this occurring *in situ*, studies of ovarian cancer show that $CCR2^{+}$ monocytes are recruited to tumors, where they downregulate expression of CCR2 as they mature into macrophages to prevent migration away from the tumor tissue (Sica et al., 2000). It may be – in addition to providing angiogenic and growth factors – that one important functional consequence of monocytes maturing into TAMs is to induce cancer cell expression of signals that recruit additional macrophages into tumor tissues at a later time.

Other groups have shown that the numbers of macrophages in MMTV-PyMT tumors is increased 7 days after chemotherapy is administered (DeNardo et al., 2011; Shree et al., 2011).

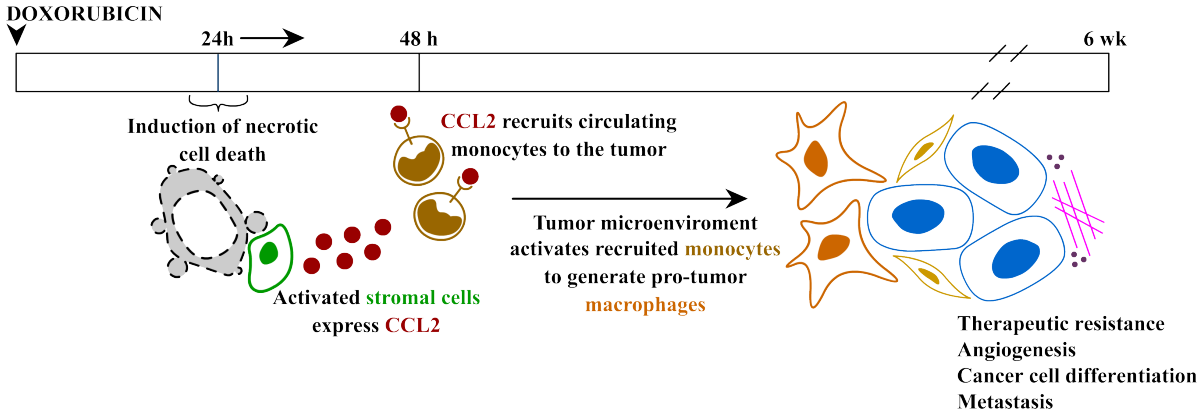

Figure 38. Hypothesis describing how stromal CCL2/CCR2 signaling might influence chemotherapeutic response. Activation of a stromal cell by interaction with cancer cells that have undergone necrotic cell death results in stromal expression of CCL2. CCL2 recruites $CCR2^{+}$ monocytes to tumors, where they differentiate into tumor-associated macrophages and go on to enhance pro-tumorigenic functions, including therapeutic resistance, angiogenesis, cancer cell differentiation, and metastasis.

Macrophages recruited in this manner can promote cancer cell survival by secreting cathepsin cysteine proteases (Shree et al., 2011), which are capable of releasing and modifying growth factors, cytokines, and other proteases sequestered in the ECM to promote angiogenesis and cancer cell invasion (Joyce et al., 2004). Recruitment of these macrophages – unlike the monocyte recruitment we observe – depends on signaling through the colony-stimulating factor-1 (CSF-1) pathway. It is possible, that $CCR2^{+}$ monocytes and tumor-associated macrophages are recruited through independent pathways and influence therapeutic response via different mechanisms. Furthermore, there may be additional pathways through which monocytes and macrophages are recruited to tumors after chemotherapy. Another such mechanism is the activation of a CXCL12/CXCR4 signaling cascade that recruits $Tie2^{+}$ macrophages into tissues that have suffered hypoxic injury (Welford et al., 2011). Because each of these myeloid cell subpopulations has a very different effector function, they can influence progression in very different ways once they have infiltrated the tumor tissue. Differentiating between these subpopulations and tracking their activity *in vivo* will require a combination of live imaging and carefully constructed reporter mice that can distinguish between monocytes and macrophages.

Inhibiting myeloid cell recruitment to enhance chemotherapeutic response

Monocyte/macrophage recruitment into solid tumors of many different origins has been shown to be an important prognostic factor, driver of tumor progression, and mediator of chemotherapeutic response. In breast cancers, accumulation of myeloid cells – macrophages in particular – is associated with advanced disease and increased risk of relapse in human breast cancer patients (Leek et al., 1996), as is elevated expression of monocyte/macrophage chemoattractant molecules like CSF-1 (Scholl et al., 1994). Furthermore, antibody-mediated depletion of myeloid cells (by targeting CD11b) and neutralization of CSF-1, improve tumor responses to both radiation therapy and chemotherapy (Ahn et al., 2010; DeNardo et al., 2011).

Here we show that a stromal CCL2/CCR2 signaling pathway modulates chemotherapeutic response, and that inhibiting myeloid cell recruitment by removing CCR2 expression from the stromal compartment delays tumor relapse. This is of clinical importance because upregulation of CCL2 has been reported in human breast tumors and is associated with decreased relapse free survival (Ueno et al., 2000; Fujimoto et al., 2009). Thus, the addition of CCL2 neutralization or CCR2 antagonism to current chemotherapeutic strategies may improve tumor responses and patient outcome. While we were unable to successfully antagonize CCR2 (CCR2 antagonists have been tested primarily for treatment of rheumatoid arthritis and have been relatively unsuccessful, Vergunst et al., 2008), work done in pre-clinical cancer models, including prostate (Loberg et al., 2007) and glioma (Zhu et al., 2011), show that combining neutralizing antibodies against CCL2 with standard of care chemotherapy treatment improves tumor responses over chemotherapy alone and prolongs survival. Studies looking at CCL2 and CCR2 antagonism for the treatment of cancer have recently moved into the clinical setting, where a monoclonal antibody against CCL2 (Janessen Biotech) is in a Phase I trial as a combination therapy with standard of care chemotherapy regimens for the treatment of various solid tumors and a Phase II trial as a stand alone therapy for metastatic prostate cancer, and a monoclonal antibody against CCR2 (Millennium Pharamceuticals) is in a Phase II trial for the treatment of bone metastases.

Altering tumor grade after chemotherapy treatment

In addition to delaying tumor relapse following doxorubicin treatment, chronic loss of CCR2 expression in the stromal compartment shows a strikingly lower tumor grade at 6 weeks after administration of the first dose of doxorubicin as compared to mice that express CCR2 normally. Whereas tumors in wildtype mice are necrotic, undifferentiated, and as advanced as the tumors of untreated control mice, tumors in *Ccr2*$^{-/-}$ hosts are differentiated with structures resembling ducts. These phenotypic changes imply that the cues present in the microenvironment are altered in *Ccr2*$^{-/-}$ hosts, and that cancer cells are responding to these changes. CCL2/CCR2 signaling may be acting

directly on cancer cells or indirectly via other CCL2-responsive cellular stromal components to derive growth factors and other cues involved in directing differentiation and motility. Thus, CCL2/CCR2 signaling may affect not only tumor-infiltrating myeloid cells, but cancer cells as well.

There is some clinical evidence based on histopathologic examination of breast tumors implicating CCL2 expression in promoting both cancer cell proliferation and invasiveness (Valkovic et al., 1998; Dwyer et al., 2007). In a laboratory model of breast cancer, the glycoprotein dysadherin upregulated expression of CCL2 in the MDA-MB-231 breast cancer cell line and acted in an autocrine fashion to drive cancer cell migration (Nam et al., 2006). Further, in prostate cancer, CCL2 expression has been found to regulate the migratory and proliferative potential of prostate cancer epithelial cells in a phosphoinositide 3-kinase-dependent manner (Loberg et al., 2006).

While the effects of CCL2/CCR2 signaling on cancer cell proliferation and invasion are still being determined, there are significant clinical implications underlying this lower tumor grade. Both understanding mechanistically how the differentiation of invasive, highly undifferentiated tumors occurs and determining whether this is entirely CCL2/CCR2-dependent or dependent on more general signaling pathways, are of clinical importance because low-grade tumors are generally far easier to treat than higher-grade tumors (Elston and Ellis, 1991). Moreover, having the ability to force the differentiation of any highly aggressive solid tumor – even in those where CCL2/CCR2 expression is not a factor in tumor progression – would be a potentially powerful therapeutic tool.

Normalization of tumor vasculature

In addition to being more differentiated, tumors derived from *Ccr2*$^{-/-}$ hosts exhibited a distinctly different vascular phenotype from the tumors of wildtype hosts. These differences include, an increase in vascular density, a decrease in the leakiness of tumor vasculature, and improved pericyte coverage of blood vessels. All of these changes are indicative of vascular normalization, which has been proposed as a model for anti-angiogenic cancer therapy (Jain, 2001). This model postulates that highly abnormal tumor vasculature impedes proper blood flow through vessels and

diffusion of molecules into tissues, and that normalizing vessel architecture will reestablish normal blood flow and tissue pressure gradients, thereby improving delivery of cytotoxic chemotherapeutics.

Our results do not establish a causal role for CCL2/CCR2-signaling in the normalization of tumor blood vessels. It may be that chemokine-receptor interaction directly influences this change in tumor vasculature, as endothelial cells are purported to express CCR2 and can respond to CCL2 (Salcedo et al., 2000). Furthermore, recent finding suggest that CCL2/CCR2 signaling might have a direct effect on angiogenesis by upregulating expression of the Ets-1 transcription factor in endothelial cells (Stamatovic et al., 2006). However, we did not detect CCR2 expression by any cellular components of the tumor vasculature in MMTV-PyMT tumors.

Another plausible explanation for the normalization phenotype we observe is that it is an indirect effect resulting from inhibiting myeloid cell recruitment into tumors. Tumor-associated macrophages and other tumor-infiltrating myeloid cells produce a variety of factors (including VEGF and matrix metalloproteinases) that promote tumor angiogenesis (Murdoch et al., 2008). Blockade of tumor angiogenesis via antibody-mediated neutralization of VEGF has been shown to induce tumor normalization and improve chemotherapeutic response (Tong et al., 2004; Vosseler et al., 2005). Given the effects we observe in our transplantation model, CCL2/CCR2 antagonism may represent another approach to targeting tumor angiogenesis.

Perspectives

Innate immunity as a modulator of therapeutic response

Many *in vitro* studies and a handful of *in vivo* studies have shown that the tumor microenvironment plays an important role in therapeutic response, often by transiently altering cancer cell-intrinsic transcriptional programs that protect cells from drug-induced death. However, the majority of these resistance mechanisms have been observed primarily in the context of hematologic malignancies, and those studies that do focus on resistance in solid tumors frequently concern either the biochemical and biophysical properties that hinder drug activity and distribution or interactions between cancer cells and the ECM (Minchinton and Tannok, 2006 [review]; Heldin et al., 2004 [review]; Mahoney et al., 2003; Rohwer and Cramer, 2011 [review]; Teicher et al., 1981 [*in vitro* study]; Shain et al., 2001 [review]). While these studies represent an important step forward in understanding the processes that drive environment-mediated drug resistance, many other components of the tumor microenvironment influence a wide range of tumor processes, and so it is highly likely that factors produced by tumor stromal cells (e.g. chemokines, cytokines, ECM-remodeling molecules) or the structures formed by these cells (e.g. blood or lymphatic vessels) play an equally important role in the response to therapy. One component that would be predicted to have a strong influence on therapeutic response is the tumor-associated immune cell population. Inflammation has received much scrutiny as an important mediator of tumor initiation, progression, and metastasis, but the role of immune cells in therapeutic response has been, until recently, widely neglected.

In breast cancers, infiltration of macrophages in particular is a major predictor of progression and relapse-free survival, so it stands to reason that these cells would also be important for therapeutic response. In recent years, pre-clinical studies in mouse models of breast cancer have shown that the depletion of mature myeloid cells using depleting antibodies against the mature myeloid cell marker CD11b (Ahn et al., 2010), inhibition of myeloid cell recruitment using neutralizing antibodies

against CSF-1 (the receptor for which is expressed to varying degrees in different myeloid lineage populations; DeNardo et al., 2011), or inhibition of macrophage-derived factors (e.g. cathepsins [Shree et al., 2011], MMP9 [Nakasone et al., 2012]) can improve chemotherapy and radiation therapy responses. In each of these cases, therapeutic response is dependent on the recruitment and/or activity of macrophages.

Because macrophages are the most common myeloid cells associated with breast tumors, they have been the chief focus of studies involving immune-mediated therapeutic resistance. However, we show here that the recruitment of immature monocytic cells plays just as critical a role in the response to chemotherapy as do macrophages. This is an important finding, as it implies that multiple pathways can recruit myeloid cells, multiple myeloid cell populations influence therapeutic responses, each of these populations exerts a different effect on tumor phenotype and outcome, and that immune-directed strategies may have to target several different signaling molecules.

Questions that remain

While we, and others, have shown that myeloid cells negatively influence the response to chemotherapy, one of the major details that is lacking in all of these studies is the mechanism by which resistance arises. It is clear that multiple mechanisms exist to recruit myeloid cells into tumors, including the CCL2/CCR2 pathway, and that the increased presence of these myeloid cells in tumors contribute both to host relapse and response to later rounds of chemotherapy. What remains unclear is how these myeloid cells promote resistance.

Identifying the molecular mechanism(s) by which CCL2/CCR2 signaling promotes chemotherapeutic resistance in the MMTV-PyMT mouse model of breast cancer is inherently challenging for three major reasons. First, explication of the molecular pathways driving monocyte-dependent chemoresistance requires the use of *in vivo* models with intact immune systems, where other cellular stromal components can both contribute to therapeutic responses themselves and alter

the activities of recruited immune cells (which are highly sensitive to external cues) by adapting their own functional outputs to changes in the environment arising from the altered immune cell population. Furthermore, the presence of the intact tumor microenvironment makes it difficult to distinguish the effects due to one stromal population versus another, and it is possible that other stromal components regulate (both positively and negatively) therapeutic responses *in vivo*.

The second major challenge in determining how CCL2/CCR2 signaling promotes chemoresistance is determining the effector functions of the monocytes recruited into tumors following chemotherapy treatment. Identification of these functions requires that two major considerations be addressed. The first consideration is a confirmation of our prediction that the monocytes recruited into tumors following doxorubicin treatment are differentiating into mature, tumor-associated macrophages (TAMs) based on cues in the tumor microenvironment. This is important, as functions driving chemoresistance are expected to be macrophage-dependent. Perhaps the only way to determine whether this differentiation process occurs *in vivo* is to use intravital imaging to track the fate(s) of the infiltrating cells.

The simplest way to track monocyte differentiation is to observe the loss of expression of a monocyte-specific marker with the gain of expression of a macrophage-specific marker. Subsequently, a marker of alternatively activated, M2-like macrophages is required, to track activation of these newly differentiated macrophages. While this is a straightforward task, confirming this process is not quite feasible yet, as our current imaging capabilities prevent the imaging of more than four colors in live animals (imaging this process would probably require five to six colors), and the available markers of myeloid cell differentiation and activation are not specific enough to distinguish monocytes and macrophages using a single marker. Several fluorescent markers would be required to track this process *in vivo*, the first of which is a CCR2 reporter to identify infiltrating myeloid cells responding to CCL2 (e.g. the Charo laboratory has generated an RFP knock-in mouse, in which RFP replaces the first 270 bp of the N-terminus of *Ccr2*, which can be maintained as a

hemizygous line; Saederup et al., 2010). To distinguish between monocytes and macrophages, a monocyte marker (Ly6C could be used, but it is also expressed on other myeloid cell types) and a marker of mature macrophages (F4/80 could be used but experience in our lab as well as others [Engelhardt et al., 2012] have shown that this is also expressed on dendritic cells) are also needed. The last marker that is required is one that is specific for TAMs (for example, Arginase-1, but this is not specific to an M2 phenotype), to confirm tumor-promoting functionality of differentiated macrophages. Other markers that are not necessarily required, but would be useful for providing tissue context are the ACTB-ECFP, which would give us information about tumor stage, and the c-fms-EGFP (or a CD11b reporter line such as the CD11b-DTR/EGFP line) reporters that would allow us to identify most myeloid cells.

The second consideration required in explicating how monocytes recruited through CCL2/CCR2 signaling promote chemoresistance is to determine the final effector functions of these immune cells once they have reached their target and matured. TAMs are known to exert multiple effects on tumor progression including, cancer cell proliferation, angiogenesis, metastasis, and ECM remodeling. We have shown that there are changes in the differentiation state of tumors and in tumor vasculature, and we have preliminary data strongly suggesting an effect on metastasis, following chronic loss of CCR2 expression in the stromal compartment. However, the major question is whether these effects are due to macrophage activity, or whether these are secondary effects due to a changing tumor microenvironment. Untangling the effects that can be ascribed to macrophage activity from those that result from changes in the microenvironment (e.g. changes in fibroblast signaling due to changes in environmental cues) will be challenging, as the degree to which we can manipulate different stromal components *in vivo* is limited. We may need to utilize more complex *in vitro* systems to recapitulate various aspects of the tumor microenvironment to dissect these different pathways, before returning to *in vivo* models to confirm these pathways. One aspect that we have not yet looked at, that may provide some insight into secondary effects of TAM function is whether there are changes in ECM organization and distribution following chronic loss of CCR2. Macrophages are

known to express various proteases capable of remodeling ECM, thereby altering the bioavailability of not only chemotherapeutics, but also growth factors important for angiogenesis and tumor proliferation. One recent study demonstrating that this may be true shows that cathepsins (proteases capable of remodeling ECM) are produced by TAMs that infiltrate tumors following chemotherapy treatment, and inhibition of cathepsin activity improves chemotherapeutic response. Thus, a TAM-derived, ECM-remodeling enzyme may be altering the bioavailability of various growth factors and survival signals that were previously sequestered, thereby explaining changes in both tumor differentiation status as well as sensitivity to chemotherapy observed after CCR2 depletion. If this proves to be the case, identifying and targeting this ECM-remodeling factor, may prove to be an important means of overcoming therapeutic resistance.

The final major challenge to identifying how CCL2/CCR2 signaling promotes chemoresistance is determining whether chemoresistance is dependent solely on the recruitment of CCR2-positive monocytes, or whether other cell types that express CCR2 also responding directly to CCL2 and contributing to therapeutic resistance. Other such populations include endothelial cells, which may respond to CCL2 to form new blood vessels, and cancer cells themselves, which may use CCL2 as a metastatic cue. Determining whether CCL2/CCR2 influences chemoresistance will require the specific identification of each of the populations expressing CCR2 within MMTV-PyMT tumors, and the ability to manipulate each of these components *in vivo*. To identify CCR2-positive cell populations beyond the monocytic population we have identified will require careful immunohistochemical analyses, and potentially flow cytometric analyses, to confirm these results. Manipulation of each of these cell populations will prove to be the more difficult task, and will most likely require specific genetic ablation of CCR2. Two systems that may be of use include, (1) a Cre-lox model in which a tissue-specific promoter-driven, self-excising, inducible Cre recombinase (e.g. CD31-CreER) is paired with homozygous CCR2 floxed alleles, or (2) an inducible transgenic CCR2 short hairpin mouse model that expresses a TRE-shCCR2 transgene paired with mice expressing tissue-specific rtTA promoters (e.g. CD31-rtTA) in which knock down of CCR2 can be reversibly

regulated. There are a few caveats, however, as these transgenics do not currently exist, promoters specific for only monocytes or cancer cells have yet to be identified to properly regulate Cre, and careful characterization of such multiple-transgene models will be necessary to confirm that the increased number of transgenes does not affect the pathology and behavior of MMTV-PyMT tumors.

While a large amount of work is needed to understand the role of CCL2/CCR2 signaling in chemoresistance, another area that requires focus is determining why tumors in which there is a chronic loss of CCR2 expression still relapse despite improved responses to doxorubicin. Although, we have never performed the long-term follow-up studies to determine how CCR2 inhibition affects overall survival (we suspect that CCR2 blockade will improve overall survival), it appears that the tumor burden in all animals will eventually reach the experimental endpoint. Two major questions that need to be answered with respect to combining doxorubicin treatment with CCR2 blockade are (1) whether treatment with another class of chemotherapeutics (e.g. a taxane) after completion of the doxorubicin regimen will further shrink tumors, and (2) whether surgical resection following completion of the chemotherapy regimen would prevent minimal residual disease.

A toolkit for the future

What is evident from the work herein described is that tumor responses to systemic therapies can be dramatically different *in vitro* and *in vivo*, and often microenvironment-dependent resistances that can only be observed in the intact tumor will arise. Thus, determining how the tumor microenvironment drives chemoresistance and identifying the underlying mechanisms by which this process occurs using *in vivo* models will be an important step in treating cancer relapse and metastasis. However, there are currently many obstacles to studying the contributions of the tumor microenvironment to chemoresistance *in vivo*.

Perhaps the biggest obstacle to explicating chemoresistance pathways *in vivo* is the complexity of the tumor microenvironment. To an extent, solid tumors behave as any other normal

organ does, in that perturbations in tissue homeostasis will result in compensatory shifts in various components of the tumor to maintain proper homeostatic balance. However, because tumors are abnormal organs, perturbations to the system may result in dramatic changes in the bioavailability of growth factors and cytokines, as well as in tissue organization (e.g. changes in blood vessel structure), creating an environment that enhances tumor growth, progression, and metastasis. Even procedures such as tumor transplantation, can alter the way tumors develop and progress, as they require injection or surgery, which disrupts the recipient tissue (wounding) and results in an inflammatory environment that may not exist prior to spontaneous tumor development.

To circumvent the obstacles mentioned above, tumor microenvironment research will necessarily rely on intravital imaging to visualize in real-time the interactions and processes occurring *in vivo* following chemotherapy administration. With the technology currently available, we have made major progress in understanding how myeloid cells influence therapeutic response; however, because the tumor microenvironment is so complex, major advancements are still needed to begin to delve mechanistically into the processes underlying environment-mediated drug resistance.

One of the most important advancements required is the identification of individual markers that are specific for a single cell population (or sub-population). The importance of better markers is perhaps best illustrated in two of the most prominent stromal cell components of the breast tumor microenvironment, fibroblasts and cells of the immune system. Frequently the markers used to identify fibroblasts are also expressed on other cell. For example, in breast tumors, α-SMA can be expressed on fibroblasts, pericytes, and myoepithelial cells. While in immunostaining assays, these cell types can sometimes be distinguished based on localization, using localization to distinguish different microenvironmental components is much more challenging during intravital imaging experiments. Markers in the immune system are at least as big a problem as are markers of fibroblasts, as multiple markers are usually required to identify immune cell sub-populations, and frequently, the same sets of markers will often be used to identify different populations. Thus the

complexity of the currently available marker system used to identify various cellular components of the microenvironment poses a major problem for intravital imaging, as ideally, one would like to be able to use a single marker to identify a specific cell type so that multiple microenvironmental components can be simultaneously visualized.

New transgenic reporter lines must also be developed in conjunction with the identification of these new markers, as they are preferable to injectable reporters (the use of biologics such as fluorescently-conjugated antibodies have the potential to alter the microenvironment). In addition to requiring cell-specific promoters to drive expression of these reporters, new reporters utilizing a greater diversity of fluorescent proteins will also be necessary. Currently, most transgenic reporter lines express GFP, CFP, or RFP, even though a wider range of fluorescent proteins is available (including yellow, orange, and infrared fluorescent proteins) and used *in vitro*. We are currently working on developing a reporter line expressing IFP1.4, the only infrared fluorescent protein that has been developed.

The other major advancement that will be needed is improvements in the technologies required to perform these intravital imaging experiments, that is, primarily in the image capturing systems and analysis software. While these technologies are continually improving, there are several important considerations involved in increasing the number of fluorescent labels being imaged, including increases in the speed of photon detection-to-analog conversion (the CCD camera), acquisition and conversion of analog to digital images (imaging software). One of the consequences of increasing the number of fluorescent labels that are being imaged is increasing the number of images that need to be acquired for each time point. For example, in our laboratory, we will image approximately seven *x*,*y* positions in three z-planes during a typical four-color imaging experiment. Thus for each time point, 84 images (1 image × 4 channels × 3 z-planes × 7 positions) need to be acquired before the next time point is reached. Adding a single color channel to this increases the number of images that need to be taken per time point by 21 (1 image × 1 channel × 3 z-planes × 7

positions). This increases both the time required to acquire the data for a single time point, and the sophistication of the software used to control stage movement and laser switching, image acquisition, and data analysis. Thus, advancements in current software or new software that can increase the speed at which the microscope stage moves between z-planes and *x*,*y* positions, the rate of analog-to-digital conversion of very large datasets, and efficiently handle the analysis of these very large datasets must also be developed.

Is antagonism of CCL2/CCR2 signaling clinically relevant?

Irrespective of the new questions that need answering and the new tools that need constructing, the most important question that needs to be addressed is whether inhibition of CCL2/CCR2 signaling is clinically relevant. Much of the evidence showing that antagonizing this pathway would be beneficial to cancer therapy comes from pre-clinical models of prostate cancer. In this system, administration of neutralizing antibodies against CCL2 to syngeneic or xenograft mouse models shrinks tumors in monotherapy and improves the response to docetaxel (trade name Taxotere) in polytherapy (Loberg et al., 2007). Because the evidence supporting antagonism of CCL2/CCR2 as a useful adjuvant to chemotherapy has been quite strong in the prostate models, phase I and II clinical trials have been undertaken to combine this treatment with standard of care in prostate and metastatic cancer.

Whether combining CCL2/CCR2 antagonism with chemotherapy treatment will improve patient outcome in breast cancer remains to be seen. The mechanisms by which CCL2/CCR2 signaling drives tumor progression in prostate cancer are different when compared to those observed in our breast cancer model. In prostate cancer, CCL2/CCR2 signaling has been shown to directly affect cancer cell motility and proliferation (Loberg et al., 2006) and enhance angiogenesis via the recruitment of myeloid cells in to tumors (Loberg et al., 2007). In contrast, in our breast cancer models, there appears to be no effect of CCL2/CCR2 signaling on tumor growth, as MMTV-PyMT;*Ccr2*$^{+/-}$ and MMTV-PyMT;*Ccr2*$^{-/-}$ littermates show the same tumor latency, and the tumors

arising in *Ccr2*$^{+/+}$ and *Ccr2*$^{-/-}$ hosts show the same latency and growth rates. Although we cannot exclude that CCL2/CCR2 signaling has no direct effect on cancer cells, as some of these cells do express CCR2 by immunofluorescence staining (data not shown), an effect on cancer cell proliferation seems unlikely. Furthermore, the angiogenesis phenotype that we observe following inhibition of CCL2/CCR2 signaling is opposite to that observed in the prostate model. In the prostate model, neutralizing CCL2 inhibits angiogenesis, while in our model it appears as though inhibiting CCL2/CCR2 signaling *enhances* angiogenesis. While the differences in the effect of inhibiting CCL2/CCR2 between these two models are striking, a recent study using a glioma model shows similar results to our breast cancer results, in that anti-CCL2/CCR2 monotherapy has little effect on tumor growth, but combination therapy with temozolomide (trade name Temodar) significantly improves survival (Zhu et al., 2011). Thus, polytherapy consisting of an anti-CCL2/CCR2 agent plus chemotherapy may prove to be a feasible and potentially powerful therapeutic strategy for the treatment of breast cancer.

Concluding Remarks

Treatment of mammary tumors with the cytotoxic chemotherapeutic doxorubicin alters the tumor-associated inflammatory microenvironment by inducing a reactive recruitment of immature myeloid cells via a stromal CCL2/CCR2 signaling axis. The increased presence of these myeloid cells promotes chemoresistance, and blockade of this signaling pathway delays host relapse and improves overall therapeutic response.

CCL2/CCR2 blockade results in several phenotypic changes in tumor pathology, including tumor grade and vascular organization, implying broader effects than just those indirectly resulting from the recruitment of tumor-promoting myeloid cells. While further work is needed to mechanistically untangle the *in vivo* effects of recruiting monocytes cells into tumors and the role of CCL2/CCR2 signaling in breast cancer epithelial cell proliferation and tumor angiogenesis, it is apparent that targeting CCL2 or CCR2 in combination with chemotherapeutic treatment is a potentially powerful therapeutic strategy.

Experimental Procedures

Animals

MMTV-PyMT (FVB/n), ACTB-ECFP (FVB/n), ACTB-H2B-EGFP (obtained on mixed background and backcrossed to FVB/n for 6 generations) and *Ccr2-/-* (C57BL/6) mice were purchased from Jackson Labs. C3(1)-Tag (FVB/n) mice (Green et al., 2000) were from the NIH Mouse Repository. MMTV-PyMT (C57BL/6) mice were provided by Dr. Kasper Almholt and c-fms-EGFP mice were provided by Dr. Jeffrey Pollard and backcrossed to FVB/n mice for 6 generations. All animal experiments were conducted in accordance with procedures approved by the IACUC at the University of California, San Francisco or Cold Spring Harbor Laboratory.

Tumor transplantation experiments

Virgin females of 6-16 weeks of age were used as hosts for transplantation. Primary cancer cells were isolated from tumors derived from MMTV-PyMT (C57BL/6) mice approximately 10-14 weeks of age with tumors approximately 6-12 mm in size. Briefly, 2-3 tumors at 8-10 mm diameter (necrotic and/or cystic tumors were excluded from use for transplantation) were harvested, mechanically dissociated, and digested in an RPMI-1640-based solution containing 0.2% w/v collagenase A (Sigma), 0.2% w/v trypsin (GIBCO), 5 μg/mL insulin, 50 μg/mL gentamycin (GIBCO), and 5% v/v fetal bovine serum (GIBCO). Single cells and debris were removed from the resulting carcinoma organoid preparation by repeated rounds of differential centrifugation. Purified carcinoma organoids were dissociated into single cell suspension by incubation in 0.25% trypsin with 0.1% EDTA solution for 30 min at 37°C, and subsequently washed in PBS. Cells (4×10^5 in 20 mL PBS) were injected into each inguinal mammary gland of host mice.

Refer to Appendices I and II for detailed protocols.

Tumor response to doxorubicin, cisplatin, and cyclophosphamide

Mice were administered 8 mg/kg doxorubicin hydrochloride (in PBS, Sigma-Aldrich), 10 mg/kg cisplatin (in 10% DMSO in PBS, MBL International), or 75 mg/kg cyclophosphamide monohydrate (in distilled H_2O, MP Biomedicals) intraperitoneally on days 0, 7 and 14. Control mice were administered sterile PBS. Tumor size was tracked by caliper measurement 2-3 times a week, and tumor volumes were calculated using the equation. Refer to Appendix III for a detailed protocol.

Tumor response to combination therapy with doxorubicin and RS 504393

MMTV-PyMT tumor-bearing mice were administered the CCR2 small molecule inhibitor RS 504393 (Roche/Iconix, ordered from Tocris) intraperitoneally at a dose of 2 mg/kg every 12 hours beginning three days prior to doxorubicin or PBS treatment, with the last dose being given just prior to euthanization. Mice were administered doxorubicin (8 mg/kg) or PBS intraperitoneally and euthanized 48 hours after treatment. Tumor size was taken every day by caliper measurement, and tumor volumes were calculated using the equation $\frac{\text{length} \times (\text{width})^2}{2}$.

Refer to Appendix IV for a detailed protocol.

Detection of necrosis and intratumoral cysts by ultrasound

Ultrasound was used to detect changes in necrosis and intratumoral cysts in MMTV-PyMT tumor-bearing mice treated with RS 504393. Animal hair was removed using a chemical hair remover the day prior to imaging, and the same tumors were imaged the day inhibitor (or vehicle) treatment started, the day doxorubicin (or PBS) treatment started, and just prior to sacrifice using a VEVO 770^{TM}-120 Imaging System (VisualSonics). Necrotic areas were defined as those areas that appeared black in ultrasound images. Cystic areas where areas that appeared dark in ultrasound images and showed some fluid movement. Measurements were determined using the in-system software.

Spinning disk confocal imaging of live mice

Details of the microscope design and imaging procedure have been previously described (Egeblad et al., 2008; Ewald et al., 2011a). Briefly, a micro-lensed spinning disk confocal microscope (Solamere technologies, Salt Lake City, UT) equipped with 405, 488, 560 and 647 nm laser lines and selective emission filters was used with an ICCD camera (XR-Mega-10EX S-30, Stanford Photonics, Palo Alto, CA). Images were acquired using either a Fluar 10×/0.5NA or 40×/1.1NA LD C-Apochromat lens (Zeiss).

For all live animal experiments, the inguinal mammary fat pad was imaged. To prepare the tissue for imaging, the animal was anesthetized with isoflurane and the fat pad was surgically exposed. Following the surgical procedure, the mouse was transferred to the microscope stage and positioned so the exposed mammary gland was flush against a glass cover slip attached to an imaging port on the stage. To prevent body temperature from dropping too low, the animal was covered with a heated blanket (Gaymar, Orchard Park, NY; [Ewald et al., 2011c]). Animal hydration was maintained by administration 50 μL of sterile PBS was administered via an indwelling intraperitoneal line every hour for the duration of each imaging session. For the duration of each imaging session, mice received isoflurane at a concentration that was adjusted over time for each individual mouse using vital signs monitored using an oximeter probe that indicates the level of anesthesia (MouseOx, Starr Life Sciences, PA; [Ewald et al., 2011b]).

The acute *in vivo* response to doxorubicin was tracked in MMTV-PyMT;ACTB-ECFP;c-fms-EGFP or MMTV-PyMT;ACTB-ECFP mice. Mice were administered a single dose of doxorubicin (8mg/kg, intraperitoneally) 14 to 30h prior to the start of imaging, and imaged for 10 to 40h. Controls were untreated MMTV-PyMT;ACTB-ECFP;c-fms-EGFP or MMTV-PyMT;ACTB-ECFP mice imaged for similar time frames. During each imaging session, animals were administered 50 μL/h propidium iodide (0.05-0.1 mg/mL in PBS, Invitrogen) rather than PBS, to visualize cell death. Time-lapse movies were acquired at 10× or 40× magnification.

MMTV-PyMT;ACTB-ECFP;ACTB-H2B-EGFP mice were used to determine the *in vivo*

mechanism of doxorubicin-induced cell death. Mice were administered a single dose of doxorubicin (8 mg/kg, intraperitoneally) 28 to 30h prior to imaging start time, and animals were administered 50 μL/h propidium iodide (0.05-0.1 mg/mL in PBS, Invitrogen) rather than PBS, to visualize cell death. Time-lapse movies were acquired at 40× magnification.

The ability of myeloid cells to migrate into tissues containing necrotic debris was determined in c-fms-EGFP mice. Tumors from MMTV-PyMT mice were minced and digested with collagenase (essentially as described above), cultured overnight, and labeled with CellTracker™ Red (Invitrogen). Stained cancer cells were then freeze-thawed to generate necrotic debris. Debris was co-injected with 10 kD Alexa Fluor® 647-conjugated dextran (in PBS, Invitrogen) into the surface of the exposed inguinal mammary glands of c-fms-EGFP mice. Neighboring tissues were injected with the dextran alone as controls. Time-lapse movies were acquired at 10× magnification. Dependency on G-protein-coupled receptor signaling was determined by pre-treating mice with pertussis toxin (2 mg per mouse in PBS, intraperitoneally) 12h prior to, and immediately before imaging.

Refer to Appendices XI and XII for detailed protocols.

Analysis of *in vivo* imaging experiments

Images and movies were assembled in Imaris (Bitplane, version 7.0 for Windows XP Professional x64). An increase in cell death in a single field was defined as a gain of or visible increase in areas positive for propidium iodide (PI) over time. For each field imaged, a time series of single optical section images at 1h intervals (roughly covering 26 to 32h post-doxorubicin treatment or the corresponding imaging time for control mice) was generated, and the percentage of each field positive for PI at each time point was measured using Volocity (PerkinElmer, version 4.1.0 for Windows). All images were analyzed without knowledge of the treatment mice received.

Infiltration of myeloid cells into tumor tissues was similarly defined as a gain of or a visible increase in areas of a single field that were positive for EGFP. A time series of maximum intensity projection images at 1h intervals (roughly covering 26 to 32h post-doxorubicin treatment or the

corresponding imaging time for control mice) was generated, and the percentage of each field positive for EGFP at each time point was measured using Volocity. All images were analyzed without knowledge of the treatment mice received.

To quantify the *in vivo* mechanisms of cell death, maximum intensity projection images of each field at 32 and 42h after doxorubicin administration were generated. Dying cancer cells were identified based on propidium iodide positivity and morphology, and counted manually using the Cell Counter plugin for the ImageJ software (NIH, version 1.45).

Refer to Appendix XIII for a detailed protocol.

Histology and immunostaining

Tumor samples harvested for analysis by histology or immunostaining were fixed overnight in paraformaldehyde. Animals were administered either PBS or doxorubicin (8 mg/kg intraperitoneally) and euthanized 48h later. Animals used for BrdU incorporation studies were administered BrdU (100 mg/kg intraperitoneally, Sigma) two hours prior to treatment with PBS or doxorubicin and euthanized 24 or 48h after treatment. Tumor tissues were either processed through graded ethanol and embedded in paraffin or through graded sucrose and embedded in OCT medium (Tissue-Tek).

For histological analyses, paraformaldehyde-fixed, paraffin-embedded sections were deparaffinized, rehydrated, and stained with Mayer's hematoxylin and eosin. The antibodies used for immunostaining are as follows: αSMA (1:1500, Sigma-Aldrich), BrdU (1:200, clone G3G4, Developmental Studies Hybridoma Bank, University of Iowa), CCL2 (1:100, AbD Serotec), CCR2 (1:100, clone E68, Novus Biologicals), CD206 (1:200, clone MR5D3, AbD Serotec), CD31 (1:25 Abcam), F4/80 (1:200, clone CI:A3-1, AbD Serotec), MECA-32 (1:50, Developmental Studies Hybridoma Bank, University of Iowa), phospho-histone H2AX (Ser139, 1:500, clone 20E3, Cell Signaling), phospho-VE cadherin (Tyr731, 1:300, Abcam), and neutrophils/monocytes (1:400, clone 7/4, Cedarlane).

Frozen tissue sections were used for CD206 and F4/80 immunostains, while paraffin-embedded tissue sections were used for all other immunostains. In paraffin-embedded tissues, epitopes were exposed by boiling in either Tris-EDTA or citrate buffer at high pressure. For all immunostaining procedures, tissues were blocked with Fc Receptor Block (Innovex) prior to incubation with primary antibody, except for histone immunostains, in which tissues were blocked with 10% bovine serum albumin with goat serum, or immunostains involving αSMA, where tissues were blocked with Mouse-on-Mouse blocking kit (Vector Labs). Histone and BrdU immunostains were visualized using horseradish peroxidase-conjugated secondary antibodies with 3,3'-diaminobenzidine (DAB) substrate (Vector Labs) and counterstained with Mayer's hematoxylin. All other immunostains were visualized with a goat-derived Alexa Fluor® 568-conjugated secondary antibody for single label immunostains or goat-derived Alexa Fluor® 568- and Alexa Fluor® 647-conjugated secondary antibodies for double label immunostains. All fluorescently labeled, immunostained tissues were counterstained with 4',6-diamidino-2-phenylindole (DAPI, 0.05 mg/ml, Invitrogen).

Images of immunostains visualized with DAB were acquired using a Zeiss AX10 microscope equipped with a Zeiss AxioCam HRc camera. Images of immunostains visualized with fluorescent secondary antibodies were acquired with the spinning disk confocal microscope described above for live imaging experiments. Single label immunostains for CCL2, CD206, phospho-histone H2AX, and phospho-histone H3, and double label immunostains for 7/4 and CCR2, CCL2 and MECA-32, and CCR2 and MECA-32 were quantified manually using the Cell Counter plugin for the ImageJ software (NIH, version 1.45). Nuclear morphology was also used as a classifier for the BrdU and 7/4 and CCR2 double label immunostains. The F4/80 and phospho-VE-cadherin single label, and the CD31 and αSMA double label immunostains were quantified based on fluorescence intensity in Volocity (PerkinElmer). All analyses were performed without knowledge of genotype and/or treatment.

Refer to Appendices VI, VII, VIII, and IX for detailed protocols and Appendix XIV for

detailed antibody information.

Analysis of myeloid cell infiltration by flow cytometry

All flow cytometric analyses were performed on tumors harvested from transplantation models. Primary cancer cells derived from MMTV-PyMT (C57BL/6) mice were transplanted into wildtype and *Ccr2-/-* C57BL/6 hosts as described above. Tumor-bearing mice were administered a single dose of doxorubicin (8 mg/kg, intraperitoneally), and euthanized 48h after treatment. Tumors were harvested, mechanically dissociated, and digested in a DMEM-based solution containing 0.1% w/v collagenase A (Sigma) with 4 U/mL DNase I (Sigma) for 90 min at 37°C on a rocking platform. The resulting cell suspensions were filtered through 100 μm cell strainers, and erythrocytes were lysed by incubation in ammonium chloride potassium lysis buffer for 20 min. The cells were washed in a fluorescent activated cell sorting (FACS) buffer containing 1% v/v fetal bovine serum (GIBCO), 0.02% w/v sodium azide in PBS, and incubated for 20 min in FACS buffer containing 40 μL/mL Seroblock (BD Biosciences) at 4°C. Cells were labeled with fluorescently-conjugated antibodies against various cell surface markers for 30 min at 4°C, washed in FACS buffer, and analyzed using a BD™ LSR II flow cytometer. The antibodies used for flow cytometry were as follows: Gr-1-allophycocyanin-Cy™7 (1:100, BD Bioscience), CD11b-phycoerythrin (1:200, BD Biosciences), 7/4-Alexa Fluor® 647 (1:100, AbD Serotec), and F4/80-fluorescein isothiocyanate (1:100, AbD Serotec).

Refer to Appendices V and XV for detailed protocol and antibody information, respectively.

Cytokine/chemokine array and ELISA

MMTV-PyMT tumor-bearing mice were euthanized 48h following intraperitoneal administration of doxorubicin or PBS, and tumors were harvested, flash frozen in liquid nitrogen, and stored at -80°C until use. Tumor samples were homogenized on ice in a 1% NP-40 lysis buffer and incubated at 4°C with gentle rocking for 30 min. Following this incubation, samples were centrifuged at 13,000×g at 4°C for 10 min and the supernatants collected. Undiluted protein samples were applied

to the Proteome Profiler Mouse Cytokine Array Kit, Panel A (R&D Systems) according to the manufacturer's protocol to identify treatment-induced changes in protein level between control- and doxorubicin-treated tumors. For the chemokines CCL2 and CCL12, treatment-dependent changes in protein levels were confirmed by ELISA. Protein concentrations were first determined using the Bradford assay (Bio-Rad), and equal amounts of total protein were assayed using the Quantokine Mouse CCL2 and CCL12 Immunoassay kits (R&D Systems) according to the manufacturer's protocol.

***In vitro* drug sensitivity**

The protocol used to isolate primary mammary organoids is based on that described for the isolation of normal mammary epithelial organoids (Ewald et al., 2008). A fluorescence dissecting microscope was used to stage and harvest tumors as from MMTV-PyMT;ACTB-ECFP mice. Harvested tissues were mechanically dissociated and subsequently digested in a DMEM-based collagenase/trypsin solution containing 0.2% w/v collagenase A (Sigma), 0.2% w/v trypsin (GIBCO), 5 μg/mL insulin, 50 μg/mL gentamycin (GIBCO), and 5% v/v fetal bovine serum (GIBCO) in DMEM (GIBCO), for 50 min at 37°C on a rocking platform. Collagenase/trypsin digestion was followed by incubation in DNase I (Sigma, 20 U/μL in DMEM) for 5 min at room temperature on a rocking platform. After treatment with DNAse I, single cells and debris were removed from organoids by repeated rounds of differential centrifugation.

Organoids were seeded at approximately 150 per well in Growth Factor Reduced Matrigel (BD Biosciences) in 24-well plates (Falcon, non-tissue culture treated), incubated for 45 min at 37°C, and overlaid with 750 μL of a DMEM-based organoid growth medium containing 1% v/v insulin-transferrin-selenium, 1% v/v penicillin/streptomycin, and 2.5 nM basic fibroblast growth factor (Sigma F0291). Medium was replaced 48h after seeding, and organoids were treated with medium containing doxorubicin 24h later. Cell proliferation was determined 48h after doxorubicin treatment using the CellTiter 96 Aqueous One Solution Cell Proliferation Assay (Promega), according to the

manufacturer's protocol. To collect cells for the Cell Proliferation Assay, organoid-Matrigel drops were solubilized by mixing with 80 μL of ice cold growth medium.

Lapatinib sensitivity in 2D culture was measured using single cells from dissociated tumor organoids (isolated as described above) dissociated in a 0.25% trypsin with 0.1% EDTA solution. Cells were seeded in 10-cm dishes, allowed to proliferate to subconfluency, and re-seeded at 6000 cells per well in 96-well plates. Medium was exchanged for organoid medium containing the indicated drug concentrations 48h after re-seeding. Cell viability was measured 48h after drug treatment, as described above.

Vascular permeability

Vascular permeability was analyzed in tumors harvested from transplantation models. Primary cancer cells derived from MMTV-PyMT (C57BL/6) mice were transplanted into wildtype and *Ccr2*-/- (C57BL/6) hosts as described above. When tumors reached approximately 8 to 10 mm in diameter, mice were injected intravenously with a 100 μL PBS-based solution containing fluorescein isothiocyanate-conjugated *Lycopersicon esculentum* (tomato) lectin (1 mg/mL, Vector Laboratories), and rhodamine-conjugated *Ricinus communis* agglutinin I (2.5 mg/mL, Vector Laboratories). Tissues were perfused and fixed with 4% paraformaldehyde in PBS 10 min after lectin injection through cardiac puncture. The tissues were harvested and post-fixed in 4% paraformaldehyde in PBS overnight, processed through graded sucrose and embedded in OCT medium (Tissue-Tek®). Frozen sections were cut at thickness of approximately 40 μm and counterstained with DAPI. Images were acquired using the spinning disk confocal microscope described above for live animal imaging at 1 μm resolution in the Z-plane.

Images were assembled and analyzed in Imaris (Bitplane, version 7.0 for Windows XP Professional x64). The vascular volume outlined by either the tomato lectin or *Ricinus communis* agglutinin I was calculated as a percentage of the total volume using the Surfaces function, with

smoothing set to 0.66 μm, Filter Type set to 500, and the absolute intensity threshold set to 1.3× the background intensity. Co-localization of the two lectins was determined by first generating a masked channel for each lectin (voxels set to: 0 for inside surface, 255 for outside surfaces). The Co-Localization View was then used to generate a co-localization channel representing the percentage of the masked *Ricinus communis* agglutinin I channel that co-localizes with the masked tomato lectin channel.

Refer to Appendix XIII for a detailed protocol.

Statistical methods

Prism® 4 (GraphPad) software was used for all statistical analyses, with $\alpha = 0.05$. Fisher's exact tests were performed to compare cell death and myeloid cell infiltration between tumor stages. All other statistical analyses were performed using ANOVA or two-tailed Student's t-tests, as indicated.

References

AACR Cancer Progress Report 2011. 2011. American Association for Cancer Research.

Ahn G-O, Tseng D, Liao C-H, Dorie, MJ, Czechowicz A, Brown JM. 2010. Inhibition of Mac-1 (CD11b/CD18) enhances tumor response to radiation by reducing myeloid cell recruitment. *Proc Natl Acad Sci USA* **107**(18), 8363–8368.

Albini A, Sporn MB. 2007. The tumour microenvironment as a target for chemoprevention. *Nat Rev Cancer* **7**(2), 139–147.

Ali SH, DeCaprio JA. 2001. Cellular transformation by SV40 large T antigen: interaction with host proteins. *Semin Cancer Biol* **11**, 15–23.

Andreu P, Johansson M, Affara NI, Pucci F, Tan T, Junankar S, Korets L, Lam J, Tawfik D, Denardo, DG, et al. 2010. FcRgamma activation regulates inflammation-associated squamous carcinogenesis. *Cancer Cell* **17**, 121–134.

Ausprunk DH, Folkman J. 1977. Migration and proliferation of endothelial cells in preformed and newly formed blood vessels during tumor angiogenesis. *Microvasc Res* **14**, 53–65.

Balkwill F. 2004. Cancer and the chemokine network. *Nat Rev Cancer* **4**(7), 540–550.

Bergers G, Benjamin LE. 2003. Tumorigenesis and the angiogenic switch. *Nat Rev Cancer* **3**(6), 401–410.

Bergers G, Song S, Meyer-Morse N, Bergsland E, Hanahan D. 2003. Benefits of targeting both pericytes and endothelial cells in the tumor vasculature with kinase inhibitors. *J Clin Invest* **111**(9), 1287–1295.

Bhaskar V, Zhang D, Fox M, Seto P, Wong MHL, Wales PE, Powers D, et al. 2007. A function blocking anti-mouse integrin alpha5beta1 antibody inhibits angiogenesis and impedes tumor growth in vivo. *J Transl Med*, **5**, 61.

Bhowmick NA, Chytil A, Plieth D, Gorska AE, Dumont N, Shappell S, Washington MK, et al. 2004. TGF-beta signaling in fibroblasts modulates the oncogenic potential of adjacent epithelia. *Science* **303**(5659), 848–851.

Bilancia D, Rosati G, Dinota A, Germano D, Romano R, Manzione L. 2007. Lapatinib in breast cancer. *Ann Oncol* **18** Suppl 6, vi26–30.

Bingle L, Brown NJ, Lewis CE. 2002. The role of tumour-associated macrophages in tumour progression: implications for new anticancer therapies. *J Pathol* **196**(3), 254–265.

Bisping G, Leo R, Wenning D, Dankbar B, Padró T, Kropff M, Scheffold C, Kröger M, Mesters RM, Berdel WE, et al. 2003. Paracrine interactions of basic fibroblast growth factor and interleukin-6 in multiple myeloma. *Blood* **101**, 2775–2783.

Blick T, Hugo H, Widodo E, Waltham M, Pinto C, Mani SA, Weinberg RA, Neve RM, Lenburg ME, Thompson EW. 2010. Epithelial mesenchymal transition traits in human breast cancer cell lines parallel the CD44(hi)/CD24 (lo/-) stem cell phenotype in human breast cancer. *J Mammary Gland Biol Neoplasia* **15**, 235–252.

Boissonnas A, Fetler L, Zeelenberg IS, Hugues S, Amigorena S. 2007. In vivo imaging of cytotoxic T cell infiltration and elimination of a solid tumor. *J Exp Med* **204**(2), 345–356.

Bombonati A, Sgroi DC. 2011. The molecular pathology of breast cancer progression. *J Pathol* **223**(2), 307–317.

Breart B, Lemaître F, Celli S, Bousso P. 2008. Two-photon imaging of intratumoral CD8+ T cell cytotoxic activity during adoptive T cell therapy in mice. *J Clin Invest* **118**(4), 1390–1397.

Brewster AM, Hortobagyi GN, Broglio KR, Kau S-W, Santa-Maria CA, Arun B, Buzdar AU, et al. 2008. Residual risk of breast cancer recurrence 5 years after adjuvant therapy. *J Natl Cancer Inst* **100**(16), 1179–1183

Brown E, McKee T, diTomaso E, Pluen A, Seed B, Boucher Y, Jain RK. 2003. Dynamic imaging of collagen and its modulation in tumors in vivo using second-harmonic generation. *Nat Med* **9**(6), 796–800.

Calabrese C, Poppleton H, Kocak M, Hogg TL, Fuller C, Hamner B, Oh EY, Gaber MW, Finklestein, D, Allen M, et al. 2007. A perivascular niche for brain tumor stem cells. *Cancer Cell* **11**, 69–82.

Camerer E, Qazi AA, Duong DN, Cornelissen I, Advincula R, Coughlin SR. 2004. Platelets, protease-activated receptors, and fibrinogen in hematogenous metastasis. *Blood* **104**, 397–401.

Campiglio M, Somenzi G, Olgiati C, Beretta G, Balsari A, Zaffaroni N, Valagussa P, et al. 2003. Role of proliferation in HER2 status predicted response to doxorubicin. *Int J Cancer* **105**(4), 568–573.

Carlson RW, Allred DC, Anderson BO, Burstein HJ, Carter WB, Edge SB, Erban JK, et al. 2009. Breast cancer. Clinical practice guidelines in oncology. *J Natl Compr Canc Netw*.

Carmeliet P. 2000. Mechanisms of angiogenesis and arteriogenesis. *Nat Med* **6**(4), 389–395.

Casares N, Arribillaga L, Sarobe P, Dotor J, Lopez-Diaz de Cerio A, Melero I, Prieto J, Borras-Cuest F, Lasarte JJ. 2003. CD4+/ CD25+ regulatory cells inhibit activation of tumor-primed CD4+ T cells with IFN-gamma-dependent antiangiogenic activity, as well as long-lasting tumor immunity elicited by peptide vaccination. *J Immunol* **171**, 5931–5939.

Courtneidge SA. 1986. Transformation by polyoma virus middle T antigen. *Cancer Surv* **5**, 173–182.

Courtneidge SA, Smith AE. 1983. Polyoma virus transforming protein associates with the product of the c-src cellular gene. *Nature* **303**, 435–439.

Coussens LM, Raymond WW, Bergers G, Laig-Webster M, Behrendtsen O, Werb Z, Caughey GH, Hanahan D.1999. Inflammatory mast cells up-regulate angiogenesis during squamous epithelial carcinogenesis. *Genes Dev* **13**, 1382–1397.

Coussens LM, Tinkle CL, Hanahan D, Werb Z. 2000. MMP-9 supplied by bone marrow-derived cells contributes to skin carcinogenesis. *Cell* **103**, 481–490.

Coussens LM, Werb Z. 2002. Inflammation and cancer. *Nature* **420**(6917), 860–867.

Cubillos S, Norgauer J, Lehmann K. 2010. Toxins-useful biochemical tools for leukocyte research.

Toxins **2**(4), 428–452.

Curiel TJ, Coukos G, Zou L, Alvarez X, Cheng P, Mottram P, Evdemon-Hogan M, Conejo-Garcia JR, Zhang L, Burow M, et al. 2004. Specific recruitment of regulatory T cells in ovarian carcinoma fosters immune privilege and predicts reduced survival. *Nat Med* **10**, 942–949.

De Palma M, Venneri MA, Galli R, Sergi Sergi L, Politi LS, Sampaolesi M, Naldini L. 2005. Tie2 identifies a hematopoietic lineage of proangio- genic monocytes required for tumor vessel formation and a mesenchymal population of pericyte progenitors. *Cancer Cell* **8**, 211–226.

De Palma M, Venneri MA, Roca C, Naldini L. 2003. Targeting exogenous genes to tumor angiogenesis by transplantation of genetically modified hematopoietic stem cells. *Nat Med* **9**(6), 789–795.

Dean M. 2009. ABC transporters, drug resistance, and cancer stem cells. *J Mammary Gland Biol Neoplasia* **14**, 3–9.

Dejana E, Orsenigo F, Lampugnani MG. 2008. The role of adherens junctions and VE-cadherin in the control of vascular permeability. *J Cell Sci* **121**(13), 2115–2122.

Demaria S, Pikarsky E, Karin M, Coussens LM, Chen Y-C, El-Omar EM, Trinchieri G, et al. 2010. Cancer and inflammation: promise for biologic therapy. *J Immunother* **33**(4), 335–351.

Dembinski JL, Krauss S. 2009. Characterization and functional analysis of a slow cycling stem cell-like subpopulation in pancreas adenocarcinoma. *Clin Exp Metastasis* **26**, 611–623.

Demoy M, Minko T, Kopecková P, Kopecek J. 2000. Time- and concentration-dependent apoptosis and necrosis induced by free and HPMA copolymer-bound doxorubicin in human ovarian carcinoma cells. *J Cont Rel* **69**(1), 185–196.

DeNardo DG, Coussens LM. 2007. Inflammation and breast cancer. Balancing immune response: crosstalk between adaptive and innate immune cells during breast cancer progression. *Breast Canc Res* **9**(4), 212.

DeNardo DG, Barreto JB, Andreu P, Vasquez L, Tawfik D, Kolhatkar N, Coussens LM. 2009. CD4(+) T cells regulate pulmonary metastasis of mammary carcinomas by enhancing protumor properties of macrophages. *Cancer Cell* **16**(2), 91–102.

DeNardo DG, Brennan DJ, Rexhepaj E, Ruffell B, Shiao SL, Madden SF, Gallagher WM, et al. 2011. Leukocyte Complexity Predicts Breast Cancer Survival and Functionally Regulates Response to Chemotherapy. *Cancer Discovery* **1**, 54–67.

DeSantis C, Siegel R, Bandi P, Jemal A. 2011. Breast cancer statistics, 2011. *CA Cancer J Clin* **61**, 409–418.

Deshmane SL, Kremlev S, Amini S, Sawaya BE. 2009. Monocyte chemoattractant protein-1 (MCP-1): an overview. *J Interferon Cytokine Res* **29**(6), 313–326.

Dirkx AEM, Oude Egbrink MGA, Wagstaff J, Griffioen AW. 2006. Monocyte/macrophage infiltration in tumors: modulators of angiogenesis. *J Leuk Biol* **80**(6), 1183–1196.

Dive C, Gregory CD, Phipps DJ, Evans DL, Milner AE, Wyllie AH. 1992. Analysis and

discrimination of necrosis and apoptosis (programmed cell death) by multiparameter flow cytometry. *Biochim et Biophys Acta*, **1133**(3), 275–285.

Dong-Le Bourhis X, Berthois Y, Millot G, Degeorges A, Sylvi M, Martin PM, and Calvo F. 1997. Effect of stromal and epithelial cells derived from normal and tumorous breast tissue on the proliferation of human breast cancer cell lines in co-culture. *Int J Cancer* **71**, 42–48.

Du R, Lu KV, Petritsch C, Liu P, Ganss R, Passegue E, Song H, Vandenberg S, Johnson RS, Werb Z, et al. 2008. HIF1alpha induces the recruitment of bone marrow-derived vascular modulatory cells to regulate tumor angiogenesis and invasion. *Cancer Cell* **13**, 206–220.

Dwye RM, Potter-Beirne SM, Harrington KA, Lowery AJ, Hennessy E, Murphy JM, Barry F, et al. 2007. Monocyte chemotactic protein-1 secreted by primary breast tumors stimulates migration of mesenchymal stem cells. *Clin Cancer Res* **13**(17), 5020–5027.

Egeblad M, Ewald AJ, Askautrud HA, Truitt ML, Welm BE, Bainbridge E, Peeters G, et al. 2008. Visualizing stromal cell dynamics in different tumor microenvironments by spinning disk confocal microscopy. *Dis Model Mech* **1**(2-3), 155–67.

Egeblad M, Nakasone ES, Werb Z. 2010. Tumors as organs: complex tissues that interface with the entire organism. *Dev Cell* **18**(6), 884–901.

Elston CW, Ellis IO. 1991. Pathological prognostic factors in breast cancer. I. The value of histological grade in breast cancer: experience from a large study with long-term follow-up. *Histopathology* **19**(5), 403–410.

Engelhardt JJ, Boldajipour B, Beemiller P, Pandurangi P, Sorensen C, Werb Z, Egeblad M, Krummel MF. 2012. Marginating dendritic cells of the tumor microenvironment cross-present tumor antigens and stably engage tumor-specific T cells. *Cancer Cell* **21**, 402–417.

Ewald AJ, Brenot A, Duong M, Chan BS, Werb Z. 2008. Collective epithelial migration and cell rearrangements drive mammary branching morphogenesis. *Dev Cell* **14**(4), 570–581.

Ewald AJ, Werb Z, Egeblad M. 2011a. Dynamic, long-term in vivo imaging of tumor-stroma interactions in mouse models of breast cancer using spinning-disk confocal microscopy. *CSH Protoc* **2011**(1), pdb.top97.

Ewald AJ, Werb Z, Egeblad M. 2011b. Preparation of mice for long-term intravital imaging of the mammary gland. *CSH Protoc* **2011**(1), pdb.prot5562.

Ewald AJ, Werb Z, Egeblad M. 2011c. Monitoring of vital signs for long-term survival of mice under anesthesia. *CSH Protoc* **2011**(1) pdb.prot5563.

Fojo T, Bates S. 2003. Strategies for reversing drug resistance. *Oncogene* **22**(47), 7512–7523.

Fridlender ZG, Sun J, Kim S, Kapoor V, Cheng G, Ling L, Worthen GS, Albelda SM. 2009. Polarization of tumor-associated neutrophil phenotype by TGF-beta: ‘‘N1’’ versus ‘‘N2’’ TAN. *Cancer Cell* **16**, 183–194.

Fujimoto H, Sangai T, Ishii G, Ikehara A, Nagashima T, Miyazaki M, Ochiai A. 2009. Stromal MCP-1 in mammary tumors induces tumor-associated macrophage infiltration and contributes to tumor

progression. *Int J Cancer* **125**(6), 1276–1284.

Gabrilovich DI, Nagaraj S. 2009. Myeloid-derived suppressor cells as regulators of the immune system. *Nat Rev Immunol* **9**(3), 162–174.

Giantonio BJ, Catalano PJ, Meropol NJ, O'Dwyer PJ, Mitchell EP, Alberts SR, Schwartz MA, et al. 2007. Bevacizumab in combination with oxaliplatin, fluorouracil, and leucovorin (FOLFOX4) for previously treated metastatic colorectal cancer: results from the Eastern Cooperative Oncology Group Study E3200. *J Clin Oncol* **25**(12), 1539–1544.

Gilbert LA, Heman MT. 2010. DNA damage-mediated induction of a chemoresistant niche. *Cell* **143**, 355–366.

Gilbert LA, Hemann MT. 2011. Chemotherapeutic resistance: surviving stressful situations. *Cancer Res* **71**, 5062–5066.

Girardi M, Oppenheim DE, Steele CR, Lewis JM, Glusac E, Filler R, Hobby P, Sutton B, Tigelaar RE, Hayday AC. 2001. Regulation of cutaneous malignancy by gammadelta T cells. *Science* **294**, 605–609.

Gonzalez-Angulo AM, Morales-Vasquez F, Hortobagyi GN. 2007. Overview of resistance to systemic therapy in patients with breast cancer. *Adv Exp Med Biol* **608**, 1–22.

Goss KJ, Brown PD, Matrisian LM. 1998. Differing effects of endogenous and synthetic inhibitors of metalloproteinases on intestinal tumorigenesis. *Int J Cancer* **78**(5), 629–635.

Green JE, Shibata MA, Yoshidome K, Liu ML, Jorcyk C, Anver MR, Wigginton J, Wiltrout R, Shibata E, Kaczmarczyk S, et al. 2000. The C3(1)/SV40 T-antigen transgenic mouse model of mammary cancer: ductal epithelial cell targeting with multistage progression to carcinoma. *Oncogene* **19**, 1020–1027.

Gudjonsson T, Ronnov-Jessen L, Villadsen R, Rank F, Bissell MJ, and Petersen OW. 2002. Normal and tumor-derived myoepithelial cells differ in their ability to interact with luminal breast epithelial cells for polarity and basement membrane deposition. *J Cell Sci* **115**, 39–50.

Guy CT, Cardiff RD, Muller WJ. 1992. Induction of mammary tumors by expression of polyomavirus middle T oncogene: a transgenic mouse model for metastatic disease. *Mol Cell Biol* **12**(3), 954–961.

Hadjantonakis A-K, Papaioannou VE. 2004. Dynamic in vivo imaging and cell tracking using a histone fluorescent protein fusion in mice. *BMC Biotechnology* **4**, 33.

Hawinkels LJAC, Zuidwijk K, Verspaget HW, de Jonge-Muller ESM, van Duijn W, Ferreira V, Fontijn RD, et al. 2008. VEGF release by MMP-9 mediated heparan sulphate cleavage induces colorectal cancer angiogenesis. *Eur J Cancer* **44**(13), 1904–1913.

Hazlehurst LA, Argilagos RF, Dalton WS. 2007. Beta1 integrin mediated adhesion increases Bim protein degradation and contributes to drug resistance in leukaemia cells. *Br J Hematol* **136**(2), 269–275.

Heldin C-H, Rubin K, Pietras K, Ostman A. 2004. High interstitial fluid pressure - an obstacle in cancer therapy. *Nat Rev Cancer* **4**, 806–813.

Heissig B, Hattori K, Friedrich M, Rafii S, Werb Z. 200. Angiogenesis: vascular remodeling of the extracellular matrix involves metalloproteinases. *Curr Op Hematol* **10**(2), 136–141.

Hennighausen, L. (2000). Mouse models for breast cancer. *Breast Cancer Res* **2**, 2–7.

Herschkowitz JI, Simin K, Weigman VJ, Mikaelian I, Usary J, Hu Z, Rasmussen KE, et al. 2007. Identification of conserved gene expression features between murine mammary carcinoma models and human breast tumors. *Genome Biology* **8**(5), R76.

Higgins PJ, Schwartz CE, Nicolas J-M. 2007. Small molecule CCR2 antagonists. in *Chemokine Biology - Basic Research and Clinical Application* (eds. K Neote, LG Letts, B Moser), pp. 115–123. Birkhauser, Switzerland.

Hirahara N, Nio Y, Sasaki S, Minari Y, Takamura M, Iguchi C, Dong M, Yamasawa K, Tamura K. 2001. Inoculation of human interleukin-17 gene-transfected Meth-A fibrosarcoma cells induces T cell-dependent tumor-specific immunity in mice. *Oncology* **61**, 79–89.

Hiscox S, Barrett-Lee P, Nicholson RI. 2011. Therapeutic targeting of tumor-stroma interactions. *Exp Opin Ther Targets* **15**(5), 609–621.

Hodi FS, O'Day SJ, McDermott DF, Weber RW, Sosman JA, Haanen JB, Gonzalez R, et al. 2010. Improved survival with ipilimumab in patients with metastatic melanoma. *New Engl J Med* **363**(8), 711–723.

Holash J, Maisonpierre PC, Compton D, Boland P, Alexander CR, Zagzag D, Yancopoulos GD, et al. 1999. Vessel cooption, regression, and growth in tumors mediated by angiopoietins and VEGF. *Science* **284**(5422), 1994–1998.

Hu M, Yao J, Carroll DK, Weremowicz S, Chen H, Carrasco D, Richardson A, Violette S, Nikolskaya T, Nikolsky Y, et al. 2008. Regulation of in situ to invasive breast carcinoma transition. *Cancer Cell* **13**, 394–406.

Inoue S, Leitner WW, Golding B, Scott D. 2006. Inhibitory effects of B cells on antitumor immunity. *Cancer Res* **66**, 7741–7747.

Iyengar P, Espina V, Williams TW, Lin Y, Berry D, Jelicks LA, Lee H, Temple K, Graves R, Pollard J, et al. 2005. Adipocyte-derived collagen VI affects early mammary tumor progression in vivo, demonstrating a critical interaction in the tumor/stroma microenvironment. *J Clin Invest* **115**, 1163–1176.

Jain RK. 2001. Normalizing tumor vasculature with anti-angiogenic therapy: a new paradigm for combination therapy. *Nat Med* **7**(9), 987–989.

Jain RK, Munn LL, Fukumura D. 2002. Dissecting tumour pathophysiology using intravital microscopy. *Nat Rev Cancer* **2**(4), 266–276.

Jemal A, Bray F, Center MM, Ferlay J, Ward E, Forman D. 2011. Global cancer statistics. CA *Cancer J Clin* **61**, 69–90.

Joyce JA, Baruch A, Chehade K, Meyer-Morse N, Giraudo E, Tsai FY, Greenbaum DC, Hager JH, Bogyo M, Hanahan D. Cathepsin cysteine proteases are effectors of invasive growth and angiogenesis during multistage tumorigenesis. *Cancer Cell* **5**(5), 443-453.

Joyce JA. 2005. Therapeutic targeting of the tumor microenvironment. *Cancer Cell* **7**(6), 513–520.

Karnoub, AE, Dash AB, Vo AP, Sullivan A, Brooks MW, Bell GW, Richardson AL, Polyak K, Tubo R, and Weinberg RA. 2007. Mesen- chymal stem cells within tumour stroma promote breast cancer metastasis. *Nature* **449**, 557–563.

Kepp O, Tesniere A, Schlemmer F, Michaud M, Senovilla L, Zitvogel L, Kroemer G. 2009. Immunogenic cell death modalities and their impact on cancer treatment. *Apoptosis* **14**(4), 364–375.

Kidd P. 2003. Th1/Th2 balance: the hypothesis, its limitations, and implications for health and disease. *Alt Med Rev* **8**(3), 223–246.

Kim JB, Stein R, O'Hare MJ. 2004. Three-dimensional in vitro tissue culture models of breast cancer-- a review. *Breast Canc Res Treat* **85**(3), 281–291.

Kim M, Koh YJ, Kim KE, Koh BI, Nam D-H, Alitalo K, Kim I, et al. 2010. CXCR4 signaling regulates metastasis of chemoresistant melanoma cells by a lymphatic metastatic niche. *Cancer Res* **70**(24), 10411–10421.

Knight SC, Hunt R, Dore C, Medawar PB. 1985. Influence of dendritic cells on tumor growth. *Proc Natl Acad Sci USA* **82**, 4495–4497.

Kolf CM, Cho E, Tuan RS. 2007. Mesenchymal stromal cells. Biology of adult mesenchymal stem cells: regulation of niche, self-renewal and differentiation. *Arth Res Ther* **9**(1), 204.

Landskroner-Eiger S, Qian B, Muise ES, Nawrocki AR, Berger JP, Fine EJ, Koba W, Deng Y, Pollard JW, Scherer PE. 2009. Proangiogenic contribution of adiponectin toward mammary tumor growth in vivo. *Clin Cancer Res* **15**, 3265–3276.

Leder K, Foo J, Skaggs B, Gorre M, Sawyers CL, Michor F. 2011. Fitness conferred by BCR-ABL kinase domain mutations determines the risk of pre-existing resistance in chronic myeloid leukemia. *PLoS ONE* **6**, e27682.

Lee J, Fassnacht M, Nair S, Boczkowski D, Gilboa E. 2005. Tumor immunotherapy targeting fibroblast activation protein, a product expressed in tumor-associated fibroblasts. *Cancer Res* **65**(23), 11156–11163.

Leek RD, Lewis CE, Whitehouse R, Greenall M, Clarke J, Harris AL. 1996. Association of macrophage infiltration with angiogenesis and prognosis in invasive breast carcinoma. *Cancer Res* **56**(20), 4625–4629.

Leonessa F. 2003. ATP binding cassette transporters and drug resistance in breast cancer. *Endocr Relat Cancer* **10**(1), 43-73.

Lesokhin A, Hohl TM, Kitano S, Cortez C, Hirschhorn-Cymerman D, Avogadri F, Rizzuto GA, et al. 2011. Monocytic CCR2+ Myeloid Derived Suppressor Cells Promote Immune Escape By Limiting Activated CD8 T Cell Infiltration Into The Tumor Microenvironment. *Cancer Research* Epub ahead of print.

Levental KR, Yu H, Kass L, Lakins JN, Egeblad M, Erler JT, Fong SFT, et al. 2009. Matrix crosslinking forces tumor progression by enhancing integrin signaling. *Cell* **139**(5), 891–906.

Li X, Lewis MT, Huang J, Gutierrez C, Osborne CK, Wu M-F, Hilsenbeck SG, Pavlick A, Zhang X, Chamness GC, et al. 2008. Intrinsic resistance of tumorigenic breast cancer cells to chemotherapy. *J Natl Cancer Inst* **100**, 672–679.

Lin EY, Nguyen AV, Russell RG, Pollard JW. 2001. Colony-stimulating factor 1 promotes progression of mammary tumors to malignancy. *J Exp Med* **193**(6), 727–740.

Lin EY, Jone JG, Li P, Zhu L, Whitney KD, Muller WJ, Pollard JW. 2003. Progression to malignancy in the polyoma middle T oncoprotein mouse breast cancer model provides a reliable model for human diseases. *Am J Pathol* **163**(5), 2113–2126.

Lin EY, Li J-F, Gnatovskiy L, Deng Y, Zhu L, Grzesik DA, Qian H, et al. 2006. Macrophages regulate the angiogenic switch in a mouse model of breast cancer. *Cancer Res* **66**(23), 11238–11246.

Liotta LA, Kohn EC. 2001. The microenvironment of the tumour-host interface. *Nature* **411**(6835), 375–379.

Loberg RD, Day LL, Harwood J, Ying C, St John LN, Giles R, Neeley CK, et al. 2006. CCL2 is a potent regulator of prostate cancer cell migration and proliferation. *Neoplasia* **8**(7), 578–586.

Loberg RD, Ying C, Craig M, Day LL, Sargent E, Neeley C, Wojno K, et al. 2007. Targeting CCL2 with systemic delivery of neutralizing antibodies induces prostate cancer tumor regression in vivo. *Cancer Res* **67**(19), 9417–9424.

Loberg RD, Ying C, Craig M, Yan L, Snyder LA, Pienta KJ. 2007. CCL2 as an important mediator of prostate cancer growth in vivo through the regulation of macrophage infiltration. *Neoplasia* **9**, 556–562.

Lohela M, Werb Z. 2010. Intravital imaging of stromal cell dynamics in tumors. *Curr Opin Genet Dev* **20**(1), 72–78.

Luo Y, Zhou H, Krueger J, Kaplan C, Lee S-H, Dolman C, Markowitz D, et al. 2006. Targeting tumor-associated macrophages as a novel strategy against breast cancer. *J Clin Invest* **116**(8), 2132–2141.

Lyden D, Hattori K, Dias S, Costa C, Blaikie P, Butros L, Chadburn A, Heissig B, Marks W, Witte L, et al. 2001. Impaired recruitment of bone- marrow-derived endothelial and hematopoietic precursor cells blocks tumor angiogenesis and growth. *Nat Med* **7**, 1194–1201.

Mahoney BP, Raghunand N, Baggett B, Gillies RJ. 2003. Tumor acidity, ion trapping and chemotherapeutics. I. Acid pH affects the distribution of chemotherapeutic agents in vitro. *Biochem Pharmacol* **66**, 1207–1218.

Malhotra GK, Zhao X, Band H, Band V. 2010. Histological, molecular and functional subtypes of breast cancers. *Cancer Biol Ther* **10**, 955–960.

Mani SA, Guo W, Liao M-J, Eaton EN, Ayyanan A, Zhou AY, Brooks M, Reinhard F, Zhang CC, Shipitsin M, et al. 2008. The epithelial-mesenchymal transition generates cells with properties of stem cells. *Cell* **133**, 704–715.

Mantovani A, Sozzani S, Locati M, Allavena P, Sica A. 2002. Macrophage polarization: tumor-associated macrophages as a paradigm for polarized M2 mononuclear phagocytes. *Trends Immunol*

23(11), 549–555.

Maquoi E, Sounni NE, Devy L, Olivier F, Frankenne F, Krell H-W, Grams F, et al. 2004. Anti-invasive, antitumoral, and antiangiogenic efficacy of a pyrimidine-2,4,6-trione derivative, an orally active and selective matrix metalloproteinases inhibitor. *Clin Cancer Res* **10**(12 Pt 1), 4038–4047.

Maroulakou IG, Anver M, Garrett L, Green JE. 1994. Prostate and mammary adenocarcinoma in transgenic mice carrying a rat C3(1) simian virus 40 large tumor antigen fusion gene. *Proc Natl Acad Sci USA* **91**(23), 11236–11240.

Martin LP, Hamilton TC, Schilder RJ. 2008. Platinum resistance: the role of DNA repair pathways. *Clin Cancer Res* **14**, 1291–1295.

Mayordomo JI, Zorina T, Storkus WJ, Zitvogel L, Celluzzi C, Falo LD, Melief CJ, Ildstad ST, Kast WM, Deleo AB, et al. 1995. Bone marrow-derived dendritic cells pulsed with synthetic tumour peptides elicit protective and therapeutic antitumour immunity. *Nat Med* **1**, 1297–1302.

Meads MB, Gatenby RA, Dalton WS. 2009. Environment-mediated drug resistance: a major contributor to minimal residual disease. *Nat Rev Cancer* **9**(9), 665–674.

Minchinton AI, Tannock IF. 2006. Drug penetration in solid tumours. *Nat Rev Cancer* **6**(8), 583–592.

Mosmann TR, Coffman RL. 1989. TH1 and TH2 cells: different patterns of lymphokine secretion lead to different functional properties. *Annu Rev Immunol* **7**, 145–173.

Murdoch C, Muthana M, Coffelt SB, Lewis CE. 2008. The role of myeloid cells in the promotion of tumour angiogenesis. *Nat Rev Cancer* **8**(8), 618–631.

Nakasone ES, Askautrud HA, Kees T, Park J-H, Plaks V, Ewald AJ, Fein M, Rasch MG, Tan Y-X, Qiu J, Park J, Sinha P, Bissell MJ, Frengen E, Werb Z, Egeblad M. 2012. Imaging tumor-stroma interactions during chemotherapy reveals contributions of the microenvironment to resistance. *Cancer Cell*. In press.

Nam J-S, Kang M-J, Suchar AM, Shimamura T, Kohn EA, Michalowska AM, Jordan VC, et al. 2006. Chemokine (C-C motif) ligand 2 mediates the prometastatic effect of dysadherin in human breast cancer cells. *Cancer Res* **66**(14), 7176–7184.

Nieswandt B, Hafner M, Echtenacher B, Mannel DN. 1999. Lysis of tumor cells by natural killer cells in mice is impeded by platelets. *Cancer Res* **59**, 1295–1300.

Nozawa H, Chiu C, Hanahan D. 2006. Infiltrating neutrophils mediate the initial angiogenic switch in a mouse model of multistage carcinogenesis. *Proc Natl Acad Sci USA* **103**, 12493–12498.

Numasaki M, Watanabe M, Suzuki T, Takahashi H, Nakamura A, McAllister F, Hishinuma T, Goto J, Lotze MT, Kolls JK, et al. 2005. IL-17 enhances the net angiogenic activity and in vivo growth of human non- small cell lung cancer in SCID mice through promoting CXCR-2-dependent angiogenesis. *J Immunol* **175**, 6177–6189.

O'Sullivan C, Lewis CE. 1994. Tumour-associated leucocytes: friends or foes in breast carcinoma. *J Pathol* **172**(3), 229–235.

Olumi AF, Grossfeld GD, Hayward SW, Carroll PR, Tlsty TD, and Cunha GR. 1999. Carcinoma-

associated fibroblasts direct tumor progres- sion of initiated human prostatic epithelium. *Cancer Res* **59**, 5002–5011.

Orimo A, Gupta PB, Sgroi DC, Arenzana-Seisdedos F, Delaunay T, Naeem R, Carey VJ, et al. 2005. Stromal fibroblasts present in invasive human breast carcinomas promote tumor growth and angiogenesis through elevated SDF-1/CXCL12 secretion. *Cell* **121**(3), 335–348.

Park CC, Zhang H, Pallavicini M, Gray JW, Baehner F, Park CJ, Bissell MJ. 2006. Beta1 integrin inhibitory antibody induces apoptosis of breast cancer cells, inhibits growth, and distinguishes malignant from normal phenotype in three dimensional cultures and in vivo. *Cancer Res* **66**(3), 1526–1535.

Perou CM, Sørlie T, Eisen MB, van de Rijn M, Jeffrey SS, Rees CA, Pollack JR, Ross DT, Johnsen H, Akslen LA, et al. 2000. Molecular portraits of human breast tumours. *Nature* **406**, 747–752.

Pfeifer H, Lange T, Wystub S, Wassmann B, Maier J, Binckebanck A, Giagounidis A, Stelljes M, Schmalzing M, Dührsen U, et al. 2012. Prevalence and dynamics of bcr-abl kinase domain mutations during imatinib treatment differ in patients with newly diagnosed and recurrent bcr-abl positive acute lymphoblastic leukemia. *Leukemia* Epub ahead of print.

Pittet MJ, Weissleder R. 2011. Intravital imaging. *Cell*, *147*(5), 983–991.

Pollard JW. 2004. Tumour-educated macrophages promote tumour progression and metastasis. *Nat Rev Cancer* **4**(1), 71–78.

Polyak K, Kalluri R. 2010. The role of the microenvironment in mammary gland development and cancer. *Cold Spring Harb Perspect Biol* **2**(11), a003244.

Pommier Y, Leo E, Zhang H, Marchand C. 2010. DNA topoisomerases and their poisoning by anticancer and antibacterial drugs. *Chem Biol* **17**(5), 421–433.

Provenzano PP, Eliceiri KW, Campbell JM, Inman DR, White JG, Keely PJ. 2006. Collagen reorganization at the tumor-stromal interface facilitates local invasion. *BMC Med* **4**(1), 38.

Qian B-Z, Li J, Zhang H, Kitamura T, Zhang J, Campion LR, Kaiser EA, Snyder LA, Pollard JW. 2011. CCL2 recruits inflammatory monocytes to facilitate breast-tumor metastas. *Nat Med* **475**(7355), 222-225.

Redon C, Pilch D, Rogakou E, Sedelnikova O, Newrock K, Bonner W. 2002. Histone H2A variants H2AX and H2AZ. *Curr Opin Genet Dev* **12**(2), 162–169.

Rohwer N, Cramer T. 2011. Hypoxia-mediated drug resistance: novel insights on the functional interaction of HIFs and cell death pathways. *Drug Resist Updat* **14**, 191–201.

Romero P, Dunbar PR, Valmori D, Pittet M, Ogg GS, Rimoldi D, Chen JL, Lienard D, Cerottini JC, Cerundolo V. 1998. Ex vivo staining of metastatic lymph nodes by class I major histocompatibility complex tetramers reveals high numbers of antigen-experienced tumor-specific cytolytic T lymphocytes. *J Exp Med* **188**, 1641–1650.

Saederup N, Cardona AE, Croft K, Mizutani M, Cotleur AC, Tsou C-L, Ransohoff RM, Charo IF. 2010. Selective chemokine receptor usage by central nervous system myeloid cells in CCR2-red fluorescent protein knock-in mice. *PLoS ONE* **5**, e13693.

Salcedo R, Ponce ML, Young HA, Wasserman K, Ward JM, Kleinman HK, Oppenheim JJ, et al. 2000. Human endothelial cells express CCR2 and respond to MCP-1: direct role of MCP-1 in angiogenesis and tumor progression. *Blood* **96**(1), 34–40.

Sarafi MN, Garcia-Zepeda EA, MacLean JA, Charo IF, Luster AD. 1997. Murine monocyte chemoattractant protein (MCP)-5: a novel CC chemokine that is a structural and functional homologue of human MCP-1. *J Exp Med* **185**(1), 99–109.

Sato M, Goto S, Kaneko R, Ito M, Sato S, Takeuchi S. 1998. Impaired production of Th1 cytokines and increased frequency of Th2 subsets in PBMC from advanced cancer patients. *Anticancer Res* **18**(5D), 3951–3955.

Schmielau J, Finn OJ. 2001. Activated granulocytes and granulocyte- derived hydrogen peroxide are the underlying mechanism of suppression of t-cell function in advanced cancer patients. *Cancer Res* **61**, 4756–4760.

Scholl SM, Pallud C, Beuvon F, Hacene K, Stanley ER, Rohrschneider L, Tang R, et al. 1994. Anti-colony-stimulating factor-1 antibody staining in primary breast adenocarcinomas correlates with marked inflammatory cell infiltrates and prognosis. *J Natl Cancer Inst* **86**(2), 120–126.

Shain KH, Dalton WS. 2001. Cell adhesion is a key determinant in de novo multidrug resistance (MDR): new targets for the prevention of acquired MDR. *Mol Cancer Ther* **1**, 69–78.

Shain KH, Yarde DN, Meads MB, Huang M, Jove R, Hazlehurst LA, Dalton WS. 2009. Beta1 integrin adhesion enhances IL-6-mediated STAT3 signaling in myeloma cells: implications for microenvironment influence on tumor survival and proliferation. *Cancer Res* **69**, 1009–1015.

Shree T, Olson OC, Elie BT, Kester JC, Garfall AL, Simpson K, Bell-McGuinn KM, et al. 2011. Macrophages and cathepsin proteases blunt chemotherapeutic response in breast cancer. *Genes Dev* **25**(23), 2465–2479.

Shojaei F, Singh M, Thompson JD, Ferrara N. 2008. Role of Bv8 in neutrophil-dependent angiogenesis in a transgenic model of cancer progression. *Proc Natl Acad Sci USA* **105**, 2640–2645.

Siegel R, Ward E, Brawley O, Jemal A. 2011. Cancer statistics, 2011: the impact of eliminating socioeconomic and racial disparities on premature cancer deaths. *CA Cancer J Clin* **61**(4), 212–236.

Sica A, Saccani A, Bottazzi B, Bernasconi S, Allavena P, Gaetano B, Fei F, et al. 2000. Defective expression of the monocyte chemotactic protein-1 receptor CCR2 in macrophages associated with human ovarian carcinoma. *J Immunol* **164**(2), 733–738.

Sinha P, Clements VK, Ostrand-Rosenberg S. 2005. Reduction of myeloid-derived suppressor cells and induction of M1 macrophages facilitate the rejection of established metastatic disease. *J Immunol* **174**, 636–645.

Sinha P, Clements VK, Bunt SK, Albelda SM, Ostrand-Rosenberg S. 2007. Cross-talk between myeloid-derived suppressor cells and macrophages subverts tumor immunity toward a type 2 response. *J Immunol* **179**(2), 977–983.

Skobe M, Hawighorst T, Jackson DG, Prevo R, Janes L, Velasco P, Riccardi L, et al. 2001. Induction of tumor lymphangiogenesis by VEGF-C promotes breast cancer metastasis. *Nat Med* **7**(2), 192–198.

Song S, Ewald AJ, Stallcup W, Werb Z, Bergers G. 2005. PDGFRβ+ perivascular progenitor cells in tumours regulate pericyte differentiation and vascular survival. *Nat Cell Bio* **7**(9), 870–879.

Sørlie T, Tibshirani R, Parker J, Hastie T, Marron JS, Nobel A, Deng S, Johnsen H, Pesich R, Geisler S, et al. 2003. Repeated observation of breast tumor subtypes in independent gene expression data sets. *Proc Natl Acad Sci USA* **100**, 8418–8423.

Sørlie T, Perou CM, Tibshirani R, Aas T, Geisler S, Johnsen H, Hastie T, Eisen MB, van de Rijn M, Jeffrey SS, et al. 2001. Gene expression patterns of breast carcinomas distinguish tumor subclasses with clinical implications. *Proc Natl Acad Sci USA* **98**, 10869–10874.

Soucek L, Lawlor ER, Soto D, Shchors K, Swigart LB, Evan GI. 2007. Mast cells are required for angiogenesis and macroscopic expansion of Myc-induced pancreatic islet tumors. *Nat Med* **13**, 1211–1218.

Stamatovic SM, Keep RF, Mostarica-Stojkovic M, Andjelkovic AV. 2006. CCL2 regulates angiogenesis via activation of Ets-1 transcription factor. *J Immunol* **177**(4), 2651–2661.

Strauss-Ayali D, Conrad SM, Mosser DM. 2007. Monocyte subpopulations and their differentiation patterns during infection. *J Leuk Biol* **82**(2), 244–252.

Sumida T, Kitadai Y, Shinagawa K, Tanaka M, Kodama M, Ohnishi M, Ohara E, et al. 2011. Anti-stromal therapy with imatinib inhibits growth and metastasis of gastric carcinoma in an orthotopic nude mouse model. *Int J Cancer* **128**(9), 2050–2062.

Teicher BA, Herman TS, Holden SA, Wang YY, Pfeffer MR, Crawford JW, Frei E. 1990. Tumor resistance to alkylating agents conferred by mechanisms operative only in vivo. *Science* **247**(4949 Pt 1), 1457–1461.

Teicher BA, Lazo JS, Sartorelli AC. 1981. Classification of antineoplastic agents by their selective toxicities toward oxygenated and hypoxic tumor cells. *Cancer Res* **41**, 73–81.

Thurston G, Baluk P, Hirata A, McDonald DM. 1996. Permeability-related changes revealed at endothelial cell borders in inflamed venules by lectin binding. *Am J Physiol* **271**(6 Pt 2), H2547–62.

Tlsty TD, Coussens LM. 2006. Tumor stroma and regulation of cancer development. *Annu Rev Pathol 1*, 119–150.

Tong RT, Boucher Y, Kozin SV, Winkler F, Hicklin DJ, Jain RK. 2004. Vascular normalization by vascular endothelial growth factor receptor 2 blockade induces a pressure gradient across the vasculature and improves drug penetration in tumors. *Cancer Res* **64**(11), 3731–3736.

Tortora G. 2011. Mechanisms of resistance to HER2 target therapy. *J Natl Cancer Inst Monographs* **2011**, 95–98.

Trédan O, Galmarini CM, Patel K, Tannock IF. 2007. Drug resistance and the solid tumor microenvironment. *J Natl Cancer Inst* **99**(19), 1441–1454.

Tsui P, Das A, Whitaker B, Tornetta M, Stowell N, Kesavan P, Kaiser E, et al. 2007. Generation,

characterization and biological activity of CCL2 (MCP-1/JE) and CCL12 (MCP-5) specific antibodies. *Hum Antibodies* **16**(3-4), 117–125.

Ueno T, Toi M, Saji H, Muta M, Bando H, Kuroi K, Koike M, et al. 2000. Significance of macrophage chemoattractant protein-1 in macrophage recruitment, angiogenesis, and survival in human breast cancer. *Clin Cancer Res* **6**(8), 3282–3289.

Vakkila J, Lotze MT. 2004. Inflammation and necrosis promote tumour growth. *Nat Rev Immunol* **4**(8), 641–648.

Valković T, Lucin K, Krstulja M, Dobi-Babić R, Jonjić N. 1998. Expression of monocyte chemotactic protein-1 in human invasive ductal breast cancer. *Pathol Res Pract* **194**(5), 335–340.

Vergunst CE, Gerlag DM, Lopatinskaya L, Klareskog L, Smith MD, van den Bosch F, Dinant HJ, et al. 2008. Modulation of CCR2 in rheumatoid arthritis: a double-blind, randomized, placebo-controlled clinical trial. *Arthritis Rheum* **58**(7), 1931–1939.

Visvader JE, Lindeman GJ. 2008. Cancer stem cells in solid tumours: accumulating evidence and unresolved questions. *Nat Rev Cancer* **8**, 755–768.

Vosseler S, Mirancea N, Bohlen P, Mueller MM, Fusenig NE. 2005. Angiogenesis inhibition by vascular endothelial growth factor receptor-2 blockade reduces stromal matrix metalloproteinase expression, normalizes stromal tissue, and reverts epithelial tumor phenotype in surface heterotransplants. *Cancer Res* **65**(4), 1294–1305.

Weaver VM, Petersen OW, Wang F, Larabell CA, Briand P, Damsky C, Bissell MJ. 1997. Reversion of the malignant phenotype of human breast cells in three-dimensional culture and in vivo by integrin blocking antibodies. *J Cell Biol* **137**(1), 231–245.

Welford AF, Biziato D, Coffelt SB, Nucera S, Fisher M, Pucci F, Di Serio C, Naldini L, De Palma M, Tozer GM, Lewis CE. 2011. TIE2-expressing macrophages limit the therapeutic efficacy of the vascular-disrupting agent combrestatin A4 phosphate in mice. *J Clin Invest* **121**, 1969-1975.

White DE, Kurpios NA, Zuo D, Hassell JA, Blaess S, Mueller U, Muller WJ. 2004. Targeted disruption of beta1-integrin in a transgenic mouse model of human breast cancer reveals an essential role in mammary tumor induction. *Cancer Cell 6*(2), 159–170.

Wyckoff JB, Wang Y, Lin EY, Li J-F, Goswami S, Stanley ER, Segall JE, et al. 2007. Direct visualization of macrophage-assisted tumor cell intravasation in mammary tumors. *Cancer Res* **67**(6), 2649–2656.

Xian X, Hakansson J, Stahlberg A, Lindblom P, Betsholtz C, Gerhardt H, Semb H. 2006. Pericytes limit tumor cell metastasis. *J Clin Invest* **116**, 642–651.

Yang L, DeBusk LM, Fukuda K, Fingleton B, Green-Jarvis B, Shyr Y, Matrisian LM, Carbone DP, Lin PC. 2004. Expansion of myeloid immune suppressor Gr+CD11b+ cells in tumor-bearing host directly promotes tumor angiogenesis. *Cancer Cell* **6**, 409–421.

Yang FC, Ingram DA, Chen S, Zhu Y, Yuan J, Li X, Yang X, Knowles S, Horn W, Li Y, et al. 2008a. Nf1-dependent tumors require a microenvironment containing Nf1+/- and c-kit-dependent bone marrow. *Cell* **135**, 437–448.

Yang L, Huang J, Ren X, Gorska AE, Chytil A, Aakre M, Carbone DP, Matrisian LM, Richmond A, Lin PC, et al. 2008b. Abrogation of TGF beta signaling in mammary carcinomas recruits Gr-1+CD11b+ myeloid cells that promote metastasis. *Cancer Cell* **13**, 23–35.

Yang D, Tong L, Wang D, Wang Y, Wang X, Bai C. 2010. Roles of CC chemokine receptors (CCRs) on lipopolysaccharide-induced acute lung injury. *Respir Physiol Neurobiol* **170**(3), 253–259.

Yang SJ, Iglay-Reger HB, Kadouh HC, Bodary PF. 2009. Inhibition of the chemokine (C-C motif) ligand 2/chemokine (C-C motif) receptor 2 pathway attenuates hyperglycaemia and inflammation in a mouse model of hepatic steatosis and lipoatrophy. *Diabetologia*, **52**(5), 972–981.

Yoshimura T, Yuhki N, Moore SK, Appella E, Lerman MI, Leonard EJ. 1989. Human monocyte chemoattractant protein-1 (MCP-1). Full-length cDNA cloning, expression in mitogen-stimulated blood mononuclear leukocytes, and sequence similarity to mouse competence gene JE. *FEBS Lett* **244**(2), 487–493.

Yu D-C, Lee J-S, Yoo JY, Shin H, Deng H, Wei Y, Yun C-O. 2012. Soluble Vascular Endothelial Growth Factor Decoy Receptor FP3 Exerts Potent Antiangiogenic Effects. *Mol Ther* Epub ahead of print.

Yuan F, Salehi HA, Boucher Y, Vasthare US, Tuma RF, Jain RK. 1994. Vascular permeability and microcirculation of gliomas and mammary carcinomas transplanted in rat and mouse cranial windows. *Cancer Res* **54**(17), 4564–4568.

Zhu X, Fujita M, Snyder LA, Okada H. 2011. Systemic delivery of neutralizing antibody targeting CCL2 for glioma therapy. *J Neurooncol* **104**(1), 83–92.

Appendices

I. Isolation of cancer cells from primary tumor samples

PREPARATION OF BUFFERS:

1. Prepare 75mL of **Collagenase Buffer** immediately prior to addition to tumor tissue.
2. Prepare **RPMI with 1% Penicillin and Streptomycin** and store at room temperature.
3. Warm 1X PBS, 0.25% Trypsin with EDTA in 37°C until use.

PREPARATION OF SURGICAL TOOLS:

1. Prepare mouse hood: move glass bead sterilizer into the hood and turn it on, prepare procedure area.
2. Wash dissecting tools in soap and water (one pair of forceps and scissors for opening the mouse, one pair for removing mammary tumors). Sterilize dissecting tools at >200°C for 30s.
3. Replace blade for retractable scraper (Techni-Edge, Cat No TE05-503) and sterilize at >200°C for 30s.

ISOLATION PROTOCOL:

1. Sacrifice mouse in the microscope room and transfer her to the procedure area in the mouse hood.
2. Remove tumor(s) (with caliper measurement of ~8-12 mm). Be careful to avoid harvesting LN, muscle, and adipose tissue.
3. Place tumor in appropriately labeled tissue culture dish containing ~6 mL collagenase buffer.
4. Mechanically dissociate tumors with scraper. Chop tumors until they are small chunks, ~1x1 mm (~2-3 min).
5. Transfer chopped tumors to 50 mL Falcon tubes (split dissociated tumors into 2-3 tubes).
6. Add enough Collagenase buffer for a total volume of 35 mL.
7. Cap tubes and seal with parafilm.
8. Shake for 1 hour at 120 rpm at 37°C.
9. Spin tubes at 1500 rpm for 10 minutes at 25°C.
10. Discard supernatant.
11. Resuspend pellet in 6 mL RPMI with penicillin and streptomycin.
12. Spin tubes at 1500 rpm for 10 minutes at 25°C.
13. Discard supernatant.
14. Resuspend pellet in 10 mL RPMI with penicillin and streptomycin, and transfer to 15 mL Falcon tubes.
15. Pulse to 1500 rpm, the press STOP button as soon as speed reaches 1500 rpm.
16. Discard supernatant.
17. Repeat Steps 14-16 four times.
18. Resuspend pellet in 10 mL warm PBS.
19. Spin tubes at 1500 rpm at 25°C for 10 minutes.
20. Discard supernatant.
21. Repeat Steps 18-20.
22. Resuspend pellet in 5 mL 0.25% Trypsin with 0.1% EDTA.
23. Incubate at 37°C for 15 min.
24. Gently pipette up and down to dissociate cells.
25. Add 10 mL RPMI + 10% FBS to inactivate trypsin. Gently invert tubes to mix.
26. Spin tubes at 1500 rpm at 25°C for 10 minutes.
27. Discard supernatant.
28. Resuspend pellets in 10 mL 1X PBS.
29. Combine all samples into one 50 mL tube, by straining through a 40 μm cell strainer.
30. Spin tube at 500 rpm at 25°C for 15 min.

31. Discard supernatant.
32. Resuspend pellets in 35 mL 1X PBS.
33. Spin tube at 500 rpm at 25°C for 15 min.
34. Discard supernatant.
35. Spin tube at 500 rpm at 25°C for 15 min.
36. Discard supernatant.
37. Resuspend supernatant in 5 mL 1X PBS.

BUFFERS AND SOLUTIONS:

Collagenase Buffer – Prepare Fresh

Reagent	Final Solution
1× RPMI	72.5 mL
FBS (5% final)	2.5 mL
Gentamycin	50 μL
Insulin (10 mg/mL stock, 5μg/mL final)	25 μL
Trypsin	0.15 g
Collagenase A	0.15 g
DNAse I, 2U/μL (Final conc. 8U/mL)	600 μL
Total	75 mL

1) Mix RPMI, FBS, Gentamycin, and Insulin (warmed to 37°C).
2) Incubate in 37°C water bath.
3) Weigh trypsin and collagenase A, and add to solution.
4) Mix solution at RT for ≥ 15 min.
5) Filter sterilize (0.2 μm filter).
6) Add DNase I to solution (NOTE: **this step must be done in the hood!**)

RPMI+10% FBS – Store at 4°C

Reagent	Final Solution
1× RPMI	45 mL
Fetal Bovine Serum (FBS)	5 mL
Total	50 mL

II. Transplantation of primary cancer cells

PREPARATION OF PRIMARY CELLS FOR TRANSPLANTATION:

1. Calculate the final volume of cell suspension required. Use the following guidelines: calculate for 20 μL of cell suspension per injection, and then double this number (doubling the volume is necessary, because some of the volume is lost when preparing the sample for injection). For example, for 5 mice:

$$\text{Total volume} = 5 \text{ mice} \times 2 \text{ glands per mouse} \times 20\ \mu\text{L} \times 2 = 800\ \mu\text{L}$$

2. Calculate the number of cells required for this (400,000 cells per injection = 400,000 cells per 20 μL of cell suspension). For example, for 5 mice:

$$\text{Total cell count} = 5 \text{ mice} \times 2 \text{ glands per mouse} \times 400{,}00 \text{ cells} \times 2 = 1.6 \times 10^7 \text{ cells}$$

3. Count fresh cells using a hemacytometer (See "Isolation of Cells from Primary Tumor Samples" for directions on how to isolate cells).
4. Determine the volume of cells that has the number of acquired cells and transfer this volume to a sterile Eppendorf tube (the number of cells that have isolated usually run between 10^7 and 10^9 cells per mL, depending on the amount of tumor tissue originally harvested and the volume in which washed cells have been resuspended).

$$\text{Volume of fresh cells} = 1.6 \times 10^7 \text{ cells} / (1.5 \times 10^8 \text{ cells / mL}) = 106.7\ \mu\text{L}$$

5. Adjust the final volume to the volume calculated in Step 1.

$$\text{Volume of PBS} = 800\ \mu\text{L} - 106.7\ \mu\text{L} = 693.3\ \mu\text{L}$$

6. Gently mix cells and leave at room temperature until injection.

PREPARATION OF SURGERY AREA:

1. Sterilize the flow hood.
2. Cover the surface of the flow hood with a disposable surgical underpad. Tape the pad in place with laboratory tape.
3. Set up the anesthesia system. Be sure to weigh the activated charcoal canister (it should be replace after a 50 gram increase in weight), and replace if necessary. The nose cone may need to be taped to the surgical underpad to prevent it from moving.
4. Place insulin syringes (0.5 mL; 28 gauge, ½ inch, Becton-Dickinson, Cat. No. 329461) and sharps container near the procedure area.

TRANSPLANTATION PROCEDURE:

1. Induce anesthesia at 4% isoflurane. Once the animal's breathing has slowed, switch the anesthesia to the nose cone in the procedure area and transfer the animal. Place the animal ventral side up on the surgical underpad (the animal does not have to be completely anesthetized at this point). Make sure to secure her nose in the nose cone.
2. Restrain the mouse with surgical tape. It is easiest to do this by fastening a long piece of tape across the ribcage (this will hold the animal in place and ensure she stays in the nose cone) and taping the hind limbs to the surgical pad. Make sure the hind limbs are restrained such that the lower portion of the mouse is stretched out.
3. Decrease the anesthesia to 2.5% for the remainder of the procedure.

4. Prepare two syringes for injection. Gently flick the tube containing the cell suspension for transplantation to mix the cells (primary cells are very sticky). Each syringe should contain 20 µL of cell suspension. Always make sure the rubber portion of the syringe plunger is at the same location with respect to the 20 µL line, preparing the syringe. Be sure to avoid touching the tip of the needle to any surface.
5. Disinfect the site of injection with ethanol.
6. Locate the number 4 and 5 nipples. Location of these two nipples on the right side of the animal.

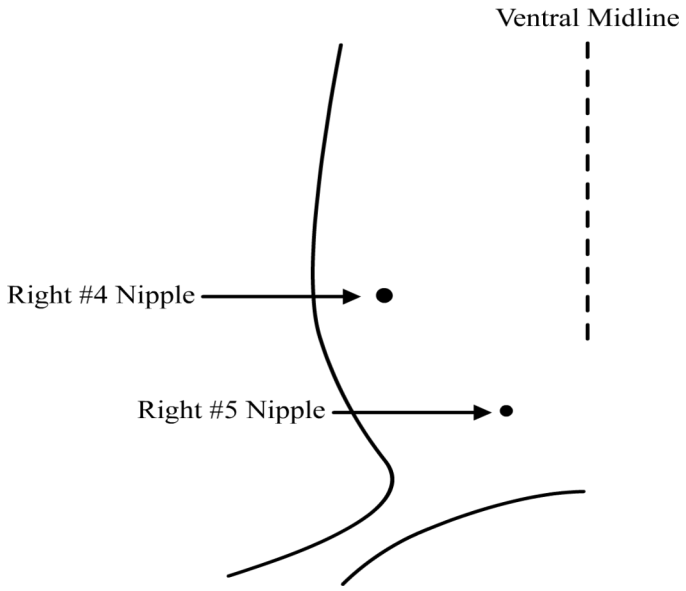

7. With the beveled edge of the needle facing away from the skin, insert the needle just above the number 5 nipple, making sure to avoid piercing the peritoneum.

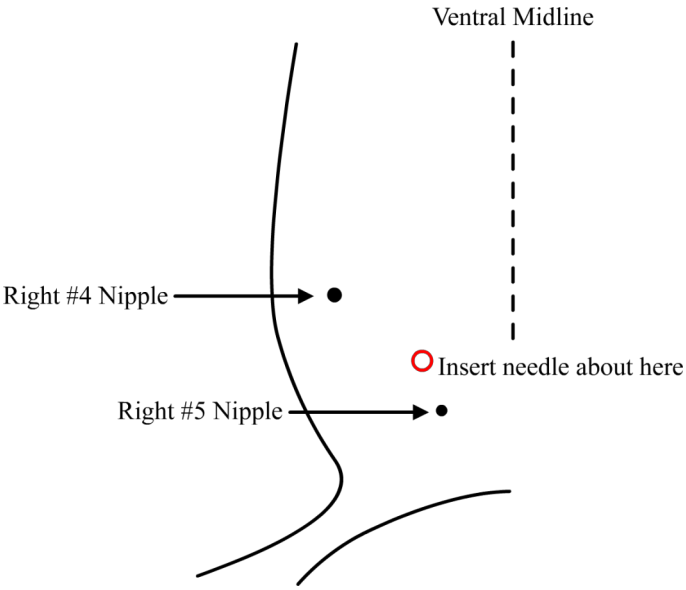

8. Gently angle the needle toward the number four nipple until the needle hits the epithelium resting under the nipple. There should be some resistance to when the needle has entered this epithelium.

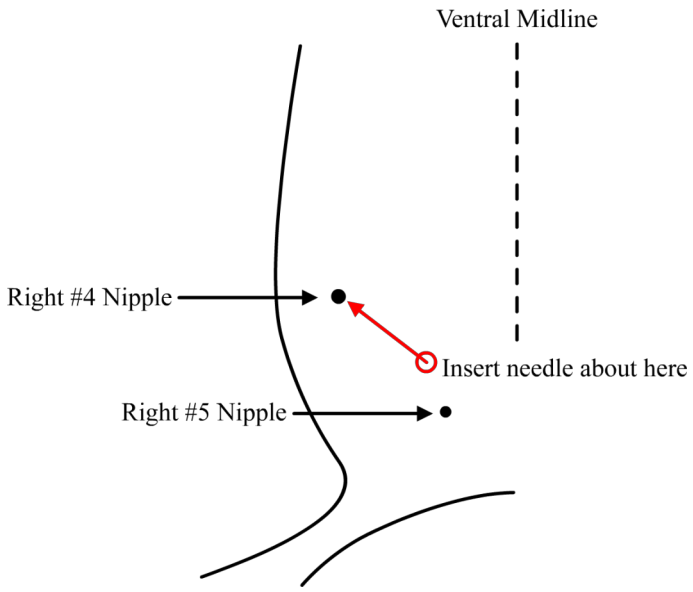

9. Slowly and gently inject the cell suspension into the mammary epithelium (this avoids causing too much damage to the tissue). A bubble of liquid should form after the injection.
10. Gently remove the syringe and dispose of it.
11. Repeat Steps 1-10 for the contralateral mammary gland.
12. Once both injections have been performed, remove the laboratory tape restraining the animal, and allow the animal to recover. The entire procedure should take no more than ~5-7 min.

FOLLOW-UP:

Allow the animal 1 week to recover from the procedure before beginning to palpate the mammary glands for tumors. Tumors arising in animals transplanted with cancer cells isolated from MMTV-PyMT mice take approximately 3 weeks before they are palpable. This same procedure can be used to transplant cell lines into syngeneic or immunocompromised hosts.

III. Treatment of animals with chemotherapy

All solutions *must* be prepared in a sterile hood.

DOXORUBICIN RECIPE

REAGENT	SUPPLIER	CAT. NO.	SIZE
Doxorubicin Hydrochloride	Sigma-Aldrich	44583-10MG	10 mg

DOXORUBICIN STOCK SOLUTION: 10 mg / mL

COMPONENT	Volume
Doxorubicin Hydrochloride	10 mg
Sterile dH_2O	1 mL
TOTAL VOLUME	1 mL
FINAL CONCENTRATION	10 mg/mL

Store Stock Solution at 4°C. Doxorubicin is soluble to 50 mg / mL in dH_2O.

DOXORUBICIN WORKING SOLUTION: 0.8 mg / mL (12.5× Dilution of Stock Solution)

COMPONENT	1×
Doxorubicin Stock (10 mg/mL)	24 µL
Sterile PBS	276 µL
TOTAL VOLUME	300 µL
FINAL CONCENTRATION	0.8 mg / mL

Working solution must be prepared fresh.

(10 µg / µL) × 24 µL = 240 µg
240 µg / 300 µL = 0.8 µg / µL = 0.8 mg / mL
0.8 µg / µL × 10 µL / g = 8 µg / g = 8 mg / kg

Dosage: 10 µg / µL (8 µg / g of body weight)

CYCLOPHOSPHAMIDE RECIPE

REAGENT	SUPPLIER	CAT. NO.	SIZE
Cyclophosphamide Monohydrate	MP Biomedicals (via Fisher)	IC15074905	5g

WORKING SOLUTION: 7.5 mg / mL

COMPONENT	Volume
Cyclophsophamide Monohydrate	3 mg
Sterile dH_2O	400 µL
TOTAL VOLUME	400 µL
FINAL CONCENTRATION	7.5 mg / mL

Cyclophosphamide working solution is prepared fresh.

NOTE: Weigh out appropriate amount of cyclophosphamide and filter-sterilize the final solution. Cyclophosphamide is soluble to 40 g/L in water.

(7.5 µg / µL) × (10 µL / g) = 75 µg / g = 75 mg / kg

Dosage: 10 μL / g (75 μg / g of body weight)

CISPLATIN RECIPE

REAGENT	SUPPLIER	CAT. NO.	SIZE
Cisplatin	MBL International Corp.	JM-1550-100	1g

STOCK SOLUTION: 10 mg / mL

COMPONENT	Volume
Cisplatin	0.5 g
Sterile DMSO	500 μL
TOTAL VOLUME	500 μL
FINAL CONCENTRATION	10 mg/mL

WORKING SOLUTION: 1 mg / mL

COMPONENT	1×
Cisplatin Stock	30 μL
Sterile PBS	270 μL
TOTAL VOLUME	300 μL
FINAL CONCENTRATION	1 mg/mL

(10 μg / μL) × 30 μL = 300 μg
300 μg / 300 μL = 1 μg / μL = 1 mg / mL
1 μg / μL × 10 μL / g = 10 μg / g = 10 mg / kg

Dosage = 10 μL / g (10 μg / g of body weight)

Cisplatin stock solution is stable for up to 1 week at -20°C (it is better to prepare it fresh). A stock solution is prepared so mice are not treated with pure DMSO.

NOTE: Weigh out appropriate amount of cisplatin and filter-sterilize final solution. Cisplatin is soluble to 10 mg/mL in DMSO.

SAFETY

Doxorubicin, cyclophosphamide, and cisplatin are strong cytotoxic agents. Always wear gloves and appropriate safety equipment when handling these drugs.

ADMINISTRATION

1. Palpate mammary glands and measure tumors with calipers.
2. Divide mice into two groups with tumors of approximately the same size.
3. Weigh animals. Calculate the volume of chemotherapy needed to administer to each animal.
4. Inject each animal with the working drug solution or the control solution intraperitoneally. Record the time at injection (this time point is 0 hours).
5. Euthanize mice at the specified time point(s).
6. Harvest tissue. If tissue is to be used for immunohistochemistry, collect tissue in cassette and fix in 4% paraformaldehyde overnight. If tissue is to be used for DNA, RNA, or protein analysis, flash freeze tissue in liquid nitrogen and store at -80°C.

NOTE: Controls receive 10 μL / g of the control solution. For doxorubicin, this is 1× PBS. For cyclophosphamide, this is sterile water. For cisplatin, this is DMSO diluted 1:10 in 1× PBS.

IV. Treatment of animals with RS 504393 and doxorubicin

SOLUTIONS AND REAGENTS

Prepare doxorubicin according to the protocol "Treatment of animals with doxorubicin."

RS 504393 STOCK SOLUTION: 10 mg/mL

COMPONENT	Volume
RS 504393 (CCR2 inhibitor)	10 mg
Sterile dH_2O	1 mL
TOTAL VOLUME	1 mL
FINAL CONCENTRATION	10 mg/mL

Store stock solution at 4°C.

RS 504393 WORKING SOLUTION: 0.2 mg/mL (50× Dilution of Stock Solution)

COMPONENT	1×
RS 504393 (10 mg/mL)	6 μL
Sterile dH_2O	294 μL
TOTAL VOLUME	300 μL
FINAL CONCENTRATION	0.2 mg/mL

Prepare working solution fresh.

(10 μg / μL) × 6 μL = 6 μg
6 μg / 300 μL = 0.2 μg / μL = 0.2 mg / mL
0.2 μg / μL × 10 μL / g = 2 μg / g = 2 mg / kg

Dosage = 10 μL / g (2 μg / g of body weight)

ADMINISTRATION

1. Palpate mammary glands and measure tumors with calipers.
2. Divide mice into four groups with tumors of approximately the same size.
3. Weigh animals. Calculate the volume of doxorubicin needed to administer to each animal.
4. Administer the first dose of RS 504393 (two groups) or the DMSO control (two groups) 25 hours prior to administration of doxorubicin or PBS.
5. Continuing administering RS 504393 or the DMSO control every 12 hours until euthanization.
6. Administer doxorubicin (one RS 504393 and one DMSO group) or PBS (one RS 504393 and one DMSO group) 25 hours after the first RS 504393 or DMOS treatment.
7. Euthanize mice 48 hours after administration of doxorubicin or PBS.
8. Harvest tissue. If tissue is to be used for immunohistochemistry, collect tissue in cassette and fix in 4% paraformaldehyde overnight. If tissue is to be used for DNA, RNA, or protein analysis, flash freeze tissue in liquid nitrogen and store at -80°C.

NOTE: The control for RS 504393 is DMSO diluted in water (6 μL DMSO with 294 μL sterile water; RS 504393 precipitates in PBS so water must be used instead).

V. Isolation of primary tumor cells for flow cytometric analyses

PREPARATION OF BUFFERS:

1. Prepare **FACS Buffer** up to 5 days prior to use.
2. Prepare ~15-20 mL of **Collagenase Buffer** immediately prior to addition to tumor tissue; warm 1× RPMI and FBS in 37°C incubator until preparation of buffer.
3. Prepare **ACK Lysis Buffer** and store at room temperature (RBC Lysis Buffer (10x) from BioLegend, Cat No 420301, may be used in place of ACK Lysis Buffer; dilute RBC Lysis Buffer 1:10 in dH_2O prior to use).

PREPARATION OF SURGICAL TOOLS:

1. Wash dissecting tools in soap and water (one pair of forceps and scissors for opening the mouse, one pair for removing mammary tumors). Sterilize dissecting tools at >200°C for 30s.
2. Replace blade for retractable scraper (Techni-Edge, Cat No TE05-503) and sterilize at >200°C for 30s.

ISOLATION PROTOCOL:

1. Sacrifice mice and remove tumor (generally R5 or L5 with a caliper measurement of ~12-15 mm). If removing L4 or R4, take care to avoid taking the lymph node with the tumor tissue.
2. Place tumor in appropriately labeled tissue culture dish containing 6 mL ice cold RPMI (without FBS) and place on ice.
3. Weigh tumor samples and calculate amount of Collagenase Buffer required (1 mL / 0.3 g tumor tissue; for tumors of size ~12-15 mm, this should require ~3-3.5 mL of Collagenase Buffer).
4. Mechanically dissociate tumors with scraper. Chop tumors until they are mostly fluid, with almost no chunks (~7-10 minutes).
5. Remove Collagenase Buffer from 37°C incubator (or water bath). Add appropriate volume of Collagenase Buffer to each sample (1 mL / 0.3 g tumor tissue, as calculated in Step 3) and transfer samples to appropriately labeled 50 mL Falcon tubes.
6. Tighten Falcon tube covers and wrap cover with parafilm.
7. Lay Falcon tubes flat on the base of a 37°C shaking incubator, and tape down tubes to secure them in place.
8. Shake tubes at 37°C for 90 min at 70 rpm.
9. Remove tubes from incubator.
10. Add 10 mL of R-10 to each sample.
11. Centrifuge at 1500 rpm for 8 min at 4°C.
12. Transfer supernatants to new 50 mL Falcon tubes spin at 1500 rpm for 8 min at 4°C. Meanwhile, resuspend pellets in 8 mL ice cold R-10 with 8 mL ice cold 1× PBS.
13. Discard supernatant from second spin.
14. Resuspend second pellet in 2 mL ice cold R-10 with 2 mL ice cold 1× PBS. Transfer resuspension to that from Step 14.
15. Filter each sample into new 50 mL Falcon tube using a 100 μm cell strainer.
16. Centrifuge samples at 1500 rpm for 8 min at 4°C.
17. Resuspend pellets in 10 mL ACK Red Blood Cell Lysis Buffer.
18. Incubate on ice for 3-5 min.
19. Add 20 mL ice cold R-10 and 20 mL ice cold 1× PBS to each sample.
20. Centrifuge at 1500 rpm for 6 min at 4°C.
21. Discard supernatant.
22. Resuspend pellets in ice cold R-10 (5-10 mL).

23. Strain each resuspension into a new 50 mL Falcon tube using a 40 μm cell strainer. KEEP CELLS ON ICE.
24. Count cells using hemacytometer.

STAINING PROTOCOL:
1. Plate cells in a 96-well round-bottom plate according to pre-determined template. Each well should contain approximately 1×10^6 cells.
2. Centrifuge plate at 2000 rpm for 30s at 4°C.
3. Discard supernatant by flicking plate. Make sure there are cells collected at the bottom of each inoculated well.
4. Resuspend cells in 50 μL ice cold FACS Buffer with Fc Block (1:50 dilution for a concentration of 0.5 μg per well).
5. Incubate at 4°C for >15 min.
6. While cells are incubating in Fc Block, prepare antibody solutions. All antibodies are used at a dilution of 1:100, except for CD11b-PE, which is used at a dilution of 1:200.
7. Add 50 μL of antibody solution to appropriate wells. Incubate in the dark at 4°C for $\geq$30 min.
8. Adjust volume of each well to 200 μL with ice cold FACS Buffer.
9. Centrifuge plate at 2000 rpm for 30s at 4°C.
10. Discard supernatant by flicking plate. Wash 2× with 150 μL ice cold FACS buffer.

FIXING CELLS:
1. Add 200 μL of 0.5% paraformaldehyde in 1× PBS.
2. Incubate cells at 4°C overnight (8-12 hours).
3. Centrifuge plate at 2000 rpm for 30s at 4°C.
4. Discard supernatant by flicking plate. Wash 2× with 150 μL ice cold FACS buffer.
5. Resuspend in 150 μL ice cold FACS Buffer (for cells to be stained with 7-AAD, add 2.5 μL 7-AAD per 150 μL of FACS Buffer).

ANALYSIS:
1. Transfer cells to labeled 12×75 mm polystyrene test tubes. Keep in dark on ice or at 4°C until Flow Cytometry appointment.
2. Run samples on a LSR II (BD Biosciences) flow cytometer.
3. Analyzed FACS data using FACSDiva™ (BD Biosciences) software.

BUFFERS AND SOLUTIONS:

Collagenase Buffer – Prepare Fresh

Reagent	Final Solution
1× RPMI	10 mL
Collagenase (Final conc. 2mg/mL)	2 mg/mL
DNAse I, 1U/μL (Final conc. 4U/mL)	40 μL
Total	10 mL

ACK Lysis Buffer – Filter sterilize and store at room temperature

Reagent	Final Solution
NH_4Cl (0.15 M)	8.024 g
$KHCO_3$ (10 mM)	1.001 g
$Na_2EDTA{\cdot}2H_2O$	3.722 mg
dH_2O	1000 mL
Total	1000 mL

R-10 – Store at 4°C

Reagent	Final Solution
1× RPMI	45 mL
Fetal Bovine Serum (FBS)	5 mL
Total	50 mL

FACS Buffer – Store at 4°C up to 5 days

Reagent	Final Solution
1× PBS	49.4 mL
Fetal Bovine Serum (FBS)	0.5 mL
Sodium Azide (10% w/v)	0.1 mL
Total	50 mL

VI. Immunohistochemical staining of phospho-histone H3 (DAB staining)

NOTE: This is a sample immunohistochemical stain. Antigen retrieval and incubation times may vary depending on the antibody. Most antibodies work in sodium citrate buffer (pH 6.0) with a retrieval time of 6 min at 6 psi, 60 min primary antibody, and 30 min secondary incubation. This protocol, which can also be used to stain for phospho-histone H2AX, is an exception.

1. Warm slides in 56°C oven for 20 min.
   (Tissue slides are kept in slide holder for entire procedure – until drying and mounting)

2. While slides are warming, prepare pressure cooker.

   Fill the cooking pot with water up to the 11-cup line. Properly cover and lock the pressure cooker. Make sure the dots on the pressure valve and cooker cover are aligned. Plug in the pressure cooker. Press Menu twice to set to High Pressure. Press Time four times to set the clock to 05 minutes. Press start.

   Also during this time, check that all containers for tissue rehydration are full with 'clean' fluids – if not, refill.

3. Begin rehydration of tissue:
   - Histoclear 5 min
   - Histoclear 5 min

     By this point, the pressure cooker should have beeped to signal completion of the pressurization cycle. Release pressure valve to depressurize the pressure cooker. **BE CAREFUL, HOT STEAM IS RELEASED FROM PRESSURE VALVE.** When the red pin on the cover slides down, unlock and uncover the pressure cooker, and place Coplin jar containing **Sodium Citrate** buffer into pressure cooker. Re-cover the pressure cooker without locking it. Press Start/Cancel to turn off the Keep Warm setting. Press Menu until the Simmer setting is selected, then press Start/Cancel. This will keep the water in the pressure cooker heated until antigen retrieval.

   - 100% Ethanol 3 min
   - 100% Ethanol 3 min
   - 95% Ethanol 3 min
   - 95% Ethanol 3 min
   - 70% Ethanol 3 min
   - 70% Ethanol 3 min
   - dWater 3 min

4. Antigen retrieval:
   Press Start/Cancel to turn off the Simmer setting. Press Menu once to select the Low Pressure setting. Press Time five times to set the clock to ***15 minutes***. Cover and lock the pressure cooker. Make sure the dots on the pressure valve and cooker cover are aligned. Press Start/Cancel. When pressure cooker beeps to signal completion of the cycle, release the pressure valve to depressurize the pressure cooker. **BE CAREFUL, HOT STEAM IS RELEASED FROM PRESSURE VALVE.** When the red pin on the cover slides down, unlock and uncover the pressure cooker. Using forceps or autoclave gloves, transfer the Coplin jar to sink and run cold water into the jar for 10 min to cool down slides. Transfer

cooled slides to PBS to keep slides hydrated. Using a PAP pen, draw around tissue (**do not let tissue dry out**). Transfer slides to clean PBS.

5. Antibody staining:
   - Block endogenous peroxidase activity: 3% H_2O_2 in PBS — 20 min
   - PBS — 5 min
   - PBS — 5 min
   - Block in 1× Blocking Solution — 1 hour
   - PBS — 3 min
   - Block with Avidin solution — 15 min
   - PBS — 10 dips
   - Block with Biotin solution — 15 min
   - PBS — 10 dips
   - Apply α-pH3 antibody, diluted 1:50 in 0.5× blocking buffer to bottom section in humidified chamber at room temperature — 1 hour
   - Apply Ready-Made Rabbit Isotype Control to top section in humidified chamber at room temperature — 1 hour
   - PBS — 3 min
   - PBS — 3 min
   - PBS — 3 min
   - Block in × antibody blocking buffer — 15 min
   - Apply biotinylated secondary antibody, α-rabbit, diluted 1:400 in 0.5× blocking buffer, in humidified chamber — 30 min
   - Make up ABC-Elite solution during secondary incubation
   - PBS — 3 min
   - PBS — 3 min
   - PBS — 3 min
   - Apply ABC-Elite solution to sections, in humidified chamber — 30 min
   - PBS — 2 min
   - PBS — 2 min
   - Make up DAB solution during second PBS wash
   - Apply DAB solution **KEEP TIME CONSTANT for all slides** — 6 min
   - Wash in dH_2O — 10 dips

6. Counterstaining with Hematoxylin – **NO EOSIN**
   - Hematoxylin — 5 min
   - PBS — 5 min
   - 95% Ethanol — 10 dips
   - 95% Ethanol — 10 dips
   - 100% Ethanol — 10 dips
   - 100% Ethanol — 10 dips
   - Histoclear — 2 min
   - Histoclear — 2 min

7. Mounting
   a. Take slides out of slide holder, put them on slide tray covered with paper towels (*make sure the right side is up!!!*). Add 2-3 drops of Cytoseal 60 on top of tissue.
   b. Carefully cover with cover glass, avoiding air bubbles. Remove any excess Cytoseal with KimWipes before it dries.
   c. Leave to dry in flow hood for several hours on slide tray

Reagents:

Histoclear:	Fisher Scientific
Hematoxylin:	From Zymed / Invitrogen
PBS:	Phosphate Buffered Saline (1× PBS)
Cover glass:	No. 1.5 24×50 mm (Corning)
3% H_2O_2:	25 mL of 30% H_2O_2 and 225 mL 1× PBS
1× Blocking Buffer:	1 mL: 50 µL goat serum, 250 µL 10% BSA, 700 µL 1× PBS
0.5× Blocking Buffer:	1 mL: 25 µL goat serum, 125 µL 10 BSA, 850 µL 1× PBS
Fc Receptor Blocker:	Innovex; NB309-15
10% BSA:	1 g BSA (bovine serum albumin, in fridge) in 10 mL Milli-Q water; store in 1 mL aliquots in freezer.
Avidin / Biotin Kit:	Vector Laboratories, SP-2001
ABC-Elite Solution:	Add 1 drop of solution A to 2.5 mL PBS and mix. Add 1 drop of solution B and mix. **Allow 30 minutes to pass before use**.
DAB-Solution:	Liquid DAB black substrate kit, Vector Labs. Keep in the dark until use. Add 1 drop of Buffer pH 7.5 to 2.5 mL dH_2O and mix. Add 2 drops of DAB substrate and mix. Add 1 drop of H_2O_2 and mix. **Minimize light exposure and use immediately after preparation.**
α-pH3 antibody:	Rabbit-α-mouse, Cell Signaling, #9701S
Control Rabbit IgG:	Rabbit isotype control, Invitrogen #08-6199
Secondary Antibody:	Biotinylated α-Rabbit IgG, Fab fragment, made in goat; Santa Cruz, # sc-3840
Cytoseal60:	Fisher Scientific, #23-244-256
Sodium Citrate Buffer:	10 mM Sodium Citrate, 0.05% Tween 20, pH 6.0 Dissolve 2.94 g of sodium citrate (dihydrate) in 1000 mL of distilled water. Adjust to pH 6.0 with 1N HCl (initially the solution will have a pH of ~8.5; 2-3 mL of 1N HCl may be required to adjust the pH properly). Add 0.5 mL Tween 20 to the solution and mix well. Solution may be stored at room temperature for 3 months, or at 4ºC for a longer period of time.

VII. Immunofluorescence staining of α-SMA (Mouse on Mouse staining)

NOTE: This protocol is adaptable for use with any mouse-anti-mouse antibody. Overnight incubations should not be used for mouse-α-mouse antibodies, as this results in very low positive staining signal with a high level of background. This is protocol is also used for performing dual labeling in which one of the primary antibodies is a mouse-α-mouse antibody.

1. Warm slides in 56°C oven for 20 min.

2. While slides are warming, prepare pressure cooker.

   Fill the cooking pot with water up to the 11-cup line. Properly cover and lock the pressure cooker. Make sure the dots on the pressure valve and cooker cover are aligned. Plug in the pressure cooker. Press Menu twice to set to High Pressure. Press Time four times to set the clock to 05 minutes. Press start.

   Also during this time, check that all containers for tissue rehydration are full with 'clean' fluids – if not, refill.

3. Begin rehydration of tissue:
   - Histoclear 5 min
   - Histoclear 5 min

     By this point, the pressure cooker should have beeped to signal completion of the pressurization cycle. Release pressure valve to depressurize the pressure cooker. **BE CAREFUL, HOT STEAM IS RELEASED FROM PRESSURE VALVE.** When the red pin on the cover slides down, unlock and uncover the pressure cooker, and place Coplin jar containing **Sodium Citrate** buffer into pressure cooker. Re-cover the pressure cooker without locking it. Press Start/Cancel to turn off the Keep Warm setting. Press Menu until the Simmer setting is selected, then press Start/Cancel. This will keep the water in the pressure cooker heated until antigen retrieval.

   - 100% Ethanol 3 min
   - 100% Ethanol 3 min
   - 95% Ethanol 3 min
   - 95% Ethanol 3 min
   - 70% Ethanol 3 min
   - 70% Ethanol 3 min
   - dWater 3 min

4. Antigen retrieval:
   Press Start/Cancel to turn off the Simmer setting. Press Menu once to select the Low Pressure setting. Press Time five times to set the clock to 06 minutes. Cover and lock the pressure cooker. Make sure the dots on the pressure valve and cooker cover are aligned. Press Start/Cancel. When pressure cooker beeps to signal completion of the cycle, release the pressure valve to depressurize the pressure cooker. **BE CAREFUL, HOT STEAM IS RELEASED FROM PRESSURE VALVE.** When the red pin on the cover slides down, unlock and uncover the pressure cooker. Using forceps or autoclave gloves, transfer the Coplin jar to sink and run cold water into the jar for 10 min to cool down slides. Transfer

cooled slides to PBS to keep slides hydrated. Using a PAP pen, draw around tissue (**do not let tissue dry out**). Transfer slides to clean PBS.

8. Blocking of non-specific binding:
   - PBS 5 min
   - Block in M.O.M. IgG Block Reagent 1 hour
   - PBS 2 min
   - PBS 2 min

9. PBS Primary antibody staining:
   - Incubate tissue sections in working solution M.O.M. diluent 5 min
   - Apply αSMA antibody (1:1500 in M.O.M. diluent) to bottom section in humidified chamber at RT 1 hour
   - Apply ready-made Mouse IgG control to top section, in humidified chamber at RT 1 hour
   - PBS 3 min
   - PBS 3 min
   - PBS 3 min

FROM THIS POINT, KEEP SLIDES IN THE DARK WHENEVER POSSIBLE

10. Secondary antibody staining:
    - Apply α-Mouse-Alexa568 secondary in M.O.M. diluent in a humidified chamber at RT 30 min
    - PBS 10 min
    - PBS 5 min
    - PBS 5 min
    - dH_2O 5 min
    - Counterstain with DAPI (diluted 1:100 in dH_2O) 10 min
    - dH_2O 3 min

11. Mounting:
    a. Add 2-3 drops of FluoroGel on top of tissue.
    b. Carefully cover with cover slip, avoiding air bubbles.
    c. Let dry 30 minutes in the dark.
    d. Seal the edges of the cover slip with Cytoseal 60 and let dry.

Reagents:

Histoclear:	Fisher Scientific
PBS:	Phosphate Buffered Saline (1× PBS)
Cover slip:	No. 1.5 24×50 mm (Corning)
M.O.M. Kit	Vector Labs, Cat. No. BMK-2202
M.O.M. Mouse Ig Blocking Reagent:	Add 2 drops of stock solution to 2.5 ml of PBS.
M.O.M. Diluent:	Add 600 µl Protein Concentrate to 7.5 ml of 1× PBS
α-Smooth muscle actin:	Monoclonal Anti-Actin α Smooth Muscle; Sigma, #A5228
Control Mouse IgG:	Mouse isotype control, Invitrogen #08-6599
α-Mouse-IgG-Alexa568:	Alexa Fluor 568 F(ab')2 fragment of goat anti-mouse IgG (H+L), Invitrogen #A11019
DAPI:	Invitrogen, D3571; Frozen stock 5 mg/mL in dH_2O
FluoroGel:	with PIPE buffer, Electron Microscopy Sciences, #17985-40
Cytoseal60:	Fisher Scientific, #23-244-256
Sodium Citrate Buffer:	10 mM Sodium Citrate, 0.05% Tween 20, pH 6.0 Dissolve 2.94 g of sodium citrate (dihydrate) in 1000 mL of distilled water. Adjust to pH 6.0 with 1N HCl (initially the solution will have a pH of ~8.5; 2-3 mL of 1N HCl may be required to adjust the pH properly). Add 0.5 mL Tween 20 to the solution and mix well. Solution may be stored at room temperature for 3 months, or at 4ºC for a longer period of time.

VIII. Immunofluorescence staining of CD206 (staining of frozen tissue)

NOTE: This protocol can be used for the immunofluorescence staining of most frozen samples. Step 3 is not required, but results in better tissue staining.

1. Remove slides from -80°C freezer and allow slides to warm to room temperature (~5 minutes). If tissues already contain fluorescent molecules (e.g. lectins, dextran, ECFP, EGFP) keep slides in dark as much as possible.

2. Using a scalpel, carefully remove the sticky OCT from the slide. If the OCT does not easily pull away from the slide, gently pipette PBS onto the slide and let the slide sit for 3 minutes at room temperature. Gently tip off the PBS onto a paper towel and then using a scalpel, remove the OCT.

3. Post-fix the tissue by gently placing the labeled slides into an upright **glass** Coplin jar containing a 1:1 mixture of ice cold methanol and acetone. Incubate at room temperature for 10 min.

4. Draw a circle around each tissue section using a PAP pen, and place slides onto a rack in a humidifying chamber (from now on, all steps will be done in a humidifying chamber).

5. Using a pipette, gently add 200 μL PBS to each tissue section and incubate at room temperature for 5 minutes. Repeat this wash step once.

6. Antibody staining (gently add 200 μL or 2-3 drops of each solution to tissue sections; to remove liquid once the incubation has been completed, gently tip off the fluid onto a paper towel):
   - Block in Fc Receptor Blocker — 30 min
   - PBS — 5 min

7. Primary antibody staining:
   - Apply antibody solution (α-CD206 diluted in 1:200 0.5× blocking buffer) to bottom section in humidified chamber at room temperature — 1 hour
   - Apply Rat IgG2a negative isotype, diluted 1:400 in 0.5× blocking to top section in a humidified chamber at room temperature — 1 hour
   - PBS — 3 min
   - PBS — 3 min
   - PBS — 3 min

FROM THIS POINT, KEEP SLIDES IN THE DARK WHENEVER POSSIBLE

8. Secondary antibody staining:
   - Block in 1× antibody blocking buffer — 15 min
   - Apply antibody solution (α-Rat-Alexa568 diluted 1:150 in 0.5× blocking buffer) in humidified chamber at room temperature — 30 min
   - PBS — 10 min
   - dH_2O — 5 min
   - dH_2O with DAPI (diluted 1:100) — 10 min
   - dH_2O — 3 min

Reagents:

Histoclear:	Fisher Scientific
PBS:	Phosphate Buffered Saline (1× PBS)
Cover glass:	No. 1.5 24×50 mm (Corning)
3% H_2O_2:	25 mL of 30% H_2O_2 and 225 mL 1× PBS
1× Blocking Buffer:	1 mL: 50 μL goat serum, 250 μL 10% BSA, 700 μL 1× PBS
0.5× Blocking Buffer:	1 mL: 50 μL goat serum, 125 μL 10 BSA, 850 μL 1× PBS
Fc Receptor Blocker:	Innovex; NB309-15
10% BSA:	1 g BSA (bovine serum albumin, in fridge) in 10 mL Milli-Q water; store in 1 mL aliquots in freezer.
α-CD206 antibody:	Rat-α-mouse, AbD Serotec, MCA2235GA
Control Rat IgG:	Rat Negative Isotype IgG2a
Secondary Antibody:	Biotinylated α-Rat IgG, Fab fragment; made in goat (Santa Cruz)
DAPI:	Invitrogen, D3571; Frozen stock 5 mg/mL in dH_2O
Vectashield:	Vector Labs, H-1000

IX. Immunofluorescence staining of CCR2 and 7/4 (double label staining)

NOTE: This is a sample double label immunostain. Antigen retrieval and incubation times may vary depending on the antibody combination. Most antibodies work in sodium citrate buffer (pH 6.0) with a retrieval time of 6 min at 6 psi, 60 min primary antibody, and 30 min secondary incubation. This protocol is an exception.

1. Warm slides in 56°C oven for 20 min.

2. While slides are warming, prepare pressure cooker.

   Fill the cooking pot with water up to the 11-cup line. Properly cover and lock the pressure cooker. Make sure the dots on the pressure valve and cooker cover are aligned. Plug in the pressure cooker. Press Menu twice to set to High Pressure. Press Time four times to set the clock to 05 minutes. Press start.

   Also during this time, check that all containers for tissue rehydration are full with 'clean' fluids – if not, refill.

3. Begin rehydration of tissue:
   - Histoclear 5 min
   - Histoclear 5 min

     By this point, the pressure cooker should have beeped to signal completion of the pressurization cycle. Release pressure valve to depressurize the pressure cooker. **BE CAREFUL, HOT STEAM IS RELEASED FROM PRESSURE VALVE.** When the red pin on the cover slides down, unlock and uncover the pressure cooker, and place Coplin jar containing **Sodium Citrate** buffer into pressure cooker. Re-cover the pressure cooker without locking it. Press Start/Cancel to turn off the Keep Warm setting. Press Menu until the Simmer setting is selected, then press Start/Cancel. This will keep the water in the pressure cooker heated until antigen retrieval.

   - 100% Ethanol 3 min
   - 100% Ethanol 3 min
   - 95% Ethanol 3 min
   - 95% Ethanol 3 min
   - 70% Ethanol 3 min
   - 70% Ethanol 3 min
   - dWater 3 min

4. Antigen retrieval:
   Press Start/Cancel to turn off the Simmer setting. Press Menu once to select the Low Pressure setting. Press Time five times to set the clock to ***20 minutes***. Cover and lock the pressure cooker. Make sure the dots on the pressure valve and cooker cover are aligned. Press Start/Cancel. When pressure cooker beeps to signal completion of the cycle, release the pressure valve to depressurize the pressure cooker. **BE CAREFUL, HOT STEAM IS RELEASED FROM PRESSURE VALVE.** When the red pin on the cover slides down, unlock and uncover the pressure cooker. Using forceps or autoclave gloves, transfer the Coplin jar to sink and run cold water into the jar for 10 min to cool down slides. Transfer cooled slides to PBS to keep slides hydrated. Using a PAP pen, draw around tissue (**do not let tissue dry out**). Transfer slides to clean PBS.

5. Antibody staining:
   - PBS — 5 min
   - 1× Blocking Buffer — 1-2 hours
   - PBS — 3 min
   - Block in Fc Receptor Blocker — 30 min
   - PBS — 5 min
   - Apply α-CCR2 antibody (diluted 1:100) and α-7/4 (diluted 1:400) in 0.5× blocking buffer to bottom section in humidified chamber at room temperature — 30 min
   - Apply Ready-Made Rabbit Isotype Control to top section in humidified chamber at room temperature — 30 min
   - PBS — 3 min
   - PBS — 3 min
   - PBS — 3 min

FROM THIS POINT, KEEP SLIDES IN THE DARK WHENEVER POSSIBLE

6. Secondary antibody staining:
   - Block in 1× antibody blocking buffer — 15 min
   - Apply antibody solution (α-Rabbit-Alexa568 and α-Rat-Alexa647 both diluted1:150 in 0.5× blocking buffer) in humidified chamber at room temperature — 30 min
   - PBS — 10 min
   - dH_2O — 5 min
   - dH_2O with DAPI (diluted 1:100) — 10 min
   - dH_2O — 3 min

7. Mounting:
   e. Add 2-3 drops of Vectashield on top of tissue.
   f. Carefully cover with cover slip, avoiding air bubbles.
   g. Let dry 30-60 minutes in the dark.
   h. Seal the edges of the cover slip with clear nail polish and let dry overnight.

Reagents:

Histoclear:	Fisher Scientific
Hematoxylin:	From Zymed / Invitrogen
PBS:	Phosphate Buffered Saline (1× PBS)
Cover glass:	No. 1.5 24×50 mm (Corning)
3% H_2O_2:	25 mL of 30% H_2O_2 and 225 mL 1× PBS
1× Blocking Buffer:	1 mL: 50 μL goat serum, 250 μL 10% BSA, 700 μL 1× PBS
0.5× Blocking Buffer:	1 mL: 25 μL goat serum, 125 μL 10 BSA, 850 μL 1× PBS
Fc Receptor Blocker:	Innovex; NB309-15
10% BSA:	1 g BSA (bovine serum albumin, in fridge) in 10 mL Milli-Q water; store in 1 mL aliquots in freezer.
α-CCR2 antibody:	Rabbit-α-mouse, Abcam, #AB32144
α-7.4 antibody:	Rat-α-mouse, Cedarlane Labs, #CL8993AP
Control Rabbit IgG:	Rabbit isotype control, Invitrogen #08-6199
α-Rabbit-IgG-Alexa568:	Alexa Fluor® 568 F(ab')2 fragment of goat anti-rabbit IgG (H+L), Invitrogen #A21069
α-Rat-IgG-Alexa647:	Alexa Fluor® 647 Goat Anti-Rat IgG (H+L), Invitrogen, #A-21247
DAPI:	Invitrogen, D3571; Frozen stock 5 mg/mL in dH_2O
Vectashield:	Vector Labs, #H-1000
Sodium Citrate Buffer:	10 mM Sodium Citrate, 0.05% Tween 20, pH 6.0 Dissolve 2.94 g of sodium citrate (dihydrate) in 1000 mL of distilled water. Adjust to pH 6.0 with 1N HCl (initially the solution will have a pH of ~8.5; 2-3 mL of 1N HCl may be required to adjust the pH properly). Add 0.5 mL Tween 20 to the solution and mix well. Solution may be stored at room temperature for 3 months, or at 4ºC for a longer period of time.

X. Detection of vascular permeability by lectin staining

SOLUTIONS AND REAGENTS

All solutions ***must*** be prepared in a sterile hood.

REAGENT	SUPPLIER	CAT. NO.	SIZE	STOCK
Rhodamine-*Ricinus communis* Agglutinin I	Vector Labs	RL-1082	5 mg/mL	As is
Fluorescein-*Lycopersicon esculentum* lectin	Vector Labs	FL-1171	2 mg/mL	As is

WORKING SOLUTION	VOLUME	[FINAL]
Ricinus lectin	50 μL	2.5 mg/mL
Lycopersicon lectin	50 μL	1 mg/mL
Total	100 μL	

PREPARATION FOR PERFUSION:

1. Prepare fresh 4% paraformaldehyde (PFA) and store at 4°C until use. Keep in mind that ~20-30 mL will be needed to flush the tubing prior to perfusion, and ~50-60 mL will be needed to perfuse the mouse, so calculate the total volume required based on the approximation that ~100 mL of fixative will be required per animal).
2. Prepare the fume hood: move the glass bead sterilizer and dissection tray (the base should be wax or rubber) into the hood. This procedure should be performed in a fume hood to avoid prolonged exposure to paraformaldehyde.
3. Place an absorbent blue mat on top of the dissection tray (the blue mat should be cut into fourths before use), and pin the corners to the dissection tray.
4. Set up the anesthesia equipment. Be sure to fasten the nose cone to the dissection tray (tape the nose cone down with laboratory tape, and pin the tape to keep the cone immobilized).
5. Prepare four strips of laboratory tape to restrain the animal for the procedure.
6. Prepare a 60 syringe and winged infusion set. Draw in ~60 mL of 4% PFA into the syringe, and screw the female Luer-Lok™ end of the infusion set into the male Luer-Lock™ end of the syringe. Flush 10-15 mL of 4% PFA through the system to remove air bubbles. Keep the syringe on ice.
7. Wash surgical tools in soap and water (two pairs of forceps, two pairs of scissors). Sterilize dissecting tools at >200°C for 30s.

VASCULAR LABELING AND PERFUSION:

1. Induce anesthesia at 4% isoflurane. Keep animal in induction chamber until she is completely anesthetized.
2. Switch the anesthesia from the induction chamber to the nose cone in the procedure area.
3. Transfer the animal to the procedure area, ventral side up. Make sure the animal's nose is secured in the nose cone.
4. Gently restrain the animal by fastening the limbs to the procedure area with laboratory tape. Leave one limb unrestrained.
5. Decrease the flow rate of isoflurane to 2.5%.
6. Make sure the animal is fully anesthetized by performing a footpad pinch on the unrestrained limb. The animal **should not react** to this. If she does, she is not sufficiently anesthetized for the procedure. This is a very harsh procedure that causes a lot of pain. The animal cannot be awake for any portion of it.
7. When the animal is sufficiently anesthetized, restrain the final limb.
8. Inject 100 μL of the *Ricinus communis* lectin / *Lycopersicon esculentum* lectin mixture intravenously via the tail vein. Wait 10 minutes.

9. During the 10-minute wait, disinfect the ventral surface of the animal with an ethanol wipe.
10. Carefully make a subcutaneous midline incision beginning from approximately 0.5 cm from above the urethra to the top of the ribcage.
11. Make an incision from the middle of the peritoneal cavity to the base of the rib cage.
12. Gently pierce the connective tissue below the diaphragm to collapse the lungs and the thoracic cavity.
13. Quickly cut open the ribcage. Make two incisions, one ~2 mm from the left of the midline, and one ~2 mm from the right of the midline.
14. Fold the middle portion of the ribcage up and expose the heart.
15. Hold the heart steady with a pair of forceps (be sure to use the forceps with the serrated tips, not the forceps with teeth – you do not want to puncture the heart).
16. Using the winged infusion set, gently cannulate the left ventricle, and slide the needle straight up into the descending aorta. Be careful not to push the needle to far up (not more than 5 mm), because you may puncture the heart and disrupt circulation. **Systemic circulation must remain intact to perfuse the whole body**.
17. Cut the right atrium (pulmonary circulation), and begin to slowly perfuse the tissue. Maintain constant pressure on the syringe plunger. Blood should flow steadily out of the incision you made in the right atrium. Continue to perfuse until the fluid that flows out of the heart is clear (~30-50 mL). Be careful not to perfuse the tissue too quickly, as high perfusion rates will rupture vessels (if you are using a sphygmomanometer paired with a gravity drip system or a controlled perfusion system, the pressure should be between 60 and 100 mm Hg).
18. At this point, the animal should be dead. If she is not, quickly remove the heart.
19. Turn off the anesthesia.
20. Harvest the tissue and post-fix overnight at 4°C in 4% PFA.
21. Process the tissue through a graded sucrose solution (12% for ≥ 2 hours, 15% for ≥ 2 hours, 18% for ≥ 2 hours, 25% over night).
22. Embed tissue in O.C.T. freezing medium (Tissue-Tek).
23. Store blocks at -80°C.

COUNTERSTAINING:

1. Cut thick tissue sections (40 to 80 μm).
2. Store slides at -80°C until use.
3. Thaw tissue sections at room temperature (~ 5 min).
4. Gently remove O.C.T. medium.
5. Draw a circle around the tissue section with a wax pen.
6. Wash the tissue in 1× PBS for 5 min at room temperature.
7. Incubate tissue in dH_2O for 5 min at room temperature.
8. Counterstain with DAPI (diluted 1:100) for 10 min.
9. Wash in dH_2O for 3 min.
10. Mount cover slips using Vectashield.
11. Acquire image using confocal microscope.

XI. Operating the Egeblad laboratory spinning disk confocal microscope

1. Turn the computer on.
2. Turn on the argon laser.
   a. Flip the I/O switch on.
   b. Turn the key to the on position (with the clock).
   c. Adjust the laser power to its minimum level (about 4.75 Amps) using the level on the table to the right of the microscope.
3. Turn on the solid-state lasers (405 nm, 561, 641 nm).
   a. Turn on power strip for laser table.
   b. Turn all three keys to the "on" position.
   c. Verify that the Solamere box (on top of box covering laser path) is turned on.

4. Turn on the microscope accessories and controllers.
   a. Turn on power strip for microscope table.
   b. Check that the following are turned on:
      – X-cite lamp for looking at fluorescence signal through the microscope eyepieces (on the shelf behind and above microscope)
      – AOTF controller (on shelf behind and above microscope)
      – Piezo controller (on shelf behind and above microscope)
      – Filter wheel controller (on shelf behind and above microscope)
      – ASI stage controller (on the table to the right of the microscope)
      – Microscope power supply

5. Turn on the microscope.
   a. Turn on the microscope (button on the left side, to the very back of the microscope).
   b. Move the stage to its lowest position using the focus knob on microscope – the monitor will say "Lower z reached."
   c. Turn on the spinning disk (attached to the left of the microscope): turn key to the "on" position and push button labeled "shutter". The light next to the key should turn red.

6. Turning on the software and camera:
   d. Make sure the camera controller (on the table to the left of the computer screen) is in the standby position.
   e. Turn on the camera controller.
   f. Double check that the microscope stage is in its lowest position.
   g. Open μManager (all equipment except the camera controller must be turned on before opening the software).

7. Troubling-shooting tips
   a. ***Always leave the camera controller in "standby" when not actively using the camera***
   b. ***Do not turn off microscope if less than 3 hours before next user***
   c. The camera controller should be used between 0.65 and 0.9.
   d. If the signal is too bright, even at lowest exposure (33 ms), adjust the laser power with the Solamere box (using the relevant knob for the dye).
   e. If the signal is too low for one laser line, increase the exposure time.
   f. If the signal is too low for several laser lines or for a single line (even after attempting to increase the exposure time), increase the camera gain (but do not use above 0.9). If the signal for GFP (488 nm) is still too low, adjust the laser power using the level on table to the right of the microscope.

8. Shutting down the system:
    a. Make sure camera controller (on the table to the left of the computer screen) is in the standby position and at 0.65-0.85 before turning off camera controller
    b. Close μManager software
    c. Transfer images to server (shut down computer when transfer is complete).
    d. Adjust laser power for argon laser to lowest level possible.
    e. Switch off the **key** to argon laser (488 nm) – ***ONLY THE KEY, do not turn off the exhaust***.
    f. Lower the microscope stage to the lowest possible setting.
    g. Remove the microscope stage insert.
    h. Turn off the spinning disk (using key, it is not necessary to press button).
    i. Turn off the power strip on the microscope table and check that all equipment is turned off.
    j. Cover the microscope up.
    k. Turn off the keys to the solid-state lasers (405, 561, 641 nm).
    l. Turn off the power strip to laser table.

9. Turn off Argon laser (I/O button, controls exhaust and may continue even after turned off if laser was used for a long period of time)

XII. Preparation of Animals for Intravital Imaging

PREPARATION OF PBS (**Do this in a sterile hood!**)

1. Dilute the propidium iodide (1 mg/mL, Invitrogen) 1:15 in 1× PBS in a sterile hood. For a 24 hour imaging session, prepare ~3 mL.
2. Draw ~1 mL of the PI solution into a 1 mL syringe.
3. Attach a winged infusion set (23 gauge, ¾ inch needle, 12 inch tubing, Terumo) to this syringe and pump the PI solution through the tubing so that just a drop of PI solution exits the needle.
4. Remove the syringe from the infusion set, and refill it with PI solution.
5. Reattach the syringe to the infusion set, taking care not to introduce too many bubbles into the line.
6. Attach the syringe to the microscope and cover it with foil.

PREPARATION OF THE MICROSCOPE:

1. Turn on the microscope computer and the microscope (see protocol "Operating the Egeblad laboratory spinning disk confocal microscope").
2. Turn on the heating blanket (this is not attached to the microscope system, so it needs to be turned on separately).
3. Disinfect the microscope stage insert with ethanol wipes.
4. Disinfect two cover slips (No. 1.5, 24 × 50 mm glass) with ethanol wipes.
5. Place the two cover slips side by side on the microscope stage insert, so that they are covering the two imaging ports.

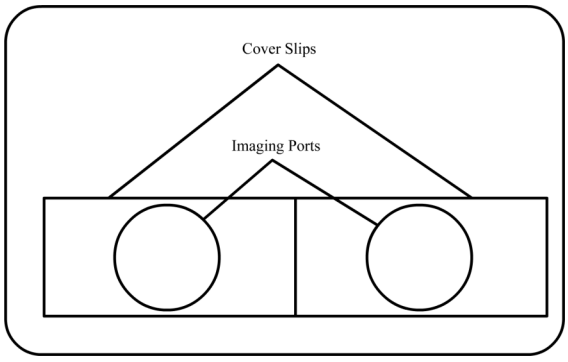

6. Gently apply pressure to the two cover slips to hold them in place, and tape them down with laboratory tape (½ inch tape works best).
7. Disinfect the prepared microscope stage insert with ethanol wipes.
8. Cover the prepared microscope stage insert with a piece of sterile gauze.
9. Position the microscope stage insert on the microscope stage with the imaging ports appropriately positioned for imaging the mouse. The nose cone that delivers anesthesia to the microscope is placed on the left side of the microscope. Thus, if the tumor to be imaged is on the right side of the animal, the side of insert with the imaging ports should sit away from the eyepieces. Conversely, if the tumor to be imaged is on the left side of the animal, the side of the insert with the imaging ports should sit next to the eyepieces.
10. At the microscope, tear 4 to 6 pieces of tape (1 inch width), approximately 6 inches in length and attach them to the side of the microscope. These pieces of tape will be used to position the nose cone delivering anesthesia and fasten it in place.

11. Tear two more pieces of tape (½ inch width) that are about an inch in length. These will be used to keep the butterfly needle delivering PBS to the mouse and the microscope slide used to expose the tumor in place.

PREPARATION OF THE ANESTHESIA SYSTEM:

1. Locate the anesthesia system to the right of the microscope.
2. Add water to the humidifier and screw it in place. If the water in this humidifier evaporates very quickly or there is a hissing sound coming from the humidifier, there is probably a crack in the plastic, and it needs to be replaced.
3. Check to make sure the isoflurane tank is filled. If the tank is half full or less, fill it to the top line.
4. Turn on the oxygen sensor (it should not yet be attached to the anesthesia system; if it is, unhook it). When the sensor has been equilibrated to the room, attach the oxygen sensor to the anesthesia system.
5. There are two gas tanks attached to the anesthesia system. Turn on both the oxygen tank and the nitrogen tank. The nitrogen should be at around 1.0, while the oxygen should be at around 0.2.
6. Turn on the in-house vacuum. The vacuum should fluctuate between about 0.5 and 1.0.
7. Make sure the line to the induction chamber is open, and the lines to the surgery area and the microscope are closed.
8. Check the black rubber bag attached to the anesthesia system to make sure it is inflated. If there is a tear in it replace the bag (if there is no replacement, remove the bag, tape it up, and replace it).
9. Check the rubber gauze on each the nose cones delivering anesthesia to the microscope stage and the surgical platform. If the gauze is starting to thin, change the gauze.

PREPARATION OF SURGERY AREA:

1. Collect the lid to a Styrofoam shipping cooler. This will be your surgical platform.
2. Cover the lid with a piece of blue absorbent mat (cut these mats in fourths, only a fourth of the mat is needed).
3. Place this surgical platform on the empty space in front of the anesthesia system.
4. Collect two pins (i.e. two pink needles).
5. Tape (1 inch width) the nose cone to the surgery platform. Insert pins (one on each side of the nose cone) into the tape to secure the nose cone in place.
6. Tape the blue hose delivering the anesthesia into the nose cone to the microscope bench if it is not already (this will ensure that the surgical platform remains flat – it is often too light to stay flat once the nose cone has been fastened to it).
7. Set aside two ethanol wipes, a microscope slide, Krazy Glue®, and 4 pieces of tape (½ inch width).

PREPARATION OF SURGICAL TOOLS:

1. Turn on glass bead sterilizer.
2. Wash dissecting tools in soap and water (one pair of forceps [preferably with teeth] and scissors for opening the mouse, one pair of forceps [preferably serrated] and scissors for exposing the tumor). Sterilize the dissecting tools at >200°C for 30s.
3. Place the dissecting tools on the side (making sure to avoid touching the sterilized areas of the tools with anything), to let the tools cool enough to perform the procedure.

SURGICAL PROCEDURE:

1. Transfer the mouse to the induction chamber.
2. Induce anesthesia at 4% isoflurane.

3. Once the mouse is breathing slowly and deeply, open the anesthesia line to the surgery platform.
4. Transfer the mouse to the surgical platform, placing her ventral side up. Close the anesthesia line to the induction chamber.
5. Turn the anesthesia down to 2.5% isoflurane.
6. Restrain three of the mouse's limbs with laboratory tape.
7. Perform a footpad pinch on the unrestrained limb. The mouse **should not** react to this. If she does, she is not sufficiently anesthetized for the procedure; wait a couple of minutes and perform the footpad pinch again.
8. Once the mouse is sufficiently anesthetized, restrain the final limb with laboratory tape.
9. Disinfect the ventral surface of the mouse with an ethanol wipe (do this twice).
10. Using the pair of forceps with teeth and a pair of scissors, make a subcutaneous midline incision from approximately 0.5 cm above the urethra to just below the ribcage. Be careful not to cut through the peritoneum.
11. Set this pair of forceps and scissors aside.
12. Using the second pair of forceps (serrated) and scissors, gently separate the skin covering the inguinal mammary gland/tumor to be imaged. The connective tissue that attaches the skin to the peritoneum is weak, so the skin pulls away relatively easily. Try to avoid cutting this connective tissue, as you may accidentally pierce blood vessels in the skin or puncture the peritoneum.
13. Take the glass microscope slide and position it against the skin flap that you have just created. Position the flap so that the bulk of the tumor will sit flat when the mouse is placed on the stage, and it does not interfere with the mobility of the hind legs.
14. Once the microscope slide has been properly positioned, attach it to the skin flap using Krazy Glue®.

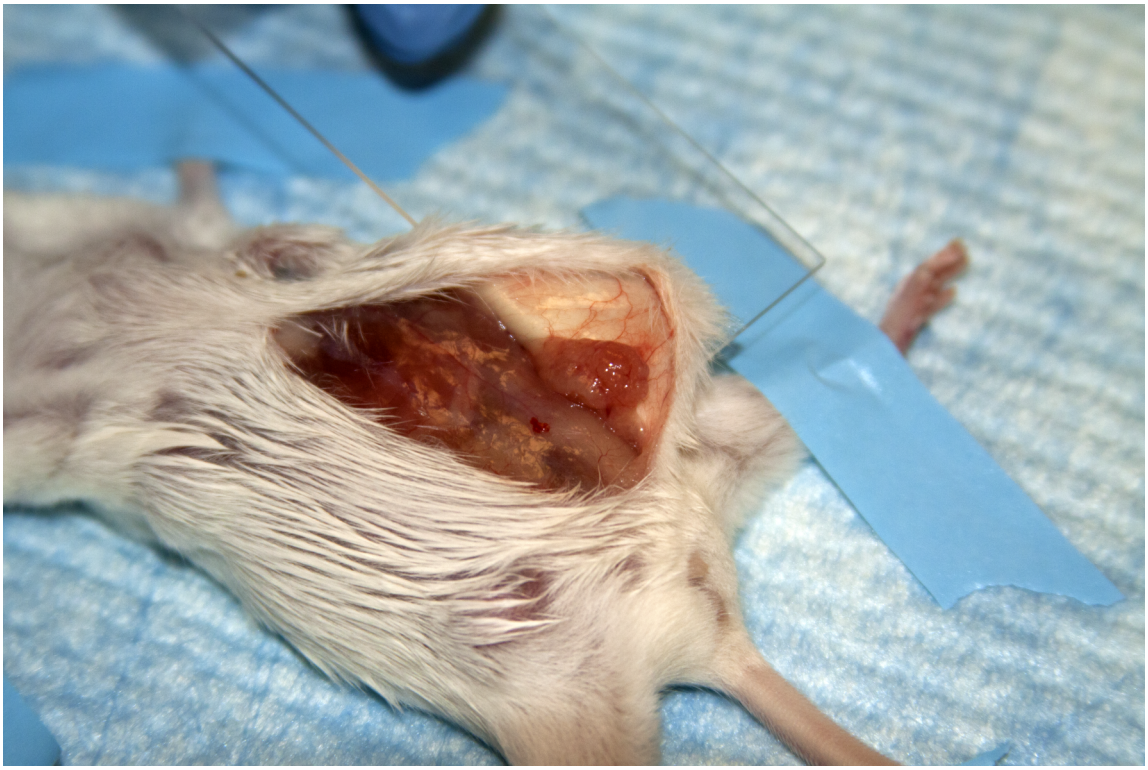

15. Fold the skin flap back over to cover the exposed peritoneum (this will limit desiccation of the tissues as well as limit the collection of dust and other particles, while shifting the mouse to the microscope stage).

TRANSFERRING THE MOUSE TO THE STAGE:

1. Open the anesthesia line to the microscope stage.
2. Gently remove the laboratory tape restraining the mouse.
3. Quickly transfer the animal to the microscope stage, ventral side down.
4. Once the mouse has been transferred, make sure to insert her nose into the nose cone.
5. Close the anesthesia line to the surgery area.
6. Carefully position the mouse so that the tumor is in the center of the imaging port (this will usually be the imaging port on the right) and that the mouse is in a comfortable position with respect to the nose cone.
7. Once the mouse has been positioned, tape the nose cone down (using the 1 inch tape previously prepared).
8. Insert the butterfly needle into the peritoneum. Avoid puncturing any of the abdominal organs.
9. Attach the oximeter probe either to the hind leg opposite the side being imaged or fix a throat collar around the mouse's neck (the throat collar is more reliable, but can only be used if the mouse has small or no tumors in the neck area).
10. Open the MouseOx software (STARR Life Sciences) on the computer. Select the correct probe and settings (adult, anesthetized mouse). Begin monitoring the mouse. Vitals under optimal anesthesia conditions should be:

Heart Rate:	≥300 bpm and ≤450 bpm
Oxygen Saturation:	97-98%
Breath Rate:	55-65 breaths per minute

    The oximeter probe will take several minutes to stabilize, and may need to be repositioned.

11. Once the oximeter probe has been attached to the animal and is reading stable vital signs, tape down double check that the mouse is appropriately positioned for imaging.
12. Tape down the microscope slide and the butterfly needle.
13. Cover the mouse with the heating pad.

XIII. Using Imaris

CALCULATING TIME STAMPS AND FRAME RATES:

1. Locate and open the folder containing the raw images captured using the Egeblad laboratory spinning disk confocal microscope. µManager saves the files in the following manner (names in bold, except for the top two, are sample names for each of these folders):

   egeblad (main server folder)
   Name (folder with your name on it)
   Top Folder (usually saved as YY_MMDD)
   Sample Folder (usually saved as MouseID_color1_color2_color3_ genotype_lens_Exp#)
   Positions Folder (automatically saved by µManager as Pos0, Pos1, …)
   Original TIFFs Folder (this folder will have three types of files: an acquisition file [this will be an XML file], the original TIFF outputs [these are saved as TIFFs, and will vary in number], and a metadata file [this will be a .txt file])

   µManager automatically stores each individual image that is captured with a certain format. Each of your original TIFF files should be named something like this:

   img_000000113_2_000

   The numbers are interpreted as follows: img_timepoint_channel_zslice

2. In general, the time between frames that you set in µManager is the time between each frame. However, if you have set the time between frames to be 90s, when it actually takes 120s to capture the entire stack of images in each channel at each position, you need to calculate this value manually for each experiment. In Excel, make a spreadsheet that looks like this:

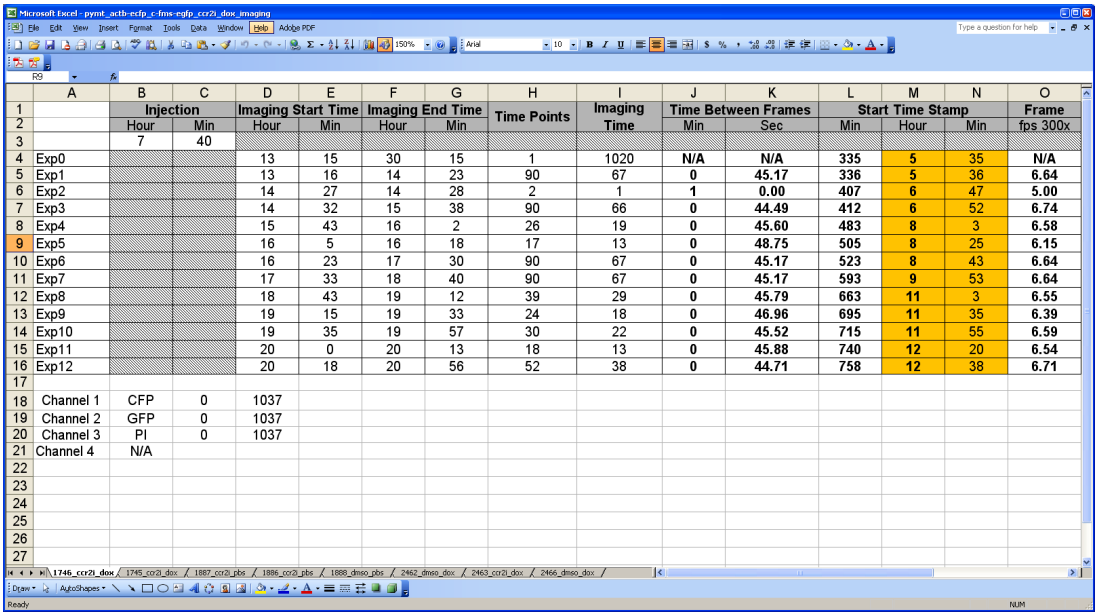

	A	B	C	D	E	F	G	H	I	J	K	L	M	N	O
1		Injection		Imaging Start Time		Imaging End Time		Time Points	Imaging Time	Time Between Frames		Start Time Stamp			Frame
2		Hour	Min	Hour	Min	Hour	Min			Min	Sec	Min	Hour	Min	fps 300x
3		7	40												
4	Exp0			13	15	30	15	1	1020	N/A	N/A	335	5	35	N/A
5	Exp1			13	16	14	23	90	67	0	45.17	336	5	36	6.64
6	Exp2			14	27	14	28	2	1	1	0.00	407	6	47	5.00
7	Exp3			14	32	15	38	90	66	0	44.49	412	6	52	6.74
8	Exp4			15	43	16	2	26	19	0	45.60	483	8	3	6.58
9	Exp5			16	5	16	18	17	13	0	48.75	505	8	25	6.15
10	Exp6			16	23	17	30	90	67	0	45.17	523	8	43	6.64
11	Exp7			17	33	18	40	90	67	0	45.17	593	9	53	6.64
12	Exp8			18	43	19	12	39	29	0	45.79	663	11	3	6.55
13	Exp9			19	15	19	33	24	18	0	46.96	695	11	35	6.39
14	Exp10			19	35	19	57	30	22	0	45.52	715	11	55	6.59
15	Exp11			20	0	20	13	18	13	0	45.88	740	12	20	6.54
16	Exp12			20	18	20	56	52	38	0	44.71	758	12	38	6.71
17															
18	Channel 1	CFP	0	1037											
19	Channel 2	GFP	0	1037											
20	Channel 3	PI	0	1037											
21	Channel 4	N/A													
22															
23															
24															
25															
26															
27															

Column A: Experiment Number (Imaging experiments are saved sequentially. Each experiment is saved in a new folder in the **Sample Folder**, where the experiment number is the number at the end of each folder name).

Columns B and C: This is the time at which you have treated the animal (in this case, with doxorubicin) on the 24-hour clock. In this example, the animal was treated at 7:40 am, so the time is given as is.

Columns D and E: This is the imaging start time for the experiment. We arbitrarily set this time to the time at which the first image of the first position was acquired. This value represents the hours elapsed since treatment. The hour value requires a little bit of math. This is the time elapsed since treatment. For example, if the animal was treated at 22:40 the previous night, and imaging was started at 18:33 as in the example below, the hour setting would be 20 (Column D). The Minutes column would be entered as simply the actual minute value given (33 in this case, for Column E). If instead, the animal has been injected at 22:40 two days prior to imaging, the hour quantity becomes 24 + 20. This same calculation is performed for injections 48, 72, etc. hours prior to imaging. For untreated mice, the time would simply be 6:33 PM = 18 hours (Column D) and 33 min (Column E). If 24, 48, etc. hours have elapsed since the start of imaging, this hour quantity becomes 18 + 24, 18 + 48, etc.

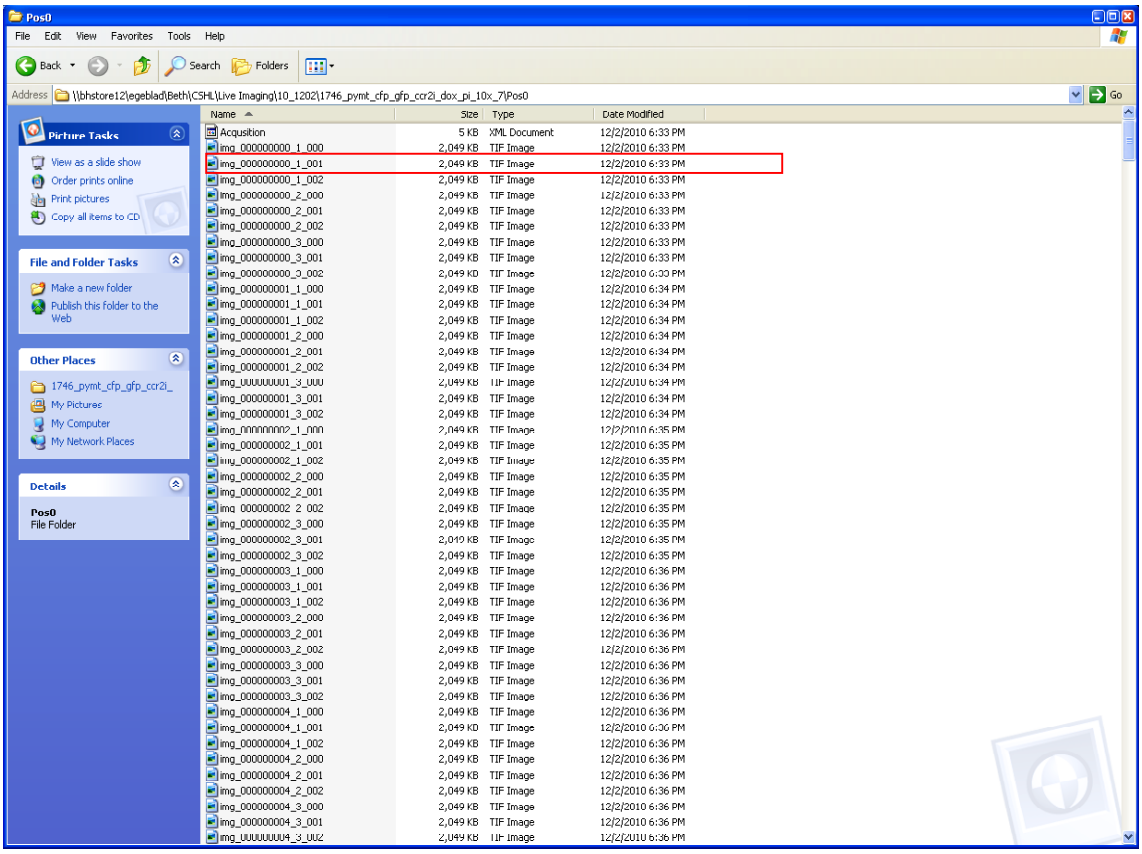

Columns F and G: This is the imaging end time for the experiment. We arbitrarily set this time to the time at which the last image of the first position was acquired. The same considerations apply as per Columns D and E.

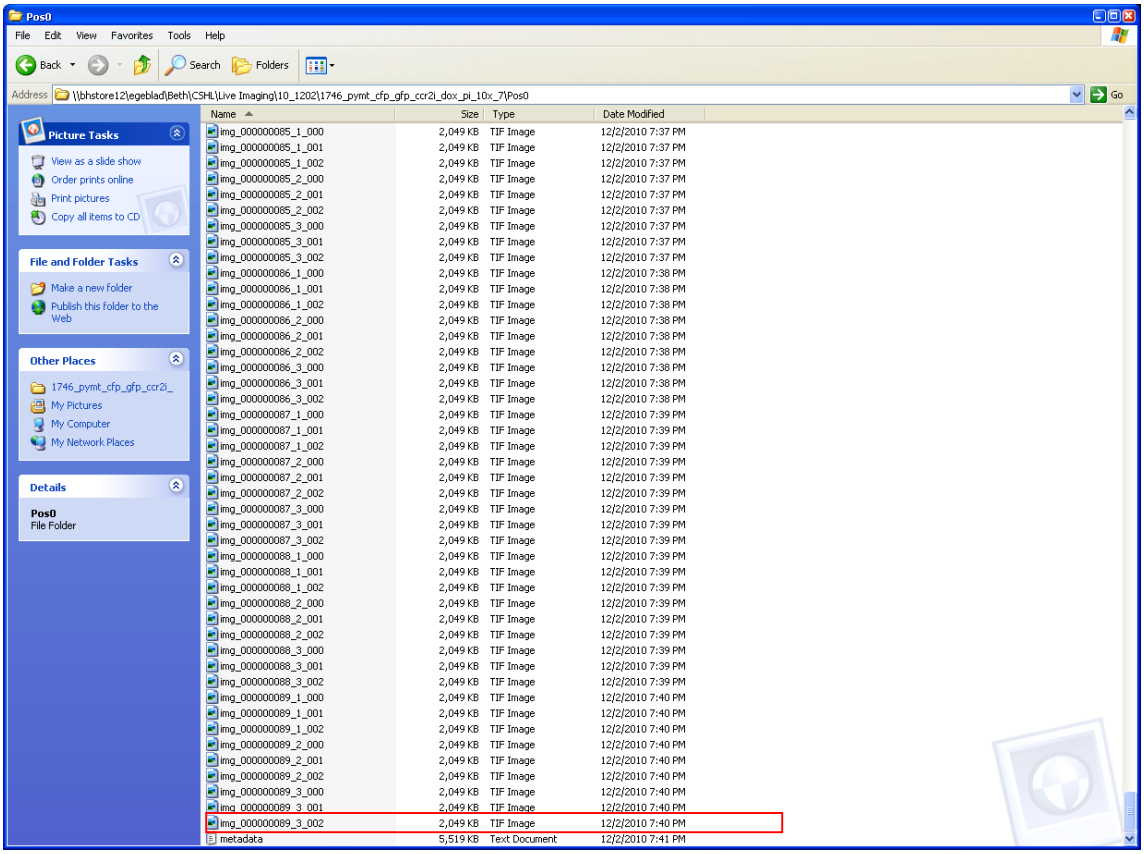

Column H: This is the number of time points in the Experiment. Look at the last TIFF file in the experiment. The file reads img_**000000089**_3_002. The number in bold represents the last time point acquired. The number of time points in the experiment is **89 + 1**. µManager starts counting at **0**, not 1.

Column I: This is the imaging time. This is calculated in minutes. To do this, subtract the hour quantity of the **Start Time** from the **End Time**, and multiply this by 60 minutes. Do the same for the minute quantity. Add the resulting values.

Imaging Time: (Column F – Column D) × 60 min + (Column G – Column E)

Columns J and K: This is the time that elapses between each frame (this is generally on the order of 1 min and several seconds). The calculations are as follows:

Minutes (Column J): INT(Imaging Time) / (Time Points – 1)
= INT(Column I) / (Column H – 1)

The INT function rounds this value to the nearest integer. You must subtract 1 from the number of time points, so that the last time point will have the same value as your imaging end time.

Seconds (Column K): (((Imaging Time) / (Time Points– 1)) – Minutes) × 60 sec
= (((Column I) / (Column H – 1)) – Column J) × 60 sec

The expression enclosed by the red parentheses gives you the imaging time in minutes (the value should appear as X.XX, where the X to the left of the decimal point is the same value that appears

in Column J). The expression enclosed by the blue parentheses gives you the values after the decimal point. This fraction needs to be converted into a value of seconds, so you need to multiply the final number by 60 sec.

Columns L, M, and N: This gives you the time stamp for your movie. We first need to calculate the number of **minutes elapsed since treatment**. The equation for this is as follows:

Minutes (Column L): (Hour Value at Imaging Start) × 60 min + (60 – Min Value at Injection + Min Value at Imaging Start)
= (Column D) × 60 min + (60 – Column C+ Column E)

We go on to calculate the time stamp at the start of the movie, using the following equations.

Hour (Column M): INT(Elapsed Time in minutes) / (60 min)
= INT(Column L) / (60 min)
If 24, 48, etc. hours have passed the calculation becomes:
INT((Column L) / (60 min) – 24 hours)

Minutes (Column N): (Elapsed Time in minutes, i.e. Column L) – (60 min × Hour)
= (Column L) – (60 min × Column M)
If 24, 48, etc. hours have passed the calculation becomes:
(Column L) – (60 min × Hour) – (24 hours × 60 min)

Column O: This is the frame rate. We usually set this to 600× real time speed. The calculation is as follows:

Frame Rate: (Desired Frame Rate) / (Minute Value for Time Between Frames × 60 seconds + Seconds Value for Time between Frames

COMPILING ORIGINAL TIFF FILES INTO AN IMARIS FILE:

1. Open Imaris.
2. Open Batch Convert by going to File > Batch Convert.
3. The Imaris File Converter window should open.

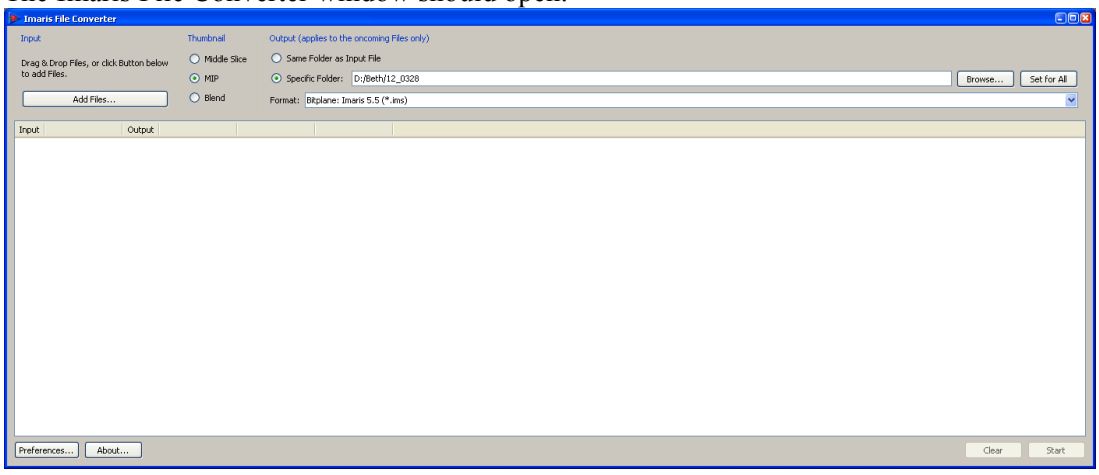

4. Check “Specific Folder,” and then Click on the button that says “Browse…”. Create a new folder or choose a location to save the final output file. Then click OK.

Once this has been done, click the button that says “Set for All.”

5. Locate and open the folder containing the raw images captured using the Egeblad laboratory spinning disk confocal microscope.
6. Drag a single TIFF file from this folder into the Imaris File Converter window.

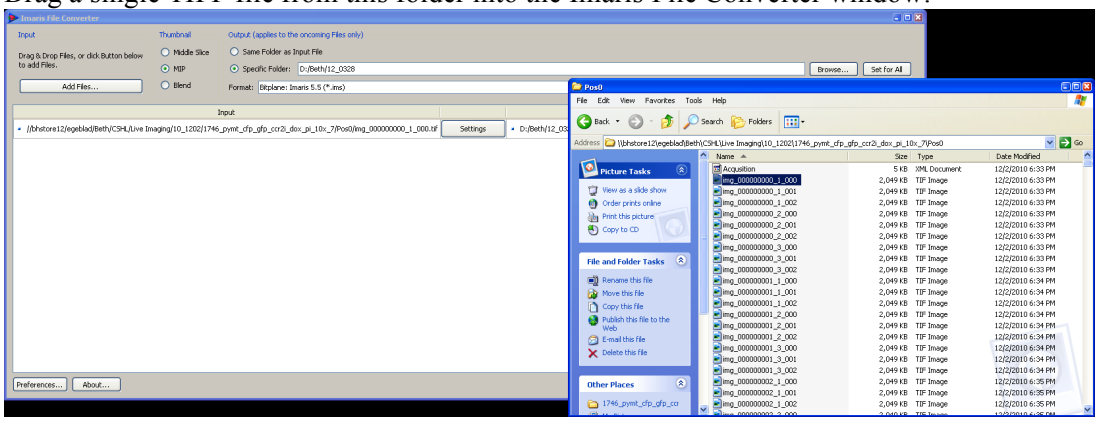

7. Do this for each position for each experiment.
8. Click on the “Settings” button next to the first file. The following window will appear.

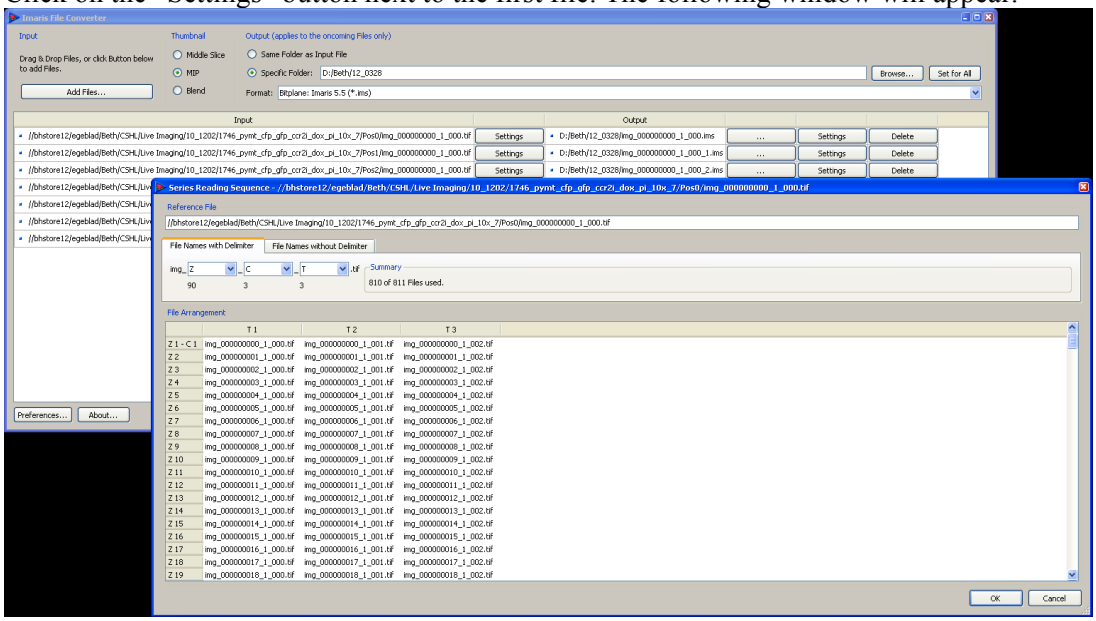

9. Remember that µManager automatically stores each individual image as img_timepoint_channel_zslice. Change each box accordingly and click on the “OK” button.

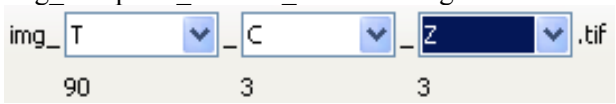

10. Click on the “ … ” button next to the Output for the first file. This button will allow you to change the name of the file. The default pathway for saving files in µManager gives you a file

that says something like “img_000000000_1_000.” When Imaris converts files, the original Input name is the same as the final Output name, so if this is not changed, all information about the experiment is lost. **You need to change the names manually before you convert the TIFFs to an Imaris file**.

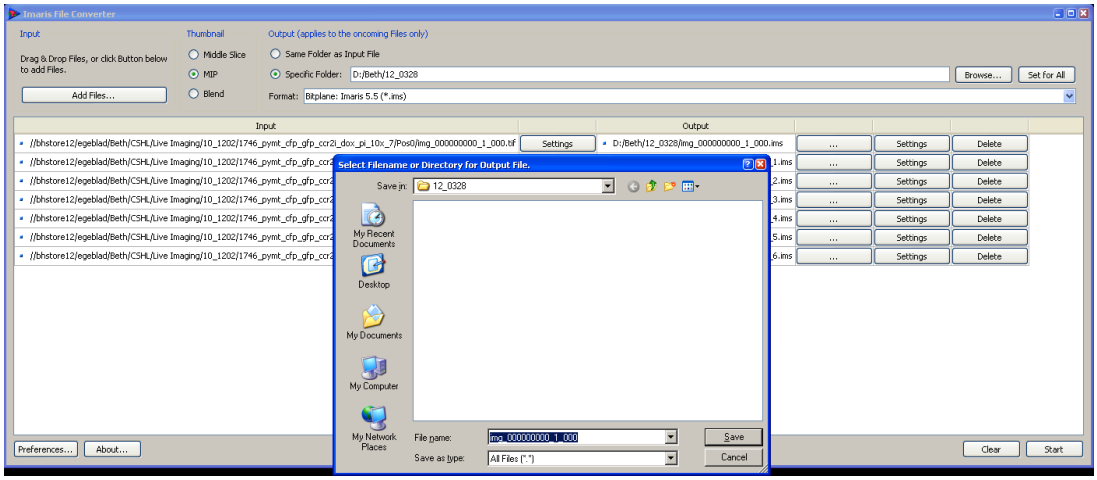

11. Click the “Save” button.
12. Repeat Steps 8-11 for each file that you have dragged into the Imaris File Converter window.
13. Click the “Start” button. Your files will automatically be saved in the specified folder.

ADJUSTING THE IMAGE SETTINGS:

1. Open an Imaris file. You will get two windows: the Imaris window and the Display Adjustment window (if the Display Adjustment window does not open automatically, go to Edit > Show Display Adjustment).

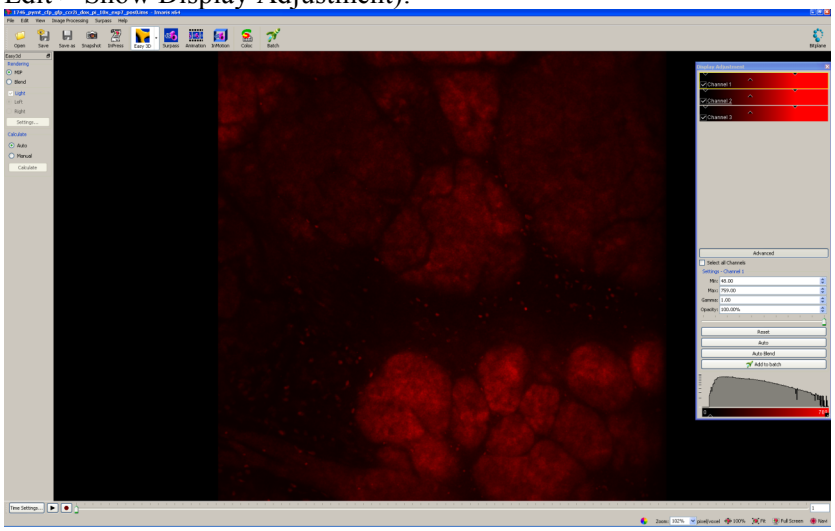

2. In the Display Adjustment window, click on the “Channel 1” button. The Image Properties window will appear.

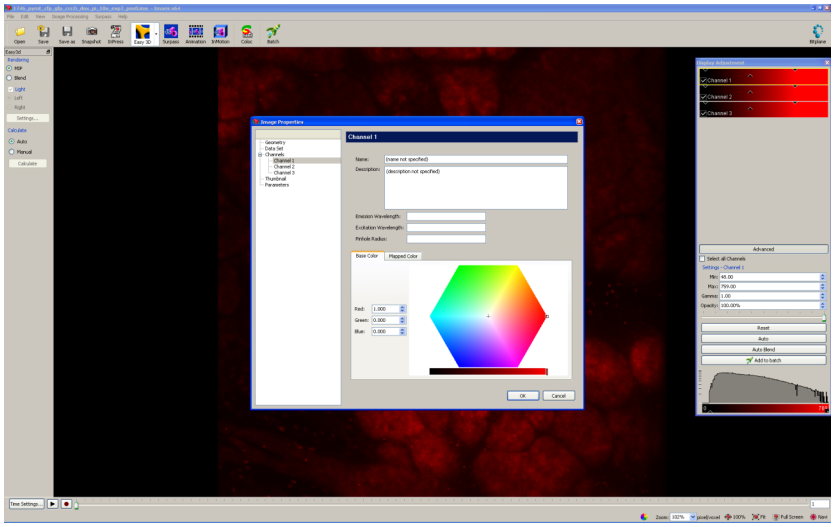

3. Channel 1 should be highlighted on the left. Change the Name of this channel and the color. In this example, this is a β-actin mouse, so the name will be "ACTB-ECFP," and the color will be blue. Generally, Channel 1 = CFP signal, Channel 2 = GFP signal, Channel 3 = RFP signal, and Channel 4 = Far Red signal.

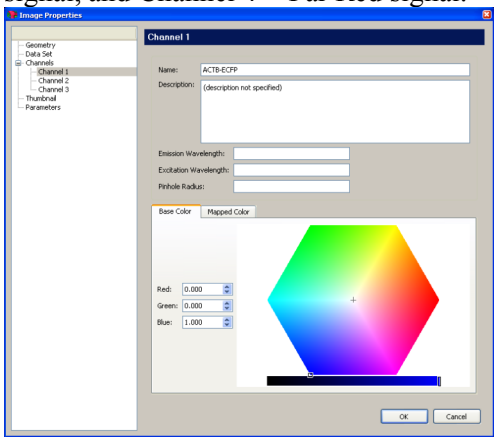

4. Repeat Step 3 for each channel.
5. Click on Geometry. The window will now look like this.

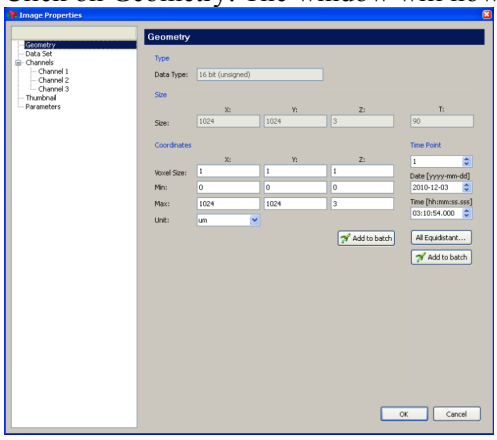

6. Input the correct voxel size. (A voxel is a *volumetric pixel*: this is the three-dimensional volume represented by each pixel.)

	x	*y*	*z*
10× Objective	0.66	0.66	8
20× Objective	0.33	0.33	8
40× Objective	0.167	0.167	2

These values are in µm. The values input for *z* will change depending on how many µm apart each step between z-slices has been set to. For the *z* setting, these values are what we usually use for intravital imaging experiments (although this may change depending on the experiment); for slides, this may be 1-2 µm.

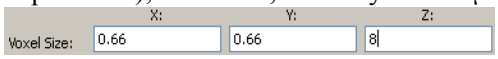

7. Click on the "All Equidistant" button. This will allow you to set the time between frames and the start time. The Set Equidistant Time Points window will appear.

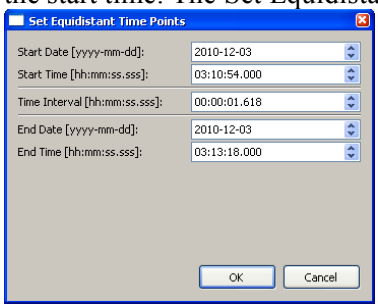

8. Using the information you calculated in the previous section, input the appropriate values for "Start Time" and "Time Interval."

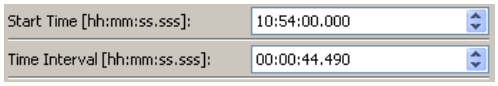

9. Click the "OK" button. The Set Equidistant Time Points window will close.
10. Click the "OK" button in the Image Properties window. It will close.
11. On the bottom right corner of Imaris, click on the "Fit" button.

Your screen will now look something like this:

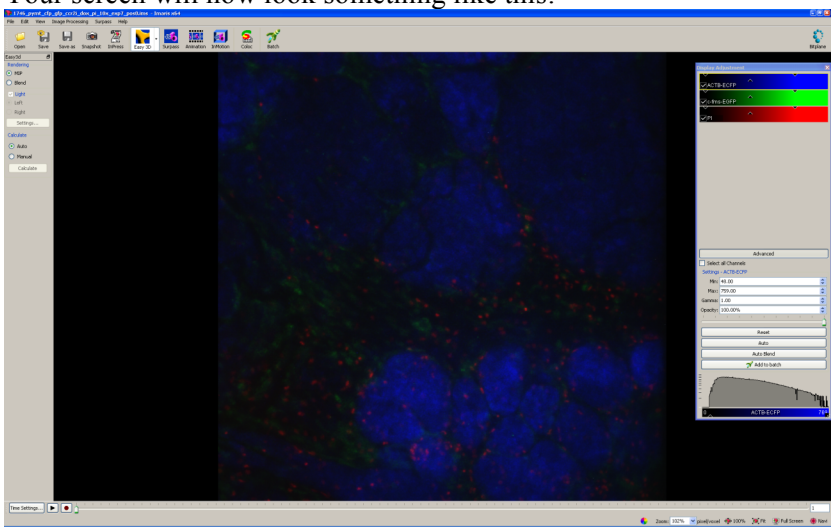

12. You can change the color intensity and background levels for each channel in the Display Adjustment window, by dragging the black arrows in each channel or inputting specific values under Settings.

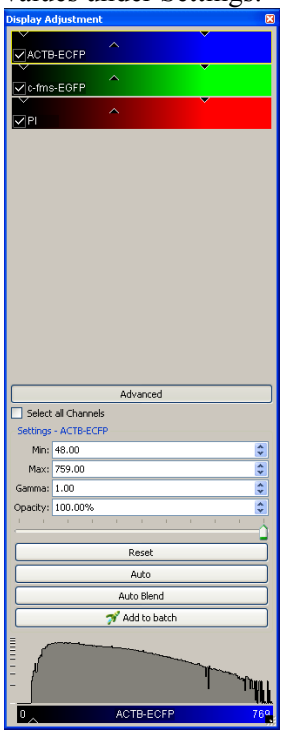

Adjusting the color using the arrows: The channel surrounded by the yellow box is the channel that has been selected. The arrow on the left shows the lower limit cutoff, and will usually help to get rid of some of the background as it moves right. The arrow on the right shows the upper limit, and enhances the intensity of the signal as it moves left.

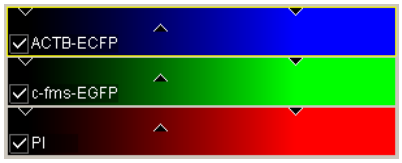

Numbers can be input manually (for example, if you already known your cutoff values for quantification purposes). The Gamma should always = 1.00 and the Opacity should always = 100%.

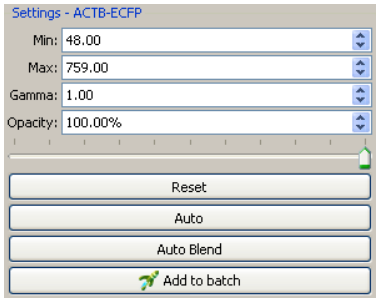

TAKING PICTURES IN IMARIS:

1. Click on the "Snapshot" button (the default is usually to have the image in Easy 3D – this will give you a maximum intensity projection consisting of the entire z-stack).

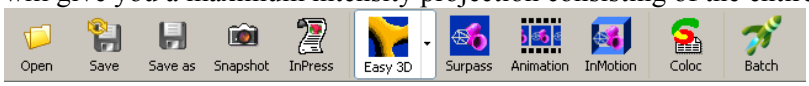

Your screen will now look like this.

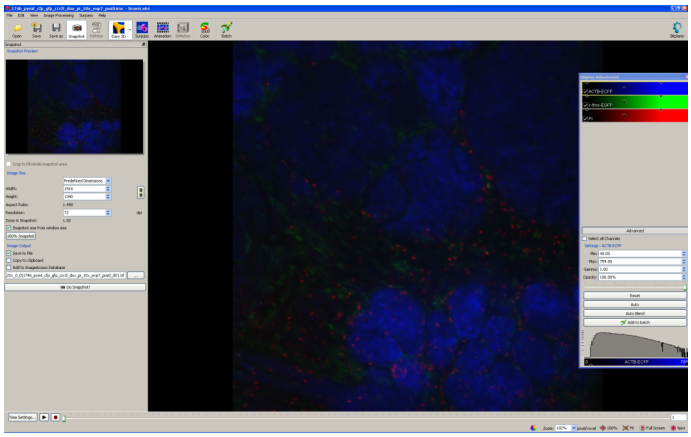

2. In the Snapshot Panel

Uncheck the box next to "Crop to fill whole snapshot area."
Image Size: select "Predefined Dimensions"
Width: 1024 (this is in pixels)
Height: 1024 (this is in pixels)
Resolution: 600 (this is in dpi)
Uncheck the box next to "Snapshot size from window size."
Designate the location and name for the snapshot by clicking the " … " button.

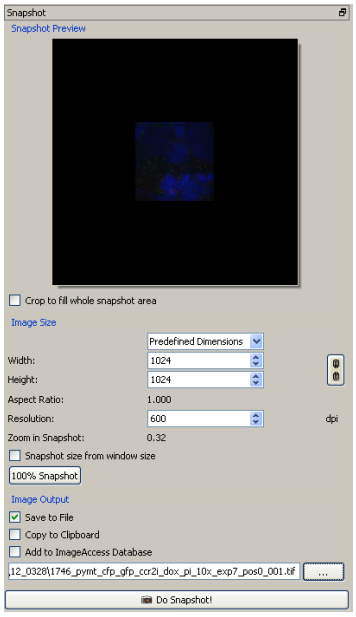

3. Click the "Do Snapshot!" button.

4. To take images of a single z-slice, click on the Easy 3D button, and select Slice.

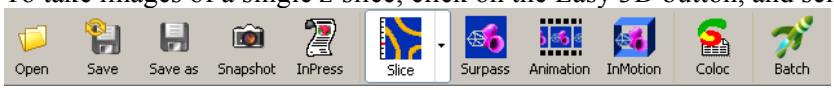

5. Your work area will now look like this.

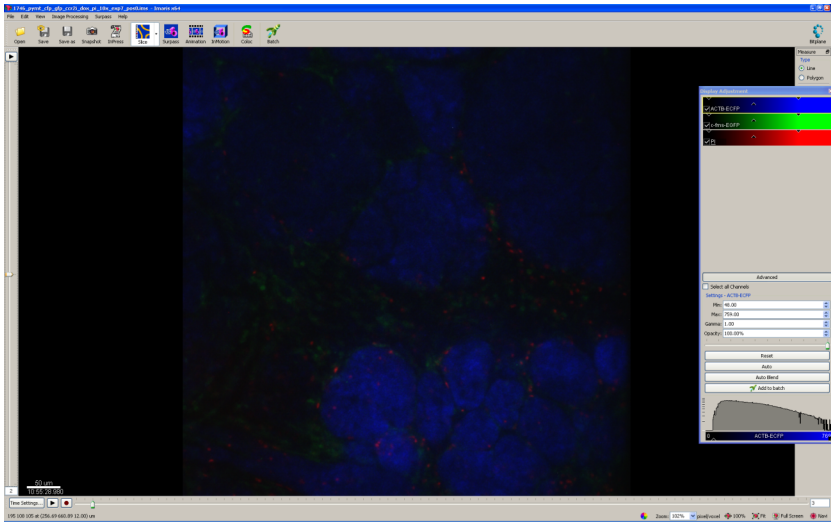

6. You can scroll through the z-slices on the left, either by moving the pointer up and down to another tick, or by manually inputting the slice you want to take a snapshot of (bottom left). Frames in the experiment are similarly arranged below the image, so you can scroll between each frame or manually input the frame you want to be on (bottom right).

SHOWING THE SCALE BAR AND TIME STAMP:

1. To show the scale bar, scale size, and image time, go to Edit > Preferences. The Preferences window will appear.

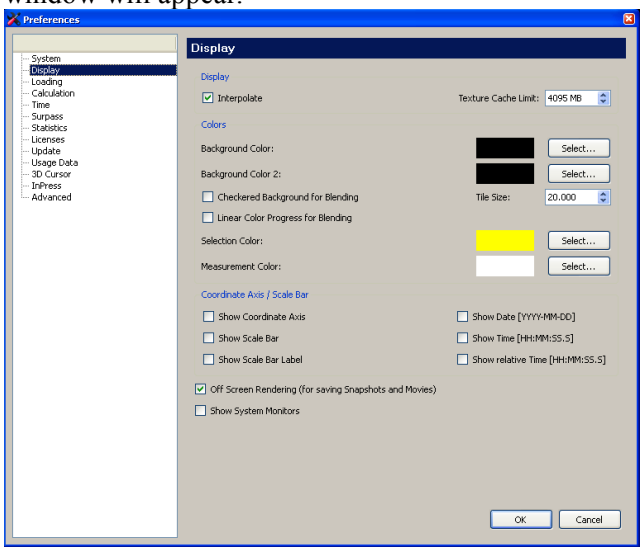

Under Coordinate Axis / Scale Bar, check boxes next to “Show Scale Bar,” “Show Scale Bar Label,” and the “Show Time [HH:MM:SS.S].”

2. Click the "OK" button.
3. The scale bar can be adjusted by clicking on the scale bar and stretching or shrinking it.

EXPORTING MOVIES FROM IMARIS:

1. Put Imaris into window resize mode. To do this, the buttons at the top right in the Imaris window should look like this:

If this not what you see, click on the middle button.

2. On the bottom right corner of Imaris, click on the "Fit" button

3. Resize the Imaris window so that Zoom: 50%. Click on the "Fit" button each time you resize the Imaris window, so that you know the actual zoom size.

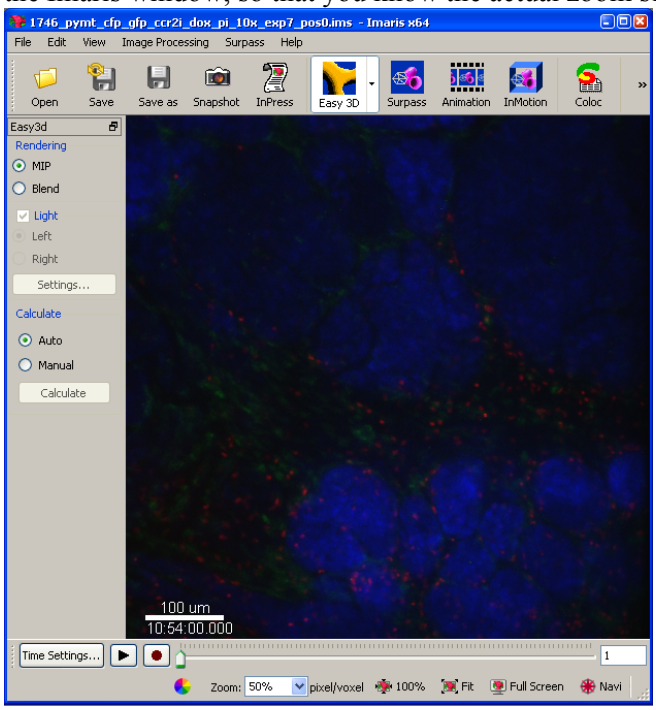

4. Click on the Record button (this is the button with the red dot).

The Save As Movie window will open.

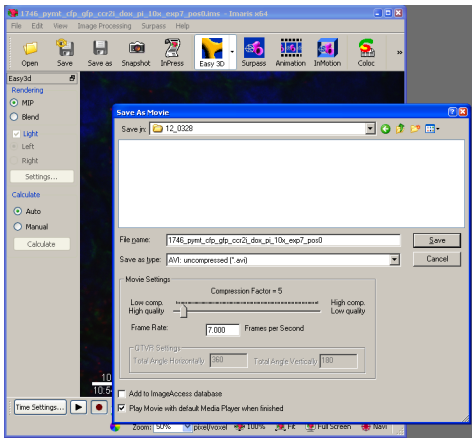

5. Designate a location to save the movie and the movie name (the default is the same name as the Imaris file).
6. Under movie settings, change the Frame Rate to the rate that you previously calculated. The compression factor can be left at 5. (You don't need to compress the movie, but this makes the movie file very big).

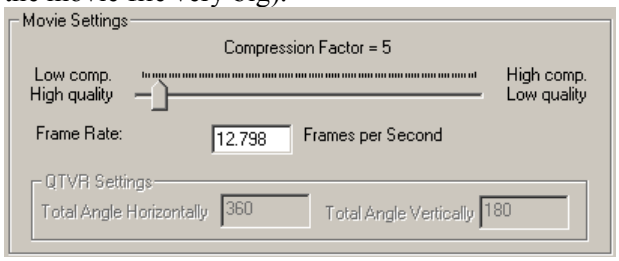

7. Click the "Save" button.

CROPPING 3D IMAGES IN IMARIS:

1. Go to Edit > Crop 3D. The Crop 3D window will appear.

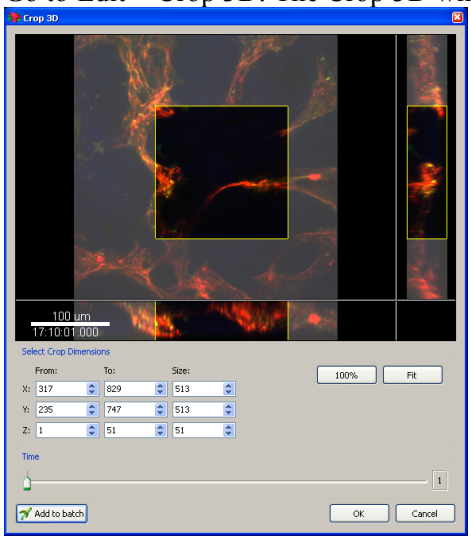

2. Enter in the desired crop dimensions. For *x* and *y*, From and To give the location of the area to be cropped, while Size gives you the dimension in each direction of the cropped field.

These values are in pixels. For *z*, From and To designate the slice number (number goes from 1 = lowest slice to X = top slice), and Size is the number of total slices in the cropped image.

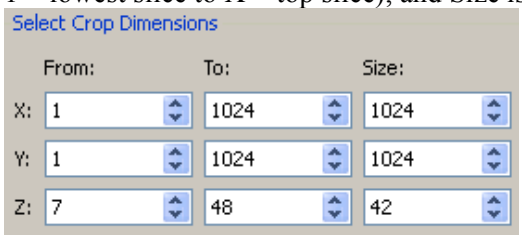

In this example, we only want to crop in *z*, so we set the From and To for *x* and *y* to 1 and 1024, respectively, and just change the values of From and To for *z*.

3. Click on the "OK" button.
4. Go to File > Save As, and save cropped Imaris file. Clicking on Save will overwrite the original file, and in most cases you want to save the original file.

QUANTIFICATION OF VASCULAR LEAKAGE:

1. Crop each image so that the *z*-slices without any information are removed. Each field will have a different number of z-slices after this. The final volume for each field will be (n – 1) μm.
2. Save the cropped Imaris file.
3. Click on Surpass.

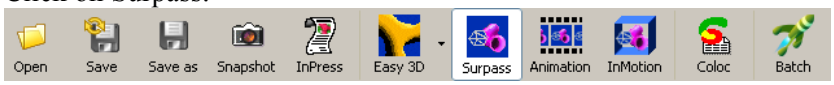

Your work area will now look like this.

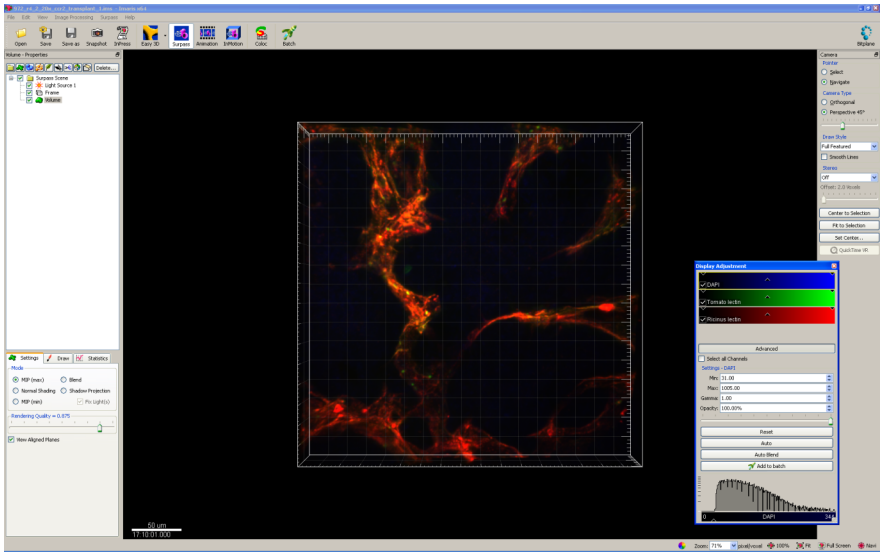

4. In the Camera Panel on the right hand of the work space, check the boxes next to "Select" and "Orthogonal."

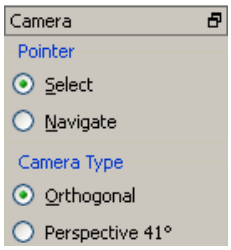

5. In the Surpass panel, the “Surfaces” button.

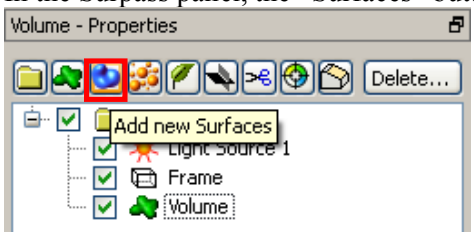

A new line called “Surfaces 1” will appear.

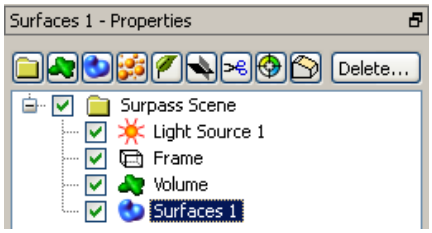

6. When you highlight this line, a Settings Panel will appear below.

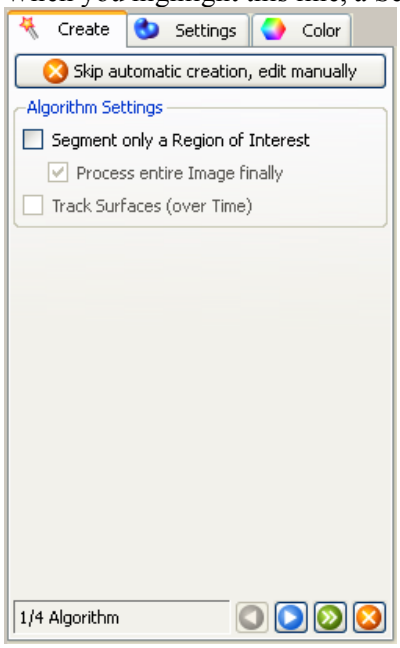

7. Click on the Create tab.

a. Under Algorithm Settings, check the box next to “Segment Only a Region of Interest”

b. Click on the button.

c. In the Display Adjustment window, uncheck the boxes next to the DAPI channel and the *Ricinus* lectin channel, and make sure that for the two lectin channels, the left black arrows are at the minimum value and the left black arrows are at the maximum value.

d. Create 3 regions of interest (50 to 100 pixels in size).

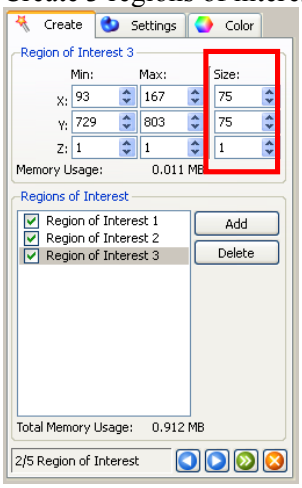

Place your regions of interest in areas near blood vessels or in areas containing the highest degree of background.

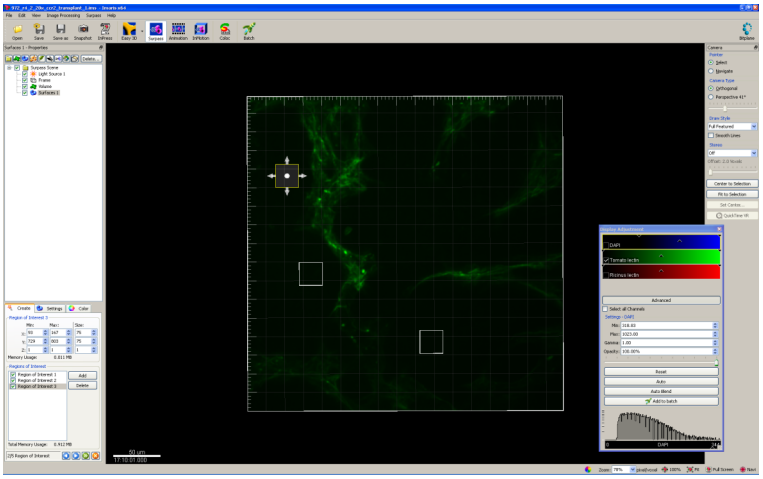

e. Click on the button.

f. Select the tomato lectin channel and then check the boxes next to “Smooth” and “Absolute Intensity.” You can use the default setting for “Smooth” (this is calculated as the *x*,*y* voxel size multiplied by 2, so for an image acquired using the 20× objective, the value is 0.33 × 2 = 0.66).

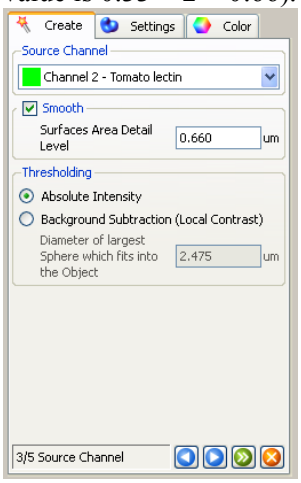

g. Click on the button. Your work space will now look like this.

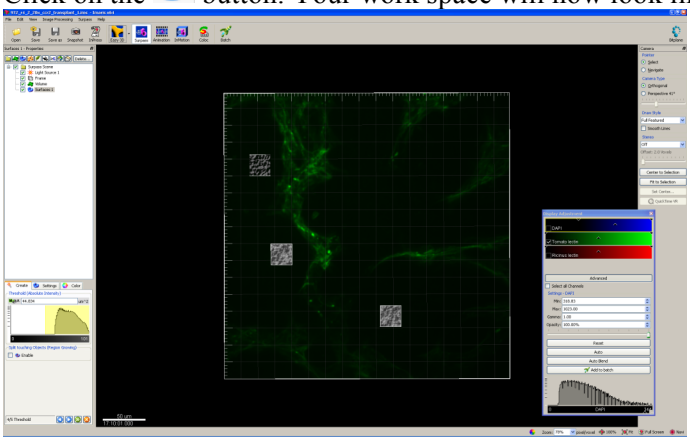

h. Change the area of the yellow shading in the Surpass panel (leave the box next “Enable” unchecked), so that there are no pixels in any of the three regions of interest that you have selected.

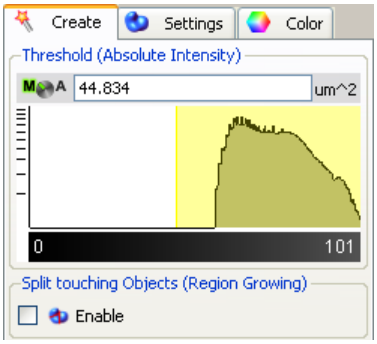

Your work space should look like this.

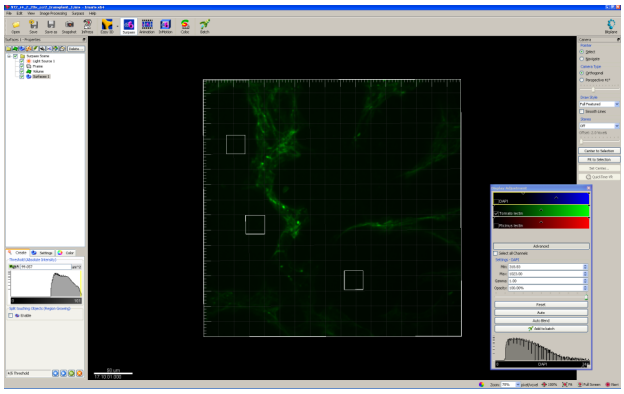

i. Record the number that appears above the histogram. This number multiplied by 1.3 is the background setting. (The 1.3 multiplier is not set in stone. You may need to use a background cutoff that is higher or lower depending on the tissue sample and how well it stained.

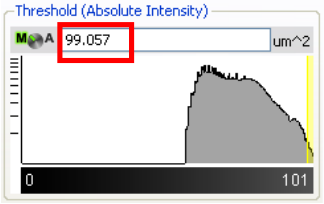

j. Click the button until you reach the "Algorithm" page (the first one) of the Surpass panel.

k. Repeat steps 9a through 9i for the *Ricinus* lectin channel.

8. Click the button until you reach the "Algorithm" page (the first one) of the Surpass panel.

9. Check the boxes next to "Segment Only a Region of Interest" and "Process entire Image finally."

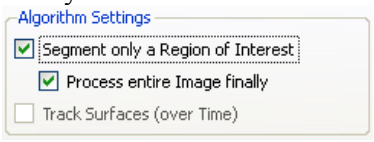

10. Click on the button. Make 1 region of interest that encompasses the entire field. The workspace should look like this:

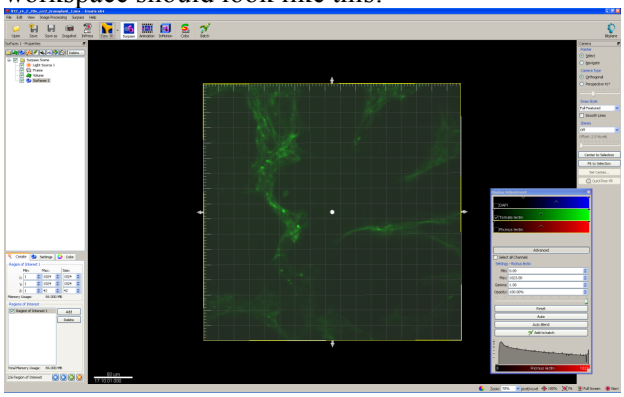

The Surpass panel should look like this:

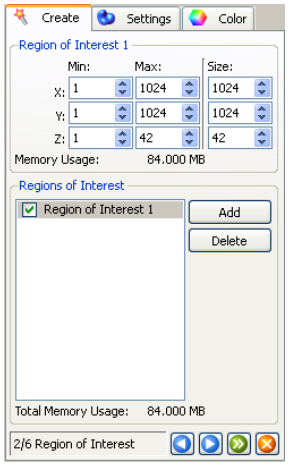

11. Click on the button.
12. Select the tomato lectin channel. Make sure that in the Display Adjustment window, only the tomato lectin channel is selected.
13. In the Surpass panel, select the tomato lectin channel and then check the boxes next to "Smooth" and "Absolute Intensity." You can use the default setting for "Smooth" (this is calculated as the *x*,*y* voxel size multiplied by 2, so for an image acquired using the 20× objective, the value is 0.33 × 2 = 0.66).

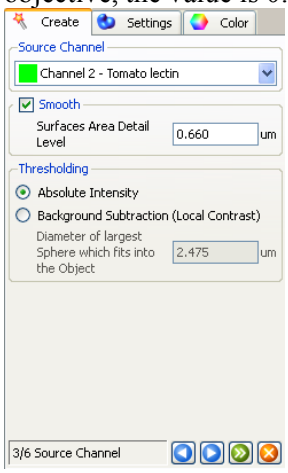

14. Click on the button.
15. In the Threshold panel, input the value that you calculated in 7i.

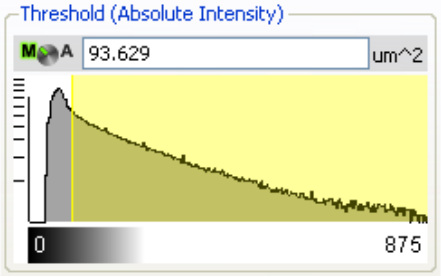

Your workspace should look like this. If the calculated threshold is too stringent, adjust the threshold until you get most of the blood vessels and very little background.

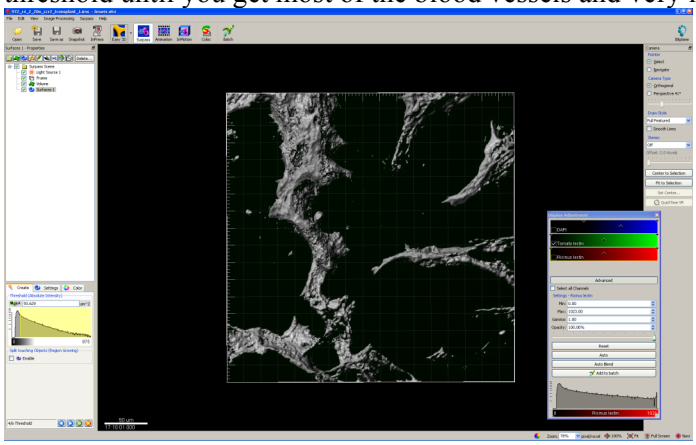

16. Click on the button.
17. In the Filters panel, click on the "+ Area" button to add a filter. Under Filter Type, select "Number of Voxels." The left limit should be green and have a value between 100 and 500. The right limit should be red.

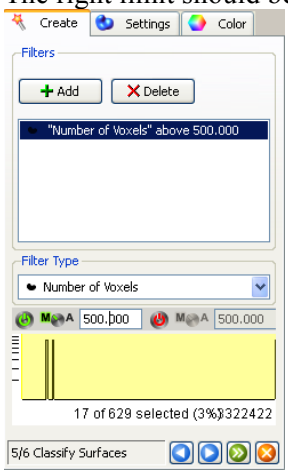

18. Click on the button.
19. Click on the button. Your work space will now look like this.

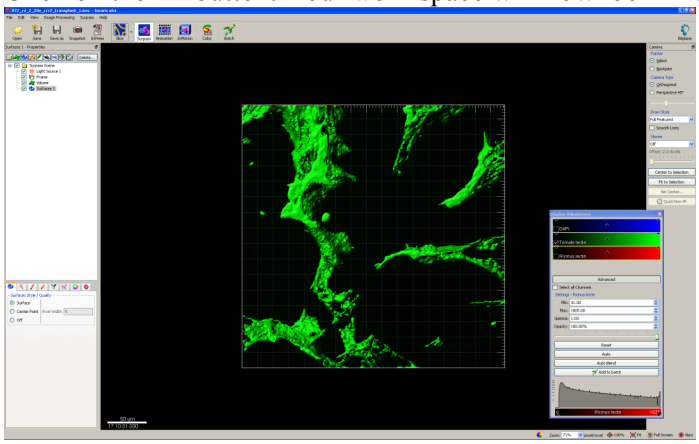

20. In the Surpass panel, click on the Edit button.

21. Click on the “Mask All…” button.

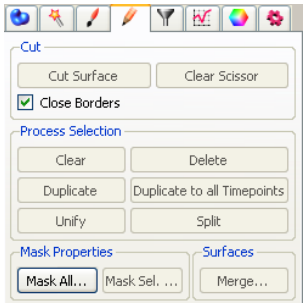

22. In the Mask Channel window, select the tomato lectin channel. Check the box next to “Duplicate channel before applying mask.” Select the “Constant inside/outside” option.

    Set voxels outside surface to: 0
    Set voxels inside surface to: 255

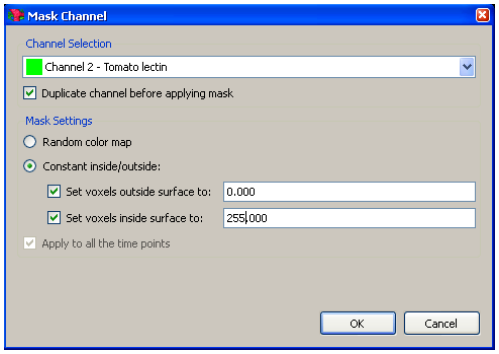

23. Click on the “OK” button. Another channel should appear in the Display Adjustment window.

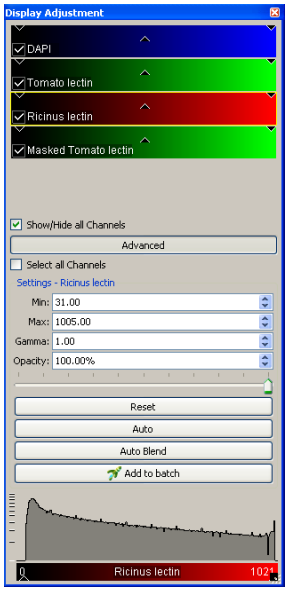

Your work space should look like this.

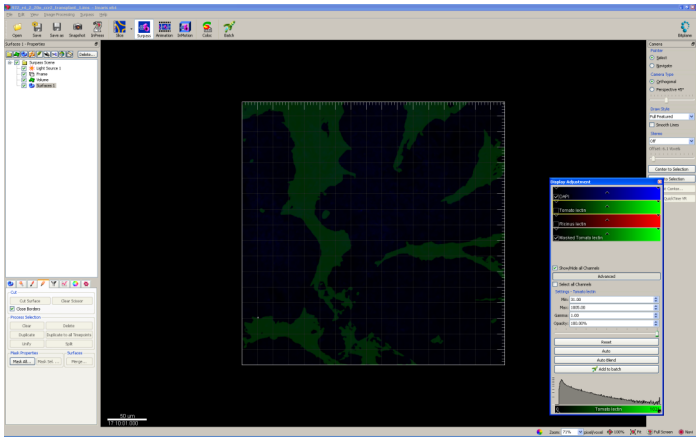

24. Create a new Surface, then repeat Steps 8-23 for the *Ricinus communis* lectin.
25. Switch to the Colocalization mode by clicking on the “Coloc” button.

26. Select the two channels you want to colocalize (these will be the two masked channels).

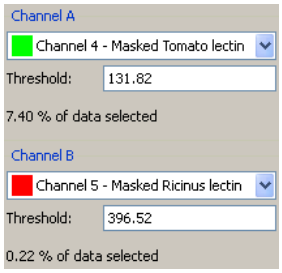

27. In the 2D histogram, set the thresholds so that the pink dot (at the tip of the white arrow) is included in this threshold.

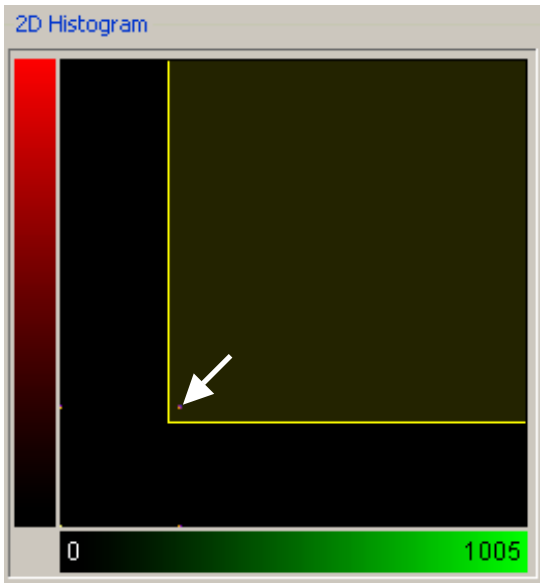

28. Click on the “Build Coloc Channel” button.

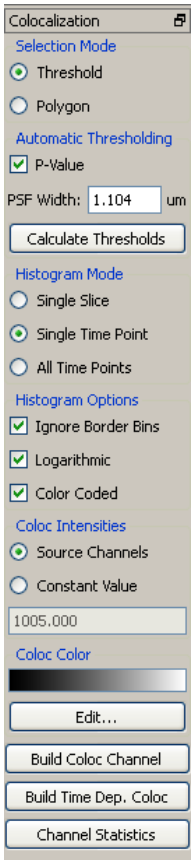

29. Click on the new Colocalization channel. The Image Properties window will appear.

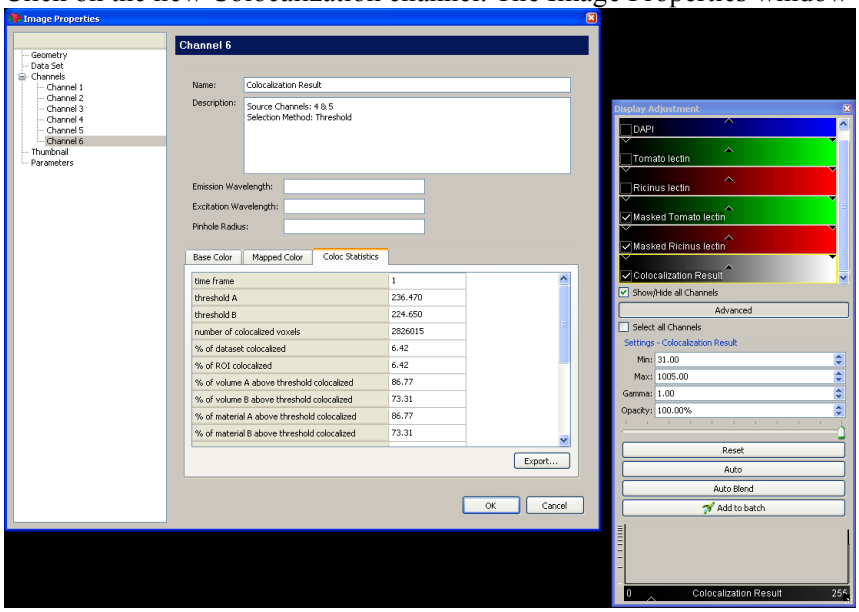

30. Click on the “Export” button.

XIV. Immunostaining antibody information

PRIMARY ANTIBODY PURCHASING INFORMATION

Antigen	Host Species	Clonality	Clone	Supplier	Cat. No.
α-Smooth Muscle Actin	Mouse	Monoclonal	1A4	Sigma Aldrich	A5228
BrdU	Mouse	Polyclonal	—	Developmental Studies Hybridoma Bank	G3G4
Mouse Neutrophils	Rat	Monoclonal	7/4	Cedarlane Laboratories Ltd.	CL8993AP
CCR2	Rabbit	Monoclonal	E68	Novus Biologicals	NB110-55674
CD31	Rabbit	Polyclonal	—	Abcam	ab28364
CD206	Rat	Monoclonal	MR5D3	AbD Serotec	MCA2235GA
Endothelial Cell Marker	Rat	Monoclonal	MECA-32	Developmental Studies Hybridoma Bank	MECA-32
F4/80	Rat	Monoclonal	CI:A3-1	AbD Serotec	MCA497R
MCP-1	Rabbit	Polyclonal	—	AbD Serotec	AAM43
p-Histone H2A.X	Rabbit	Monoclonal	20E3	Cedarlane Laboratories Ltd.	9718S
p-Histone H3 (Ser10)	Rabbit	Polyclonal	—	Cell Signaling Technology	9701S
p-VE Cadherin (Tyr731)	Rabbit	Monoclonal	19A10	Cell Signaling Technology	2478S

PRIMARY ANTIBODY EXPERIMENTAL CONDITIONS (SINGLE LABEL STAIN)

Antigen	Tissue	Antigen Retrieval	Blocking	Dilution	Incubation Time	Visualization
BrdU	Paraffin	6 min, citrate	Mouse on Mouse	1:200	30 min room temp	Fluorescence
Mouse Neutrophils	Paraffin	6 min, citrate	Fc Receptor Block (Innovex)	1:400	1 hour room temp	Fluorescence
CD206	Frozen	—	Fc Receptor Block (Innovex)	1:200	1 hour room temp	Fluorescence
F4/80	Frozen	—	Fc Receptor Block (Innovex)	1:200	1 hour room temp	Fluorescence
MCP-1	Paraffin	6 min, citrate	Fc Receptor Block (Innovex)	1:100	1 hour room temp	Fluorescence
p-Histone H2A.X	Paraffin	15 min, citrate	Fc Receptor Block (Innovex)	1:500	1 hour room temp	DAB
p-Histone H3 (Ser10)	Paraffin	15 min, citrate	Fc Receptor Block (Innovex)	1:50	1 hour room temp	DAB
p-VE Cadherin (Tyr731)	Paraffin	6 min, Tris-EDTA	Fc Receptor Block (Innovex)	1:300	1 hour room temp	Fluorescence

PRIMARY ANTIBODY EXPERIMENTAL CONDITIONS (DOUBLE LABEL STAIN)

Antigen	Tissue	Antigen Retrieval	Blocking	Dilution	Incubation Time	Visualization
CD31 αSMA	Paraffin	6 min, Tris-EDTA	Mouse on Mouse (Vector Labs)	1:1500 1:25	Over night at 4°C* 1 hour room temp	Fluorescence
CCR2 MECA-32	Frozen	—	Mouse on Mouse (Vector Labs)	1:200 1:50	30 min room temp	Fluorescence
CCR2 7/4	Paraffin	20 min, citrate	Fc Receptor Block (Innovex) AND 1× Blocking Solution	1:200 1:400	30 min room temp	Fluorescence
MCP-1 (CCL2) 7/4	Paraffin	6 min, citrate	Fc Receptor Block (Innovex)	1:100 1:400	1 hour room temp	Fluorescence
MCP-1 (CCL2) CD206	Paraffin	6 min, citrate	Fc Receptor Block (Innovex)	1:100 1:200	1 hour room temp	Fluorescence
MCP-1 (CCL2) αSMA	Paraffin	6 min, citrate	Mouse on Mouse (Vector Labs)	1:100 1:1500	1 hour room temp	Fluorescence
MECA-32 MCP-1 (CCL2)	Paraffin	6 min, citrate	Fc Receptor Block (Innovex)	1:200 1:50	Over night at 4°C* 1 hour room temp	Fluorescence

*Double labeling was done with serial staining of the blood vessel antibody overnight, followed by a 1 hour room temperature incubation with the second primary antibody. For all other double label stains, antibodies were applied to the tissue simultaneously in the same 0.5× blocking buffer solution.

SECONDARY ANTIBODY PURCHASING INFORMATION

Antigen	Conjugate	Target Species	Supplier	Cat. No.
Alexa Fluor® 568 F(ab')2 fragment of goat anti-mouse IgG (H+L)	Alexa568	Mouse	Invitrogen	A-11019
Alexa Fluor® 568 F(ab')2 fragment of goat anti-rabbit IgG (H+L)	Alexa568	Rabbit	Invitrogen	A-21069
Alexa Fluor® 568 goat anti-rat IgG (H+L)	Alexa568	Rat	Invitrogen	A-11077
Alexa Fluor® 647 F(ab')2 fragment of goat anti-mouse IgG (H+L)	Alexa647	Mouse	Invitrogen	A-21237
Alexa Fluor® 647 F(ab')2 fragment of goat anti-rabbit IgG (H+L)	Alexa647	Rabbit	Invitrogen	A-21246
Alexa Fluor® 647 goat anti-rat IgG (H+L)	Alexa647	Rat	Invitrogen	A-21247
Goat Anti-Rabbit IgG, F(ab')2-B	Biotin	Rabbit	Santa Cruz Biotechnology, Inc.	sc-3840

SECONDARY ANTIBODY EXPERIMENTAL CONDITIONS (SINGLE AND DOUBLE LABEL STAINS)

Antigen	Dilution	Incubation Time	Application
Alexa Fluor® 568 F(ab')2 fragment of goat anti-mouse IgG (H+L)	1:150	30 min at room temp	Fluorescence
Alexa Fluor® 568 F(ab')2 fragment of goat anti-rabbit IgG (H+L)	1:150	30 min at room temp	Fluorescence
Alexa Fluor® 568 goat anti-rat IgG (H+L)	1:150	30 min at room temp	Fluorescence
Alexa Fluor® 647 F(ab')2 fragment of goat anti-mouse IgG (H+L)	1:150	30 min at room temp	Fluorescence
Alexa Fluor® 647 F(ab')2 fragment of goat anti-rabbit IgG (H+L)	1:150	30 min at room temp	Fluorescence
Alexa Fluor® 647 goat anti-rat IgG (H+L)	1:150	30 min at room temp	Fluorescence
Goat Anti-Rabbit IgG, F(ab')2-Biotin	1:400	1 hour at room temp	Histochemistry

For all double label stains, antibodies were applied to the tissue simultaneously in the same 0.5× blocking buffer solution.

XV. Flow cytometry antibody information

Antigen	Conjugate	Clone	Supplier	Cat. No.	Blocking	Dilution	Incubation Time
CD11b	RPE	M1/70	BD Pharmingen	557397	Fc Block (Abd Serotec)	1:200	30 min at 4°C
F4/80	FITC	CI:A3-1	AbD Serotec	MCA497FA	Fc Block (Abd Serotec)	1:100	30 min at 4°C
Gr1 (Ly-6G and Ly-6C)	APC/Cy7	RB6-8C5	BD Pharmingen	557661	Fc Block (Abd Serotec)	1:100	30 min at 4°C
Ly6B.2 (7/4)	Alexa 647	7/4	AbD Serotec	MCA771A647	Fc Block (Abd Serotec)	1:100	30 min at 4°C